Development of gold enhanced surface plasmon resonance polymer and nanowire waveguides for optical sensing

Charusluk Viphavakit

School of Mathematics, Computer Science & Engineering

A thesis submitted to the City, University of London in partial fulfillment of the requirements for the degree of Doctor of Philosophy

City, University of London
London, United Kingdom
May 2018

I would like to dedicate this thesis to my parents

Table of Contents

List of Tables

List of Figures

Acknowledgement

I would like to express my sincere gratitude to all those people who supported me throughout my doctoral studies and the completion of this dissertation. Foremost, my deepest gratitude is to my advisor, Professors Azizur Rahman. He shared his endless enthusiasm and motivation with me. His scientific guidance and continuous suggestions were extremely valuable for my research. He has helped me improve my knowledge in these areas considerably. I am thankful for his patience in reading and commenting on countless revisions of all my works, especially this dissertation. His guidance made me develop valuable abilities such as paying attention to detail, organizing my work and presenting my results.

I am thankful to my co-advisors, Dr. Christos Themistos and Prof. Michael Komodromos, at Frederick University in Cyprus and Dr. Waleed S. Mohammed, at Bangkok University in Thailand, who have always been there to listen and give me good advice which helped me overcome the hardships during my PhD studies. In addition, I would like to acknowledge the National Electronics and Computer Technology Center (NECTEC), Dr. Sakoolkarn Boonruang, Thai Microelectronics Center (TMEC) and Mr. Nithi Atthi for providing me with access to use all the facilities in their laboratory and cleanroom for my experimental work performed in Thailand.

My sincere thanks to the Erasmus Mundus program StrongTies, for awarding me with a PhD scholarship. Through my PhD studies, I gained not only the scientific knowledge but life experiences. I had the chance to meet several people from all over the world and gained many friends. I am thankful to the program for the opportunity to have one of the most memorable periods in my life.

Finally, I would like to express my special thanks to my lovely family. Their understanding, encouragement and never-ending support mean everything to me.

Declaration

I grant powers of discretion to the City University Librarian to allow this thesis to be copied in whole or in part without further reference to the author. The permission covers only single copies made for study purposes, subject to normal conditions of acknowledgement.

Abstract

The recent advances in nanotechnology have created the need for the development of materials and devices with unique properties, suitable for applications in related areas such as nano-electronics, nano-photonics and high sensitivity optical sensing. Nanowires are becoming good candidates for such applications, however, most of the ongoing research is still at the early stage and therefore all the effort in this field is to improve the fabrication techniques, as well as to increase the performance of such devices, by optimizing their key parameters, in order to bring them into the production line.

Ormocomp and silicon nanowire waveguides (NWs) are studied and developed as optical waveguides intended to be used in optical sensing applications. The NWs are designed and developed as part of integrated optical devices by having tapered and feed waveguides connected at both the ends. The ormocomp and the silicon NWs are theoretically investigated using a full-vectorial **H**-field Finite Element Method (FEM). The aim is to obtain high power confinement in the sensing area, which is considered to be the core/cladding interface for the ormocomp NWs and the slot region (low-index area) for the silicon NWs. The modal field and the power confinement of the guided modes that contribute to the enhancement of the sensitivity in the corresponding sensing area of the NWs are studied, with respect to the variation of the refractive index of the cladding material and the operating wavelength. The structure parameters including the width and the height of the NWs are optimized to achieve the maximum possible sensitivity.

A biosensor structure incorporating the silicon NWs with horizontal slot structure is also studied theoretically using the full-vectorial **H**-field FEM. It is designed to detect DNA hybridisation through the change of the effective index of the NW structure. The key parameters, such as power confinement, power density, change in effective index and sensitivity of the fundamental guided optical modes are presented, by optimizing the device parameters of the slot waveguide.

Experimental characterisation of the integrated ormocomp NWs is also demonstrated. The integrated optical ormocomp NWs are used to measure the change of effective index when there is a change of refractive index of the material. An evanescent wave coupling technique is exploited for the ormocomp NW to be used as optical sensors. The evanescent field that exists at the core/cladding interface of the NWs can be enhanced by introducing surface plasmon resonance (SPR).

The SPR is introduced by coating the integrated ormocomp NWs with a thin gold layer with a thickness of around 50-100 nm. The optical power at the output, the attenuation coefficient of the NWs, the SPR peak wavelengths and their shifts are experimentally extracted over three different cladding materials. The redshift of the supermode coupling between the dielectric mode and the anti-symmetric supermode is observed with higher cladding index and larger metal thickness. The power confinement in the sensing region with the SPR effect is improved by a factor of ten compared to the performance obtained by the un-coated ormocomp NWs.

List of abbreviations and symbols

BEM	Boundary Element Method
BPM	Beam Propagation Method
CVD	Chemical Vapor Deposition
DNA	Deoxyribonucleic Acid
dsDNA	Double-stranded DNA
FDM	Finite Difference Method
FEM	Finite Element Method
GUI	Graphical User Interface
NW	Nanowire waveguide
LPCVD	Low-Pressure Chemical Vapor Deposition
LSPR	Localized Surface Plasmon Resonance
PAM	Polyacrylamide
PDMS	Polydimethylsiloxane
PMMA	Polymethylmethacrylate
PR	Photoresist
RIE	Reactive-ion Etching
RIU	Refractive Index Unit
SPR	Surface Plasmon Resonance
SOI	Silicon-On-Insulator
ssDNA	single-stranded DNA
UV	Ultraviolet

α_{wg}	Attenuation coefficient of the waveguide
α_{tp}	Attenuation coefficient of the tapered waveguide
α_{nw}	Attenuation coefficient of the nanowire waveguide
β	Propagation constant
$\tilde{\varepsilon}$	Complex dielectric constant or complex permittivity
θ	Sidewall angle
θ_c	Critical angle
θ_{tp}	Tapered angle
κ	Extinction coefficient
λ	Wavelength
μ	Permeability
π	pi = 3.14159
E	Electric field
H	Magnetic field
H	NW height

ISO11	Iso-propanol solution (Iso-propanol to water with 1:1 volume ratio)
ISO13	Iso-propanol solution (Iso-propanol to water with 1:3 volume ratio)
h_s	Slot height
k_o	Free-space Wavenumber
L_{nw}	NW length
L_o	Total length of the integrated optical NW
L_{tp}	Tapered waveguide length
L_{wg}	Feed waveguide length
ñ	Complex refractive index
n_c	Refractive index of the cladding
n_{eff}	Effective index of the NW
n_{nw}	Refractive index of the core (NW)
n_s	Refractive index of the substrate
S	Poynting vector
Si	Silicon
SiO_2	Silicon dioxide
W	Width of the designed NW
W_{bottom}	Bottom width of the fabricated NW
W_{top}	Top width of the fabricated NW
W_{wg}	Width of the feed waveguide

1. Introduction

1.1 Background

Optical sensors are optical devices consisting of a light source, optical components, and detector. The optical components include optical fibre, lenses, grating, filter, polarizer, and etc. As components can be diverse, they are considered as a modulator of the devices, which is a measuring zone, where the light can change its properties i.e. intensity, phase, polarisation, wavelength and spectral distribution [1]. They are necessary to be set up or implemented for the optical sensor to measure and/or detect different parameters such as temperature, pressure, vibration, chemical species, radiation, pH, humidity and etc. The optical sensors can be used as intensity-based sensors, frequency varying sensors, phase modulating sensors and polarisation modulating sensors. The optical sensors have immunity from the electromagnetic interference (EMI) [2]. Their uses in biomedical applications are increased. The optical sensors can have extremely high bandwidth capacity with high sensitivity and high dynamic range. In addition, they can be used remotely allowing them to have the ability to be embedded and used under harsh environments [2].

An optical waveguide was initially invented for point-to-point transportation of optical energy and its information content. However, the optical waveguide sensors are a breakthrough in sensing in the 1970s [3] because the waveguides are not limited only to guide the light to and from the modulator but they can also be considered as the modulator themselves by coiling a fibre in the modulator area. The optical waveguides commonly include optical fibre and rectangular waveguides which can be used in integrated optical circuits. They can be categorised depending on their i) geometry e.g. planar [4, 5] or strip [6, 7] waveguides, ii) mode structure e.g. single-mode [8] or multi-mode waveguides [9] and iii) material e.g. semiconductor [10], glass [11] or polymer [12]. The optical waveguide sensors can be classified as intrinsic and extrinsic sensors [3]. The intrinsic sensors are the sensors which have the waveguide to be the modulator

of the system such as microbend sensors, distributed sensors and interferometric sensors [13-16]. On the other hand, the extrinsic sensors allow the waveguide only to transmit the light to and from other optical or sensing components. The modulator of the extrinsic sensors can be a use of reflection and transmission, total internal reflection, gratings, fluorescence, evanescent and photoelastic effects [17-20] e.g. a thin film planar waveguide can be used as chemical sensor to measure liquid-phase absorbance by integrating with a pair of diffraction gratings on a substrate [21]. In comparison with the extrinsic sensors, the intrinsic sensors are more sensitive and the connection problems can be minimized. However, their structures have more complexity and require more elaboration compared to the extrinsic sensors.

Nanowire becomes a good candidate for nanotechnology applications due to their characteristic property of high surface-to-volume ratio [22]. The nanowires are approximately one-dimensional structures having a high length-to-width ratio which can be made from metal, insulator or semiconductor materials. The size of the nanowire is in the order of nanometers (10^{-9} m). They are exploited in nanoelectronic devices such as Field Effect Transistors (FET) [23-25], photonic and optoelectronic devices [26-28], including waveguides [29], photodetectors [30-33], solar cells [34] and various types of sensors [35-42].

Nanowires are commonly used as sensors in many sensing applications, such as gas sensors, chemical sensors, biosensors, medical sensors and optical sensors [35-42]. This is mainly due to their small size which allows their placement into small biological and chemical species. Therefore, they can be used, for example, as a tool for drug delivery [42]. They can be surface-functionalised so that they can exhibit unique electrical and optical properties for sensing purposes. In addition, they have a high surface-to-volume ratio promising high sensitivity and high selectivity [24, 43]. The sensitivity of the nanowires in sensing applications depends on the size of the silicon nanowires themselves. Nanowires can also be used as optical waveguides called nanowire waveguides (NWs).

Silicon nanowires used as optical waveguides are widely known in the nano-photonics area because silicon is one of the most common materials used for

photonic and optoelectronic applications. Silicon nanowire optical waveguide sensors detect a change of effective index from the light confined in the guiding area which occurs due to the change of the cladding medium refractive index called homogeneous sensing or the change of a thin layer on the waveguide surface called surface sensing [44]. The Silicon-On-Insulator (SOI) technology has increasingly being used in optical sensing because it has the advantage of improving light confinement in the waveguide, thus the sensitivity of the sensors is enhanced [44, 45].

Conventionally, the light is guided in the higher refractive index area of the waveguide which is mostly sandwiched by the SOI substrate and a cladding material such as air and/or water. Therefore, the light interaction with the materials to be sensed in the cladding medium or at the surface of the waveguide is limited, resulting in a low sensitivity of the device. The goal in sensing applications is to be able to achieve a large variation in the effective index when there is only a small change in the refractive index of the cladding material. More innovative slot type structures of silicon NWs are introduced because of their high power confinement in the sensing area compared to a conventional index guided waveguides. However, complicated techniques, complex equipment, and cleanroom facilities are required in order to fabricate silicon NWs, which make them expensive and hard to produce. Therefore, there is a significant interest to use other types of materials as optical waveguides.

Polymer NWs are considered to be an attractive alternative for use as optical waveguides in sensing applications due to their unique features. Polymer NWs have mechanical flexibility compared to semiconductor NWs and as a result, they can be applied on curved surfaces. They are also made of biocompatible materials which can accommodate various functional dopants [46]. A dopant is an element which can be added into a substance to modify the electrical or optical properties. Hence, there is a variety of possible sensing applications due to their exploitable optical and electrical properties. By means of their better chemical selectivity, polymer NWs can be used to detect a wide range of chemical compounds

depending on surface functionalisation which includes toxic gases, metal ions and DNA [47-49].

In this work, a theoretical investigation and its experimental implementation of integrated NWs are performed. NWs are designed and developed to achieve maximum light interaction in the sensing area, with the intention of developing them into highly sensitive optical sensors. Two types of NWs are studied, specifically, semiconductor NWs (silicon NWs) and polymer NWs (ormocomp NWs). Semiconductor nanowires are becoming an integral part of new generation of nanoscale electronics and optoelectronic devices. Besides group IV semiconductor nanowire e.g. silicon nanowire, III-V semiconductor nanowires are good candidates to be used in the optoelectronic field due to their novel features of nanowires [50], especially for active devices. The III-V nanowires can be fabricated using a wide range of methods, such as chemical beam epitaxy [51], molecular beam epitaxy [52], metal-organic vapour phase epitaxy [53] and laser ablation [54], providing different features compared to thin film technology. On the other hand, polymer nanowires offer the flexibility and biocompatibility properties with low a cost fabrication [55].

The work includes the design of the integrated NWs, fabrication of the NWs, simulation work to theoretically study their characteristics and experimental work to analyze and characterize the behaviour of the fabricated NWs. For the design, fabrication and simulation parts both silicon NWs and ormocomp NWs are considered. For the experimental part, only ormocomp NWs are studied. The goal of this work is to develop the NWs for optical sensing applications and to understand the underlying concept and behaviour of the demonstrated NWs.

1.2 Scope of work

The proposed ormocomp NWs are utilized in an integrated optical device in order to minimize the coupling loss when launching the light from a light source into the NW. Also, the integrated structure allows the NW to be easily incorporated in other optical devices. A possible integrated optics structure can

be realized with the use of feed and tapered waveguides attached at the ends of the NW [56] as shown in 1.1. Note that the figure is not drawn to scale.

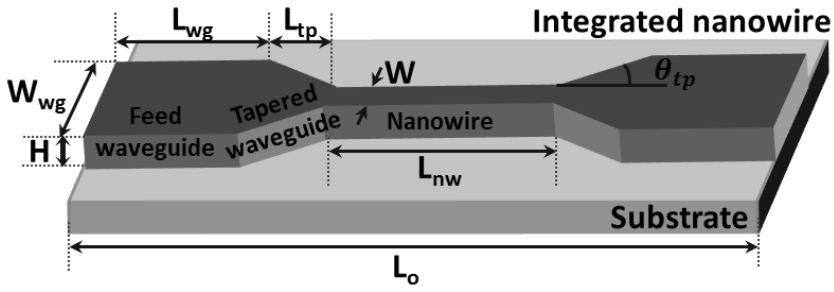

Figure 1.1: Schematic of the integrated optics NW structure. The NW is attached with feed and tapered waveguides at the ends.

The feed waveguide is designed to be large enough to be easily connected with the light source or another optical device such as an optical coupler. In this work, the tapered waveguide is optimized to have a taper angle (θ_{tp}) of 1°. The width of the feed waveguide is W_{wg}= 10 µm and the width of the NW is W= 1 µm. The height of the structure is H= 0.5 µm. The optimum taper length is L_{tp}= 260 µm. The total length of the integrated optics NW is designed to be L_o= 5000 µm. With this structure, the interaction between the evanescent field at the core/cladding interface and the analyte material can be achieved. This is discussed more in details in Chapter 6, where the theoretical study of the ormocomp NWs is presented.

An important parameter that is used to characterize the proposed NWs is the attenuation coefficient (α_{nw}). In order to perform the required experimental measurements the NWs are designed to have different lengths (L_{nw}) in one set on the same substrate. A set of NWs contains one reference feed waveguide, one reference tapered waveguide and four NWs of length 250 µm, 500 µm, 1000 µm and 2000 µm. A diagram showing the proposed set of NWs is presented in Fig. 1.2.

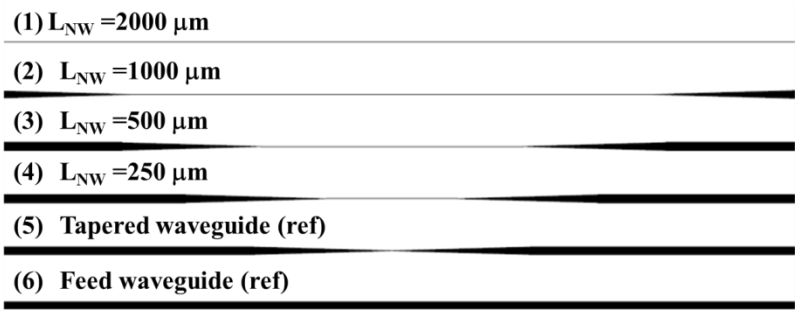

Figure 1.2: Diagram showing the set of NWs which consists of the integrated optics NWs with different lengths varied from 250 μm to 2 mm, the feed waveguide and tapered waveguide.

Since the integrated NW device consists of the feed waveguide, the tapered waveguide and a NW itself, the attenuation coefficient for the integrated NW is only a part of the combined attenuation coefficient resulting from the cascade of these three components. In order to extract the attenuation coefficient of the ormocomp NW (α_{nw}) individually, the two reference waveguides, shown as waveguides (5) and (6) in Fig. 1.2 are required. The reference waveguide (6) contains only the feed waveguide but the reference waveguide (5) consists both offeed and tapered waveguides without the NW part. These two reference waveguides are essential in order to eliminate the attenuation coefficient of the feed waveguide (α_{wg}) and the tapered waveguide (α_{tp}) in the attenuation coefficient calculation using Beer-Lambert law as discussed later in Chapter 6.

The ormocomp NWs are studied and investigated theoretically and experimentally to improve the power confinement in the sensing region which is at the core/cladding interface. The integrated ormocomp NWs are fabricated using the nanoimprint technique which is a relatively simple and inexpensive technique. Also, mass production without lengthy and complicated processes is possible. With this nanoimprint technique, the dimension and uniformity of the polymer NW can be precisely controlled. However, for the nanoimprint technique, a hard mold and soft mold are needed in order to have identical NW patterns on the ormocomp layer. The hard mold is the silicon NWs with a horizontal slot structure and the soft mold is made of PDMS (Polydimethylsiloxane).

The power confinement in the sensing region of ormocomp NWs is enhanced by sputtering gold on the NW surface to form a thin metal layer. Then, the ormocomp NWs are characterised and implemented as optical sensors by analyzing the surface plasmon resonance (SPR) signal including the resonance wavelength and their shifts. The NWs with non-vertical sidewalls are fabricated where only TM plasmonic mode is exhibited. In order to achieve polarisation independent plasmonic mode, the waveguide is fabricated to have a bigger structure with the width and height of 10x10 µm.

Silicon NWs with horizontal slot structures used as the hard molds in the nanoimprint process are also designed and fabricated as integrated NWs. The schematic of the proposed integrated-optics NW with a horizontal slot structure and its cross-section is shown in Fig. 1.3.

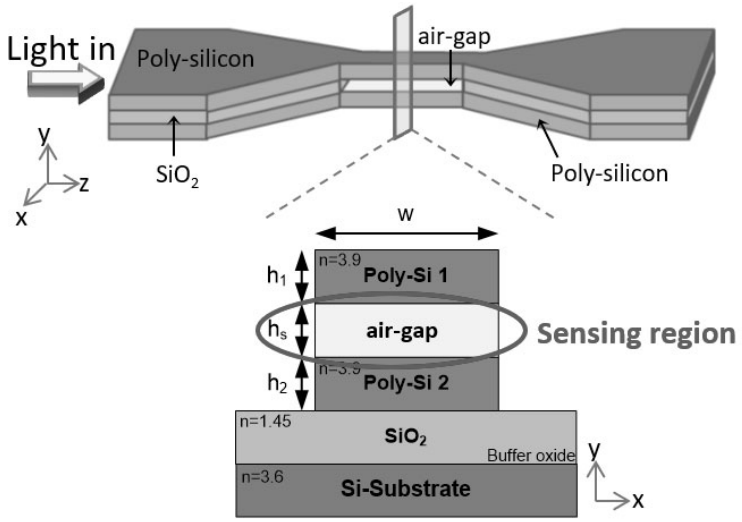

Figure 1.3: A 3D schematic of the integrated optics silicon NW with horizontal slot structure and its cross-section.

As mentioned earlier, the integrated optics structure is proposed in order to minimize the optical power losses and allow the NWs to be easily connected with other optical devices in possible sensing applications. However, this integrated structure has the additional advantage of making a slot containing possible gas or liquid medium. The horizontal slot waveguide consists of the low-index material sandwiched by two high-index materials that are poly-Si layers. The low-index area can be SiO_2, air or water. Mostly, the low-index materials in the horizontal

slot are in solid phase. However, the analyte materials are usually either gas or liquid. This integrated device allows an air gap to be implemented as the low-index material in the horizontal waveguide structure.

The NWs are fabricated layer-by-layer, starting from poly-Si, following with SiO_2, and finally depositing poly-Si again. The oxide layer then can be etched away using wet etching. The oxide layer at the NW region can be removed first due to its smaller width, leaving an air gap between the two high-index layers. Once the low-index oxide layer under the narrow waveguide region is removed the etching process is stopped so that the two high-index layers can be mechanically supported by the wider region at the two ends where the low-index material is only partially removed. Therefore, the fluid materials can fill the slot area where the light is mostly confined due to the discontinuity of the normal component of the electric fields at the dielectric boundaries. More details are presented in Chapter 4 where the fabrication of the NWs is discussed.

The fabricated silicon NWs with horizontal slot structures can be used for further theoretical studies, besides serving as master molds in the imprint process. These are studied theoretically in order to improve power confinement in the slot area. The silicon NW with horizontal structure is investigated theoretically to detect DNA hybridisation. A comparison of the sensitivity for its use as the optical sensor to detect DNA hybridisation with other devices is also presented.

1.3 Research objectives

The overall objective of this research work is to design, characterize and develop NWs for optical sensing applications. Two types of NWs are considered in this work, silicon NWs and ormocomp NWs. The silicon NWs and ormocomp NWs are designed and studied theoretically to achieve a high normalized power confinement in the sensing region in order to improve their sensitivity. Both silicon and ormocomp NWs are fabricated using the top-down technique. The silicon NWs with horizontal slot structure are studied only theoretically to be used as label-free biosensors to detect DNA hybridisation. The ormocomp NWs are

studied and analyzed both theoretically and experimentally for their optical properties. The specific objectives are listed below.

1. To design silicon and ormocomp NW structures for the best optical guiding property by optimizing the dimensions of the NWs in order to obtain the highest possible normalized power confinement in the sensing region.
2. To investigate the possible guided mode and its characteristics including the effective index, the optical modal field, the optical power and the effective mode area in the silicon NWs and the ormocomp NWs using the Finite Element Method (FEM).
3. To improve the normalized power confinement in the sensing area for the silicon NWs by introducing the horizontal slot structure and numerically investigate the silicon NWs with horizontal slot structure for DNA hybridisation detection.
4. To investigate the effect of surface plasmon resonance (SPR) on the ormocomp NWs by introducing the thin metal layer on the NWs. The polarisation independent plasmonic modes are also studied.
5. To fabricate the silicon NWs with horizontal slot structure and ormocomp NWs with the conventional structure. The silicon NWs are fabricated by using oxidisation, low-pressure chemical vapor deposition (LPCVD), photolithography and dry etching. The ormocomp NWs are fabricated by using the nanoimprint method with a silicon hard mold and a PDMS (Polydimethylsiloxane) soft mold.
6. To build the characterisation optical setup using several optical microscopes and optical spectrometer for analyzing experimentally the attenuation coefficient, the SPR signals and their shift with different cladding materials of the un-coated and gold-coated ormocomp NWs.

1.4 Structure of the thesis

This thesis describes the research performed to develop ormocomp integrated NWs for optical sensing applications and numerically study silicon NWs with horizontal slot structures to detect DNA hybridisation. The work consists of the design, fabrication, simulation and experimental characterisation of the proposed integrated NWs.

Chapter 1 provides an introduction and background information of the nanowire optical waveguides in optical sensing applications, the scope of work, the research objectives and structure of the thesis.

Chapter 2 concentrates on a literature review of various topics related to this research work and gives the theoretical background to support it. This chapter starts by providing the theoretical background of optical waveguides. Then a review of the current literature on sensing applications of silicon NWs with conventional structures, vertical slot structures, and horizontal slot structures is provided. The chapter continues with a discussion on how ormocomp NWs are used in various sensing applications. The effect of Surface Plasmon Resonance and its importance in sensing applications is examined through this literature review. In addition, the reasons for having integrated optics structures embracing the NWs are analyzed. Finally, the reasoning behind the choice of using ormocomp as the base material to fabricate the NWs and the choice to fabricate the silicon NWs with horizontal slot structure are discussed.

Chapter 3 discusses the basic theory of the Finite Element Method (FEM) which is a numerical technique used to solve complex engineering problems. This chapter first introduces the basic Maxwell's equations followed by wave equations for the electromagnetic field. The equation used to calculate the effective index, which is a significant parameter in this study, is also included in this section. The boundary conditions required to solve the wave equations are provided next. Finally, an in-house program of the full-vectorial **H**-field FEM, which is used to solve both the silicon and ormocomp NW optical waveguide problems, is described in detail.

Chapter 4 discusses the fabrication techniques and the fabrication processes for the silicon NWs with horizontal slot structure and the ormocomp NWs. Both silicon and ormocomp NWs are fabricated using a top-down approach. A basic background of the fabrication techniques for the top-down approach is first provided. For the silicon NWs with horizontal slot structure, the fabrication techniques of oxidisation, LPCVD, photolithography, and dry etching are described step-by-step. For the ormocomp NWs, the details of the nanoimprint technique are provided including the preparation of the hard mold and the soft mold. To study the gold-coated ormocomp NWs, the thin gold metal layer is deposited on the ormocomp NWs using the sputtering technique, which is also discussed in this chapter.

Chapter 5 is devoted to the theoretical studies of the silicon NWs with the use of the full-vectorial **H**-field FEM. First, the simulation results of the silicon NWs with conventional structure are described as a function of the operating wavelength, the structure width, the cladding material, and the surface plasmon resonance. Then, the theoretical results of the silicon NWs with horizontal slot structures are presented. The key parameters used for the study of the horizontal slot structure are the poly-Si core height, the structure width, and the slot height. Lastly, the horizontal slot waveguide for the DNA hybridisation detection is studied theoretically and described in detail. The sensitivity of the silicon NWs with horizontal slot structures to detect DNA hybridisation compared to other sensors is also provided.

Chapter 6 presents the theoretical studies of the ormocomp NWs. To begin with, the ormocomp NWs with the ridge waveguide structures are studied. The rectangular-shaped (vertical sidewalls) ormocomp NWs are studied with respect to the operating wavelength, the structure width, and height. Next, the trapezoidal-shaped ormocomp NWs with rib-waveguide structures (non-vertical sidewalls), which are the actual structures obtained from the fabrication, are studied. In addition, a comparison between the optical field guided inside ormocomp NWs with vertical sidewalls structure and non-vertical sidewalls structure are included. Finally, the theoretical studies of the ormocomp NWs

coated with thin gold layer are provided. The effects of the surface plasmon resonance from the thin metal layer are studied in term of their resonance wavelength and resonance shift when the cladding-index is changed. The comparison of the ormocomp NW with and without gold coating is also presented.

Chapter 7 details the experimental work which was undertaken to characterize the ormocomp NWs. First, the optical setup, which is built for the ormocomp NW characterisation, is described. The optical imaging using the in-house code to obtain the output intensity is discussed in detail. The attenuation coefficient of the ormocomp NWs before coated with the gold layer is analyzed and the scattering effect from the surface roughness is investigated. After coating with a thin gold layer, the attenuation coefficient, which is affected by the absorption of the surface plasmon resonance, is evaluated. The effect of the surface plasmon resonance (SPR) is investigated with different cladding materials, showing the surface plasmon resonance peaks and their shifts. There are two types of NW structures with non-vertical and vertical sidewalls. Only the TM plasmonic mode is considered for non-vertical sidewalls. For the vertical sidewalls structure, both TM and TE plasmonic modes are considered which exhibit polarisation independent plasmonic structure.

Chapter 8 includes the general conclusion, which summarizes the work accomplished in this research, and suggests a potential extension of the present work to improve the performance of the ormocomp NWs to be used in sensing applications.

2. Theoretical background and literature review

This chapter provides a basic background on the use of nanowires as optical waveguides. The theoretical background explains the propagation of light in the optical waveguides. The technical terms that are generally used to describe the light guidance in a waveguide, such as the propagation constant, the effective index and the cutoff wavelength are also defined. In addition, the use of taper mechanism for integrated optics is also included. The general information about the fabrication of the nanowire waveguide (NW) is also presented.

The literature review on using silicon nanowire with different designs as optical sensors is included, such as conventional silicon NWs with the vertical slot structure and the horizontal slot structure. In addition, the literature review of different types of polymer NWs is presented including ormocomp NWs. The research involving surface plasmon resonance (SPR) to enhance the optical power guided in the NWs is also described.

2.1 Optical waveguides background

Nanowire waveguide (NW) is a specific type of an optical waveguide. They exhibit high aspect ratio (length-to-width ratio $\geq$ 1000) with the diameter or transverse dimension of 1 nm or so, called one-dimensional nanostructures. They are considered as a good candidate for nanotechnology applications due to their unique properties with high surface-to-volume ratio [23, 35, 57]. In photonics, nanowires are used as optical waveguides. In particular, silicon-on-insulator (SOI) based NWs have been used as optical sensors because they have the advantage of high refractive index contrast and low optical power losses [58].

Optical waveguides are structures for guiding the electromagnetic waves. For an optical fibre, there are two regions with different refractive indices, which are the core (n_{core}) and cladding ($n_{cladding}$). For an integrated optics, the waveguide consists of three different regions with three different refractive indices specifically the cladding (n_c), the core (n_{nw}) and the substrate (n_s). By considering

geometrical (ray) optics theory of optical fibres, where the light is considered as a ray, the core is the region where the light propagates by total internal reflection [59]. However, the geometrical (ray) optics approximation is valid for structures where the dimensions of the core (in optical fibres), or those of the guiding region (in optical waveguides) are much larger than the wavelength of the light. In the NW structures, where the dimensions are comparable with the wavelength of the light, the ray optics approximation cannot be applied. Therefore, the light has to be considered in its true nature, as an electromagnetic wave and the analysis of the waveguiding properties of the NWs has to be performed in terms of the wave theory, based on the Maxwell's equations, as described in the subsequent sections.

During propagation, the light is guided in discrete waveguide modes. Modes are the allowed characteristics which light can propagate inside a guiding structure. They are characteristics of the structure itself (including geometry and material profiles) as well as the wavelength of the incident light. A thorough exploration of light mode theory can be found in [59]. Each mode has a propagation constant (β) which represents the phase of the light at a given wavelength. The propagation constant (β) is the product of the effective index (n_{eff}) and the vacuum wavenumber (k_o) given by [59]:

$$\beta = k_o . n_{eff} \tag{2.1}$$

where $k_o = \frac{2\pi}{\lambda}$.

The effective index, n_{eff}, is an effective property of optical parameters such as related to its speed in an optical waveguide. It varies with the wavelength and also the mode in which the light propagates in the waveguide. Therefore, its value depends on the whole waveguide design and can be calculated using different numerical methods, such as the Finite Element Method (FEM) [60].

The modes of light propagating inside the core of the waveguides are called guided modes which can be solved by using Maxwell's equations. The number of guided modes in the waveguide depends on the wavelength, the size of the

waveguide and the refractive index contrast (∆n) which is the difference of the refractive index between the core and the substrate, or the core and the cladding. More modes can be guided when using shorter wavelength and a larger wavelength allows a smaller number of modes. Furthermore, larger waveguide structures allow a larger number of guided modes to propagate through them. Moreover, higher ∆n also results in a higher number of modes that can be guided through a waveguide. Single-mode waveguides allow only one mode (fundamental mode) to be guided. Normally, single-mode characteristics of the waveguides are only defined in some specific range of the wavelength allowing only one mode of light to propagate. The maximum wavelength allowing a guided mode is called a cutoff wavelength. Waveguides supporting multiple modes of light to propagate are called multimode waveguides. The condition for single-mode optical fibre can be defined by the V number which has to be below 2.405 and it is formulated as follows [59, 61]:

$$V = \frac{\pi D}{\lambda}\left(n_{nw}^2 - n_{max(n_c,n_s)}^2\right)^{\frac{1}{2}} \qquad (2.2)$$

$$V < 2.405 : \text{Single-mode optical fibre}$$

where D is the diameter of the waveguide. This equation is strictly not valid for other waveguides, but can give some rough ideas. For the optical fibre, the V number below 2.405 allows only the fundamental mode to be guided while the other higher order modes are cut off. In our integrated optics waveguide, the structure dimensions are numerically designed to be in a sub-wavelength scale in order to allow only the fundamental mode to be guided. However, the waveguide needs to be carefully designed to be above the fundamental mode cut off limit because the mode properties are extensively changed and the mode is unguided, which means the light is no longer propagated inside the waveguides, below the cut off. Near the cutoff wavelength, the effective mode radius or the spot size of the optical field increases dramatically and the power confinement in the guiding region is consequently decreased. This is because unguided light spreads into either the cladding or the substrate.

For very long wavelengths and/or a very small waveguide, it is possible to have no guided modes. Therefore, the waveguides need to be carefully designed according to their prospective uses. For example, in surface sensing applications, the sensitivity can be improved by enhancing the evanescent field [36, 62, 63]. The evanescent field is the field that extends outside the guiding region. The maximum possible evanescent field can most easily be obtained from the fundamental guided mode. Therefore, the design of single-mode waveguides is preferable to be used for surface sensing applications.

In this work, the NWs are designed and developed for their use in sensing applications. Therefore, single-mode structures are required. The FEM is used to study the fundamental guided mode in the designed NWs. The structure and the dimensions of the NWs are optimized accordingly to achieve high optical power in the sensing area, which is at the core/cladding interface with the objective of enhancing the sensitivity of the NWs. The NWs are fabricated and their optical characteristics are experimentally measured and analyzed. Furthermore, surface plasmon resonance (SPR) on the top surface of the NWs is introduced to enhance the light interaction in the sensing area. Hence, the SPR wavelengths and their shift for each cladding material are also investigated.

2.2 Incorporation of Nanowire waveguides in integrated optics

Nanowire waveguides are considered sub-wavelength structures since their dimensions are less than the operating wavelength in order to attain high power levels in the evanescent field. The NWs in this work have height 0.5 µm and width about 1 µm. However, the core diameter of the single mode fibre (SMF) is around 8-10 µm [64]. This means that there will be optical power losses when connecting a NW to a SMF light source due to their size difference. In order to reduce the coupling losses, a taper mechanism is proposed.

Two possible types of tapers are the optical fibre taper [65, 66] and the integrated optics taper [67-69]. Chun *et al.* [70] used single mode fibre to make a fibre taper with a diameter of 1 µm for coupling the light into silver NWs. It was

found that the fibre taper can enhance surface plasmon and couples the light to the NW with a coupling efficiency reaching 55%. A common fabrication technique for fibre tapers involves heating the optical fibre and then stretching it out until the desired dimensions are obtained. Therefore, the fabrication process of fibre tapers requires accurate temperature control and pulling mechanism.

A tapered waveguide has been chosen as the most appropriate method for coupling the light into the NW. A tapered waveguide is a mechanism used widely in integrated optics in order to improve the power coupling coefficient between integrated optical devices such as multimode waveguides, single mode waveguides, single mode fibres and laser diodes [71-74]. Tapered waveguides can also have various shapes including linear, exponential and parabolic tapered structures [75-77] as shown in Fig. 2.1.

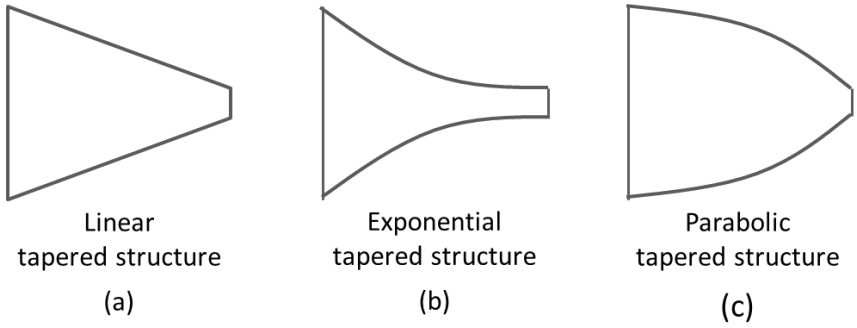

Figure 2.1: Schematics of various tapered structures including (a) linear, (b) exponential and (c) parabolic shaped.

However, the linear tapered structure is found to have the highest efficiency [75, 78] compared to the other tapered structures. In addition, it is the simplest and easiest shape to fabricate. Therefore, the linear tapered waveguide tends to be widely used in integrated optic applications.

The linear tapered waveguide plays an important role in reducing the coupling loss when the light couples from the feed waveguide to the relatively small dimension NW. In order to minimize the propagation loss in the tapered waveguide, the tapered angle, θ_{tp}, as shown in Fig. 2.2 is considered.

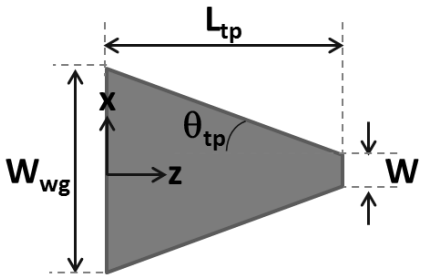

Figure 2.2: Schematic of a linear tapered waveguide showing the tapered angle, θ_{tp}.

The tapered angle, θ_{tp}, can be expressed by the following equation [75]:

$$\theta_{tp} = tan^{-1}\left(\frac{W_{wg} - W}{2L_{tp}}\right) \tag{2.3}$$

where W_{wg} is the feed waveguide width, W is the NW width and L_{tp} is the tapered length. It was found that if the taper angle is reduced, the power loss is decreased [75], however, its length increases. In addition, a symmetric taper structure about z-axis, which is also the direction of light propagation as shown in Fig. 2.2, also affects the power losses [75]. Therefore, the designed tapered waveguide should possess a symmetric shape about z-axis with the taper angle around 1°-3° in order to get the maximum power coupling coefficient and to make it a suitable taper structure [75, 79]. If the taper angle is too small, the structure becomes non-compact since it becomes too long.

2.3 Nanowire waveguide fabrication process

Generally, there are two ways to synthesize the nanowire, namely top-down and bottom-up approaches. The top-down approach starts with the bulk material which is scaled down to the nano-size material through the fabrication techniques such as deposition, electron-beam lithography, UV lithography, and etching. With the top-down approach, a nanowire with high-yield, high uniformity, and good alignment can be achieved. Therefore, this approach is mostly used for mass production in the microelectronic industry and production of nanowire arrays [23, 80]. However, the scaling down process has physical and economical limitations.

Concerning the physical limitation of top-down approach, the minimum features of 14 nm were achieved in 2014 by Intel Corporation [81, 82]. Economical limitations concern the cost of operation of the top-down approach which is more expensive compared to the bottom-up approach. The bottom-up approach relates to the synthesis of atoms or molecules combined together to form a larger complex material. This approach commonly uses the vapor-liquid-solid (VLS) growth method in order to grow the nanowires [83]. With the bottom-up approach, the physical and economical limits found in the top-down approach can be overcome [84, 85]. In addition, the selective doping of the nanowires is possible by controlling the dopant precursor gas [86]. The challenge of this approach is to control the size, orientation, and positioning of the nanowires.

Polymer nanowires can be fabricated using one of several possible techniques in both top-down and bottom-up processes. Starting with bottom-up techniques, electro-spinning is a conventional technique to fabricate nanowires with a diameter of 50-300 nm [87]. The nanowires obtained from this technique are multiple, overlapping and randomly oriented. Multiple nanowires used as optical waveguides have a slower response and lower sensitivity compared to a single NW because their response is the average of the responses from many NWs [88]. Therefore, single-NWs are more popular for sensing applications when the response time is important. A technique that uses scanned electro-spinning and direct drawing of solvated polymers have been developed to fabricate individual oriented polymer nanowires which can be used as optical waveguides [89, 90]. Another bottom-up fabrication technique used to obtain single nanowires is a combination of self-assembled mono-layer deposition and electrochemical polymerisation [91]. However, none of these bottom-up techniques enables a reliable and high throughput for large scale of patterned nanowires. In addition, it is difficult to control the interaction of the molecules for the incorporation of a single nanowire into a device [91]. On the other hand, top-down fabrication techniques, such as laser interference patterning (LIP) combined with inductively coupled plasma (ICP) and nanoimprint provide a uniform and oriented nanowire structures on a large-scale, which can be used as optical waveguides [92-94].

The silicon NWs with horizontal slot structure and the ormocomp NWs developed in this research work are fabricated using the top-down technique in order to achieve the integrated optical device structure. With the top-down technique, the dimensions of the NW can be controlled if appropriate care is taken. In addition, the mass production of a single NW is possible. The fabrication process of the silicon NWs includes oxidisation, LPCVD (low pressure chemical vapor deposition), photolithography and dry etching. For the fabrication of the ormocomp NWs, the nanoimprint method is used because it is a relatively simple method, inexpensive and not so time consuming.

2.4 Silicon slot nanowire waveguides for sensing applications

Currently, silicon-on-insulator (SOI) slot waveguide has been growing as a field of interest due to the strong power confinement achieved in the slot area, leading to an enhancement of light interaction within the sensing region and the resulting sensitivity improvement [95]. Almeida *et al.* [96] were the first to report that the intensity in the low-index area of slot region can be 20 times higher than that obtained by a conventional rectangular waveguide. Slot waveguides are fabricated by having two higher refractive indices but narrower waveguides close to each other. The narrow gap between those two NWs is arranged to have a lower refractive index. In this arrangement, the light is confined in the low-index area due to the discontinuity of the normal component (E_n) of the electric field (**E**-field) at the interface. Due to the high-intensity optical field at the low index interface, the intensity of light-matter interaction is increased and consequently, the sensitivity of the sensor is improved. Due to their unique characteristics, slot waveguides are utilized in several optics and photonics applications, such as in micro-resonators [97], optical modulators [28], directional couplers [98], beam splitters [99] and logic gates [100]. Moreover, the distinctive feature of power confinement in the low-index region also makes the slot waveguides very attractive in sensing applications [101-104].

There are two possible types of slot waveguides, according to their structural orientation, namely the (i) vertical slot waveguides and (ii) horizontal slot waveguides, as shown in Fig. 2.3.

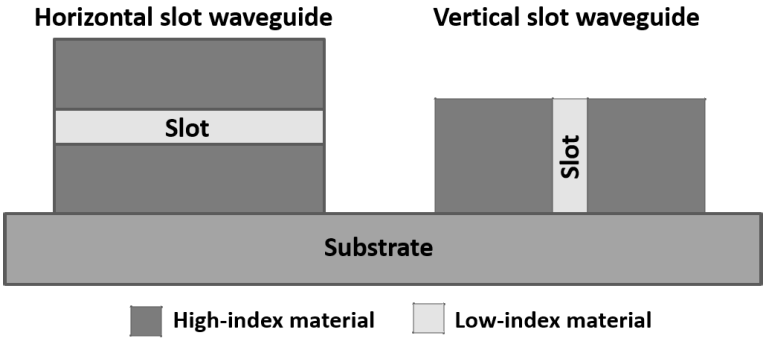

Figure 2.3: Schematic of horizontal and vertical slot waveguides.

The vertical slot structures have the slot region perpendicular to the substrate while the slot region of a horizontal slot waveguide is parallel to the substrate. The fabrication of the vertical slot waveguides includes photolithography and etching where the thermal oxidation and chemical vapor deposition (CVD) are the main processes for the horizontal slot waveguides fabrication. Therefore, the interfaces between the slot and high-index materials of the horizontal slot waveguides are smoother resulting in lower scattering loss compared to the vertical slot waveguides [105, 106]. The fabrication techniques for manufacturing the slot waveguides are described in Chapter 4. The fundamental mode obtained in the vertical slot waveguide is the TE mode (transverse electric mode) whereas the TM mode (transverse magnetic mode) is obtained for the horizontal slot waveguide.

2.4.1 Vertical slot waveguides

Dell'Olio and Passaro [44] proposed a chemical and biochemical integrated optical sensor by optimizing the vertical slot waveguide. The research concentrated on modal and sensitivity investigation for conventional SOI slot waveguides and SOI rib waveguides at the fixed operating wavelength of λ=1550 nm. The influence of the vertical sidewall in the slot region is also investigated. The vertical sidewall has a sidewall angle θ in the range between 81° and 87°.

A full-vectorial 2D FEM with triangular elements is used in the modal investigation. In their simulations, the cladding materials are assumed to be either air, silicon oxide, or water with refractive indices of 1, 1.444 and 1.33, respectively, depending on the design objectives. The results showed that the quasi-TE mode is more confined in the gap region for all vertical slot structures examined because of the discontinuity of the normal component of the electric field, which is E_x in this case [44].

In order to investigate the use of the vertical slot waveguide in sensing applications, Dell'Olio and Passaro [44] have studied the sensitivity of these waveguides by measuring the change of effective index due to the change of cladding medium refractive index. This can be used to measure the concentration of chemical species presented in a solution form such as glucose solution or ethanol solution. In addition, the change in gas concentration can also be estimated using this method. The waveguide sensitivity (S_{modal}) is defined by the following equation [44]:

$$S_{modal} = \frac{\delta n_{eff}}{\delta n_c} \tag{2.4}$$

where n_{eff} if the effective index of propagation mode and n_c is the refractive index of the unperturbed sensing region.

Dell'Olio and Passaro [44] have reported that when the width of the waveguide structure decreases, the sensitivity increases in both vertical sidewall and non-vertical sidewall structures because the optical field is pushed out of the core into the slot region for the narrower waveguide. However, the non-vertical sidewall causes an additional reduction of the sensitivity in the range of about 15% compared to a vertical sidewall structure. This reduction may reach 25% for a wider structure. The sensitivity of their vertical slot waveguide is reported to be 70% higher than that of a conventional silicon NWs [107] and also greater than the sensitivity obtained in rib waveguides [108].

Passaro *et al.* [109] have investigated the slot SOI waveguide used as a chemical sensor. The proposed sensor is a compact sensor with a device area of

1200 μm^2. The minimum refractive index change that can be detected by this sensor is about 10^{-5}. The vertical slot SOI waveguide is studied to detect the change in glucose concentration. According to the simulation, the sensitivity was expected to be in the order of 0.1 g/L.

In order to exploit this slot waveguide in a wider range of biochemical sensing applications, the surface sensing is considered. Such surface sensing slot waveguide can be used to detect, for example, DNA hybridisation and antigen-antibody reduction [44, 101, 104, 110, 111]. In surface sensing applications, the molecular adlayer is deposited on the top surface of the NW structure. The molecular adlayer acts as a receptor interacting with an analytic molecule to form the immobilisation of an ultra-thin layer. The interaction causes the change of the thickness of the adlayer leading to the change of the effective index of the optical mode (n_{eff}).

Claes *et al.* [104] have been the first to prove that vertical slot waveguide with the slot width of 100 nm can be used as a selective label-free sensor for the protein detection. They developed slot waveguide based on ring resonator, where the protein detection sensitivity increases by a factor of 3.5. Dar *et al.* [110] have used the Finite Element Method (FEM) to study the propagation mode and the sensitivity of vertical slot waveguides. They proposed a label-free biosensor to detect DNA hybridisation as shown in Fig 2.4.

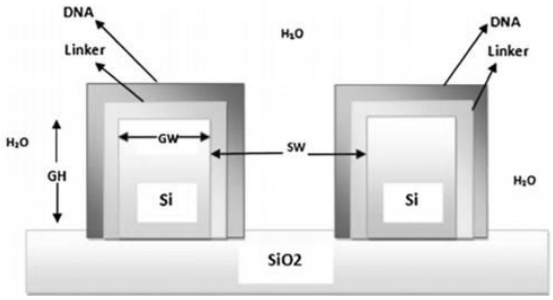

Figure 2.4: Vertical slot waveguide sensor to detect DNA hybridisation proposed by Dar *et al.* [110]

The adlayer in that research was silanes, which has refractive index of 1.42 [112]. The silanes layer acts as a linker to form a bond with single-strand DNA

(ssDNA). With the presence of complimentary DNA, the ssDNA becomes double-stranded DNA (dsDNA).

The refractive index of ssDNA and dsDNA are 1.453 and 1.53, respectively, at a wavelength of 633 nm [113]. The sensor proposed in [110] is using a surface sensing mechanism to detect DNA hybridisation. When the ssDNA becomes dsDNA, the effective index of the guiding mode is changed due to the difference in the refractive index at the surface. The dimensions of the slot structure are optimized to obtain the maximum sensitivity. The dimensions used in the optimisation exercise are the height and width of the NW and the slot width. The waveguide sensitivity (S_{modal}) in this work is given in the form of equation (2.5):

$$S_{modal} = \frac{\delta n_{eff}}{RI} \tag{2.5}$$

where δn_{eff} is the effective index difference when ssDNA becomes dsDNA and RI is the refractive index of the ssDNA layer. This will be a dimensionless parameter. Instead of comparing with the RI, it has also been reported by comparing with the change in the RI of the sensing media. The sensitivity of the sensor can also be defined as a function of the frequency or wavelength of the output signal called spectral sensitivity, $S_{spectral}$, as shown in the equation below:

$$S_{spectral} = \frac{\delta \lambda}{\delta n} \tag{2.6}$$

The spectral sensitivity is the relative efficient in the detection of a change in light intensity which can be wavelength dependent. Comparing this with the change in refractive indices, the spectral sensitivity is used to measure the shifts in the wavelength in the unit of nm/RIU. In the research from Dar *et al.* [110], a NW with waveguide width of 220 nm, height in the range between 320 and 340 nm and a slot width of 100 nm has been studied theoretically to achieve the sensitivity (S_{sensor}) of 856 nm RIU^{-1}.

An alternative way to enhance the sensitivity of the vertical slot waveguide is by increasing the number of slots [114, 115]. Sun *et al.* [116], have studied the evanescent confinement in vertical multiple-slot waveguides for sensing

applications. The research shows the enhancement of sensitivity as the number of slots is increased. In this research, they have simulated the operation of a waveguide with three slots. The sensitivity is reported to be five times higher than that of a conventional waveguide without the slot in the case of homogeneous sensing, in which the waveguide is surrounded with bulk solution. For surface sensing, the sensitivity is three times greater for the three-slot waveguides compared to the conventional waveguides.

Vivien *et al.* [117] have developed vertical multiple slot waveguide ring resonators in silicon nitride as shown in Fig. 2.5.

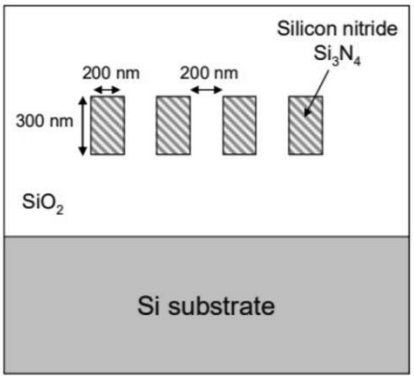

Figure 2.5: Vertical multiple slot waveguide used as ring resonator proposed by Vivien *et al.* [117].

The silicon nitride is used instead of silicon to minimize the refractive index contrast, which in turn relaxes fabrication tolerances. A triple slot waveguide has higher effective index variation than the single slot waveguide of about 20%. In addition, around 60% improvement in effective index variation compared to strip waveguide can be achieved [117]. Besides that, using silicon nitride allows the slot width to be enlarged to 200 nm [118] which gives the advantage of being able to detect bigger molecules in biosensing applications.

There is a limitation for the fabrication of vertical slot waveguides because silicon slot waveguide operates in the near infrared (IR), leading to a restriction of the slot width to be less than 100 nm which can be difficult to achieve in fabrication, especially in an etching process [117]. Surface roughness can occur in the vertical narrow-gap etching process due to the sub-micron dimension structure, leading to the scattering loss at the interface of the slot waveguide.

2.4.2 Horizontal slot waveguides

Horizontal slot waveguide structures can be fabricated using chemical vapor deposition (CVD) and thermal oxidisation. These techniques are used to produce thin films. They can be applied layer by layer and result in a smoother surface and consequently a reduction in the scattering loss [119, 120]. CVD is a chemical process used to deposit the thin films of various materials such as poly-Si, SiO_2, Si_3N_4, metal and diamond [121] while thermal oxidation is a process to produce only SiO_2 layer on the silicon surface by the diffusion of an oxidizing agent at a high temperature [122].

Mullner and Hainberger [123] have investigated and optimized the horizontal slot waveguide to improve the power confinement in the slot region. A full-vectorial 2D FEM with triangular elements was used as a simulation model for that research. The operating wavelength was at 1550 nm. The power confinement was reported to depend strongly on the thickness of the waveguide rather than the slot thickness. The width of the structure also affects the power confinement in the slot region. The power confinement is increased when the waveguide structure widens. The power confinement can be increased up to 54% when the waveguide has a width of 1400 nm. The effect of slot height on the power confinement can be negligible [123].

The horizontal single and multiple slots waveguides have also been demonstrated by Sun *et al.* [124] as shown in Fig. 2.6.

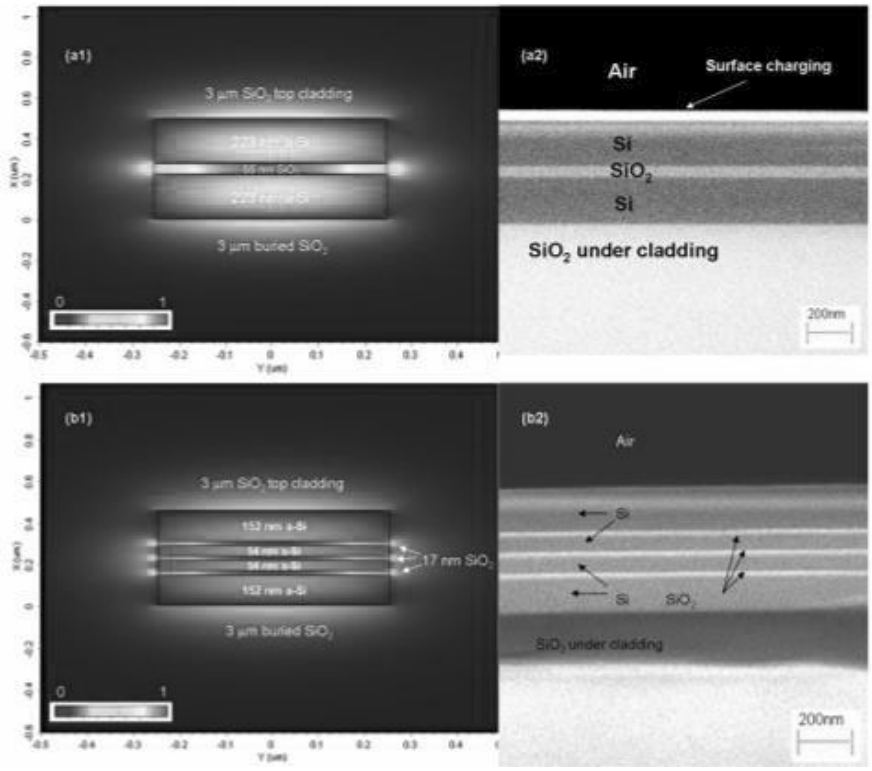

Figure 2.6: Horizontal single and multiple slots waveguide structures proposed by Sun *et al.* [124].

They have fabricated horizontal slot waveguide using thermal oxidisation. Their research shows that the low propagation loss is due to the lower absorption of the silicon material. The reported propagation loss in horizontal single and multiple slot waveguides is around 6.3 dB/cm and 7.0 dB/cm, respectively.

Horizontal slot waveguides can be utilized in various optical applications such as couplers for instance. Galan *et al.* [125] have developed high efficiency grating couplers for silicon-based horizontal slot waveguides. It is reported that the coupling efficiency between a standard single mode fibre and this horizontal slot waveguide can reach 61% in which the incident angle is 8° [125].

Considering the information collected for slot waveguides that the horizontal slot waveguides has significantly lower loss compared to the vertical slot waveguides and required tolerances are also better [45, 105, 106], it was decided that the NWs with horizontal slot structure are the most appropriate to study and fabricate in this PhD research. In addition, the silicon NWs in this work are fabricated on a silicon-on-insulator (SOI) wafer due to the significant advantages

offered over fabrication on conventional silicon wafers. The SOI technology minimizes optical losses and power dissipation in optical waveguides [45, 126].

2.5 Nanowire waveguides for sensing applications utilizing the evanescent field

2.5.1 Silicon nanowire waveguides

The silicon-on-insulator (SOI)-based NWs have been widely used as optical sensors to detect bio-molecules because they can be surface functionalised to bind with the analytes resulting in direct label-free readout [127]. This is the main advantage over the conventional biosensors which requires organic molecular dyes for labelling detection [128-131]. Due to this label-free and real-time detection properties, silicon nanowire-based sensors can be used for immune detection, pH sensing and disease diagnosis [24, 42, 43]. When the surface of silicon nanowires is linked with the receptor molecules, such as polyanionic, it is possible that a single-stranded DNA and some other proteins can be detected due to the change of their conductivities [24, 42].

The sensitivity of the nanowire-based sensor is enhanced due to the high surface to volume ratio [132]. Therefore, the sensitivity of the NW can be improved by reducing the size of the NW. Rong *et al.* [133] have developed 20-nm porous silicon NWs for label-free DNA hybridisation sensing. The porous structure of the silicon waveguide increases the surface area and provides the capability for molecular size selectivity. In addition, the sensitivity of the optical waveguide sensor can be enhanced from the evanescent field at the cladding region [134].

Research work using silicon NWs integrated with a Mach-Zehnder interferometer has also been performed by Wang *et al.* [58, 135]. With this integrated optical sensor, a resonance wavelength was measured with the change of concentration of Sodium Chloride (NaCl) which leads to the change of the effective index. The resonance wavelength linearly increases when the concentration of NaCl is increased from 1% to 5% as well as the refractive index in

the range between 1 and 1.538. It is reported that a high sensitivity of 110nm/RIU and large detection range of refractive index can be obtained [135].

2.5.2 Silica (SiO_2) nanowire waveguides

Silica NWs with a subwavelength diameter and their properties have been studied by Lou *et al.* [62]. For small diameter NWs, the propagation of light is extended outside the guiding region called evanescent field. The power of the evanescent field in the surrounding medium can be in a range from 20 to 100 percent of the overall power of the field present, depending on the core diameter of the NW. The evanescent field intensity is inversely proportional to the diameter of the silicon NWs. This evanescent field can be used to detect the change of the refractive index of the cladding medium which is the detection mechanism for several SiO_2-based optical sensors [36, 62, 63]. Higher sensitivity can be obtained by enhancing the evanescent wave propagation through the geometry of the waveguide (size and curvature) and the waveguide material (refractive index). Therefore, the subwavelength-diameter silicon NW is required in order to get the maximum evanescent wave. Tong *et al.* [136] have shown that the critical diameter for single mode Silicon NWs is 450 nm for the operating wavelength of 633 nm (visible region) and 1100 nm for the operating wavelength of 1550 nm (near-infrared region). The optical loss for these single mode NWs is less than 0.1 dB mm^{-1}.

There has been extensive research using silicon NWs as optical sensors by integrating them with a Mach-Zehnder interferometer. Themistos *et al.* [57] have characterised the silica NWs for optical sensing by incorporating the silica NWs in a Mach-Zehnder interferometer. With this Mach-Zehnder based optical sensor, the optical field profiles, the propagation constant and the power confinement of both the reference and sensing arms can be calculated while varying the NW parameters including the diameter, the refractive index, and the wavelength. It was reported that the optical field is more confined in large diameter silica NWs. Therefore, the power confinement in the core region is higher when increasing the NWs diameter. However, the change in the refractive index of the medium

has more effect to a NW with a small diameter. In addition, smaller wavelengths provide more confinement of optical fields and power in the core region of silicon NWs.

Lou *et al.* [62] have proposed the use of a single mode silica NW as an evanescent wave based optical sensor as shown in Fig. 2.7.

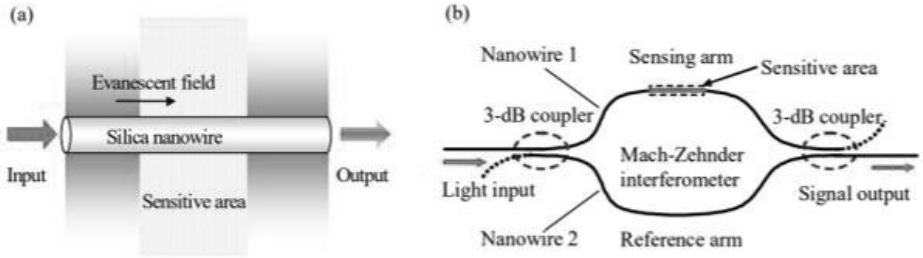

Figure 2.7: Silica NW sensor based on Mach-Zehnder interferometer using evanescent wave proposed by Lou *et al.* [62].

The sensor is assembled as a Mach-Zehnder interferometer to detect the phase shift caused by changing the refractive index of the surrounding medium. The Mach-Zehnder interferometer consists of two arms, the sensing arm, and the reference arm. For the sensing arm, the sensitive area is introduced to the medium for detecting the change of the refractive index by the evanescent wave. This leads to a phase shift between the sensing arm and the reference arm in the interferometer. It is reported that the sensitivity of this proposed optical sensor is about 7.5 μm^{-1} which is higher compared to conventional sensors [62]. The sensitivity of this NW sensor is inversely proportional to the wavelength of the light.

In addition, this single mode NW can be surface-functionalised for selective detection. The surface functionalisation forms a thin layer of a specific specimen. If the surface is modified by metal nanoparticles, the surface plasmon (SP) is dominant which can improve the evanescent field at the surface of the NWs. It is reported that the sensitivity of NW-based sensors can be enhanced by the presence of surface plasmon resonance (SPR) [137, 138].

2.5.3 Ormocomp nanowire waveguides

There are several types of NWs depending on the type of material used for their fabrication, which can be semiconductor, glass or polymer. Silicon is the most common semiconductor used to fabricate NWs. However, the fabrication of silicon NWs requires cleanroom facilities and complex equipments which can be costly. Glass NWs e.g. SiO_2 are well-suited for simple optical detection due to their transparency, which means there is low light absorption at the visible region. However, glass is fragile and vibration sensitive, the fabrication process of glass NWs is difficult and very time consuming [12].

The polymer is a distinctive alternative material which can be used to fabricate optical waveguides. Polymer NWs have flexibility and biocompatibility [55]. Their fabrication can be made simple and at a low cost. Gu *et al.* [88] have used a bottom-up technique which is direct drawing of solvated polymer doped with functional material to fabricate PAM (polyacrylamide) single-NWs. It is used in humidity sensing with response time of 30 ms.

The PAM single-NW is placed on a low-index substrate which is MgF_2 (n=1.39). A single-mode fibre is drawn to form a fibre taper and then placed at both ends of the NW for the implementation of the evanescent coupling method. A low-index fluoropolymer (n=1.38) is used to bond the NW and the fibre taper together and keep them isolated from the environment [88].

In addition, doping PMMA (Polymethylmethacrylate) NWs with bromothymol blue (BTB) has been demonstrated for NH_3 (ammonia) gas sensing. The response time is measured to be around 1.8 s which is considered to be faster than other ammonia sensors [88]. The utility of fluorescent polymer nanofibres, such as polyacrylic acid-polypyrene methanol (PAA-PM), to detect the metal ions Fe^{3+} and Hg^{2+} is also possible [48].

There are several types of polymers commonly used in photonics such as PDMS (polydimethylsiloxane), SU8, PMMA (polymethylmethacrylate) and ormocomp. The choice of what polymer to use depends on the properties and the requirements of a particular application. The main properties of interest of the

polymers mentioned above including its refractive index, UV-transparency, contact angle, thermal degradation temperature and coefficient of thermal expansion are presented in Fig. 2.1. The contact angle is the angle measured how the liquid deposited on a solid substrate. It is used to define a wettability of a solid surface of each material in which the high contact angle (>90°) refers to a hydrophobic surface. The thermal degradation temperature of polymers indicates an upper limit temperature that the polymers can maintain their physical and optical properties. The coefficient of thermal expansion (CTE) is a material property to indicate the linear expansion (length) of the material upon heating for each degree of temperature which has units of increment fraction per °C. However, a change in length of these materials is extremely small. Therefore, the CTE is usually expressed in units of 10^{-6}/°C or ppm/°C.

Table 2.1: Some properties of the main polymers used in the photonics area

Polymer	**n (589 nm)**	**Contact angle (°)**	**Degradation (°C)**	**CTE (ppm/°C)**
PDMS[139, 140]	1.43	>100	400	310
PMMA[141]	1.49	73	250-260	70-150
SU-8[142, 143]	1.59	85	>340	64
Ormocomp®[144, 145]	1.52	63	270	100-130

The refractive indices of PDMS and PMMA are 1.43 and 1.49, respectively. Their refractive indices are less than the refractive index of the glass substrate (n=1.51). Therefore, they are not suitable to be used as waveguides when deposited above the glass substrate. SU8 is a viscous material and its adhesion capabilities to glass are very poor [142]. Consequently, it is difficult to obtain uniformity of the SU8 layer on the glass substrate.

Based on the above, ormocomp has been used in the fabrication of the NWs in this work. Ormocomp has a refractive index of 1.52. Ormocomp shows hydrophilic property (affinity for water) compared to PDMS, PMMA, and SU-8. However, the hydrophilic or hydrophobic properties of the material are not

considered in this study. It is a hybrid polymer material consisting of an inorganic backbone and organic side groups at the molecular level, unlike composite materials which are mixtures at the macroscopic level [146, 147]. Hence, the ormocomp is a homogeneous material that combines the properties of different material classes as shown in Fig. 2.8.

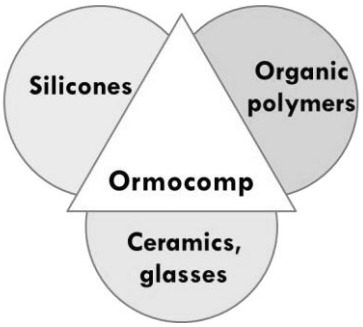

Figure 2.8: Molecular composites of ormocomp consisting of silicones, organic polymers and ceramics/glass.

Ormocomp is one of the commercial polymers in the ORMOCER®s group (trademark of Fraunhofer-Institute, Germany [144]). The reaction scheme for the ORMOCER®'s resin, which is used as an optical waveguide core region is shown in Fig.2.9 [148].

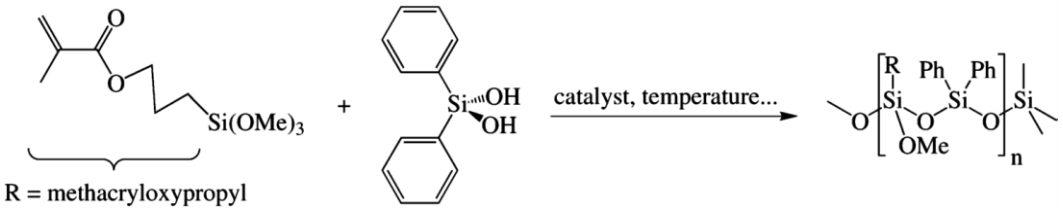

Figure 2.9: Reaction scheme of ORMOCER® for a use as the core material of optical waveguide [148].

The ORMOCERs have been used in many optical sensing applications [149] due to their wide range of refractive indices in selected silicone functional groups. Ormocomp obtains its flexibility and UV-curable property from the properties of organic polymers. The hardness and the chemical and thermal stability are obtained from the properties of ceramics where the transparency comes from the properties of glass [144]. Ormocomp is also known to have an easy and low processing cost using the nanoimprint technique [144, 150].

Referring to Fig. 2.1, ormocomp has a good wetting property with a contact angle of about 63°. It also has a good adhesion on many types of the substrate such as glass, silicon, and other polymers. Therefore, it can be used in microfluidic applications [55, 151, 152]. In addition, ormocomp has low optical losses at the NIR (near infrared: λ=1550 nm) range and this is important since optical components at these wavelengths are easily available and widely used for telecommunications [153]. This low loss property leads to its use in optical interconnection technologies [154, 155].

Wang *et al.* [156] have fabricated the inverted-rib waveguide with ormocore and ormocomp using the nanoimprint method. The fabricated waveguides were 30 mm long with a ridge width of 2 µm and a ridge height of 1.2 µm. The rib layer was about 0.8 µm thick. However, a tapered fibre was needed in order to launch the source light (1310-nm laser), into the inverted-rib waveguide, and with these dimensions, a transmittance of 58.6% was achieved at λ=1310 nm.

2.6 Surface plasmon resonance

The sensitivity of the NWs can be further improved by coating a thin metal layer usually gold or silver, on the top surface to introduce surface plasmon resonance (SPR) [157-161]. The metal-coated NWs exhibit resonance coupling between the dielectric mode in their core and the plasmonic mode in the metal layer [162-164]. There are two plasmonic modes occurring in a gold layer, the dielectric core/gold interface (internal plasmon) mode, and the cladding/gold interface (external plasmon) mode. Patskovsky *et al.* [165] have found that the internal plasmon mode is insensitive to the change of the refractive index of the cladding material, but the external mode is highly sensitive to the cladding index change. However, if the thickness of the gold layer is small enough, the two plasmonic modes can couple to each other and become an odd-like or an even-like supermode which exhibits different behaviours [159, 166, 167]. Therefore, the thickness of the metal layer is considered to be one of the most important parameters needed to be optimized for each sensing applications [168].

The evanescent field at the dielectric/metal interface is very sensitive to the change of the cladding index which is significant for sensing applications [169]. On the other hand, low-loss waveguides are mostly used in telecommunications which allow the light to travel at longer distances [170]. Therefore, SPR-based NWs have been widely used for biosensing and chemical sensing such as for the detection of NO_2 gas [171-174]. A planar waveguide SPR sensor has been studied for its use in environmental monitoring such as the monitoring of low concentration of organic pollutants in water [175].

It has been reported that optical transmission through the sub-wavelength holes in the metal film can be increased by an additional factor of 10 [176]. The use of localized surface plasmon resonance (LSPR) to enhance the sensitivity of the NW optical waveguides for biosensors have also been addressed and reported to show a sensitivity increased by more than 23 times [138, 177]. The use of colloidal Au as a nanoparticles tag for the detection of DNA hybridisation has shown great improvement in the sensitivity compared to those without Au [178]. The sensitivity of the SPR sensor integrated with a Mach-Zehnder interferometer for glycerin-water solutions is significantly improved to $5.5x10^{-8}$ RIU per 0.01° phase change in which Wu *et al.* [179] claimed to be a significant improvement, allowing the SPR biosensors to have a greater potential to replace the fluorescence-based conventional biosensors.

Chu *et al.* [180] have developed a SPR sensor based on multi-mode silica-on-silicon channel waveguide. A ridge channel waveguide was made of Ge-doped SiO_2. With a 75 nm thick gold layer attached to the top surface of the waveguide using chromium as an adhesion layer. The SPR signal occurring at the dielectric/metal interface is sensitive to the change of the cladding index. The refractive index of the cladding material was varied from 1.333 to 1.450 and the waveguide was operated in the range λ=500-800 nm. A maximum sensitivity of 4547 nm/RIU was achieved at the cladding index of 1.434 with the resolution of $4.4x10^{-5}$ RIU.

The SOI-based biosensors using the evanescent field sensing enhanced by SPR has been demonstrated with an interferometer by Debackere *et al.* [181]. The

surface plasmon interferometer-based biosensor is also capable of bulk refractory (bulk refractive index sensing). With various concentrations of NaCl solution, the sensitivity of 435.454 nm/RIU is attained with the detection limit of 10^{-3} RIU [182].

In order to detect protein interaction between avidin and biotin, the waveguide element is surface silanized to have a suitable bio-interface between silicon and biological media. The integrated biosensors can detect the change of the refractive index in the order of 10^{-6} RIU [183]. With SPR, 2 ng of nCG presence in 1 ml of 1% bovine serum albumin solution was detected with a small refractive index change which is less than $1.2x10^{-6}$ [184]. A high resolution SPR-based chemical sensor to calibrate inert electrolyte solution with different concentrations was accomplished with the sensitivity of $1.82x10^{-8}$ RIU/nm calculated based on the changes in Goos-Haenchen shift which measures the displacement of the light beam instead of the resonant wavelength and the detection limit of $4x10^{-7}$ RIU [185] was reported.

To enhance the performance of the NWs, a polarisation-independent structure is introduced in which the SPR occurring at both TE and TM polarisations have a similar effective index and show the same SPR behaviour [186].

2.7 Summary

Nanowire waveguides (NWs) can be used as optical waveguides to guide light waves. In order to couple the light into the NWs, coupling loss occurs due to the mode-size difference between single-mode fibres and the NWs, and hence, the taper mechanism is proposed to reduce the coupling loss.

NWs are synthesized using the bottom-up technique or the top-down technique. The bottom-up technique is cheaper and allows smaller size NWs to be produced. However, the top-down technique provides a better uniformity and size control. In addition, integrated NW structures are possible using the top-down technique. Integrated NWs can be easily used with other optical devices such as optical couplers.

Conventional waveguides allow light to be confined inside the high-index area which is the core of the NWs. On the other hand, light is confined in the low-index area in the case of slot waveguides. Slot waveguides are structures for which a low-index material is sandwiched in between two high-index materials. The light confined in the slot area has been found to have higher confinement compared to the conventional structure. There are two types of slot waveguides, the vertical slot waveguide, and the horizontal slot waveguide, depending on the slot orientation. The horizontal slot waveguide has better fabrication tolerances and lower loss compared to the vertical slot structure.

Silicon is the most common semiconductor material used in the fabrication of waveguides. However, the polymer is alternatively used in the fabrication of optical waveguides due to its properties. It is flexible, biocompatible and possible for various surface functionalisations. The fabrication of polymer is simpler, cheaper and less time consuming compared to semiconductor and glass.

Ormocomp is a hybrid polymer material which has the combined properties of inorganic and organic materials at the molecular level. It has high transparency in the visible region and its refractive index is 1.52, which is higher than the glass substrate so it is suitable to fabricate a waveguide on the glass. The ormocomp NWs use the evanescent field at the core/cladding interface to interact with the analyte materials. The evanescent field is sensitive to the change of the refractive index of the cladding material. In order to enhance the light interaction at the interface, surface plasmon resonance (SPR) is introduced. It was found that the power confinement and the sensitivity of the SPR-based sensor are significantly increased. Also, a polarisation-independent structure is proposed to further enhance the sensitivity of the waveguide.

3. Numerical analyses

3.1 Introduction

There are different numerical techniques available to solve the propagation of light in a Nanowire waveguide (NW), which is considered to be a special type of optical waveguides. In this chapter, the key features of some of the techniques which can be used in the analysis of such NWs and particularly the Finite element method (FEM) are described. The advantages of the use of the FEM over the other techniques, the fundamental theory of the FEM, the variational formulation utilized in the analyses of these structures and the desired parameters obtained by applying the above approach, are also presented here.

The NWs can be complex structures consisting of anisotropic materials or materials with complex refractive indices such as metals. The characteristics of the propagation of light in NWs can be analyzed by solving the Maxwell's equations. There are several numerical methods which can be used to solve these problems, such as, the Finite Difference Method (FDM), the Boundary Element Method (BEM), the Finite Element Method (FEM) and the Beam Propagation Method (BPM).

The Finite Difference Method (FDM) [187] is a popular numerical technique which has been widely used to solve boundary value problems. In this technique, the optical waveguide is defined as a finite cross-section enclosed in a rectangular box, where the fields at the boundaries are assumed to be negligible, via the use of decay parameters along the boundaries. The cross-section of the optical waveguide is mostly implemented by the uniform rectangular grid, consisting of regularly spaced nodal points. All the dielectric boundaries of any non-homogeneous optical waveguides have to lie on the nodal points in the rectangular grid, which is one of the shortcomings of the method. The approximate solution in FDM is the solution of the eigenvalue problem which can be solved base on the Taylor series expansion. By applying the continuity conditions of the optical fields at the dielectric interfaces, the eigenvalue matrix

equation ($Ax-\lambda x=0$) can be obtained and often solved using sparse matrix techniques.

The Boundary Element Method (BEM) [188] is a computational technique, where the waveguide cross-section is divided into a set of elements where the basic equations are integral equations. However, the unknown nodal fields are not assigned to the whole area of the waveguide cross-section but only at the boundary. By deriving integral equations with respect to unknowns taken on the boundaries, the integral equations are discretized to linear equations. With the linear equations, the numerical solutions can be obtained which is also expressed in integral form. This integral equation is then used again to calculate the solution numerically. In the BEM, although resulting matrix order may be smaller but often dense and less flexible for many practical waveguides.

The Finite Element Method (FEM) [189] is a powerful numerical technique originally developed for structured engineering problems and has a wide range of applications. This approach used to analyze complex structural problems such as optical waveguides. In the FEM, the differential equations defining a system under consideration can be replaced by variational expressions to which a variational principle is applied. The region of interest of the structure under consideration such as in our case, the cross-section of the optical waveguide is divided into many small simpler elements, usually triangular in shape, where the appropriate field components are approximated by polynomial expressions over these elements. Nodes can then be assigned at the vertices of the triangles, which can be shared between adjacent elements and the polynomial expressions are derived with respect to the assigned nodes. For more accurate representation of the field components, nodes can also be assigned inside the elements, thus increasing the order of the polynomial expressions and consequently the accuracy of the approach. Each element can have different shape and size with different dielectric material which may be anisotropic, non-linear, or lossy. After converting a continuous structure into a discretized structure, the variational principle is applied to the functional of the system and the problem is then reduced to a standard eigenvalue matrix equation ($Ax-\lambda Bx=0$), which can be solved by applying

the standard matrix algorithms. The FEM can be effectively used to analyze any shape of optical waveguides including 2D and 3D.

The Beam Propagation Method (BPM) [190, 191] is widely used to analyze the behaviour of the light propagating in an optical planar circuit which is similar to the strip waveguide. For the BPM, the Fourier Transform (FT) of electromagnetic fields with respect to the direction normal to the light propagation was firstly introduced by Feit and Fleck [192]. A stepwise method is used to calculate the electromagnetic fields along the axial direction. The BPM is the numerical method that is effectively used to analyze with the non-uniform structures such as tapered waveguides. The BPM can also be based on the finite element method in order to characterize 3D optical waveguides [193]. However, being a 3D approach, it is not efficient compared to the method developed specifically for the uniform structure problems because, in BPM, the discretisations in both transverse and longitudinal plane are needed.

The Finite-Difference Time Domain Method (FDTD) [194] is used to solve the electromagnetic problem in which both time and space in the Maxwell's equations are discretized using central difference approximations. It is also a grid-based differential numerical modelling method. The FDTD calculates the electric and magnetic fields as they evolve in time providing animated displays of the electromagnetic field movement. In addition, the electric and magnetic fields can be both calculated directly without conversion. However, the computation time can be very long as the entire computational domain has to be gridded and the grid has to be fine enough for the smallest feature in the waveguide [195].

By comparing the FEM with the other numerical approaches described above, the FEM is considered to be more suitable for the analysis of the NW structures, mainly due to its ability to be adapted to any kind of structure with arbitrary boundaries, since the triangular-shaped elements in the FEM can give a better fit to any structures and the density of the element discretisation can be varied in regions where there is more rapid field variation. Even though the FDM has simpler matrix eigenvalue equation compared to the FEM, which may require less computer memory storage and programming time, it is not suitable for the

irregular shaped structures due to the uniform rectangular grid used and furthermore, in the presence of dielectric corners the electric field exhibits a singular behaviour produced by its transverse components.

Similar to the FDM, the FDTD requires sufficiently fine grids to resolve the smallest part of the model leading to a long computation time. On the other hand, the BEM considers the optical fields only at the surface of the waveguide structures and the volume-discretisation also needs to be considered in order to study the light behaviour propagated inside the waveguide. The BEM is usually applied using Green's formula, however, the approach is limited to homogeneous structures and in some cases, it requires further analytical treatment and programming. In the present work, only the modal solution of the optical field across the cross-section of the optical waveguide (x-y plane) is required, not the dependence of the light along the direction of propagation (z-axis). Therefore, the FEM is chosen over the BPM.

There are several commercial photonic simulation software products available in the market such as Lumeical and RSoft. Lumerical's design tools can be used to solve for FDTD problems, mode solutions, charge transport, and heat transport. RSoft can be used to design and analyse optical components and nano-scale optical structures using FDTD-based simulation tool, BPM simulation tool, and etc. However, the cost of the commercial software products can be up to 5000 USD per year. In this work, an in-house full-vectorial $\bar{H}$-field formulation-based Finite Element Method is used to solve for the modal solution of the NWs.

A detailed description of a basic theory of the FEM and how it is applied to our specific waveguides including silicon and ormocomp NWs are presented in the next section.

3.2 The finite element method

The finite element method (FEM) is a numerical technique used to get an approximate solution of differential or integral equation problems. It has an advantage in solving the complex system in engineering problems such as elastic

problems, thermal problems, fluid flow, electrostatic and electromagnetic problems. These problems are seen in the concepts of equilibrium, in thermodynamics, in Maxwell's equations and other application areas, which can be expressed by governing differential equations and boundary conditions. The principle of the FEM is to divide the complex structure into many discrete elements, thus an equivalent discrete model for each element is constructed and all the elemental contributions to the system may be assembled. Alternatively, the FEM can be considered as the approximation of a continuous system by a discretized model. Therefore in the FEM, a differential approach is transformed into an algebraic problem, where the building blocks or finite elements have all the complex equations solved for their simple shapes [189].

A cross-section of an arbitrary shaped optical waveguide is divided into a number of sub-domains, called elements, being composed of several different materials, each of which can be described by arbitrary permittivity and permeability tensors, $\hat{\varepsilon}(x,y)$ and $\hat{\mu}$ (x,y), respectively. A uniform shape of the waveguide along the longitudinal z-axis, is assumed and time and axial dependencies are given by $\exp(j\omega t)$ and $\exp(-\gamma z)$, where, ω is the angular frequency and γ is the complex propagation constant.

All the elements in the discretized cross-section of an optical waveguide are considered to be interconnected at a discrete number of nodal points on their boundaries, as shown in Fig. 3.1.

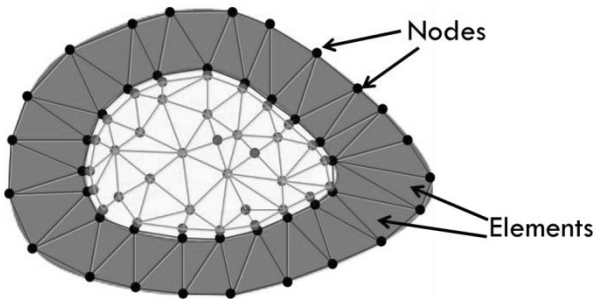

Figure 3.1: Schematic of an arbitrary waveguide structure divided into triangular elements interconnected via the nodal points on their boundaries.

The elements have triangle-shape, thus giving the best fit to any structure. Different expansions can be used over each element, such as polynomials or

sinusoids, having the same form over all the elements, but different coefficients and satisfying some conditions between the elements, such as field continuity. Throughout this work, first order triangular elements have been used, where the nodal points are assigned, one at each vertex and first-degree polynomials, which are continuous across adjacent triangles, have been considered.

The FEM is the extension of two classical numerical approaches, the Rayleigh-Ritz variational method and the Galerkin method of weighted residuals. In the variational approach, the governing differential equation is not solved directly. Instead, the variational expressions are formulated as functionals. The functional is used to solve the problems and the approximate solution is obtained by minimizing the functional. For the Galerkin method, the governing equation is discretized and solved. The solution is obtained by minimizing the residual error of the differential equation. However, both methods are related to a standard eigenvalue problem which has to be solved [189, 196-198].

There are some fundamental electromagnetic field equations involved in the FEM such as Maxwell's equations, wave equations, and boundary conditions.

3.2.1 Maxwell's equations

Maxwell's equations are a set of four partial differential equations representing the governing laws of the electromagnetic wave phenomena. The four vector quantities involved in Maxwell's equation are the electric field $\boldsymbol{E}$ (volts per meter), the magnetic field $\boldsymbol{H}$ (amperes per meter), the electric flux density $\boldsymbol{D}$ (coulombs per square meter) and the magnetic flux density $\boldsymbol{B}$ (tesla). For source-free, time independent fields can be written in integral or differential form. In Differential form Maxwell's equations can be represented as follows:

$$\nabla \times \boldsymbol{E} = -\frac{\partial \boldsymbol{B}}{\partial t} \qquad \textit{(Faraday's law)} \tag{3.1}$$

$$\nabla \times \boldsymbol{H} = \frac{\partial \boldsymbol{D}}{\partial t} + \boldsymbol{J} \qquad \textit{(Ampere's circuital law)} \tag{3.2}$$

$$\nabla \cdot \boldsymbol{D} = \rho \qquad \textit{(Gauss's law)} \tag{3.3}$$

$$\nabla \cdot \boldsymbol{B} = 0 \qquad \textit{(Gauss's law for magnetic)} \tag{3.4}$$

where $\boldsymbol{J}$ is the current density and ρ is the electric charge density (coulombs per cubic meter).

The associated constitutive equations for the medium can be written as:

$$\boldsymbol{D} = \varepsilon \boldsymbol{E} \tag{3.5}$$

$$\boldsymbol{B} = \mu \boldsymbol{H} \tag{3.6}$$

where ε is the permittivity and μ is the permeability of the medium. These are defined as:

$$\varepsilon = \varepsilon_0 \varepsilon_r \tag{3.7}$$

$$\mu = \mu_0 \mu_r \tag{3.8}$$

where ε_0 and μ_0 are the permittivity and permeability of the vacuum and ε_r and μ_r are the relative permittivity and relative permeability of the medium. ε_0 and μ_0 have value of 8.854×10^{-12} Farad per meter and $4\pi \times 10^{-7}$ Henry per meter, respectively.

In addition, the rate of the energy of an electromagnetic field per unit area is represented by Poynting vector (**S**):

$$\boldsymbol{S} = \boldsymbol{E}^* \times \boldsymbol{H} \tag{3.9}$$

The Poynting vector or the energy flux density is the cross product of electric and magnetic fields with the unit of W/m^2.

3.2.2 Wave equations

Assuming that an electromagnetic field oscillates at a single angular frequency (ω), the time-dependent electric field $\boldsymbol{E}(r,t)$ and magnetic field $\boldsymbol{H}(r,t)$ over the waveguide region can be expressed as:

$$\boldsymbol{E}(r,t) = Re\lfloor \boldsymbol{E}(r)exp(j\omega t)\rfloor \tag{3.10}$$

$$\boldsymbol{H}(r,t) = Re[\boldsymbol{H}(r)exp(j\omega t)] \tag{3.11}$$

where $\boldsymbol{E}(r)$ and $\boldsymbol{H}(r)$ are the time-independent electric and magnetic fields, respectively.

In homogeneous media with uniform permeability and constant relative permittivity ε_r, the wave equation of the electric field and magnetic field can be reduced to Helmholtz equation by eliminating the magnetic flux density and electric flux density, respectively.

$$\nabla^2\boldsymbol{E} + k^2\boldsymbol{E} = 0 \tag{3.12}$$

$$\nabla^2\boldsymbol{H} + k^2\boldsymbol{H} = 0 \tag{3.13}$$

where k is a wavenumber represented by:

$$k = \omega\sqrt{\varepsilon\mu_0} \tag{3.14}$$

The wavenumber in vacuum, called free-space wavenumber is defined as:

$$k_0 = \omega\sqrt{\varepsilon_0\mu_0} = \frac{\omega}{c_o} = \frac{2\pi}{\lambda_o} \tag{3.15}$$

where c_o is a speed of light in vacuum and λ_o is a wavelength in vacuum.

In an optical waveguide with a uniform structure in the z-direction, the derivative of the electromagnetic field with respect to the z-coordinate is γ where $\gamma = \alpha + j\beta$. For loss less case, there is no attenuation loss ($\alpha = 0$) allowing the derivative to be constant, $\gamma = j\beta$ which is called phase constant, where β is the

propagation constant. The ratio of the propagation constant to the wavenumber, as shown in the equation below, is known as the effective index, n_{eff}.

$$n_{eff} = \frac{\beta}{k_0} \tag{3.16}$$

3.2.3 Boundary conditions

In order to solve the wave equation of the electromagnetic field, the boundary conditions are required to be satisfied. These are the conditions that must be met when the boundary surfaces of two different mediums are in contact. Assuming there is no surface currents ($\boldsymbol{J}$=0) and no surface charges (ρ=0), the required boundary conditions are as shown below:

(a) The tangential components of the electric field are continuous ($E_{1t} = E_{2t}$)

$$\boldsymbol{n} \times (\boldsymbol{E}_1 - \boldsymbol{E}_2) = 0 \tag{3.17}$$

(b) The tangential components of the magnetic field are continuous ($H_{1t} = H_{2t}$)

$$\boldsymbol{n} \times (\boldsymbol{H}_1 - \boldsymbol{H}_2) = 0 \tag{3.18}$$

(c) The normal components of the electric flux density are continuous ($D_{1n} = D_{2n}$)

$$\boldsymbol{n} \cdot (\boldsymbol{D}_1 - \boldsymbol{D}_2) = 0 \tag{3.19}$$

(d) The normal components of the magnetic flux density are continuous ($B_{1n} = B_{2n}$)

$$\boldsymbol{n} \cdot (\boldsymbol{B}_1 - \boldsymbol{B}_2) = 0 \tag{3.20}$$

where $\boldsymbol{n}$ is the unit normal vector at the boundary.

In some cases, one of the mediums is considered as a perfect electric conductor or a perfect magnetic conductor. If one of them becomes the perfect

electric conductor, the electric wall boundary condition is then changed to the following:

$$\boldsymbol{n} \times \boldsymbol{E} = 0 \quad or \quad \boldsymbol{n} \cdot \boldsymbol{H} = 0 \tag{3.21}$$

For the case when one medium is a perfect magnetic conductor, the magnetic wall boundary condition becomes as follows:

$$\boldsymbol{n} \times \boldsymbol{H} = 0 \quad or \quad \boldsymbol{n} \cdot \boldsymbol{E} = 0 \tag{3.22}$$

In an optical waveguide which is a closed surface system, additional boundary conditions are needed. The field decays in some cases at the boundary and therefore, the boundary conditions can be left free. In order to take advantage of the symmetry of the waveguide leading to a reduction in the number of element in FEM, the boundary conditions can be forced. They can be classified as Dirichlet and Neuman boundary conditions [197]:

$$\varphi = 0 \qquad (\text{Homogeneous Dirichlet}) \tag{3.23}$$

$$\varphi = k \qquad (\text{Inhomogeneous Dirichlet}) \tag{3.24}$$

$$\frac{\partial \varphi}{\partial \boldsymbol{n}} = 0 \qquad (\text{Homogeneous Neuman}) \tag{3.25}$$

where φ is the electromagnetic field either electric or magnetic, k is a constant value and **n** is the unit vector normal to the surface. The Neuman boundary conditions represent the rate of change of the field when it comes out of the surface. In FEM, it can be used to obtain the field decay along the boundary of the waveguide.

3.2.4 Outline of the finite element formulation

As mentioned earlier, FEM is a numerical technique to obtain an approximate solution to boundary value problems defined by a governing differential equation in a domain, based on the Raleigh-Ritz variational method and the Galerkin method of weighted residuals, in which the domain of the differential equation is

discretized. In this case, a cross-section, Ω of an arbitrarily shaped optical waveguide, enclosed by a boundary Γ, as shown in Fig. 3.2, is divided into a number of elements, that can be composed of different material and size.

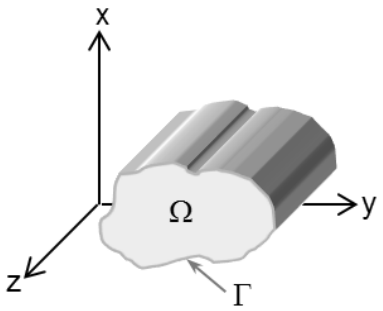

Figure 3.2: Cross-section of an arbitrarily shaped waveguide with the computational region Ω and boundary Γ.

The boundary Γ consists of an electric wall Γ_e and magnetic wall Γ_m, where the tangential electric field and tangential magnetic field are 0, respectively. The wave equation for the magnetic field, **H**, obtained from Maxwell's equations can be described as [60]:

$$\nabla \times ([\varepsilon_r]^{-1}\nabla \times \boldsymbol{H}) - k_o^2 \boldsymbol{H} = 0 \qquad (3.26)$$

where ε_r is the relative permittivity of the medium.

In the Raleigh-Ritz variation method, the boundary value problem defined by the differential wave equation can be represented by a functional term (F). The functional is a scalar quantity defined in an integral form with the differential equation and the boundary conditions expressed as [60]:

$$F = \iint_{\Omega} (\nabla \times \boldsymbol{H})^* ([\varepsilon_r]^{-1}\nabla \times \boldsymbol{H})\, d\Omega - k_o^2 \iint_{\Omega} \boldsymbol{H}^*.\boldsymbol{H} d\Omega \qquad (3.27)$$

The unknown function from the above wave equation is the magnetic field **H**, therefore the solution of the problem is a function **H**(x,y), which makes the functional F stationary with respect to small changes, δH. By expressing the functional in terms of the Euler's equation, $\delta F = 0$ and by taking the first variation δF, after applying the Gauss' divergence theorem, Euler's equation can be expressed [60]:

$$\delta F = \iint_{\Omega} \delta \boldsymbol{H}^* \cdot [\nabla \times ([\varepsilon_r]^{-1} \nabla \times \boldsymbol{H}) - k_o^2 \boldsymbol{H}] \, d\Omega - \int_{\Gamma} \delta \boldsymbol{H}^* \cdot [\boldsymbol{n} \times ([\varepsilon_r]^{-1} \nabla \times \boldsymbol{H})] d\,\Gamma \tag{3.28}$$

where Γ is the boundary of the region Ω, $\boldsymbol{n}$ is the outward normal unit vector to the boundary Γ and $\boldsymbol{n} \times ([\varepsilon_r]^{-1} \nabla \times \boldsymbol{H})$ represents the tangential electric field on the boundary Γ.

It can be seen from equation (3.28) that by applying the variational principle to equation (3.27), Euler's equation, $\delta F = 0$, coincides with the wave equation (3.26).

The boundary condition $\boldsymbol{n} \times ([\varepsilon_r]^{-1} \nabla \times \boldsymbol{H}) = 0$ is automatically satisfied along the perfect electric wall boundary, Γ_e and therefore it can be considered as the natural boundary condition. Equation (3.28) does not satisfy the boundary condition on the perfect magnetic wall boundary and therefore a forced boundary condition $\boldsymbol{n} \times \boldsymbol{H} = 0$ should be imposed if required.

In order to obtain the approximate solution, the cross-section Ω is divided into a number of elements, e and the solution of the unknown function is $\boldsymbol{H}$ for each element can be approximated by:

$$\boldsymbol{H} = \sum_{i=1}^{m} N_i H_i \tag{3.29}$$

where m is the number of nodes and N_i is a set of known basis function called shape function [197]. Equation (3.29) can be represented in matrix notation as shown below.

$$\boldsymbol{H} = [N]^T \{H\}_e \tag{3.30}$$

where $[N]^T$ is the transpose of the shape function matrix and $\{H\}_e$ is the column vector of the nodal field values for each element. By substituting **H** from equation (3.30) into equation (3.27), the solution of the optical waveguide can be obtained from the following equation:

$$\iint_{\Omega}\Big((\nabla\times[N]^{T}\{H\}_{e})^{*}([\varepsilon_{r}]^{-1}\nabla\times[N]^{T}\{H\}_{e}) - k_{o}^{2}([N]^{T}\{H\}_{e})^{*}([N]^{T}\{H\}_{e})\Big)d\Omega = 0 \tag{3.31}$$

In the FEM approach, the whole analysis region of the boundary-value problem is discretized into a finite number of elements. Therefore, the integral can be evaluated from the summation of the elements over the whole region. Equation (3.31), it can be written in the matrix form of a standard eigenvalue equation as shown in equation (3.32) [60, 199]:

$$[A]\{H\} - k_{o}^{2}[B]\{H\} = 0 \tag{3.32}$$

where $\{H\}$ is the eigenvector for each eigenvalue k_o^2. $[A]$ is the complex Hermitian matrix and $[B]$ is the real symmetric matrix.

As it has been described above, the solution of the optical waveguide problem using the finite element analysis can be expressed as a standard eigenvalue equation, as shown in equation (3.32). Element matrices A and B are formed for each triangular element over the cross-section of the optical waveguide and these are assembled into the corresponding Global matrices and the eigenvalue problem is solved using an efficient sparse matrix solver. The formation of the element matrices A and B and their global matrices can be found in Appendix A.

3.3 Finite element analysis of nanowire waveguides

There are many types of FEM-based variational formulations used to evaluate the propagation characteristics of optical waveguides. Vector formulations are preferable compared to scalar approximations in cases where the accuracy of the solution is vital. However, such formulations can lead to large memory requirements and increased computational time and therefore trade off should be applied between the desired level of accuracy, the computer memory resources and consequently the required program execution time.

The types of the FEM-based vector formulations used analyze are categorized in terms of the components of the electromagnetic fields used in each formulation. Some of these include the E_Z-H_z formulation in terms of the axial components of the electromagnetic field, the vector **E**-field formulation and the vector **H**-field formulation.

The E_z-H_z formulation is one of the oldest FEM formulations used to analyze 3D optical waveguides. However, using the above formulation to solve optical waveguide problems, nonphysical solutions called spurious solutions are also generated, while, in treating general anisotropic problems the canonical form of the eigenvalue equation is destroyed. The effective way to eliminate the spurious solutions in the above approach has not been found yet [60]. Furthermore, the axial components used are the least important components of the **E** and **H** fields.

The vector **E**-field formulation, where the electric field is used instead of the magnetic field, can treat anisotropic but loss-free problems. However, for an optical waveguide, the electric field is not continuous across the dielectric interface and this needs to be imposed in the formulations. Besides, for the full-vectorial **E**-field formula, the natural boundary conditions correspond to the magnetic wall. Hence, an enforced boundary condition on the electric wall ($\boldsymbol{n} \times \boldsymbol{E} = 0$) is required which is more difficult to be implemented in irregular shaped structures.

On the other hand, the vector **H**-field formulation is more suitable for dielectric waveguide problems, since the magnetic field is continuous everywhere, the natural boundary conditions correspond to those of the electric wall and no forced boundary conditions are required at the boundaries, while several approaches have been employed to suppress or eliminate the spurious modes.

3.3.1 A full-vectorial H-field formulation-based FEM

In this work, the full-vectorial **H**-field FEM variational formulation has been used to study and analyze the propagation characteristic of the light in the proposed nanowire waveguides (NWs). As it has already been mentioned above

that, this method is chosen because the magnetic field is continuous in all directions of the dielectric waveguides.

The formulation can be written as [199]:

$$\omega^2 = \frac{\iint_{\Omega}(\nabla\times\boldsymbol{H})^*\left([\varepsilon_r]^{-1}\nabla\times\boldsymbol{H}\right)d\Omega}{\iint_{\Omega}\boldsymbol{H}^*\hat{\mu}\boldsymbol{H}d\Omega} \tag{3.33}$$

The spurious solutions are generated while using the full-vectorial **H**-field formula because the divergence condition ($\nabla \cdot \boldsymbol{H} = 0$) is not satisfied. In order to eliminate the spurious solutions generated along with the physical solutions, a penalty function method [200] is used to force the divergence condition. With the penalty function method, the variational formula from equation (3.33) becomes as follows:

$$\omega^2 = \frac{\iint_{\Omega}(\nabla\times\boldsymbol{H})^*\left([\varepsilon_r]^{-1}\nabla\times\boldsymbol{H}\right)d\Omega + \frac{\alpha}{\hat{\varepsilon}_o}\iint_{\Omega}(\nabla\cdot\boldsymbol{H})^*\cdot(\nabla\cdot\boldsymbol{H})d\Omega}{\iint_{\Omega}\boldsymbol{H}^*\hat{\mu}\boldsymbol{H}d\Omega} \tag{3.34}$$

where α is the penalty coefficient. It can be estimated to be around $1/\varepsilon_{nw}$, where ε_{nw} is the dielectric constant of the NW. The spurious solutions can be minimized by introducing a higher penalty coefficient. However, a high value of the penalty coefficient can deteriorate the effective index of the waveguide. Therefore, the suitable penalty coefficient has to be optimized in order to obtain the precise solutions.

3.3.2 Finite element program

In the present work, an in-house Finite Element program [201] has been used to obtain the modal solution of the NW structure under investigation. In this study, the NWs were considered as trapezoidal-shaped optical waveguides, as shown in Fig. 3.3. The NWs are coated with a thin metal layer to introduce surface plasmon resonance leading to the enhancement of the light interaction at the dielectric/metal interface.

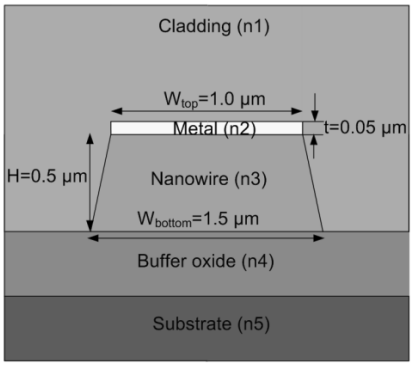

Figure 3.3: Cross-section of the trapezoidal-shaped NW coated with the thin metal layer.

The NW has a height, H, of 0.5 µm, a bottom and top width of, w_{bottom}=1.5 µm and w_{top}=1.0 µm, respectively and a metal layer thickness of 50 nm. The sidewall angle is considered to be about 65°. However, these values can be changed as required.

A low density finite element discretisation of the NW structure described in Fig. 3.3, is presented in Fig. 3.4. In order to exploit the symmetry of the structure along the y-axis, only the right-hand side half structure of the NW has been considered as the computational domain, thus reducing the memory requirements and computing execution time. To obtain the symmetric or antisymmetric modes of the NWs, either electric or magnetic wall boundary conditions were imposed along the symmetry boundary, according to the required dominant component of the magnetic field. For example, if the symmetric H_x modal field is required, to ensure its continuity along the x-axis, the $\mathbf{n} \times \boldsymbol{H} = 0$ boundary condition is imposed at the symmetry wall.

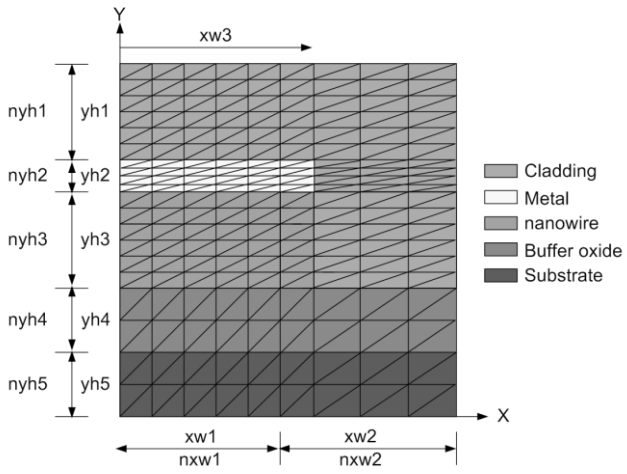

Figure 3.4: Cross-section of half-symmetry NW structure divided into small triangular-shaped elements for FEM program.

As can be seen in Fig. 3.4, the cross-section of the NW structure has been divided into small triangular-shaped first-order elements, where only the nodes at the vertices of the triangles are considered in deriving the shape functions for the triangular elements. The variables presented in Fig. 3.4, as the dimensions of the discretized structure, correspond to the input variables of the Mesh Generation Subroutine of the finite element program and these can be varied accordingly, when required to change the dimensions of the structure, and the mesh refinement in each region of the waveguide, according to the expected confinement of the modal field. In other words, in the regions where the modal field is expected to have larger confinement a finer mesh point is used to increase the accuracy of the approach, while in regions where minor field concentrations are foreseen, a low density mesh point is assigned.

The divisions of the structure presented in Fig. 3.4 along the y-axis, where the variable names start with ‘nyh’ and ‘yh’, represent the number of divisions used and the corresponding height, respectively, for each horizontal section of the waveguide considered. Similarly, along the x-axis, the division of the NW is performed with the variable names starting with ‘nxw’ for the elements in each vertical section and their corresponding widths are represented by the variable starting ‘xw’. The structure of this NW consists of the substrate, the buffer oxide layer, the core of the waveguide, the metal layer, and the cladding material. They

are all demonstrated in different colours and numbers. In this work, typically the mesh point of the NW used was 250 x250 discretisation points, along with the x- and the y-axis respectively. Therefore, resulting 62500 elements have been considered to represent these waveguides in our analyses.

It can be seen from Fig. 3.4 that each element is different in size and in refractive index creating a non-uniform mesh point through the whole structure. The non-uniform mesh point allows the program to be able to enhance the analysis on some specific part such as the sensitive area, as explained above. Hence, the accuracy of the solution can be increased with less simulation time. We have used 60 mesh points in 50 nm thick metal layer which gives a spatial solution of 0.83 nm. The operating wavelength of this work depends on the material used to fabricate the NWs. For silicon NWs, the operating wavelength is in infrared (IR) region (λ=1550 nm). For the ormocomp NWs, visible light is used as operating wavelength (λ=400-700 nm).

The dielectric constant (ε) of each material is also required in the program where $\varepsilon = n^2$. The metal layer in this case is gold where its complex refractive index is wavelength dependent. The complex refractive index of gold in this study is based on [202]. The dielectric constant of gold for the whole range of operating wavelength in this work is provided in Appendix B. The cladding material is water which has an index of 1.333 at T=25°C.

During the program execution, the coordinates of the nodes of each triangular element, as well as their refractive indices are calculated by the mesh generation subroutine. From the obtained parameters, the global matrices $[A]$ and $[B]$ are formed in order to be used in the solution of the eigenvalue problem (3.32). The above problem is solved using an in-house efficient sparse matrix solver, where the two-dimensional global matrices are reduced in one dimension, thus consequently reducing the computational time. Each eigenvalue of the solution corresponds to the propagation constant, β, of the obtained mode, while its eigenvector corresponds to the magnetic field component (H_x, H_y and H_z) of each node of the structure under consideration, of the obtained mode for the particular propagation constant β .

The program has the ability to calculate up to five modes at a time, located close to the input value of the propagation constant (β). Initially, the trial input value of the propagation constant β, is considered to be that maximum possible value of the propagation constant of the fundamental mode, estimated using equation (3.16), where n_{eff} is replaced with the refractive index of the NW n_{nw} and $k_o = 2\pi/\lambda$. The program allows the calculation of either quasi-TE (H_y) or quasi-TM modes (H_x). The field distributions of the obtained five modes for the particular input value of the propagation constant (β) are then plotted and the required mode is identified and iterated independently, by using as input the calculated value of the propagation constant of the particular mode.

As it has been mentioned earlier, by solving the eigenvalue problem (3.32) some non-physical solutions, known as spurious solutions are also obtained because the divergence condition ($\nabla \cdot \boldsymbol{H} = 0$) is not satisfied in the variational formulation (3.33). The spurious solutions may appear as separate unclassified modes, therefore they can be neglected, or, they can affect the field distribution of the guided modes, if their propagation constant is close to the propagation constant of a guided mode. The value of the penalty coefficient, α, used in equation (3.34), to reduce the effect of the spurious solutions is in the range of 0.4-0.6 depending on the studied NWs, either silicon and ormocomp.

Furthermore, the **E**-field and the energy flux density (Poynting vector: **S**) can also be computed later using Equation (3.9). The results obtained from this full-vectorial **H**-field formulation-based FEM including the effective index, the optical electromagnetic field, the spot size, and the normalized power confinement are presented in Chapters 5 and 6.

3.4 Summary

Finite Element Method (FEM) is one of the most powerful numerical techniques used to solve complex structure problems such as the optical waveguide. The concept of the FEM is to divide the continuous structure into many triangular-shaped elements. The discretized elements are connected by

nodes where the discretized optical field of the whole structure is calculated. Each element can have different size, thus forming non-uniform mesh point and different dielectric permittivity. In this study, the full-vectorial **H**-field formulation-based FEM is used as a tool to analyze the propagation characteristics of the guided modes in the NW because of the continuity of the **H**-field across the boundary. The **H**-field is continuous everywhere in the dielectric waveguide. It has the advantage over the **E**-field formula because no forced boundary condition is required. The spurious modes, which occur because the divergence condition is not satisfied, can be minimized by using the penalty function method. In the discretisation of the NW structure, 62500 elements have been used, thus achieving a spatial resolution of 0.83 nm inside the metal layer.

4. Fabrication of nanowire waveguides

4.1 Introduction

This chapter discusses the fabrication of the proposed nanowire waveguides (NWs). First, a general discussion on the existing fabrication methods is given. Then the techniques used to fabricate these NWs are described. There are different types of NWs depending on the material used to synthesize them. The NWs can be metallic, semiconducting, insulating and organics molecules. In this work, the fabrication of silicon waveguides (semiconductor waveguides) with the conventional structure, silicon NWs with horizontal slot structure and the ormocomp NWs (polymer waveguides) are considered as part of optical sensors.

For silicon waveguide fabrication, photolithography and etching are the main techniques utilized. Photolithography is the technique used to transfer the pattern from an optical mask to the light-sensitive material called photoresist (PR), which is coated on the substrate, by ultraviolet (UV) light illumination. There are two types of photoresist, the positive and negative photoresists. The positive photoresist is the type of photoresist that is soluble to the photoresist developer when it is exposed to the UV light. On the other hand, the negative photoresist is insoluble to the developer after the UV light exposure. The comparison of those two photoresists is presented in Fig. 4.1.

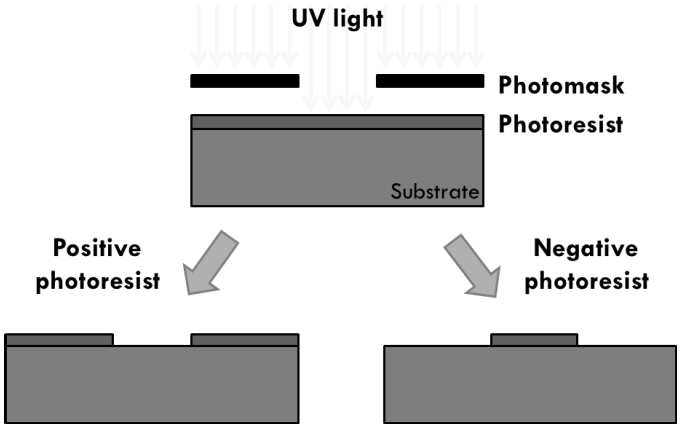

Figure 4.1: Comparison between positive and negative photoresist. The positive photoresist is soluble when it is exposed to the light whereas the negative photoresist is not.

The positive photoresist has a higher resolution compared to the negative one. The photoresist is coated on the substrate using a spin coater. The spin speed depends on the viscosity of the photoresist and the designed thickness of the photoresist layer. The optical mask is a transparent plate covered with a pattern of the metal-absorbing film. It is usually chrome on quartz.

There are three methods for the mask alignment in photolithography based on how the photomask is placed. If the mask makes a contact with the photoresist, the method is called contact photolithography [203]. This method provides high output resolution with 1:1 magnification. However, the contact of the two faces can leave some defects on the mask causing mask degradation and non-uniform resolution can occur in a subsequent processing using the same mask. In order to alleviate this drawback, another non-contact method has been developed, called proximity photolithography [203]. This method allows a small gap in the range of 10-50 μm between the mask and the photoresist layer. The gap avoids the generation of defects on the mask. The drawback of this method is the low resolution which is the result of diffraction and no magnification can be achieved. The problems discussed above can be overcome through the different method called projection photolithography [203]. In this method, the optical mask is placed at a distance from the photoresist layer. The pattern image on the mask is projected on the photoresist layer by the lens. The projection photolithography provides a higher resolution and lower defect density. Also, a de-magnified image can be obtained. Therefore, the patterns on the mask do not have to be as small as the final image. Usually, the de-magnification is about 5x. With the projection method, only a small region on the photoresist layer is exposed at a time, therefore the substrate has to be mechanically moved by a stepper. Stepper is a machine used in projection lithography to slide the mask step-by-step. Our silicon optical waveguides are fabricated using this projection technique with i-line stepper (λ=365 nm).

Another main technique used in this work is etching. The two types of etching are commonly called wet and dry etching [203]. Wet etching is the process in which the etchants are in liquid phase. Therefore, the silicon wafers can be simply

immersed in an etchant bath. The wet etching is done with a chemical process where reactants from the etchant diffuse to the surface of the wafer and have a chemical reaction to form soluble products. The soluble species are then diffused away from the surface into the bulk of the liquid. Wet etching is known to have high selectivity due to specific chemical reactions between etchants and materials. The etching achieved by this method is isotropic in the sense that the surface is etched in all directions. Therefore, the directionality cannot be achieved except for single crystalline materials and the undercut cannot be avoided.

In the dry etching method, the material removal reactions occur in the gas phase by the use of ion-bombardment in which the ions bombard on the wafer surface. The ions are usually plasma of reactive gases which are generated in vacuum under low pressure by the electromagnetic field. After the high energy ions bombard onto the surface of the silicon wafer, the volatilisation occurs from the chemical reactions. The dry etching is very directional which means the critical dimension control can be achieved. Etch rate can also be easily controlled. In our work, the dry etching is used to fabricate the silicon NWs due to its directional control.

In this work, the nanoimprint is used to fabricate the ormocomp NWs because it promises a simpler, less time consuming and lower cost process with high-throughput compared to other techniques [93]. The nanoimprint is a technique to transfer the pattern by having mechanical deformation on imprint resist. The imprint resist is a UV-curable polymer which is ormocomp is our case.

For the surface plasmon resonance (SPR) study, the ormocomp NWs need to be coated with a thin metal layer, which is gold in our work. There are two types of physical vapour deposition to deposit the thin film, namely evaporation and sputtering. In the coating of the polymer NWs used in the SPR study, the sputtering technique is used to deposit the gold layer on the ormocomp NWs because it provides a better adhesion and a better uniformity of the metal layer compared to the evaporation technique.

4.2 Silicon nanowire waveguides

Firstly, the silicon waveguides are fabricated to be used as a hard mold for the nanoimprint in order to subsequently fabricate the ormocomp waveguides at a lower cost. The silicon NWs are designed to be connected to feed waveguides at both ends through the taper as shown in Fig. 4.2.

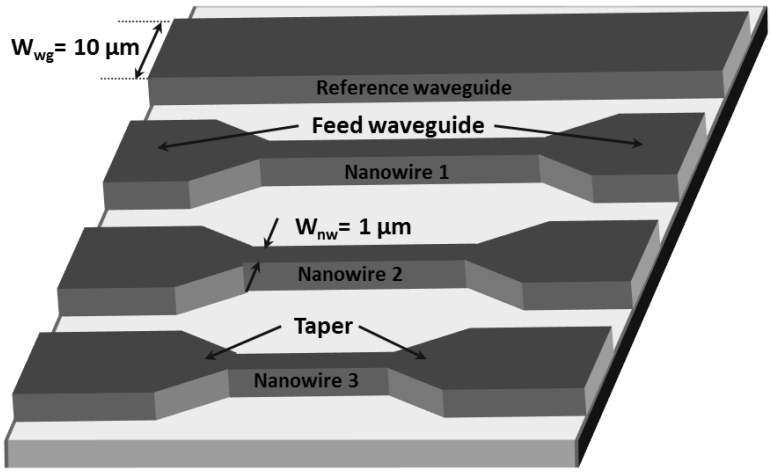

Figure 4.2: Schematic of the reference waveguide and interested NWs, which are connected to the feed waveguides through the taper, on a silicon substrate.

The reference waveguide with the width of 10 µm is also fabricated on the same silicon substrate with integrated NWs at the same time. This reference waveguide is used to study for polarisation-independent when coated with a thin gold layer in Chapters 6 and 7 because the 1 µm wide NW cannot achieve the vertical sidewalls. Hence, the polarisation-independent of surface plasmon resonance (SPR) cannot be applied, only the polarisation in the quasi-TM mode is considered in the wavelength-scale NWs.

In this part, the fabrication process of the silicon NWs with a horizontal slot structure is described. The slot waveguides are the waveguides that have low-index material sandwiched by high-index materials. In this work, the slot is horizontally oriented, so it is called the horizontal slot structure as shown in Fig. 4.3.

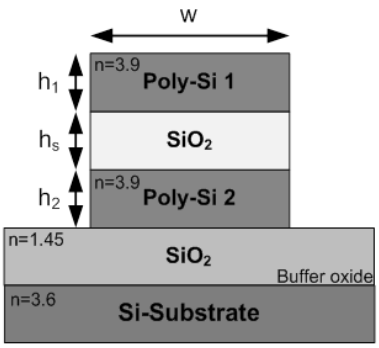

Figure 4.3: Cross-section of the designed silicon NW with horizontal slot structure.

Our horizontal slot structure NWs are fabricated with silicon-on-insulator (SOI) technology to improve the performance. The NWs consist of SiO_2 as the low-index material sandwiched by two poly-Si layers. The main fabrication process for the silicon NWs includes photolithography and dry etching. The fabrication process of the silicon NW fabrication is provided in Fig. 4.4.

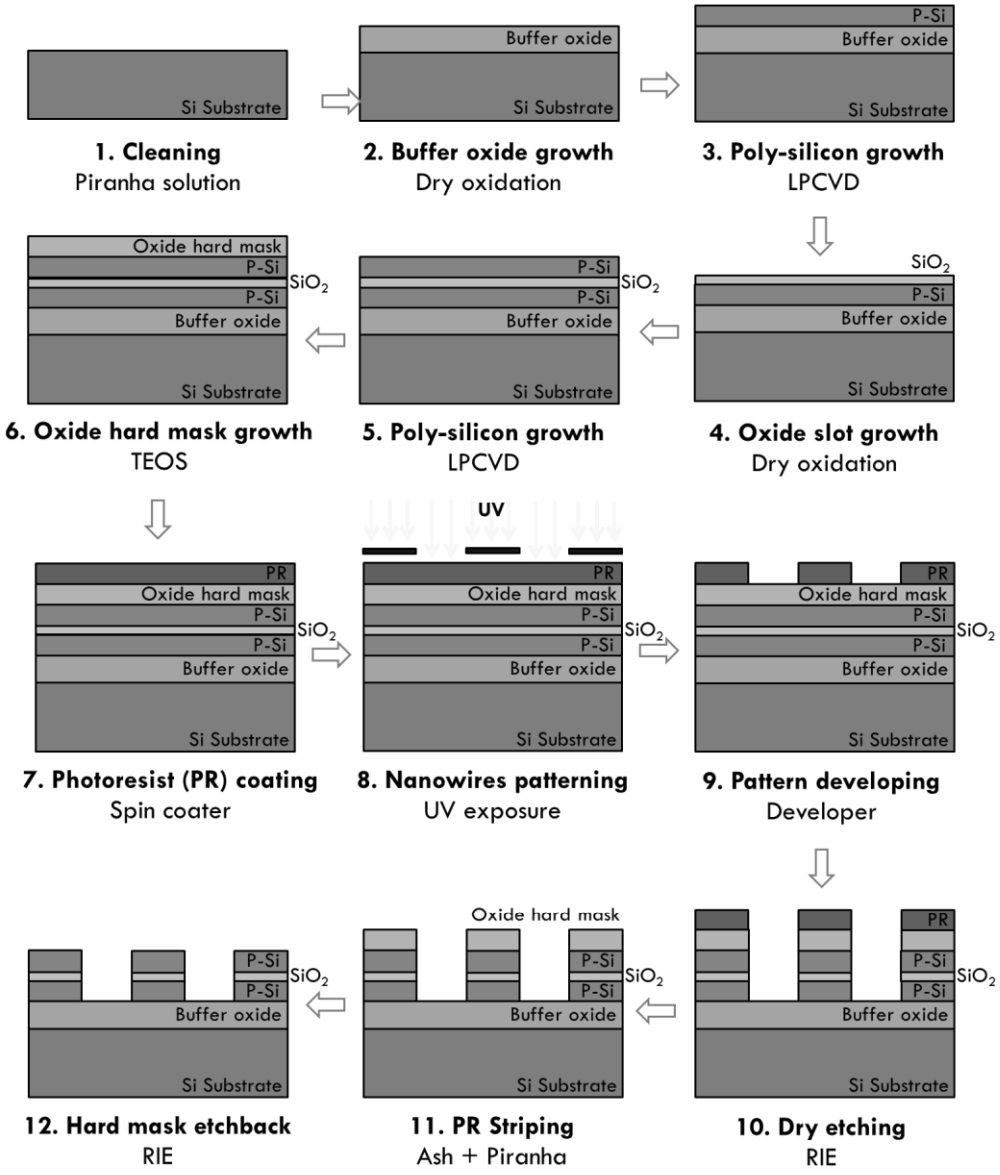

Figure 4.4: Schematic showing the fabrication process of the silicon NWs with a horizontal slot structure.

The silicon NWs and the reference waveguides are fabricated on a 6-inch silicon wafer which is first cleaned by putting in piranha solution. The piranha solution is used to remove organic materials on the wafer. The solution is made of 70% sulfuric acid (H_2SO_4) and 30% hydrogen peroxide (H_2O_2) with a volume ratio of 4:1. The buffered oxide layer for SOI technology is then grown on the silicon substrate using the low-pressure chemical vapour deposition technique (LPCVD). In a chemical vapour deposition reactor, volatile precursors are fed into a vacuum chamber and then react with the substrate causing the desired deposit some by-

products. These by-products are eliminated by gas flow inside the chamber. The chemical vapour deposition reactor used in this work is shown in Fig. 4.5

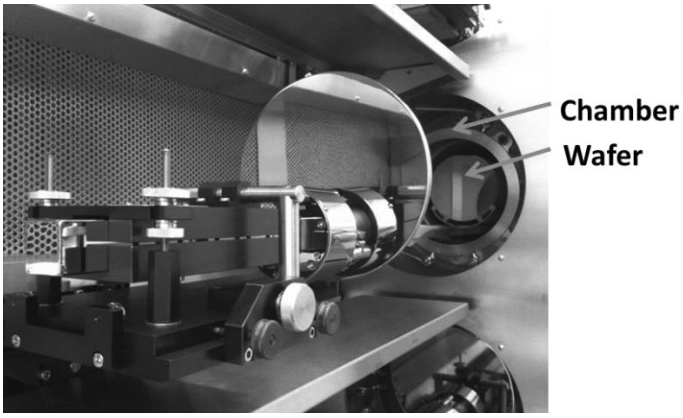

Figure 4.5: Chemical vapour deposition reactor used in this fabrication at the Thai Microelectronics Center (TMEC).

LPCVD is a chemical process used to produce a thin film on a substrate at sub-atmospheric pressure. This technique uses the dry oxidation method to grow the oxide layer because a better quality of the oxide layer can be obtained compared to the those from wet oxidation [93]. The dry oxidation uses oxygen (O_2) as an oxidant whereas water vapour (H_2O) is used for the wet oxidation. To grow the 250 nm thick oxide layer, O_2 is diffused into a chamber at the flow rate of 8 standard litres per minute (SLPM) at T=1000 ^oC. The SLPM is a unit of volume flow rate of a gas for standard conditions of temperature and pressure. The dry oxidisation reaction to grow the oxide layer can be described by:

$$Si + O_2 \rightarrow SiO_2 \tag{4.1}$$

After that, Poly-Si is deposited on the silicon substrate using the LPCVD process. In order to deposit poly-Si, silane (SiH_4) is used as the volatile precursor. The poly-Si deposition process is operated under the condition, T= 620 ^oC and P= 261 mTorr. With a flow rate of silane at 150 standard cubic centimetre per minute (SCCM), the 250 nm thick poly-Si layer is produced in 14 minutes. The SCCM is the molar flow rate of a gas for standard conditions of temperature and pressure The reaction of poly-Si depositing on the substrate from silane is described by:

$$SiH_4 \rightarrow Si + 2H_2 \tag{4.2}$$

After the deposition of the poly-Si layer, another SiO_2 layer is generated using the same technique as considered in growing the buffer oxide layer. This oxide layer will be the slot region with a thickness of 100 nm. Then, another poly-Si layer with the thickness of 200 nm is deposited to form the sandwich-structured waveguide. The total thickness is now 500 nm. With such a thick structure, the photoresist layer, which acts as a soft mask in the etching process, can degenerate during the process. Therefore, a thick oxide layer is required to act as a hard mask for the etching. The dry oxidation with TEOS (tetraethyl orthosilicate) deposition technique is carried out at T= 710 °C and P=212 mTorr. With the flow rate of TEOS is 100 SCCM and the deposition time is about 1.08 hours.

Before transferring the NWs pattern, the photoresist is dispensed onto the oxide hard mask layer. The photoresist easily comes off, so an adhesion promoter is needed in order to make the photoresist remain attached to the substrate. In this work, HMDS (hexamethyldisilazane) is used as an adhesion promoter. A gaseous HMDS is vaporized inside a chamber for 15 minutes. The photoresist used is Sumitomo: PFI-34A which is a positive photoresist. The thickness of the photoresist layer is around 1.09 μm.

The pattern of the NWs set is transferred onto the photoresist layer by photolithography. An i-line (λ=365.6 nm: UVA) stepper machine with high power mercury (HG) lamp, is used for the exposure. The exposure time is 340 ms and the exposure dose is 350.81 mW/cm^2. After the exposure, post-bake exposure is needed at T=110 °C for 3 minutes. Following that, the photoresist is developed using the developer from Tokuyama SD-W for 60 seconds. Then, hard bake is required at T=120 °C for 90 seconds to harden the photoresist pattern for the next oxide etch.

After generating the pattern on the photoresist layer, RIE (Reactive-ion etching) is used to etch all the layers of the silicon NWs. The RIE is a type of dry etching where the plasma is generated under low pressure (between 10^{-3} and 10^{-1} Torr). The plasma etchants for the silicon NWs is CF_4 (Carbon tetrafluoride). The etching process of each layer can be carried out at the same time because the material in each layer is silicon-based. Then, plasma ashing, which is the oxygen

plasma RIE, is used as a photoresist removal. The piranha solution is again used to remove the residual photoresist on the silicon NWs. Finally, the TEOS layer is etched back using the RIE.

The process flow of the silicon NW fabrication is provided in Table 4.1.

Table 4.1: Fabrication process of the silicon NW.

Process	**Technique**	**Chemicals**	**Thickness**
1. Cleaning	-	Piranha	-
2. Buffer oxide growth	Dry oxidation	O_2	250 nm
3. Poly-Si growth	LPCVD	SiH_4	200 nm
4. Oxide slot growth	Dry oxidation	O_2	100 nm
5. Poly-Si growth	LPCVD	SiH_4	200 nm
6. Oxide hard mask growth	Dry oxidation	TEOS	500 nm
7. PR coating	Spin coating	Sumitomo: PFI-34A	1.09 µm
8. NWs patterning	Exposure	UV	-
9. Developing	-	Tokuyama: SD-W	-
10. Dry etching	RIE	CF_4	-
11. PR striping	Ash	O_2	-
12. Hard mask etch back	RIE	CF_4	-

SEM images of the fabricated NW with different magnifications showing its set, the etched pattern, the sidewall and the top surface are presented in Fig. 4.6.

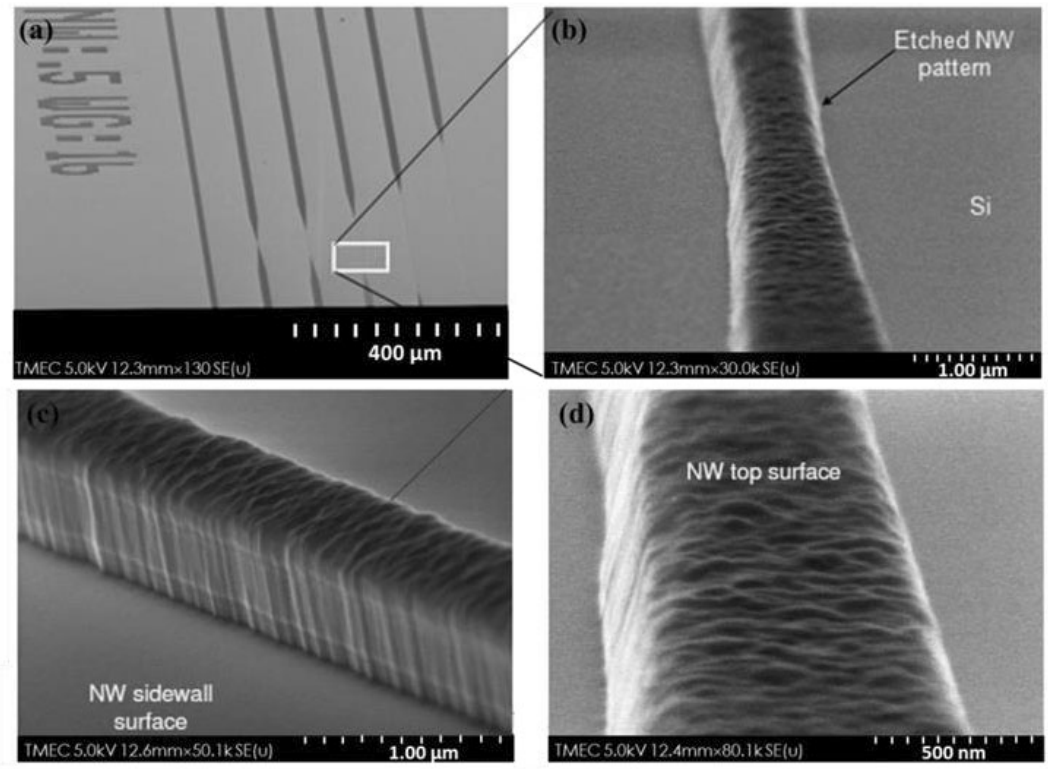

Figure 4.6: (a) SEM image of the NWs set, (b) Magnified SEM image showing the etched NW pattern, (c) Magnified SEM image showing the sidewall surface and (d) Magnified SEM image showing the top surface.

Fig. 4.6(a) shows an image of a set of four NWs of different lengths and two reference waveguides. The tip of the tapered waveguide is also clearly seen. Fig. 4.6(b) shows a magnification of a single silicon NW. Fig. 4.6(c) and Fig. 4.6(d) show the NW sidewall surface and top surface, respectively. The surface roughness can be observed from the image and it is measured to be around 0.1 µm by AFM (atomic force microscopy).

Even though the silicon NWs are designed to have vertical sidewalls, however, the fabricated NWs have non-vertical sidewalls due to the resolution limits of the stepper machine. Therefore, double exposure is required to obtain the small NWs, leading to an inaccurate pattern transferring. In addition, the by-products from the stack etching also have an effect on the sidewalls of the NWs because they can be re-deposited on the sidewalls surface and block the plasma etchants. The sidewall angle is measured to be around 65°. An SEM image showing a cross-section of a fabricated NW is shown in Fig. 4.7.

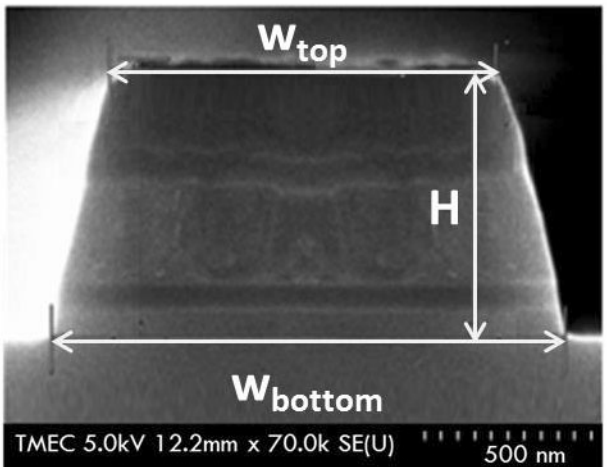

Figure 4.7: SEM image showing a cross-section of the silicon NW.

The fabricated NWs have a height of H=0.5 µm, the width at the top (W_{top}) and bottom (W_{bottom}) are 1.0 µm and 1.5 µm, respectively. These fabricated horizontal slot silicon NWs are initially used as a master mold (hard mold) to fabricate ormocomp NWs using the nanoimprint method. However, a single layer (conventional structure) poly-Si NW can also be considered to use as a hard mold for the nanoimprint technique to reduce the fabrication steps.

For the reference waveguide, it has a width of 10 µm. In order to use it as the polarisation-independent waveguide with SPR, the reference waveguide is fabricated again to achieve the thickness of 10 µm. The fabrication process is the same with growing poly-Si layer in the horizontal slot structure using LPCVD and the poly-Si is then dry etched with RIE technique. The reference feed waveguide is fabricated to have vertical sidewalls as shown in Fig. 4.8.

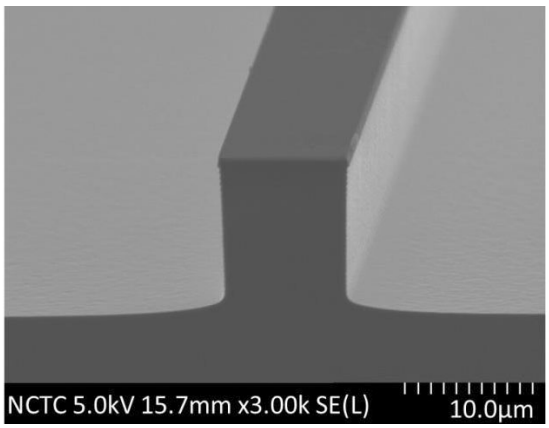

Figure 4.8: SEM image showing a cross-section of the reference waveguide with vertical sidewalls structure.

4.3 Ormocomp nanowire waveguides

In this part, the fabrication of the ormocomp NWs using the nanoimprint method is discussed. The nanoimprint is a technique used to transfer the nano-size patterns from a mold to an imprint resist. The molds used in our work are the silicon NWs with horizontal slot structure and the imprint resist is ormocomp which is a hybrid polymer material. However, the ormocomp NWs do not have the slot structure but the conventional structure instead. In addition, if the silicon NWs are directly imprinted on the ormocomp layer, the opposite pattern is obtained as shown in Fig. 4.9(a). Therefore, the additional mold is needed to transfer the pattern in order to have the ormocomp NWs with an identical pattern to the silicon NWs as shown in Fig. 4.9(b).

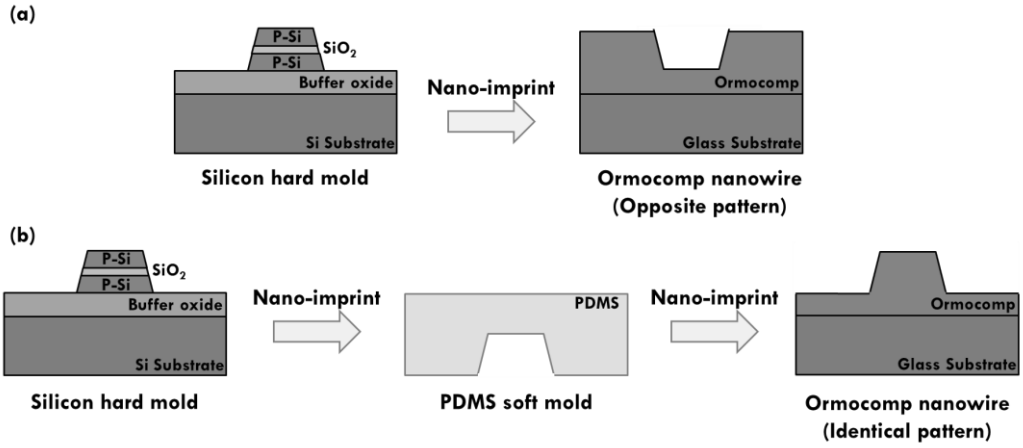

Figure 4.9: (a) Schematic of an ormocomp NW with the opposite pattern to its original. (b) Schematic of the duplicate ormocomp NW with the use of additional PDMS soft mold.

The additional mold is made of PDMS (Polydimethylsiloxane) which is considered to be a soft mold. The PDMS is a silicon-based organic polymer and transparent at the optical frequencies (λ=240 nm-1100 nm). It is normally prepared by mixing the silicone elastomer base (viscous liquid) and curing agent (liquid) with the ratio of 10:1 by weight. However, this ratio can be varied depending on the desired hardness of the PDMS mold. In our case, a harder elastomer mold is needed because the PDMS mold is mechanically stamped on

the ormocomp layer and excess applied force is required during the stamping process. If the PDMS mold is too soft, the pattern on the PDMS mold can be flattened while stamping. This would lead to a distorted pattern on the ormocomp. On the other hand, the solidity of the PDMS mold cannot be very strong because the mold can be easily torn during the demold process due to the lack of flexibility. Therefore, after some trial experimentations, the ratio of the mixture is chosen to be 7:1 in this work.

Before putting the PDMS mixture (liquid) on the silicon NWs, the HMDS is vaporized first onto the surface of silicon NWs for 30 minutes in order to improve adhesion. After that, the PDMS mixture (liquid) is slowly poured onto the silicon NWs. Then, the structure goes through a degas process for 30 minutes in order to remove all the bubbles occurring from the mixing. Next, the PDMS is hardened in a furnace at T=100 °C for 2 hours. After the curing process, the PDMS soft mold can be removed from the silicon substrate. The reverse pattern of the silicon NWs now appears on the PDMS soft mold. The process of making the PDMS soft mold is shown in Fig. 4.10.

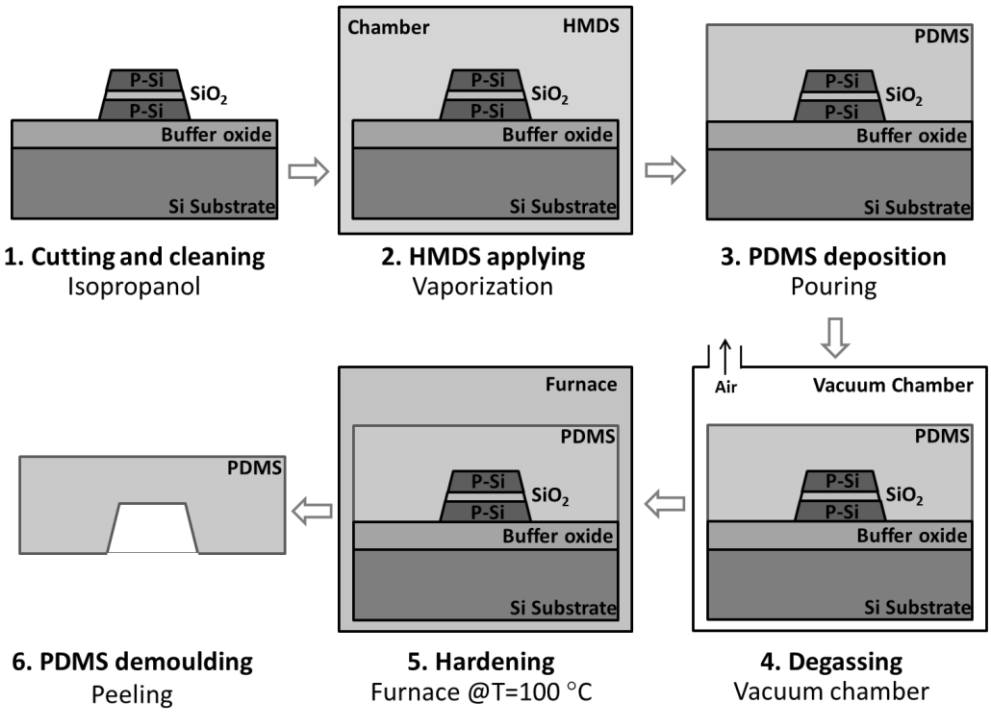

Figure 4.10: Schematic of the PDMS soft mold fabrication process. The reverse pattern of silicon NWs is obtained on the PDMS mold.

In order to transfer the pattern from the PDMS mold, ormocomp, which is a UV-curable hybrid material, is dispensed on a clean glass substrate using the spin coater. The ormocomp is a viscous material leading to a thick ormocomp layer. Normally, the ormocomp layer with a thickness of 20-25 µm is obtained when spinning at the speed of 3000 rpm for 30 seconds [145]. The thickness can be reduced by increasing the spin time. In this work, the spin time is increased to 1 minute where the 10 µm thick ormocomp layer is obtained. Then, the PDMS mold is imprinted on the ormocomp layer. In this process, air bubbles can be generated due to the height of the NW pattern. Therefore, the PDMS mold has to be pressed on the ormocomp layer until the air-bubbles are all removed in order to achieve a precise and clear pattern. The ormocomp is then cured with UV light for 5 minutes. After the UV curing, the ormocomp layer is hardened and the PDMS can be detached from the ormocomp NW. An identical pattern with the silicon NWs consequently appears on the ormocomp layer. The process flow of the nanoimprint used to fabricate the ormocomp NWs is shown in Fig. 4.11.

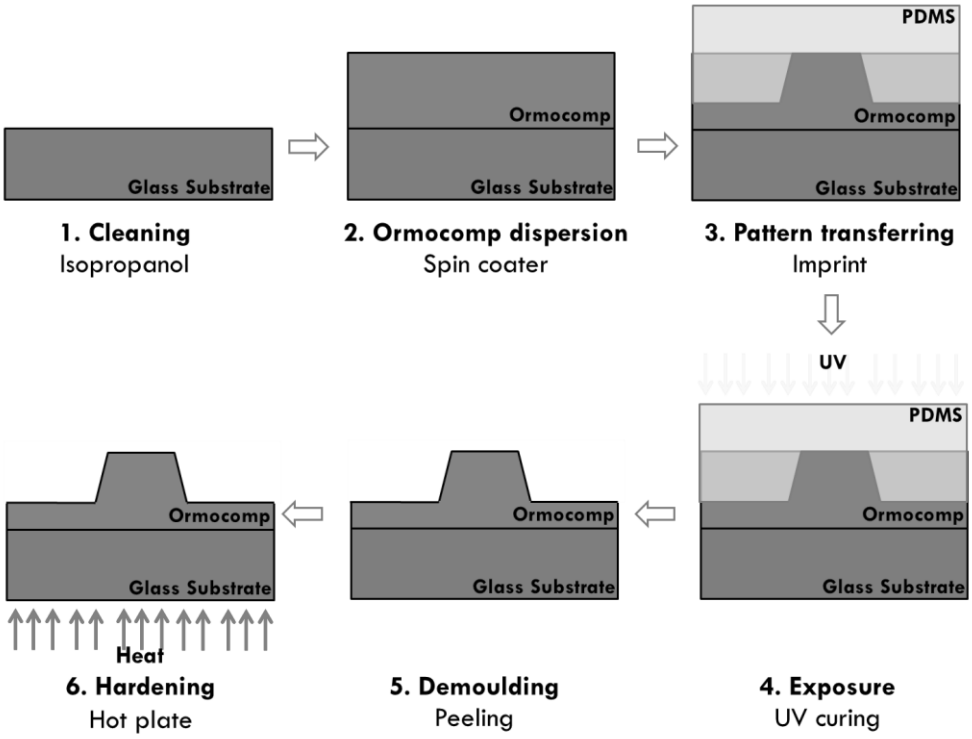

Figure 4.11: Schematic showing the process flow of the nanoimprint technique used to fabricate the ormocomp NW.

However, the ormocomp layer was too thick leading to a leftover ormocomp layer from the imprint process. Therefore, rather a rib structure ormocomp NW was obtained instead of a ridge structure. The optical microscope images of the fabricated ormocomp NW from the nanoimprint technique with different magnifications are shown in Fig. 4.12.

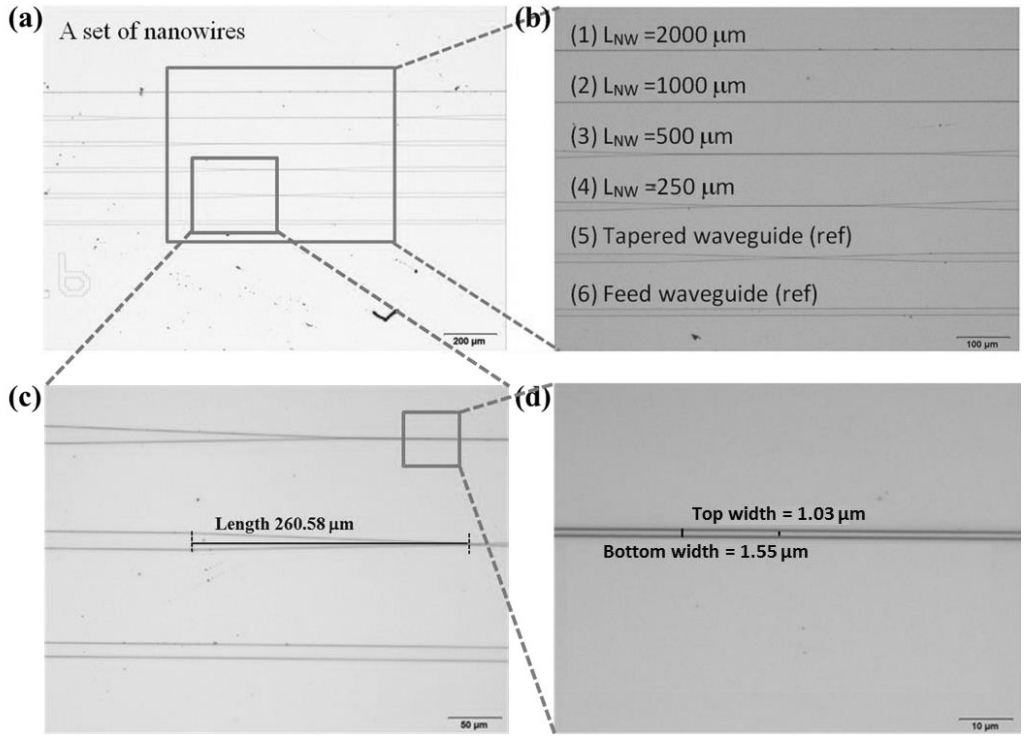

Figure 4.12: Optical microscope image of (a) a set of NWs, (b) magnified image of the NW set consisting of the feed waveguide, the tapered waveguide and four different lengths of NWs, (c) feed waveguide and tapered waveguide and (d) 1 μm wide NW.

From the optical images, it can be seen how the duplicate pattern to the silicon NWs can be produced on the ormocomp layer using the nanoimprint method. The taper length is measured to be around 260 μm as shown in Fig. 4.12(c). The taper angle is 1° which is the same as the dimensions from the initial design. The 1 μm wide NW is shown in Fig. 4.12(d). The top width (W_{top}) is measured to be 1.03 μm and the bottom width (W_{bottom}) is measured to be around 1.55 μm. This result matches the cross-section image obtained from the AFM (Atomic Force Microscope) as shown in Fig. 4.13.

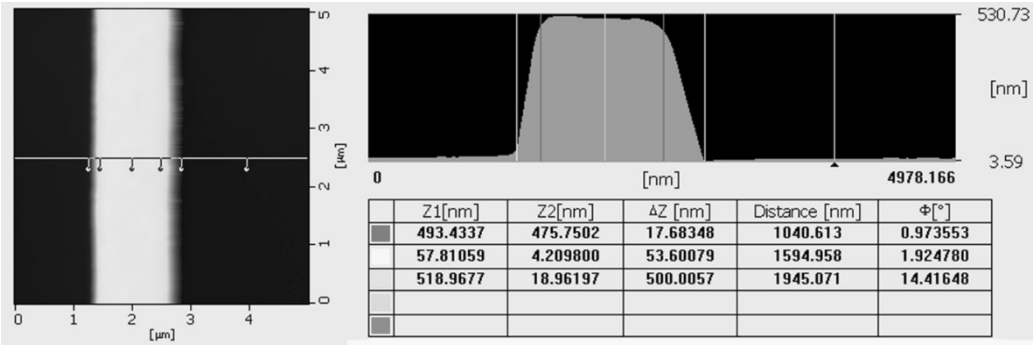

	Z1[nm]	Z2[nm]	ΔZ [nm]	Distance [nm]	Φ[°]
	493.4337	475.7502	17.68348	1040.613	0.973553
	57.81059	4.209800	53.60079	1594.958	1.924780
	518.9677	18.96197	500.0057	1945.071	14.41648

Figure 4.13: AFM image showing a cross-section of ormocomp NW and its dimensions.

The AFM is a scanning probe microscope used to image and measure nano-size materials. The tip we used for the AFM is HA_NC ETALON, which is a silicon tip with 10 nm tip curvature radius. From the AFM image in Fig. 4.13, W_{top} is measured to be 1.04 µm whereas W_{bottom} has a width of 1.59 µm. The thickness of the fabricated ormocomp NW is measured to be around 500 nm. A 3D image of the ormocomp NW can also be obtained using AFM where the scanning area is 25 μm^2 as shown in Fig. 4.14.

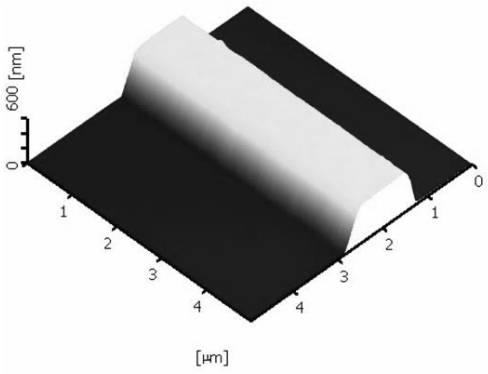

Ra	: 1.845E+02	nm
P-V	: 5.488E+02	nm
RMS	: 2.104E+02	nm
Rz	: 5.488E+02	nm
	(2 Points)	
S	: 2.813E+07	nm^2
S Ratio	: 1.11497	

Figure 4.14: 3D image of ormocomp NW with 25 μm^2 image space and a table of the surface roughness on ormocomp NW measured by the AFM.

Fig. 4.14 also shows the different types of surface roughness on the ormocomp NW. Here, Ra is the average roughness, P-V is the peak to valley ratio,

RMS is the root-mean-squares roughness, Rz is the mean roughness depth, S is the surface area and S Ratio is the surface roughness ratio. In this work, the surface roughness (RMS) is considered to be one of the important parameters which affect the loss during light propagating along the NWs.

Some of the fabricated ormocomp NWs are coated with a thin gold layer to study the SPR effect. The technique used to coat the gold layer is sputtering. Sputtering is a thin-film deposition technique which can be used with a wide range of materials. The sputtering uses plasma to bombard a solid target material causing dislodging of atoms which then deposit on the substrate to form the thin film as shown in Fig. 4.15.

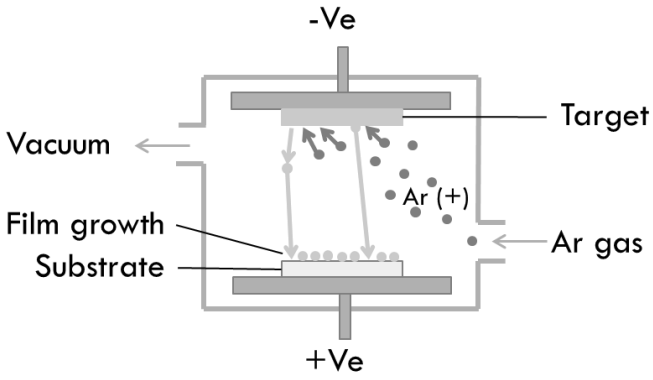

Figure 4.15: Schematic showing sputtering technique. Gold is used as the target material.

From Fig. 4.15, Argon (Ar), which is an inert gas, is fed into the chamber at low pressure. Plasma is created when applying DC voltage across the two electrodes. Positive ions in the plasma are accelerated toward the negatively biased cathode. The ions then sputter the target, which is gold in our case. After that, the gold atoms transport through the plasma and deposited themselves on the ormocomp NWs, creating a 50 nm thick gold film. The gold layer deposited using this technique has high uniformity and good adhesion with the substrate. The ormocomp NWs coated with the gold layer is presented in Fig. 4.16.

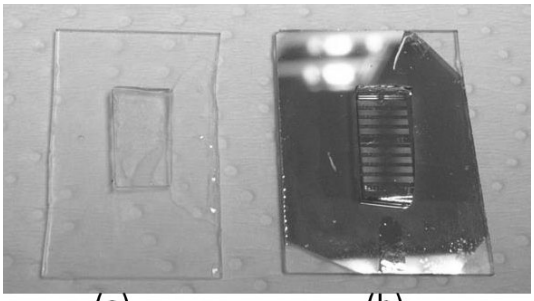

Figure 4.16: (a) Transparent ormocomp NWs and (b) Gold-coated ormocomp NWs.

A comparison between the ormocomp NWs before and after coating with the gold layer can be seen in Fig. 4.16. Before coating with gold, the ormocomp NWs are optically transparent while, the pattern of the NWs is hardly visible with the naked eye. However, the NWs pattern can be observed clearly after coating the ormocomp NWs with the gold layer. There are total 8 sets of the NWs fabricated on one glass substrate and each set contains one reference waveguide.

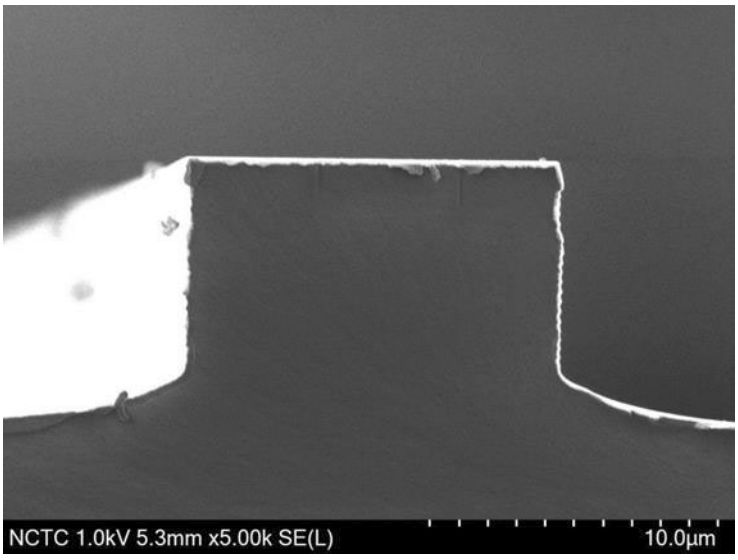

Figure 4.17: SEM image showing a cross-section of the gold-coated reference waveguide with vertical sidewalls structure.

The 10 µm x 10 µm reference waveguide is also coated with the thin gold layer as shown in Fig. 4.17. It is clearly seen from Fig. 4.17 that gold is coated at both the top and the sides of the 10x10 µm reference waveguide. Hence, the SPR is introduced in both quasi-TE and quasi-TM modes leading to the polarisation-independent behaviour which will be discussed later.

4.4 Summary

In this chapter, the fabrication of the silicon NWs with horizontal slot structure and the reference waveguides are discussed using the techniques of oxidisation, LPCVD, photolithography, and dry etching. The NWs are designed to have an integrated-optics structure for their further use in sensing applications. Therefore, the NWs are attached with tapered and feed waveguides. The horizontal slot NWs have SiO_2 as the low-index slot layer. It is sandwiched by two high-index poly-Si layers. The light is highly confined in the low-index area due to the discontinuity of the normal component of the electric fields. The NWs are fabricated on SOI substrate. The buffer oxide layer is created using the oxidisation process. Then, the first poly-Si layer is fabricated using the LPCVD technique. The oxidisation is utilized again for the 100 nm thick oxide slot layer. The second poly-Si layer is also fabricated by using the LPCVD. Both poly-Si layers have a thickness of 200 nm. The total thickness of the NWs is 500 nm which is too thick to use only photoresist as the mask for the etching process. Therefore, the oxidisation process for TEOS is required. It is used as the oxide hard mask for the etching. The stepper with i-line Hg lamp is used in the exposure. The UV light exposes the 1.09 µm thick positive photoresist which is coated by a spin coater. After developing, the NWs pattern is created on the photoresist layer. Next, RIE, which is one type of dry etching, is used to etch the silicon NWs by the CF_4 plasma. After the etching, the photoresist layer is removed by ashing. The fabricated silicon NWs have non-vertical sidewalls structure due to the resolution of the stepper which limits the size of the NWs. The sidewall angle is measured to be around 65°. The width at top, W_{top}, is about 1.0 µm whereas width at bottom, W_{bottom}, is 1.5 µm. The reference waveguide is also fabricated to have a size of 10 µm x 10 µm with vertical sidewalls in order to exhibit SPR at both the top and side surface which is considered to a polarisation-independent structure.

The ormocomp NWs can be fabricated at a lower cost by transferring the pattern from the silicon NWs onto ormocomp layer using the nanoimprint method. The silicon NWs are used as a hard mold. The additional mold is needed

in order to obtain an identical pattern on the ormocomp layer. The PDMS which is the additional elastomer mold is then fabricated also with the nanoimprint method. The hardness of the PDMS mold has to be controlled by varying the ratio of the PDMS mixture. In this case, the mixture ratio of 7:1 by weight is used. The HMDS is used as the adhesion promoter. The PDMS mold has the opposite pattern to the silicon NWs. After getting the soft mold, the ormocomp is coated on the glass substrate using the spin coater. The thickness of ormocomp layer is about 10 µm. The NWs have the thickness of 500 nm. Air-bubbles are generated during the imprint process. These bubbles need to be removed by lightly pressing the silicon NWs against the ormocomp layer. The pattern on the PDMS mold can be flattened if too much pressure is used. This leads to a distortion pattern on the ormocomp layer. After that, the ormocomp is cured by UV light and becomes harder. Then, the PDMS mold can be removed.

To study the SPR effects on the ormocomp NWs, a 50 nm thick gold layer is coated using the sputtering technique. The ormocomp NWs have non-vertical sidewalls, similar to the silicon NWs. However, there is some leftover ormocomp layer after the imprint process due to the very thick ormocomp layer. This problem can be solved by diluting the ormocomp with other chemicals such as ormothin and ma-T 1050. For the ormocomp reference waveguides, gold layer with a thickness of 100 nm is coated. Due to its vertical sidewalls, the gold-coated at the top and the sides of the waveguide can have the SPR in both quasi-TE and quasi-TM modes which will be described in Chapters 6 and 7.

5. Simulation analysis of silicon nanowire waveguides

5.1 Introduction

This chapter includes the use of a full-vectorial **H**-field FEM to study and analyze the possible guided modes and their characteristics. The analyses concentrate on characteristics of the optical modal field, the effective index of the guided modes, the normalized power confinement and power density in the silicon nanowire waveguides (NWs). The key parameters investigated are the dimensions of the NW structures, the cladding index and the operating wavelength. Since the silicon NWs are proposed to be used in optical sensing applications, the aim is to design the NWs in order to achieve the maximum possible sensitivity. The key in realizing high sensitivity is the ability to achieve high normalized power confinement in the sensing region in order to enhance the interaction between the light and the analyte material.

Initially, silica NW is considered in this study to have a comparison with the literature reviews. The silica nanowire structure is a conventional waveguide structure where the light is confined in the high-index material. The sensing area of this structure is at the core/cladding interface where the evanescent field exists. After that, a silicon NW with a horizontal slot structure, where the sensing region is in the slot area, is studied. For the slot waveguide, the light is confined in the low-index area due to the discontinuity of the normal component of the electric fields. In the horizontal slot structure, this corresponds to the E_y component, which is the dominant component for the quasi-TM mode.

As it can be seen later in the chapter, the horizontal slot waveguide NWs exhibit better confinement of the normalized power in the sensing region compared to the conventional waveguide structure NWs. Therefore, the silicon NWs with the horizontal slot structure are also studied theoretically for their possible sensing applications. The sensing application under consideration is the detection of DNA hybridisation which is described in Section 5.4.

The horizontal slot NWs can be used for the detection of DNA hybridisation. This can be achieved by functionalisation of the surface inside the slot region to make it bio-suitable in order to immobilize the bio-material which is single-stranded DNA (ssDNA) in this case. The NW is theoretically analyzed for use with ring resonator scheme and its sensitivity is compared with other optical sensors.

5.2 Conventional waveguide nanowire waveguide structure

Initially, the designed silica NWs are studied compared to the literatures. They are based on the SOI technology where the use of the buffer oxide layer is necessary to enable the propagation of electromagnetic wave in the optical waveguides [204, 205]. The buffer oxide layer, BOX, separates a guided mode from the high index silicon substrate. The buffer oxide layer is SiO_2 and the cladding material water with refractive indices, n, of 1.45 and 1.33, respectively, at an operating wavelength of 1550 nm. The core of the NW has to have a higher index than the buffer oxide layer and the cladding material in order to allow light confinement and propagation of the guided modes in the core of the NW.

Doped-silica with the refractive index, n, of 1.60 is considered to be the core of the NWs. The silica can be doped with various possible substances to either increase or decrease its refractive index. Possible dopants that increase the refractive index are GeO_2 and P_2O_5 [206] while the silica doped with F and Al_2O_3 has a lower refractive index [207].

A cross-section of the proposed waveguide structure of interest is depicted in Fig. 5.1. Conventionally, the core of the NW is the doped-silica which is located on SOI substrate. The cladding material can be air, water or other materials which has a lower refractive index than the doped-silica.

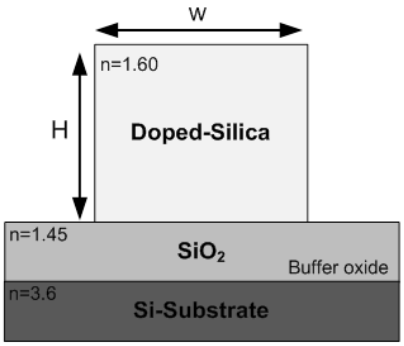

Figure 5.1: Cross-section of the proposed silica NW with the conventional structure.

For the conventional structure, the light is guided inside the core and the evanescent field is extended into the cladding area. The sensing region is the area where the evanescent field interacts with the analyte material which is at the interface of core/cladding. Therefore, the NWs are designed to have dimensions as single-mode waveguides to support the largest possible evanescent field. For an optical fibre, the single-mode waveguide is defined by the normalized frequency or V parameter;

$$V = \frac{\pi D}{\lambda}\left(n_{nw}^2 - n_{max(n_c,n_s)}^2\right)^{\frac{1}{2}} \tag{5.1}$$

where V < 2.405 is known to be the single mode condition. D is the diameter of the waveguide and λ is the operating wavelength. n_{nw} is the refractive index of the NW and $n_{\max(n_c,n_s)}$ is the maximum refractive index chosen between refractive index of the cladding and substrate. However, the value of V < 2.405 is only valid for optical fibre. Therefore, the dimensions of the single-mode NWs can only be initially approximated based on V parameter of the optical fibre. The exact dimensions must be designed later from the simulation works.

The initial silica NW structure has a width (W) of 0.5 µm and a height (H) of 1.0 µm. A full-vectorial **H**-field FEM is used to study the optical field confined in the NW. **H**-field is a vector field which is a quantity that has both direction and magnitude. For 3-dimentional (3D) structure, **H**-field consists of 3 main components, H_x, H_y and H_z, which are the magnetic field components in x, y and z directions, respectively. In this work, two polarisations of the light incident are

considered in the conventional NW structure, which are quasi-TE (Transverse Electric) and quasi-TM (Transverse Magnetic) modes. The quasi-TE mode is a mode characterised by its electric field vector being zero in the direction of propagation ($E_z = 0$) having only E_x and E_y. In this case, E_x is a dominant field in the quasi-TE mode ($E_x >> E_y$). On the other hand, the magnetic field being zero in a direction of propagation ($H_z = 0$) is called quasi-TM mode where H_x is a dominant component ($H_x >> H_y$) as shown in Fig. 5.2(a). The optical field of other components of the magnetic field in the quasi-TM mode including H_y and H_z are shown in Figs. 5.2(b) and (c), respectively.

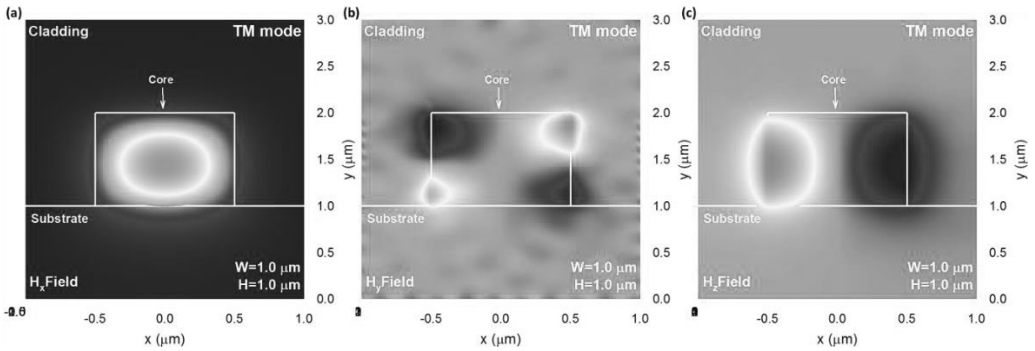

Figure 5.2: Considering the quasi-TM mode in the silica waveguide (a) H_x is the dominant field showing the field guided inside the core. (b) H_y is a non-dominant field. (c) H_z is a non-dominant field. For the quasi-TE mode, the dominant field is H_y and the non-dominant fields are H_x and H_z.

For the quasi-TM mode, H_x, which is the dominant field, has the field mostly confined inside the core. H_y is the non-dominant with its maximum fields confined at the corner of the NW and the adjacent peaks are of opposite sign. The maximum value of H_y is only 1.36% of the maximum value of the dominant H_x field. H_z field is mostly confined at the two vertical interfaces with opposite sign. Its maximum value is 15.62% of the H_x field. Subsequently, only the main component for each polarisation mode (H_y for quasi-TE mode and H_x for quasi-TM mode) is shown in this work.

In the electromagnetic wave, magnetic and electric fields are perpendicular to each other. Considering the quasi-TM mode, the main component of the magnetic field is H_x while E_y is the dominant electric field. The H_x and E_y field in the

0.5 µm wide and 1.0 µm high NW along the y-axis are shown in Figs. 5.3 (a) and (b), respectively.

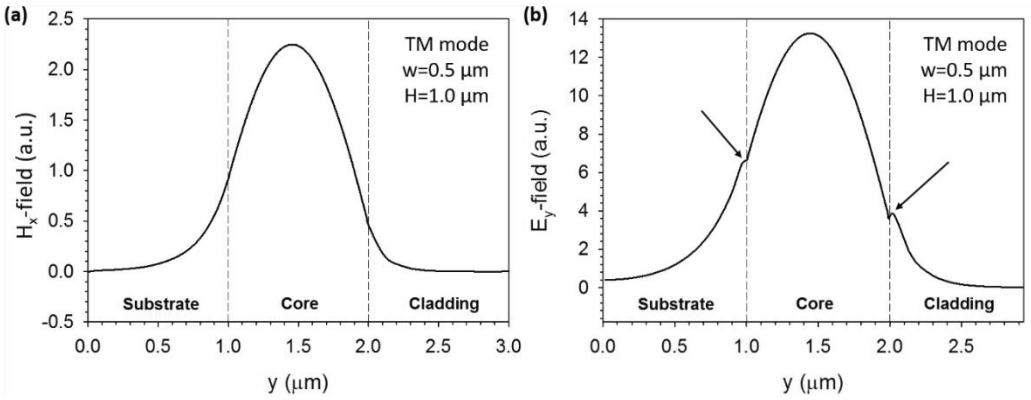

Figure 5.3: (a) Variation of the magnetic field (H_x) in the waveguide along y-axis showing the continuous field across the boundary. (b) Electric field (E_y) in the waveguide along the y-axis, showing field is discontinuous at the waveguide boundary.

From Fig. 5.3(a), the H_x field has its maximum at the centre. The H_x field at core/substrate interface has a value of 39.13% of its maximum while the H_x field of 21.74% is obtained at the core/cladding interface compared to the maximum value. The H_x field at the core/cladding interface is smaller due to higher refractive index difference at that interface. Discontinuity in the E_y field is clearly seen in Fig. 5.3(b) at the interfaces shown by two arrows. At the core/substrate interface, E_y field has a higher value similar to the H_x field. However, the discontinuity is smaller compared to the core/cladding interface which is due to lower refractive index difference at this interface.

Any numerical method, the solution accuracy can depend on different numerical parameters. Using the full-vectorial **H**-field FEM, a number of mesh point is one of the key components needed to be optimized. A large number of mesh point requires longer computing time and larger RAM space capacity. On the other hand, a small number of mesh point leads to inaccuracy of the calculated effective index. The relationship between the number of mesh point and the effective index is investigated as shown in Fig. 5.4.

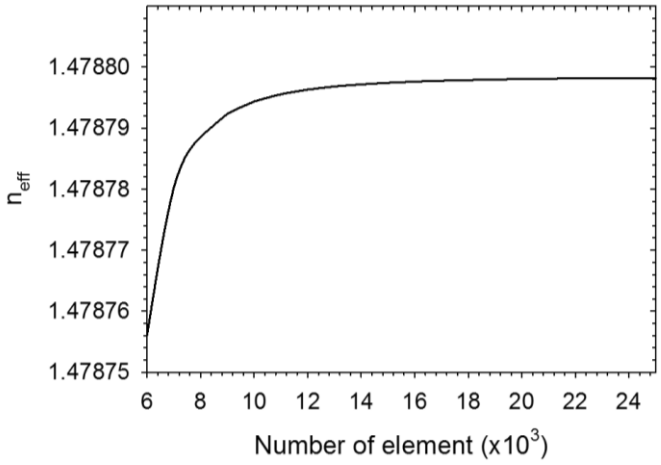

Figure 5.4: Graph between number of mesh point and effective index showing the convergence of results.

The effective index increases monotonically as the number of mesh point is increased and asymptotically reaches its stable value when the number of elements is greater than 12000. Hence, the minimum value of elements used to calculate the **H**-field inside the NWs is 12000. In this work, the number of mesh point of 17000 is applied, unless stated otherwise.

The aim of this study is to optimize the NW structures to have a high power confinement in the cladding region because it corresponds to the sensitivity of the NWs**.** In the following analysis, the normalized power confinement with the variation of the structure dimensions and the operating wavelength are studied.

5.2.1 The effect of the operating wavelength (λ)

First, the **H**-field vector formulation of FEM is used to calculate the modal properties of the initial structure of the NWs, for w=0.5 µm and h=1.0 µm with respect to the operating wavelength for both quasi-TE (transverse electric) and quasi-TM (transverse magnetic) modes. Normally, the silica NWs are operated in the infrared region. Hence, the operating wavelengths in the first study are in the range between 0.85 µm and 1.55 µm. Variation of the effective indices of the fundamental quasi-TE and quasi-TM modes of the silica NW in water cladding with the change in the operating wavelength are investigated using the FEM and presented in Fig. 5.5.

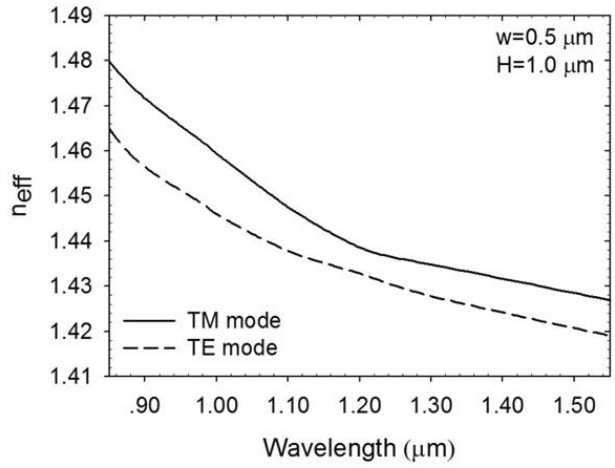

Figure 5.5: Variations of the effective indices for quasi-TE and quasi-TM modes with the operating wavelength for a width and height of 0.5 μm and 1.0 μm, respectively.

As can be seen from the above characteristics, for the single-mode NW, the effective index of the NW is decreased as the operating wavelength increases because large wavelengths cannot be guided inside the small NWs. Therefore, the power confinement in the core region is reduced as the wavelength increases as shown in Fig. 5.6.

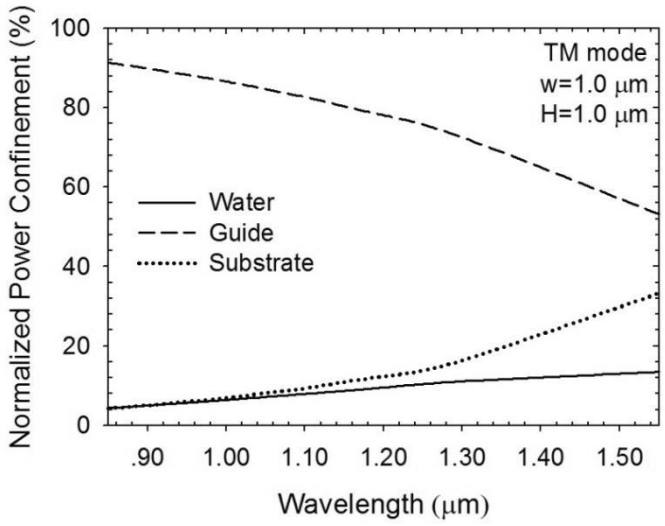

Figure 5.6: Power confinement of the quasi-TM mode in the three different regions of the structure which are the substrate, the core and the cladding.

Variations of power confinement in different regions with the operating wavelength are shown in Fig. 5.6. The power confinement in the core of the quasi-TM mode, which is shown by a dashed line, decreases as the wavelength is increased as the mode approaching cutoff. Hence, the light is extended more

outside the core into the substrate and cladding region which can be seen in the increase of power in the substrate and cladding region in Fig. 5.6. The increased rate of power confinement in the substrate, shown by a dotted line, is faster than the cladding region, which is water, due to smaller refractive index difference with the substrate as the optical field has more preference to expand in the next high index valued substrate. The maximum normalized power confinement in the water cladding region (sensing region) of 14% is achieved in this configuration at the operating wavelength of 1550 nm.

It can be noted that, Fig. 5.5 shows that the effective index of the quasi-TM mode is higher than that of quasi-TE mode because for this structure its height is larger than its width. Therefore, the light is more confined in the doped-silica for the quasi-TM mode than the quasi-TE mode. The optical field distributions of fundamental quasi-TM and quasi-TE modes at λ=1.55 µm are shown in Fig. 5.7.

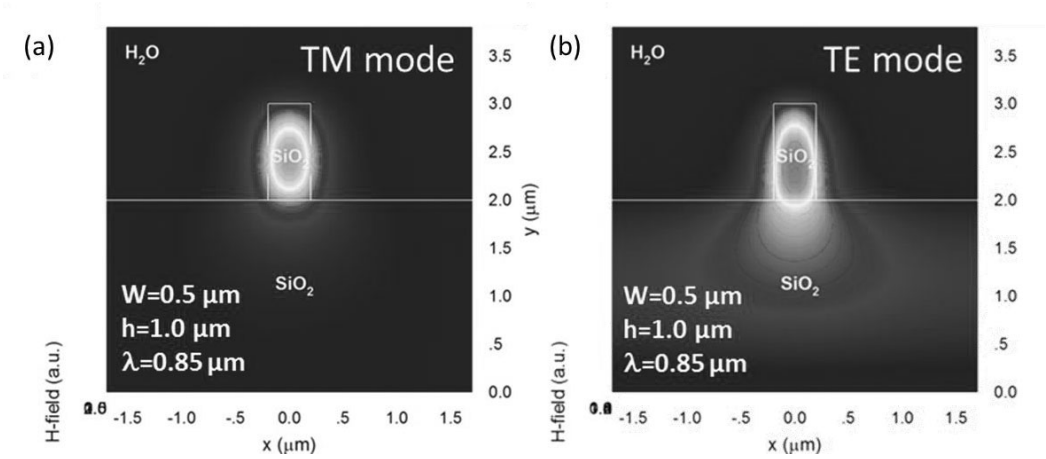

Figure 5.7: Optical field distributions of the light guided in the core region of the silica NW (a) H_x field profile for the quasi-TM mode and (b) H_y field profile for the quasi-TE mode.

For the quasi-TE mode, it can be observed that the light is spread more into the substrate leading to the reduction of the normalized power confinement in the guiding and the sensing regions.

5.2.2 The effect of the structure width (w)

Next, the operating wavelength is kept fixed at 1550 nm and the width of the NWs is varied at a constant height of 1.0 µm. The variation of the effective index with the NW width, varying from 0.5 µm to 1.0 µm, has then been examined for the quasi-TM and quasi-TE modes and the results are presented in Fig. 5.8.

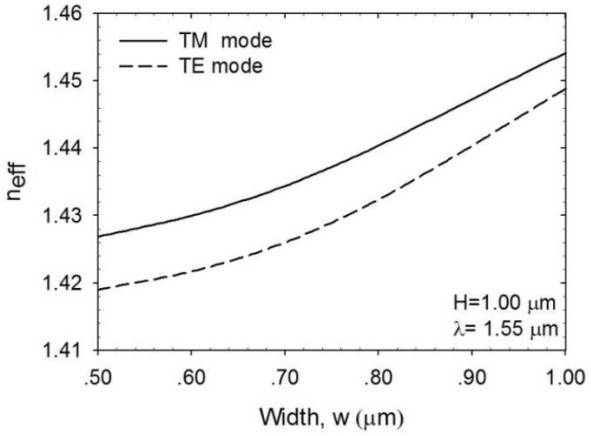

Figure 5.8: Variation of the effective index as a function of the waveguide width at λ=1550 nm.

It can be seen from the above characteristics when the waveguide width reduces, the effective index for both the modes also decreases. As the effective index becomes lower than the substrate refractive index (n=1.45) when w<0.9 µm for the quasi-TM mode, the power confinement increases in the substrate region and the mode becomes unguided. The graph of the normalized power confinement varying with the structure width is shown in Fig. 5.9.

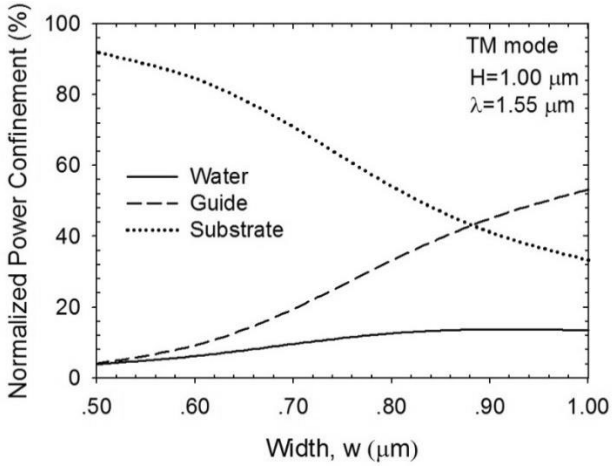

Figure 5.9: Power confinement of the quasi-TM mode in three different regions with the structure width at λ=1550 nm.

The power in the cladding region (water) is slightly increased with the structure width and it is maximized when w > 0.9 μm. However, the power confinement in the guiding region is expected to decay by reducing the width and hence higher leakage is expected. It can be noted for a quasi-TM mode when w < 0.9 μm, n_{eff} < 1.45 and the power confinement in the substrate is greater than the power confinement in the core. For values of the width smaller than 0.9 μm the light extends to the substrate region rendering the device less sensitive. Therefore, the NWs with larger width values are considered.

Here, we would like to design an optical sensor with considerable power in the sensing cladding region, and also mode is close to cutoff but still guided.

5.2.3 The effect of the cladding material (n_c)

Next, the silica NWs with the width and the height of 1.0 μm are studied as a function of the cladding index (n_c). The effective index and the normalized power confinement in the sensing cladding region of the quasi-TM and the quasi-TE modes with the variation of the cladding index, at a fixed wavelength of 1550 nm, has also been examined and is presented in Fig. 5.10.

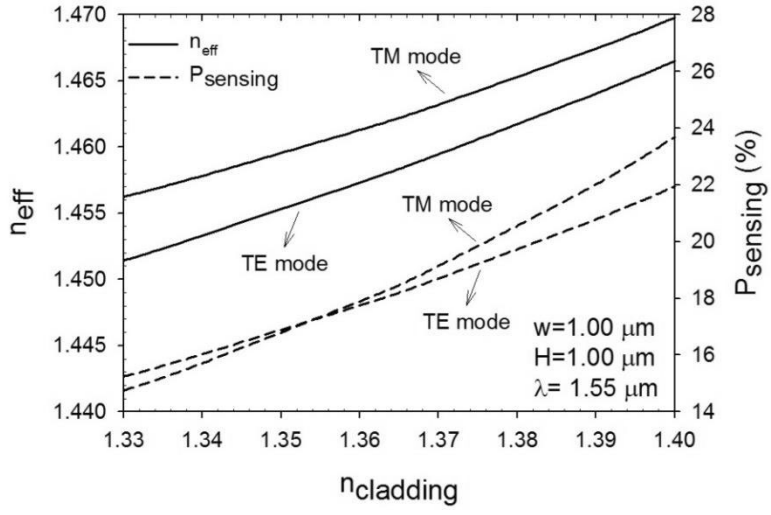

Figure 5.10: Variation of the effective index with the refractive index in the sensing region, which is at the core/cladding interface, at λ=1550 nm.

As it can be seen from the above curves the effective index for both the guided modes increases with the increase of the refractive index of the cladding

at a $\Delta n_{eff}/\Delta n_c$ ratio of about 0.2. The normalized power confinement in the sensing region, which is at the core/cladding interface, is about 15-24% with cladding index varied from 1.33 to 1.40.

5.2.4 The effect of the surface plasmon resonance (SPR)

To enhance the normalized power confinement in the sensing region, a thin gold metal layer has been considered as a top cladding of the proposed structure as shown in Fig. 5.11.

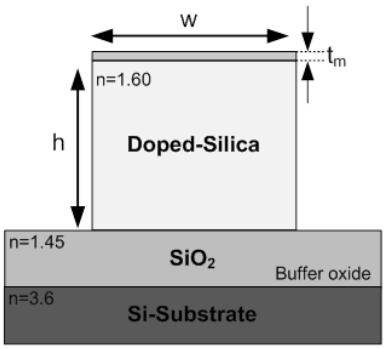

Figure 5.11: Cross-section of the conventional-structure silica NW coated with the thin gold layer.

In the present orientation of the 50 nm thick metal layer, paralleld to x-axis only the dominant H_x field (quasi-TM mode), which is tangential to the metal/dielectric interface, contributes to the excitation of the surface plasmon resonance (SPR) along the interface. Under the phase matching conditions, these modes interact with the guided modes of the device and form dielectric-plasmonic coupled supermodes. The optical field profiles for the silica NWs with guide height of 1.1 µm and 1.2 µm are shown in Figs. 5.12(a) and (b), respectively, where their H_x fields along the y-axis are presented in Fig. 5.12(c).

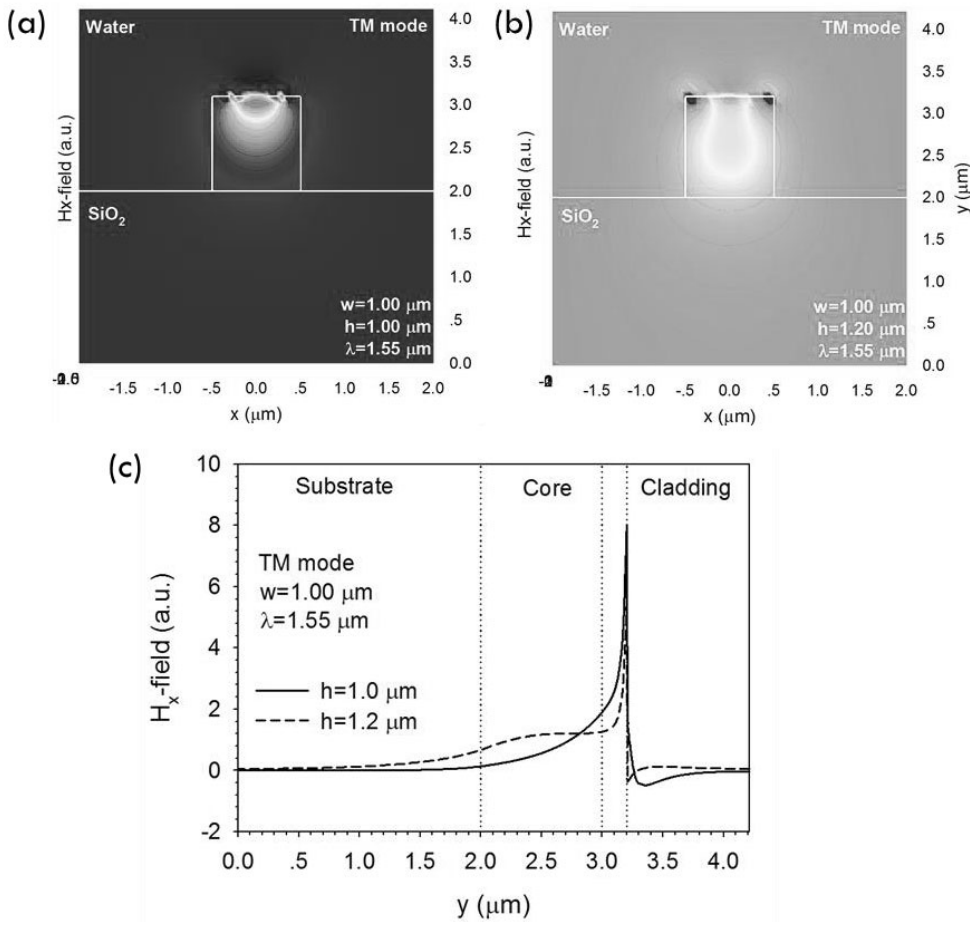

Figure 5.12: Optical field distributions of the mode guided in the core region of the silica NW for (a) h=1.0 µm and (b) h=1.2 µm. (c) H_x field profile along the y-axis for of the plasmonic mode.

There are two types of optical modes possible in gold-coated NW, which are dielectric mode inside the core and plasmonic mode at the metal interface. At a smaller height, β values of both dielectric and plasmonic modes are close to each other leading to a formation of a supermode. At a larger height, the β value of plasmonic mode becomes higher and can be distinguished from the β value of dielectric mode. With the supermode occurring in the NW, the **H**-field is 10 times expanded into the cladding region leading to the larger interaction between the light and the analyte material. Therefore, the silica NW with the thin metal layer confirms that the SPR improves the power confinement in the sensing region. However, this optical power can be further improved by the new proposed NW structure called slot NW structure [95].

5.3 Horizontal slot structure

In the slot structure NWs, the low-index material is sandwiched between two high-index materials. Unlike the conventional structure, the slot structure NWs allow more light to be confined in the low-index area due to the discontinuity of the normal component of the electric fields. The horizontal slot structure is considered here due to its lower loss and better tolerances than the vertical slot [45, 117]. For the horizontal slot structure, only the quasi-TM mode in FEM (H_x) is considered.

The proposed structure of the horizontal slot NWs is shown in Fig. 5.13. However, only a half of the silicon NW structure is used, exploiting available one-fold symmetry, for the full-vectorial **H**-field FEM which would help to increase the computational efficiency of the algorithm and reduces the computing time.

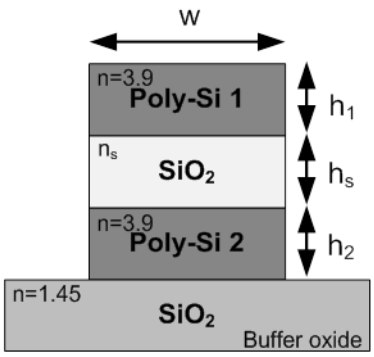

Figure 5.13: Schematic of slot NW structure, characterised by using a full-vectorial **H**-field variational formulation based FEM.

For this structure 28,000, first-order triangle elements were used, with a vertical resolution of 2.5 nm at the vicinity of the sensing area. This area is the slot region and the objective is to study the possible guided modes and their characteristics. The parameters of interest in the basic multilayer silica/silicon structure shown in Fig. 5.13 are the height of the poly-Si core 1 and 2 (h_1, h_2), the slot height (h_s), the half width of the structure (w/2), the slot refractive index (n_s) and the cladding refractive index (n_c). In the present work, two possible types of slot region have been investigated. Specifically, SiO_2 and water, with refractive indices of 1.45 and 1.33, respectively, at an operating wavelength of 1550 nm, have been studied. In the case of the SiO_2 slot, air is considered as the cladding

material while in case of water slot, water is also considered as the cladding materials.

5.3.1 The effect of poly-Si core heights (H)

First, the effect of the height of the poly-Si cores is studied. Initially, symmetric core height ($H=h_1=h_2$) structure with widths 0.6 μm and 0.8 μm are considered, while slot height, h_s, is fixed at 0.10 μm. The core height, H, is varied when the slot height and the width are fixed in order to get a large normalized power confinement in the slot region. The normalized power confinement for the two slot materials, SiO_2 and water, with respect to the core height is shown in Figs. 5.14(a) and (b), respectively.

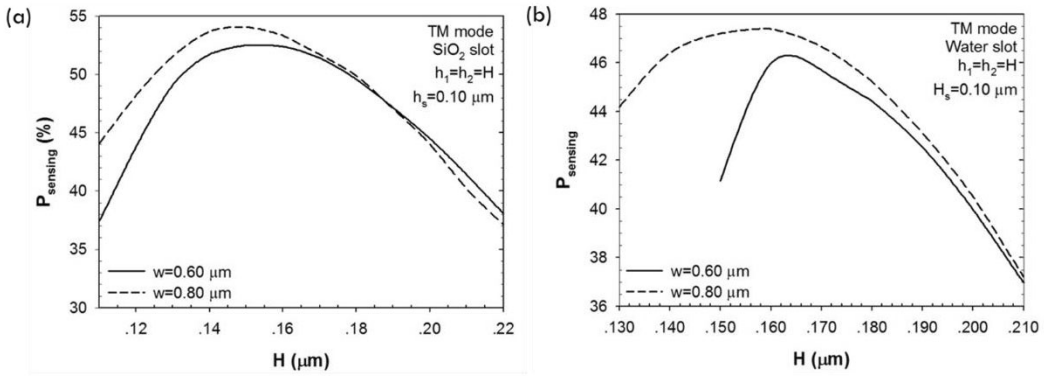

Figure 5.14: Power confinement versus core height, H, for width, W= 0.60 μm and 0.80 μm for a) SiO_2 slot and b) water slot.

The normalized power confinement in the slot region for the wider structure (w=0.8 μm), shown by a dashed line, is higher than that of the narrower structure (w=0.6 μm), shown by a solid line, for both the SiO_2 and the water slots. This is because the wider structure provides a larger volume for the light to be confined in the structure and not into the cladding medium or the substrate. The maximum power confinement for a wider structure occurs at a slightly smaller height which is clearly visible from both Figs. 5.14(a) and (b). This is because a large volume of poly-Si core region allows the light to be more confined in the core region instead of the slot region (sensing area).

For the SiO_2 slot, the highest normalized power confinement is achieved in the slot region at the core height of 0.145 μm and 0.155 μm for the width of 0.8 μm and 0.6 μm, respectively. At w=0.60 μm, the maximum normalized power confinement is about 52%. At w=0.80 μm wide structure the normalized power confinement in the slot region is about 54%. For the water slot structure, the maximum power in the slot region for a structure width of 0.6 μm is about 46%. This maximum power occurs at H=0.164 μm. If the width increases to 0.8 μm, the normalized power confinement is also increased to 47.5% at the height of 0.160 μm.

In general, the normalized power confinement in the slot region of the SiO_2 slot structure is greater than that of the water slot structure. This is because the water slot case also has water as the cladding material, so the slot and cladding material have the same refractive index. In the SiO_2 slot, air acts as the cladding material, which has a lower refractive index than SiO_2 and water. Therefore, the light is more spread out in the cladding region in the case of water slot for 18.8% at H=0.16 μm. With the same dimension, the SiO_2 slot has only 6.7% power spread out to the air cladding medium. In addition, SiO_2 has a higher refractive index than water and the light tends to confine in the higher refractive index area.

For all the cases examined, similar characteristics are shown in both the graphs. At the smaller core height, the normalized power confinement in the slot region is initially low and increases with the core height until it reaches a maximum confinement at heights, H=0.15 μm and 0.16 μm, for the SiO_2 and the water slot, respectively. As the core height increases further, the normalized power confinement decreases. At the smaller height, there is less normalized power confinement due to the cutoff limit. When the core height is increased, the guided area also increases and the light can be more guided and confined, leading to the enlargement of the normalized power confinement in the slot region. However, if the core height is too large, the light will mainly be guided only inside the poly-Si core region and only a small amount of evanescent waves from those two core regions will be overlapping. Consequently, a smaller normalized power confinement in the slot region will be obtained.

5.3.2 The effect of structure width (w)

Next, normalized power confinement in the slot region with different structure widths, for a symmetric core height of 0.16 μm and a slot height of 0.10 μm, is considered. As it has been shown earlier in Fig. 5.14, for H=0.16 μm, both the SiO_2 and water slot structures exhibit maximum normalized power confinement. The normalized power confinement in the slot region with the variation of the width under the above conditions is presented in Fig. 5.15.

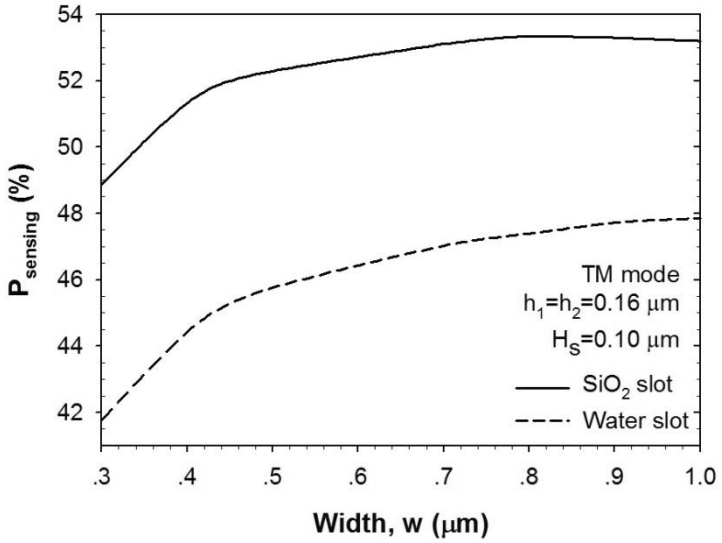

Figure 5.15: Normalized power confinement with the structure width for both SiO_2 slot and water slot.

It can be seen that both the curves, for SiO_2 and water slots exhibit a similar trend, with the curve for the water slot having lower normalized power confinement. At smaller widths, the normalized power confinement in the slot region is less due to the fact that the smaller the structure, the closer the waveguide operates near the cutoff frequency. Therefore, only some light is guided in the core region and the rest is spread into the cladding region. When the width is increased, the normalized power confinement is also slightly increased beyond the width of 0.5 μm. In the case of the SiO_2 slot, a power confinement of 53% and 47% is reached for the SiO_2 and the water slot, respectively. Due to the higher refractive index contrast in the SiO_2 structure, the light is better guided in the SiO_2 slot than in the water slot. On the other hand, the light spreads more into the water cladding than in the air cladding. At w=0.8 μm,

the optical power confinement in water cladding is 13.1% while only 4.5% of optical power is in the air cladding.

5.3.3 The effect of slot height (H_s)

Next, the horizontal slot waveguide NWs with H=0.16 μm and w=0.8 μm is considered in order to obtain high power confinement in the slot area. The normalized power confinement in the slot region for SiO_2 and water slots, with the variation of the slot height (H_s) is studied and presented in Fig. 5.16.

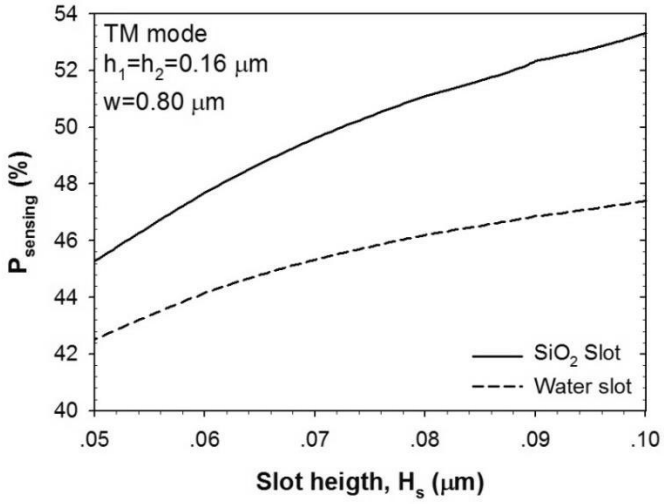

Figure 5.16: Graph between power confinement and the slot height (H_s) for both the SiO_2 and water slots.

Similar to the other cases examined, the normalized power confinement for the SiO_2 slot is higher than that of the water slot. In the range between 0.05 and 0.10 μm of slot height, the normalized power confinement increases with the slot height. When the slot height increases from 0.05 μm and 0.10 μm, the normalized power confinement in the SiO_2 slot is increased from 45.3% to 53.3%. Similarly, the power normalized confinement in the water slot is also increased from 42.5% to 47.4%. This is due to the fact that at smaller slot heights the volume of the slot region is also smaller compared to the volume of the poly-Si core. Therefore, the percentage of power confinement is higher in the poly-Si core area at smaller slot heights. However, at larger slot heights (H_s>H), the normalized power confinement in the slot region decreases due to the large separation between the

two poly-Si cores. In this work, the larger slot height is not considered due to limitations in the fabrication process. From this result, the most suitable slot height is selected to be at H_s=0.10 μm.

However, it should be noted, for a volume sensing, total confinement in the slot area would be useful but for surface sensing, power density would be more useful.

5.3.4 The optical field balancing

From the results obtained in Fig. 5.16, the H_x^{11} modal fields for the structure with w=0.6 μm, H=0.16 μm and H_s=0.10 μm are presented in Figs. 5.17(a) and (b) for the SiO_2 and water slot structures, respectively.

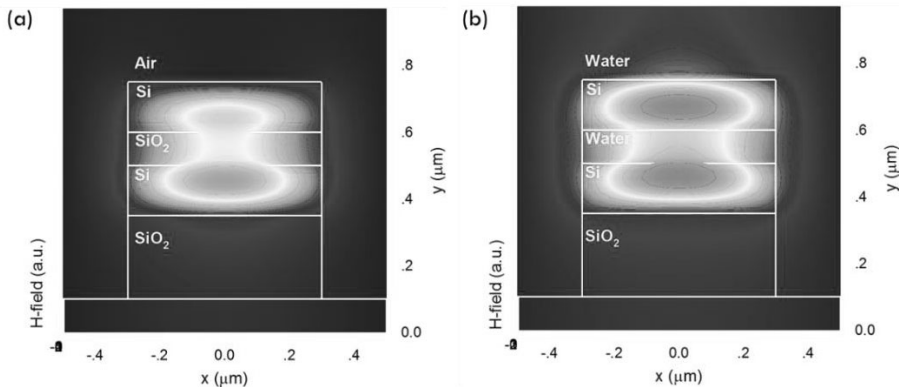

Figure 5.17: Field distribution of H_x^{11} field in (a) SiO_2 slot structure and (b) water slot structure.

As it can be seen from the field distribution in Fig. 5.17, the field is more confined in the SiO_2 slot structure compared to the water slot structure. This is due to the refractive index difference between the slot and the cladding medium. In the water slot structure, the optical field is extended into the cladding (as $n_{slot} = n_{clad}$) more than in the SiO_2 slot case, where $n_{slot} > n_{clad,}$ leading to a lower power confinement in the slot region.

In addition, there is an asymmetry of the optical field in the poly-Si core region for the SiO_2 slot structure. On the other hand, the optical field is more symmetric in the water slot structure. This is because the difference of the refractive index between air (upper cladding) and SiO_2 (substrate) is higher for SiO_2 slot than the

difference of the refractive index between water (upper cladding) and SiO_2 (substrate) for water slot. Therefore, the optical field is more confined in the bottom poly-Si core, while the optical field is almost equally distributed in both poly-Si layers in the water slot structure. The asymmetry and symmetry of the optical fields can be explained clearly when the H_X field is plotted along the y-direction as shown in Fig. 5.18.

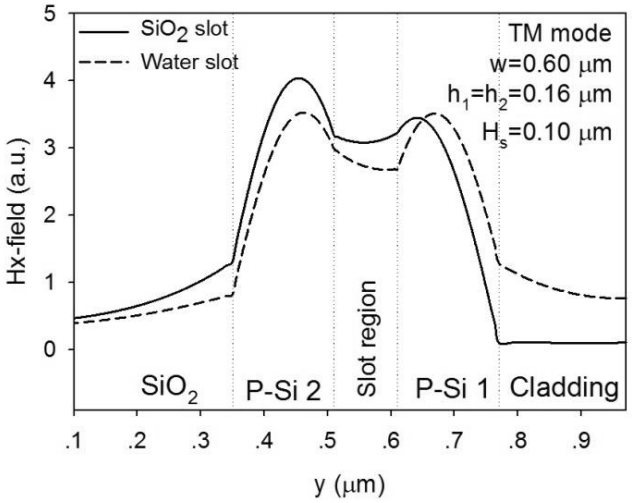

Figure 5.18: H_x field of the H_x^{11} mode along the y-direction for both the SiO_2 slot and water slot.

Form Fig. 5.18, it can be seen that the evanescent field is expanded into the cladding region for the water slot structure as presented by a dashed line. This evanescent wave causes the low normalized power confinement in the guiding area compared to the SiO_2 slot. The ratio of the H_x field in the poly-Si core1 and poly-Si core2 in the water slot structure ($|H_1^x|/|H_2^x|$) is around 0.996. Therefore, the optical field is almost symmetric in the water slot structure. For the SiO_2 slot structure, the graph obviously shows the asymmetry of the optical field between those two core layers as the magnitude ratio of H_x-field in poly-Si core1 and poly-Si core2 ($|H_1^x|/|H_2^x|$) is about 0.869. In both structures, the optical field is more confined in the bottom poly-Si core layer (poly-Si core2) because SiO_2 has a higher refractive index than both air and water.

In order to get a symmetric optical field in the SiO_2 slot structure, the height of the poly-Si1 (h_1) has to be increased to enlarge the waveguide dimension for light propagating in that region while the height of poly-Si2 (h_2) should be kept

fixed. The H_x-field along the y-direction when the height of poly-Si1 is increased is shown in Fig. 5.19.

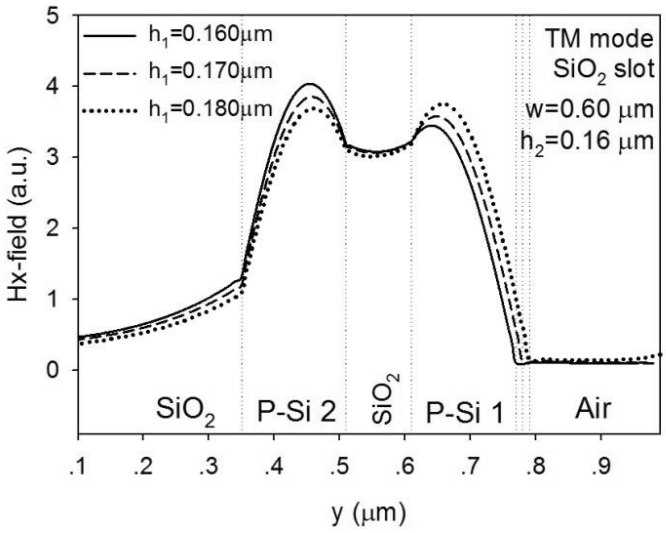

Figure 5.19: H_x field of the H_x^{11} mode along the y-direction of SiO_2 slot structure when the height of poly-Si core2 (h_2) is fixed at 0.16 μm and the height of poly-Si core1 (h_1) is increased.

For a fixed height h_2=0.16 μm, with h_1 increasing from 0.16 μm to 0.18 μm, the balance ratio of $|H_1^x|/|H_2^x|$ is increased from 0.869 to 1.017. The most symmetric field is obtained in the SiO_2 slot structure with w=0.6 μm when h_1=0.178 μm ($|H_1^x|/|H_2^x|$=0.999). In this case, the normalized power confinement in the slot region is also increased from 52.56% to 52.88%.

The ratios of the optical field in both the SiO_2 slot and water slot structures at different poly-Si core height for a width of w=0.60 μm and the core height varying from 0.15 to 0.21 μm, is presented in Fig. 5.20.

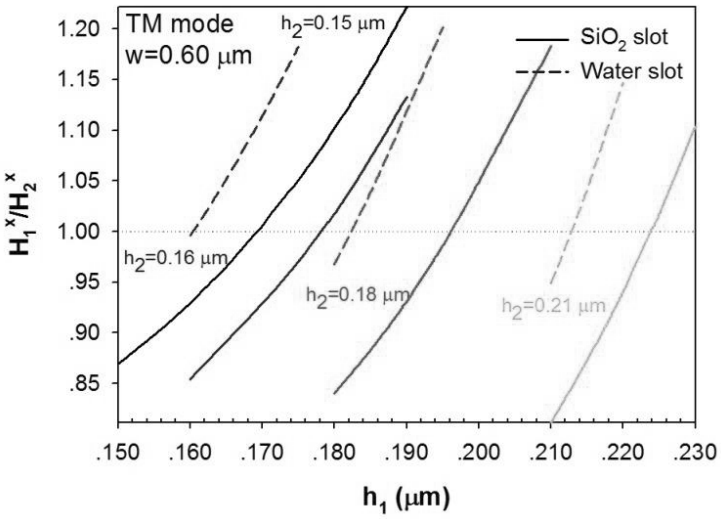

Figure 5.20: Ratio of the optical field in the core region for both SiO_2 slot and water slot at different core height.

From Fig. 5.20, the dashed lines, which represent the water slot structure, show a smaller shift between h_1 and h_2. The solid line shows a greater shift between the core heights due to the larger difference in the cladding refractive index. The shifting values to achieve equal ratio to balance values and the power confinement values of each core height are presented in Table 5.1.

Table 5.1: The values of shifting, balance ratio and power confinement of each structure at different heights. All length units are in μm.

h_2	SiO_2 slot				Water slot			
	h_1	Shift	H_1^x/H_2^x	P (%)	h_1	Shift	H_1^x/H_2^x	P (%)
0.150	0.169	0.019	0.998	53.968	-	-	-	-
0.160	0.178	0.018	0.999	52.889	0.160	0.000	0.996	45.988
0.180	0.196	0.016	0.998	48.835	0.182	0.002	0.995	44.254
0.210	0.224	0.014	1.003	39.570	0.213	0.003	1.003	36.541

According to Fig. 5.14, the optimum core height to be obtained in the SiO_2 and the water slot structures are approximately to be around 0.15 μm and 0.16 μm, respectively. For the height below these values, the power confinement in the sensing region tends to dramatically decrease. From Table 5.1, it can be observed that h_1 has to be increased in order to get the most symmetric optical field in both poly-Si core layers. For SiO_2 slot, the rate of change for h_1 is reduced from 0.019 μm to 0.014 μm when h_2 is increased from 0.150 μm to 0.210 μm. The

percentage of the normalized power confinement in the slot region is also reduced when increasing the core height since the light is more confined in the core regions. For the water slot case, the shifting values are very small and the percentage of power confinement in the slot region is not affected. Similar to the SiO_2 slot, the power confinement in the water slot is reduced when the core height is increased.

However, both the SiO_2 slot and the water slot waveguide exhibit a very high optical power in the slot region compared to the power confinement at the core/cladding interface for the conventional structure. Hence, the silicon NWs with the horizontal slot structure have a potential to be further used in sensing applications.

5.4 Horizontal slot waveguide biosensor for DNA hybridisation detection

The normalized power confinement in the slot region of the horizontal slot structure NWs is significantly higher than that of the conventional structure as it can be seen from Fig. 5.21

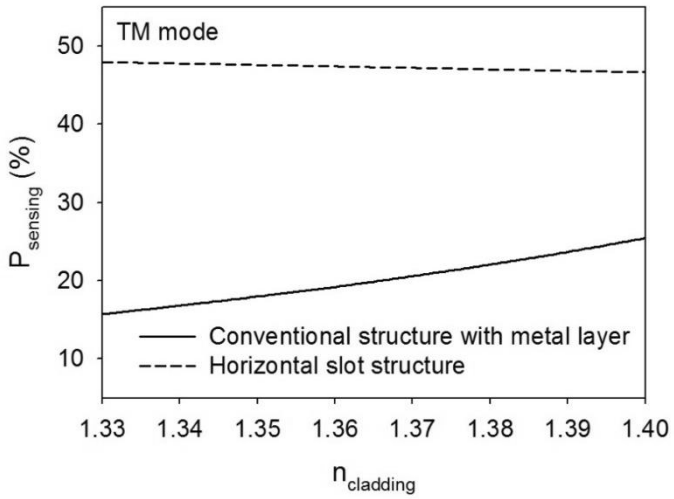

Figure 5.21: A comparison of the normalized power confinement in the sensing area between the silicon NW with gold-coated conventional structure and the silicon NW with horizontal structure.

Due to the high normalized power confinement in the sensing region, the silicon NWs with the horizontal slot structure are considered to be theoretically

investigated for the possible biosensing applications. Most of the materials to be sensed in biosensing applications are in liquid phase in which water is the main solvent. Therefore, the NW structures design is based on the water slot waveguide. The proposed silicon NWs to be studied for biosensing applications have symmetric core height, H=0.16 µm, w=1.0 µm and H_s=0.1 µm.

A more practical device based on the silicon NW structure with horizontal slot structure for sensing application is studied theoretically. The horizontal slot waveguide is proposed to be used for DNA hybridisation detection. The sensor detects the change of effective index when the analyte material has a refractive index change. In this case, the analyte materials have to be immobilized with the linker materials such as silanes. Linkers act as glue in order to form a selective physical or chemical bonding with the analyte materials. A cross-section of the horizontal slot waveguide with the sensitive layer proposed for the numerical simulations is shown in Fig. 5.22.

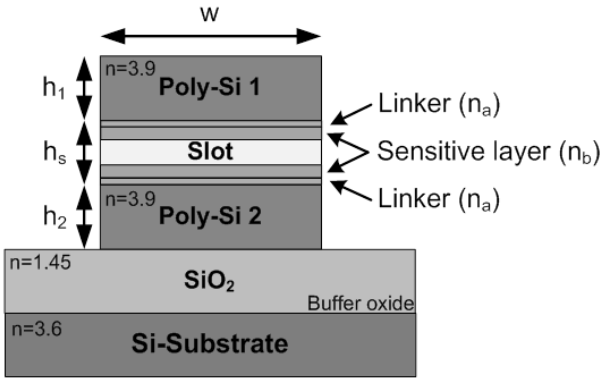

Figure 5.22: Cross-section of silicon NW with horizontal slot structure for DNA hybridisation detection.

As mentioned above, the horizontal slot waveguide is investigated as a possible sensor to detect DNA hybridisation. The DNA hybridisation is the process of combining two single-stranded DNA (ssDNA) to become double-stranded DNA (dsDNA). The ssDNA and dsDNA have different refractive indices given by 1.456 and 1.53 at the wavelength of 633 nm [113], respectively. With the change of refractive index in ssDNA and dsDNA, the effective index of the whole structure is also changed.

The thicknesses of the ssDNA and dsDNA layers are considered to be fixed at 8 nm [208] for the initial study. The refractive index of the poly-Si core layers is 3.9. In the simulation, the slot area is assumed to be filled with water. This is the same as the cladding material since it is the main constituent material of the solution [209], which has a refractive index value of 1.33. To immobilize the ssDNA, silanes with a refractive index of 1.42 (n_a) is used as the linker layer to form the covalent bond with the ssDNA and it has a thickness of 1 nm. We have exploited the existing one-fold symmetry and used 34,000 first-order triangles to represent only half of the structure. The main advantage of the FEM over the other numerical methods is that FEM can incorporate triangles of different shapes and sizes to obtain the numerical efficiency. In this case, to represent the 1 nm thick linker layer, vertical resolutions used were 0.2 nm or better. The key parameters that need to be optimized are the width (w) of the structure, the poly-Si core heights (h_1 and h_2) and the slot height (h_s). The operating wavelength in this work is taken at λ=1550 nm.

In the modal solution using the FEM approach, the existing half symmetry has been considered for the horizontal slot waveguide. The quasi-TM mode, where the dominant electric field is normal to the interface, is considered because it has a higher confinement in the slot region compared to the quasi-TE mode. For the quasi-TM mode, the H_x field is the dominant component of the **H**-field. The contour of the dominant H_x field of the waveguide with w=0.70 μm, H=0.16 μm and h_s of 0.10 μm is shown in Fig. 5.23(a). The H_x field has a maximum intensity in both the poly-Si core layers. However, the maximum intensity is not at the centre of the core region but instead, it is closer to the interface between the core region and the slot area, as it can be seen in the inset of Fig. 5.23(a), showing the H_x profile in y-directional the centre of the waveguide. It was discussed in Section 5.3.4 that if desired by using h_2 slightly larger than h_1, symmetry can be improved.

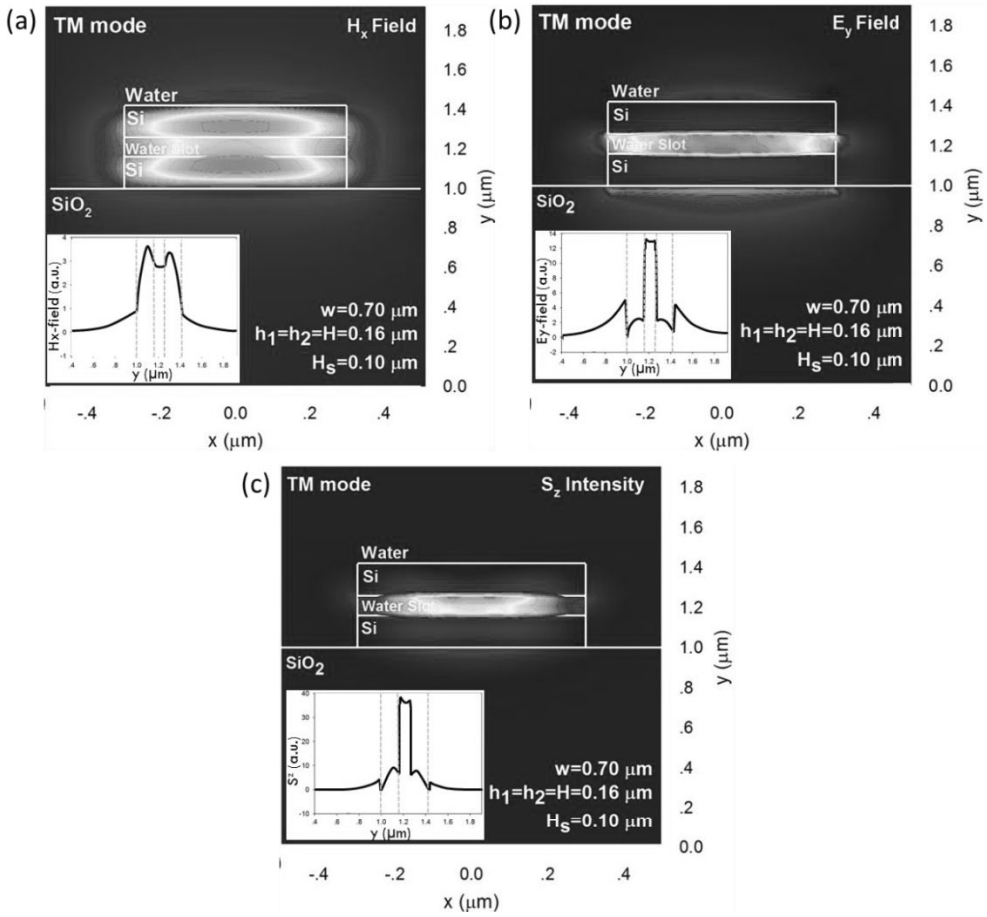

Figure 5.23: Contour plots of (a) H_x field, (b) E_y field and (c) Energy flux density Poynting vector: S. Insets are the field plots along the y-axis.

The fundamental E_y field has also been derived from the H_x-field and is shown in Fig. 5.23(b). The E_y field along the y-direction, given as an inset, shows the discontinuity at the interface of the core and slot regions providing the strong field in the slot area. The energy flux density or so-called the Poynting vector (S) calculated from the **E** and **H** fields [198] is presented in Fig. 5.23(c). It can be clearly seen that the energy is more confined in the slot area, thus confirming that the light is guided in the low-index region of the slot waveguide.

5.4.1 The effect of poly-Si core height ($h_1=h_2=H$)

The effect of the poly-Si core height, H on the power confinement and power density is studied next. It is considered H to be symmetric ($h_1=h_2=H$) and w=0.7 μm and h_s=0.10 μm, are assumed to be fixed. The normalized power confinement

and the power density in the sensing layer (DNA probe) with the variations of the core height are presented in Fig. 5.24.

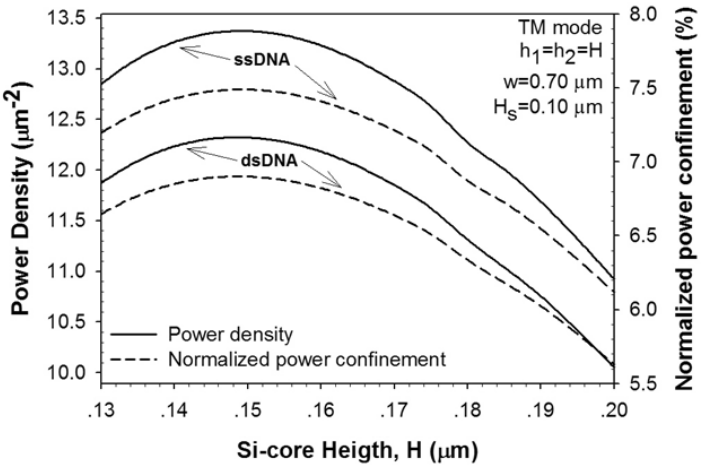

Figure 5.24: Variations of power density and power confinement in the sensing layer (DNA probe) with the core height, H.

The normalized power confinement is the ratio of the power in that region to the total power. The power density is obtained by dividing this normalized power confinement with the area of that region. The total normalized power confinement in the sensing area, as shown in Fig. 5.24 is the sum of the normalized power confinement in the upper and lower DNA probe layers, each having a thickness of 8 nm. Its power density is taken as the average power density for both DNA probe layers. The normalized power confinement and power density exhibit a similar trend when the core height is varied as the sensing area size stays constant and H is varied.

At a smaller core height, both the normalized power confinement and the power density in the sensing layers are initially low because the structure gets close to the cutoff limit. Therefore, the optical power reduction occurs due to an evanescent wave spreading into the cladding medium and the buffer oxide layer. Then the power increases with the core height, due to the enlargement of the guided area, until reaching a maximum confinement at a height, H of 0.15 μm. However, if the core height is too large, the light will mainly be guided only inside the poly-Si core region. Consequently, the normalized power confinement and power density in the sensing region are decreased as the core height increases further. It is also shown that the ssDNA (n_b=1.456) has a higher power in the

sensing medium compared to the dsDNA (n_b=1.530). This is due to the higher refractive index contrast in ssDNA compared to dsDNA which leads to the larger discontinuity in the electric field. If the whole slot region is used for a particular device operation, such as for the polymer filled electro-optic modulator, then normalized power confinement is the key design parameter. However, if an analyte material is localized only at the interfaces then the power density around that region will be a more important parameter.

One of the most important parameters in biosensing applications is the change of effective index which is used to calculate the sensitivity of the device. In a Mach-Zehnder arrangement, the change in the effective index will yield a phase change between the branches. The variations of the effective index with the core height are shown in Fig. 5.25, where the effective index due to the presence of each analyte material is included.

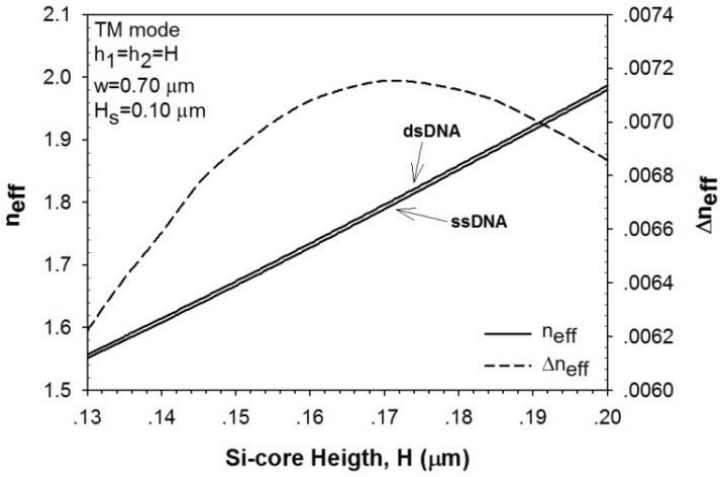

Figure 5.25: Variations of the effective index difference and the effective index in each analyte material with the core height.

Due to the smaller refractive index value of ssDNA, we found out that $n_{eff,ssDNA} < n_{eff,dsDNA}$. However, the effective index increases when the poly-Si core height is increased for both ssDNA and dsDNA because of the larger silica volume. The change in effective index, shown by the dashed line, increases when the core height is increased until it reaches a maximum value at H=0.17 μm. At a height greater than 0.17 μm, the structure becomes too large and light is mostly confined

in the core rather than in the slot. This leads to a reduction of the change of effective index as well as the sensitivity of the waveguide.

5.4.2 The effect of structure width (w)

It was shown in Fig. 5.24 that the maximum power density was achieved when H ~ 0.15 μm. On the other hand, Fig. 5.25 indicates that maximum Δn_{eff} can be obtained when H ~ 0.17 μm. Although their variations were rather small in this region, for subsequent optimisation we have considered H = 0.16 μm. The thickness of the linker layer (silanes) and the sensing medium (DNA) remained the same at 1 nm and 8 nm, respectively. Next, the normalized power confinement and power density with the variations of the width of the waveguide are simulated and presented in Fig. 5.26.

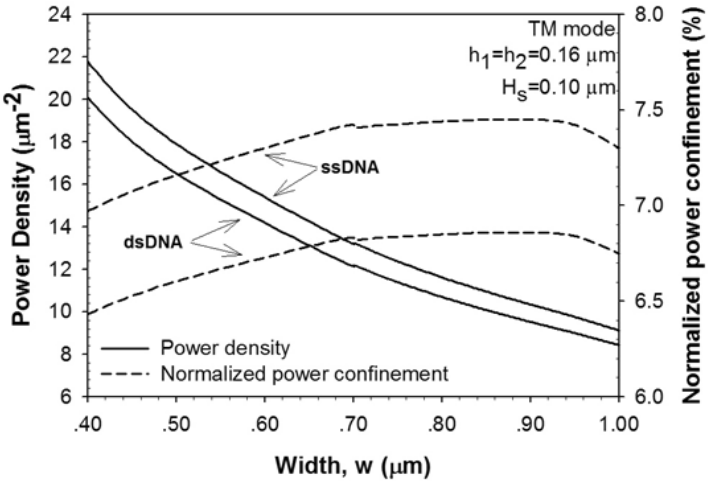

Figure 5.26: Variations of the power density and power confinement in the sensing layer (DNA probe) with the width.

At smaller width, the normalized power confinement in the slot region is less due to the smaller size of the structure, where the mode approaches cutoff. Therefore, only some light is guided in the core region and the rest is spread into the cladding region. When the width is increased, the normalized power confinement is also slightly increased. In the case of the ssDNA (n_b=1.456), the normalized power confinement is higher than that of the dsDNA (n_b=1.530), due to the higher refractive index value. On the other hand, the power density is

inversely proportional to the width. At smaller width, the power density is high because the guiding area is smaller. As the width increases, the power per unit area is reduced due to the larger guiding area. However, higher power density is observed in the ssDNA than in the dsDNA due to higher normalized power confinement.

From the results obtained above, it can be seen that the effect of the change of the core height is more significant in the normalized power confinement than the change of the width. Next, the variations of effective index and the effective index difference due to the presence of each sensing layer with respect to the structure width are examined and presented in Fig. 5.27.

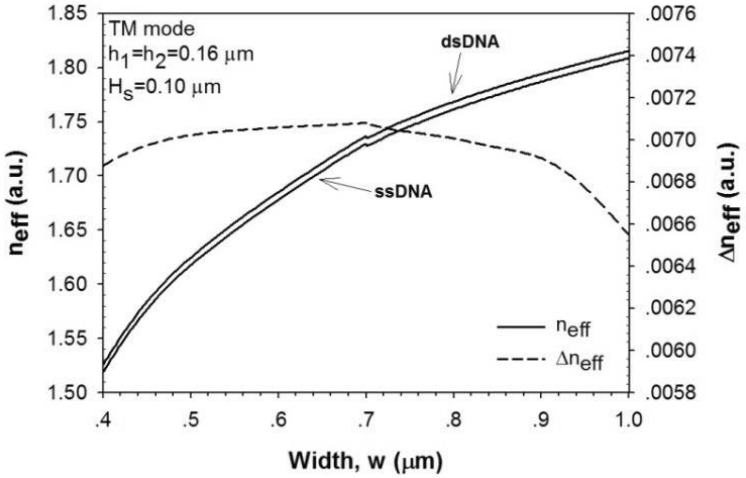

Figure 5.27: Variations of the effective index difference and the effective index in each analyte material as a function of the width (w).

The effective index due to the presence of each sensing layer increases with increasing width of the structure. This is because the light can be more confined in the larger structure. In addition, $n_{eff,dsDNA} > n_{eff,ssDNA}$ because dsDNA has larger refractive index. The effective index change is gradually affected by the structure width. The change in the effective index, shown by the dashed line, is slightly increased when the width increases up to 0.7 μm. When the width is larger than 0.7 μm, the change of effective is continuously decreased. Comparing these with the previous results shown above, the change of effective index is affected more by the core height rather than the width as the graph changes more rapidly when varying the core height.

5.4.3 The effect of slot height (h_s)

The next variable in this study is the slot height (h_s). The normalized power confinement and the change of effective index are demonstrated with various values of slot height as shown in Fig. 5.28.

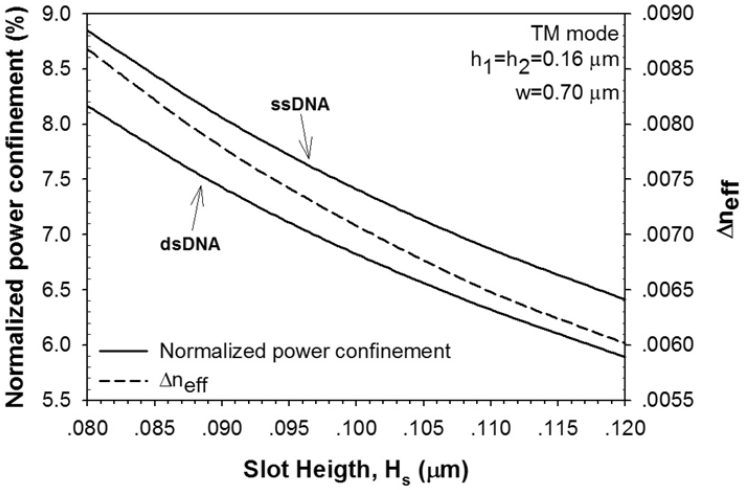

Figure 5.28: Variations of the effective index difference and the power confinements as a function of the slot height.

The slot structure has a fixed core height and width in which H=0.16 μm and w=0.70 μm, respectively. The normalized power confinements in the ssDNA and dsDNA layers, shown by two solid lines, exhibit a similar trend. Their normalized power confinement is reduced when the slot height is increased. At a larger slot height, the separation gap between the two poly-Si core layers is larger. Thus, the power is coupled more into the poly-Si core instead of the slot, leading to a reduction of the normalized power confinement in the slot area. As the ssDNA has a greater refractive index contrast than the dsDNA, it also has higher normalized power confinement. In addition, the effective index difference represented by a dashed line decreases with increasing slot height.

Even though a smaller slot height provides a larger effective index difference, it would be difficult to create a very small and uniform slot due to the fabrication limits. Besides, a coating of linker layer, adhere of DNA layer can be restricted for a very narrow slot layer. So, the slot height of 0.10 μm is selected for this work because it is a more suitable value that is easy for fabrication. Next, the change of

effective index with various values of slot height is studied again with different slot height and structure width. The relation of the effective index change with the slot height at different core heights and different widths is shown in Figs. 5.29(a) and (b), respectively.

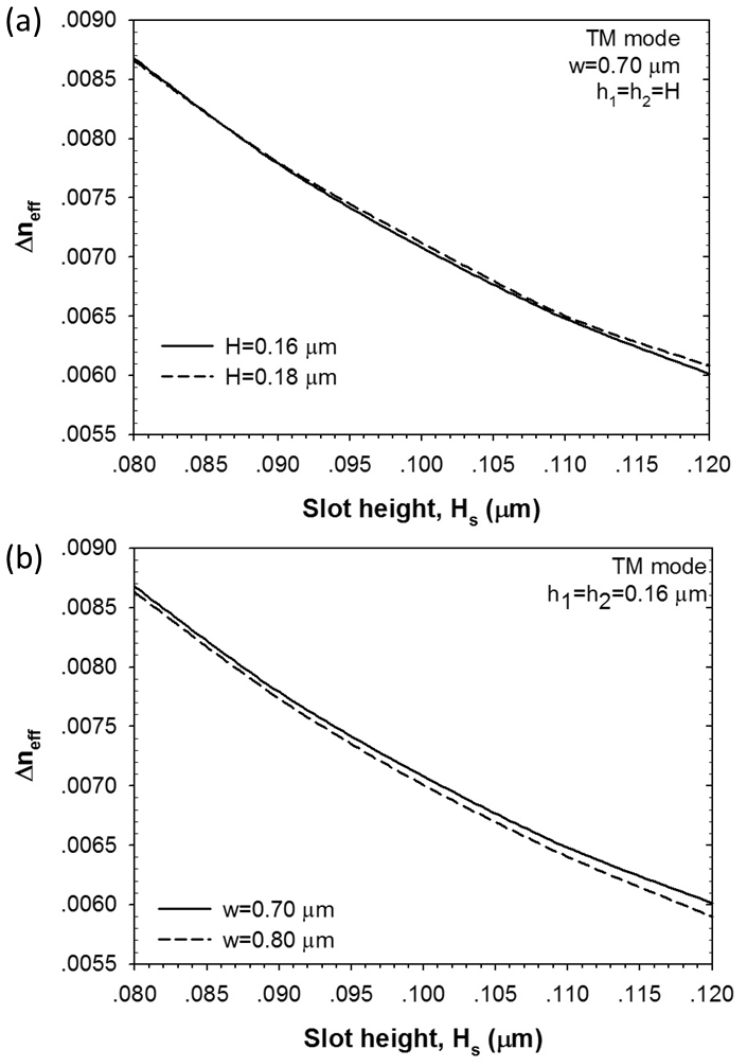

Figure 5.29: Variations of the effective index difference with the slot height at different (a) core heights and (b) core width.

Fig. 5.29(a) shows that the change of effective index has almost the same value when varying the slot height at the structure width of 0.7μm. Fig. 5.29(b) shows the comparison between the structure with a width of 0.70 μm and 0.80 μm at the fixed core height of 0.16 μm. The smaller structure width represented by the solid line has a higher change of effective index when the slot height is varied.

In order to detect the DNA hybridisation, this horizontal slot waveguide can be incorporated in a Mach-Zehnder Interferometer (MZI) system. By introducing the sensing slot waveguide in one arm of the MZI, the relative phase shift ($\Delta\phi$) can be obtained from the change in the effective index, Δn_{eff} as:

$$\Delta\phi = \Delta n_{eff} * \frac{2\pi}{\lambda} * L \tag{5.2}$$

Here, Δn_{eff} is the difference between the effective indices of the reference and sensing waveguide sections and L is the length of sensing section. The destructive interference or the minimum interference signal occurs when the phase difference is equal to π. Therefore, the length of the MZI arm (L) with horizontal slot waveguide is calculated to be 90.0 µm long at a slot height, H_s = 80 nm as can be seen in Fig. 5.29, when the maximum Δn_{eff} is obtained. It is assumed here that loss in both the branches are similar.

5.4.4 The sensitivity (S)

Since the horizontal slot waveguide is proposed for use in a biosensing application the sensitivity is a very important parameter for this waveguide. In the literature, the sensitivity or Figure-of-Merit (FOM) of a biosensor has been defined in terms of the changes in intensity [210], or wavelength shift [110, 211] or effective index with the background refractive index change [212] or other measurable parameters. For MZI based systems, the change in the effective index (Δn_{eff}) is directly related to the intensity profile, which in turn depends on the normalized power confinement and power density. The normalized power confinement and the power density with the variation of the background cladding refractive index (which changes in the presence of the analyte materials) is presented in Fig. 5.30.

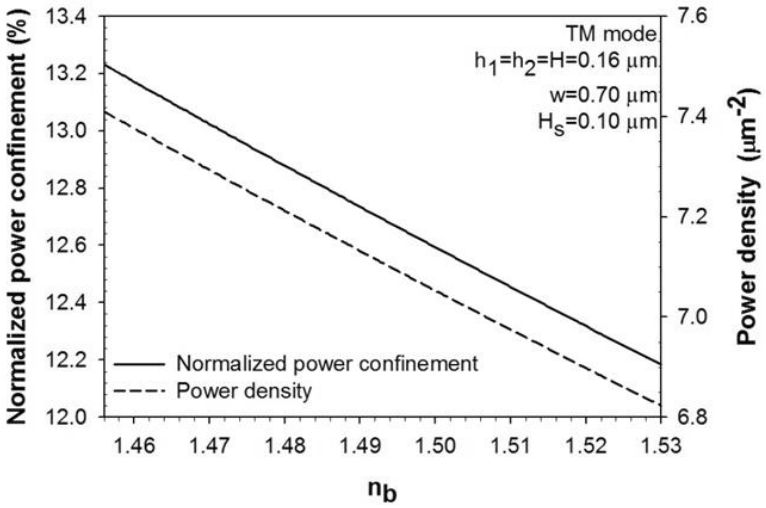

Figure 5.30: Variation of the normalized power confinement and power density with the change in refractive index of the analyte material.

It can be observed that both the power confinement and the power density decrease when the cladding index is increased. This is due to the smaller refractive index contrast between the waveguide and the slot region which reduces the field enhancement there. Consequently, the sensitivity of the horizontal slot waveguide is reduced.

The horizontal slot waveguide sensitivity (S_{modal}) can be calculated using the following equations [213].

$$n_{norm} = \frac{n_b - n_{b,ref}}{n_{b,ref}} \tag{5.3}$$

$$\Delta n_{eff} = \frac{n_{eff} - n_{eff,ref}}{n_{eff,ref}} \tag{5.4}$$

$$S_{modal} = \frac{\Delta n_{eff}}{n_{norm}} \tag{5.5}$$

where n_b is the refractive index of the material to be sensed, which in this case is either ssDNA or dsDNA, $n_{b,ref}$ is the reference refractive index which is kept fixed at 1.456 (ssDNA), n_{eff} is the effective index due to the presence of n_b and $n_{e,ref}$ is n_{eff} at $n_{b,ref}$. In this work, the horizontal waveguide is studied for detecting the DNA hybridisation, for example when ssDNA (n=1.456) becomes dsDNA

(n=1.530), in which the slot waveguide sensitivity is calculated from the equation (2.6) to be 0.082.

The horizontal slot waveguide can also be incorporated in other optical devices such as ring resonator and Mach-Zehnder interferometer to detect DNA hybridisation. To compare the results with previously reported work but using a vertical slot waveguide The sensitivity of the device ($S_{spectral}$) or the spectral sensitivity, mentioned in the Chapter 2, can be calculated using the equations below [110]:

$$S_{spectral} = \frac{\delta\lambda}{\delta n} \tag{5.6}$$

where, $\delta\lambda$ is the shift of resonance wavelength defined by [110]:

$$\delta\lambda = \frac{\delta n_{eff} * \lambda_{res}}{n_g} \tag{5.7}$$

where δn_{eff} is the effective index difference when the hybridisation occurs, λ_{res} is the resonance wavelength and n_g is the group index at wavelength of 1550 nm. The optimum horizontal slot waveguide structure proposed in this work has w=0.7 µm, H=0.16 µm and h_s=0.10 µm. With this structure, the sensitivity of 893.5 nm/RIU and the resonance wavelength shift of 6.33 nm are obtained. With the same waveguide material, the surrounding media and the analyte material which is DNA, the sensitivity of the device, incorporating horizontal slot waveguide is slightly higher compared to the vertical slot waveguide, where a sensitivity of 856 nm/RIU was reported [110]. The results presented here show improved sensitivity compared to that of 298 nm/RIU for a vertical slot on SOI [104] and 212 nm/RIU for a vertical slot waveguide using Si_3N_4 [111].

5.5 Summary

A **H**-field finite element approach based on the full-vectorial variational formulation is used to study the propagation characteristics of silicon NW structures. Two types of NW structures are used in this study, specifically the

conventional structure and the horizontal slot structure. The effects of the variation of the height (h), width (w) and wavelength excitation (λ) are investigated and optimized for the conventional structure of the NWs. To enhance the optical power in the sensing region which is at the core/cladding interface for the conventional structure, a thin metal layer is added on the top surface of the NWs to introduce the surface plasmon resonance (SPR). With the effect of a thin metal layer in the excitation of surface plasmon modes, the normalized power confinement in the sensing region is increased by 2%. However, this value can be further improved by the horizontal slot structure.

The silicon NWs with horizontal slot structure are studied to obtain the optimum parameters for the maximum possible optical power in the sensing region. The parameters of concern are the poly-Si core height (h_1, h_2), the slot height (h_s), the width (w), the slot material (n_s) and the cladding material (n_c). There are two slot types considered in this case, the SiO_2 slot (n_s=1.45) and the water slot (n_s=1.33). For the SiO_2 slot, the cladding material is air (n_c=1). For the water slot, the cladding material is water itself. In all cases, the power confinement in SiO_2 slot region is higher than in the water slot. This is due to the difference of the refractive index between the cladding material and the slot material in the SiO_2 slot structure.

The optimum core height for the SiO_2 slot waveguide in order to get maximum power confinement in the slot region is 0.15 µm. For the water slot, the core height of 0.16 µm provides the highest power confinement in the slot region. In both structures, power confinement is increased when the width of the structure increases. In this work, any width larger than 0.6 µm is suitable for the fabrication process. Also, the power confinement is directly proportional to the slot height. The slot height of about 0.10 µm is the most practical and suitable for sensing applications because it can be easily fabricated and still provides high power confinement.

The optical field in SiO_2-slot NW is asymmetric, unlike the one in the water slot waveguide, due to the larger difference of the refractive index between the cladding material and the buffer oxide layer. In order to get a symmetric field in

the SiO_2 slot waveguide, the upper silicon core height has to increase. The maximum power confinement obtained in the SiO_2 slot and water slot waveguides are around 54% and 47%, respectively.

Due to the very high optical power in the slot region, the silicon NWs with horizontal slot structure are investigated as possible practical devices in biosensing applications. These devices were found to be sensitive with the variations of the refractive index difference in the analyte material. The analyte materials considered in this work are ssDNA and dsDNA present in the DNA hybridisation process. The key parameters, such as the normalized power confinement, the power density, the effective index difference (Δn_{eff}) and the sensitivity have been investigated. Moreover, the fabrication parameters, such as the structure width (w), the core height (H) and the slot height (h_s) have been optimized through numerical analysis.

The optimum dimensions for the slot waveguide structure, in order to achieve maximum normalized power confinement and large effective index difference, were found to be at w= 0.7 μm, H= 0.16 μm and h_s= 0.10 μm and this yields a compact design with the resulting device length to be smaller than 100 μm. Furthermore, the sensitivity of this slot waveguide has been studied with the variations of the refractive index of the analyte material. For a ring resonator, a significant improvement of the sensitivity value has been obtained and found to be S=893.5 nm/RIU.

6. Numerical simulations of ormocomp waveguides

6.1 Introduction

In this chapter, the theoretical studies of the un-coated and gold-coated ormocomp waveguides using advanced numerical analysis are presented. Both un-coated and gold-coated waveguides with two different structures, ridge structure with vertical sidewalls and rib structure with non-vertical sidewalls are studied. The full-vectorial **H**-field FEM is used here to study the behaviour of light propagation along the waveguides. The existing guided modes, their normalized power confinement, and the SPR peak of the waveguides are studied over the operating wavelength, their structural dimensions, cladding index and metal thickness. For the un-coated ormocomp waveguides, the study examines both the quasi-TE and quasi-TM modes. For the gold-coated waveguides with vertical sidewalls, which are considered to be polarisation-independent structures, the surface plasmon resonance (SPR) effect in these guides are studied for both the quasi-TE and quasi-TM modes. However, only the quasi-TM mode is considered in the non-vertical sidewalls because the SPR at the sidewalls is not normal to the y-axis due to a sidewall angle. Hence, H_y dominant quasi-TE mode is not considered in this particular case and it is assumed that the waveguides are not coated with the gold layer at their sidewalls. This assumption is supported by the experimental results presented in Chapter 7. The results also show that there is no SPR effect from the sidewalls for waveguides with non-vertical sidewalls.

6.2 Non-gold-coated ormocomp nanowire waveguides

The un-coated ormocomp waveguides are theoretically studied in this section. There are two different types of structures considered in this work, which are the ridge structure with vertical sidewalls and a rib structure with non-vertical sidewalls.

6.2.1 Ridge structure with vertical sidewalls

A simple conventional ormocomp nanowire waveguide (NW) structure, which is a ridge waveguide structure, is first considered. The NW structure is designed to achieve a single mode waveguide. Therefore, the NW is assumed to have a fixed width, w, and height, h, of w=0.5 μm and height, h=1.0 μm, respectively, for the initial design. The ormocomp NW with refractive index of n=1.520 is designed to be on a fused silica substrate with the refractive index of 1.446. It is surrounded by water (n=1.333), which is considered as the cladding material. A cross-section of the ormocomp NW is shown in Fig. 6.1.

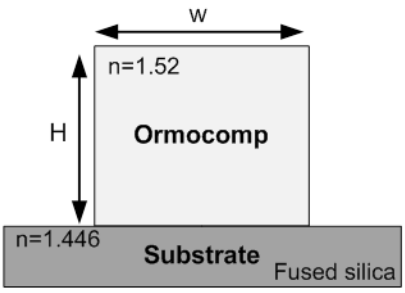

Figure 6.1: Cross-section of the ormocomp NW ridge waveguide.

Like the other conventional waveguides, the light is confined in the high-index area which is the ormocomp core. The sensing area is at the ormocomp/cladding interface where the evanescent field exists. Therefore, the study is focused on improving the power confinement at the interface to enhance the light interaction with the sensing material. The modal fields of the existing guided modes and their power confinement in ormocomp NWs are studied over the wavelength, width and height of the NW structure and the different cladding materials.

6.2.1.1. The effect of the operating wavelength (λ)

The **H**-field vector formulation of FEM is used to calculate the modal properties of this waveguide structure by varying the operating wavelength. Ormocomp is a transparent material with only a small loss in visible light. In this case, white light with operating wavelength between 400 nm and 700 nm is considered as a light source. For the above structure, both the quasi-TM and the

quasi-TE modes, where H_x and H_y are the dominant field components, respectively, have been investigated.

Variations of the effective index of the both quasi-TE and TM modes within the operating wavelength range are shown in Fig. 6.2.

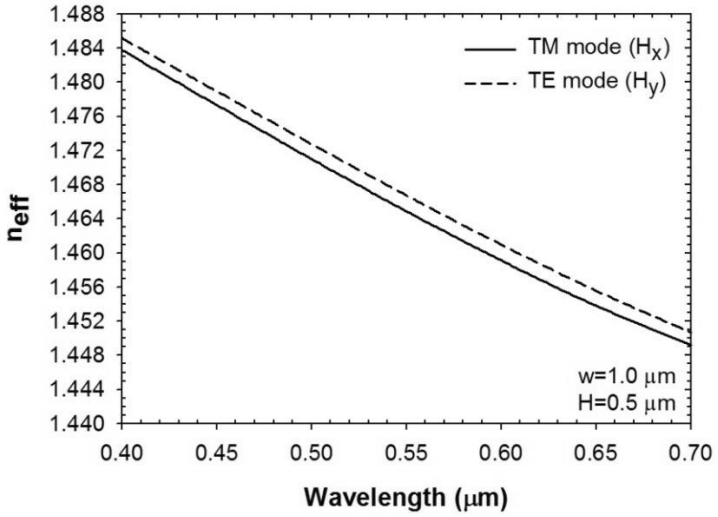

Figure 6.2: Variation of the effective index as a function of the operating wavelength in the visible region, for both quasi-TM and quasi-TE modes.

The effective index variations of the fundamental modes, as shown in Fig. 6.2, decrease with the increase in the wavelength, for both the quasi-TM and quasi-TE modes because the wavelength becomes larger compared to the waveguide dimension. The graph suggests that the light confinement is stronger in the guiding region at a lower operating wavelength. The difference between the light confinement at the short wavelength (λ=400nm) and long wavelength (λ=700nm) can also be correlated with the optical field distribution shown in Figs. 6.3(a) and (b), respectively.

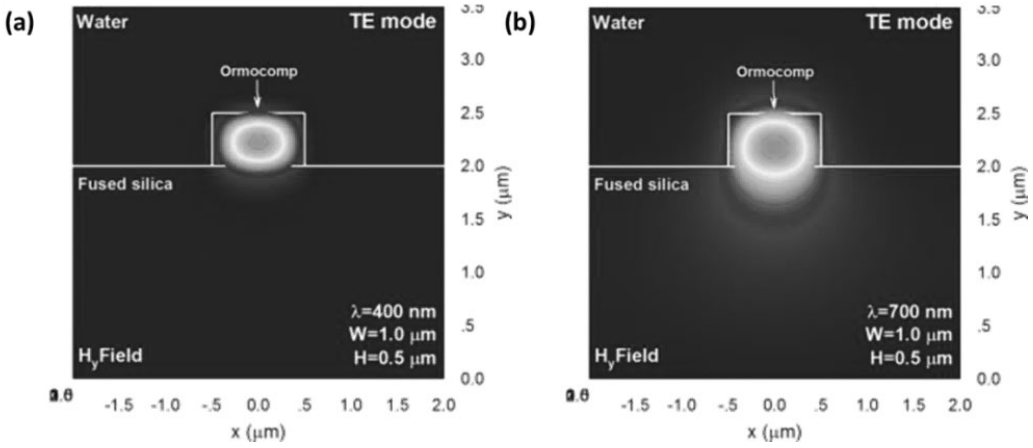

Figure 6.3: The modal field profiles excited in the ormocomp NW with 1.0 μm width and 0.5 μm height at (a) λ= 400 nm and (b) λ=700 nm for the quasi-TE mode.

It can be clearly observed from Figs. 6.3 that the field extends more into the substrate at a longer wavelength (λ=700nm) because at λ=700nm, the wavelength is relatively larger than the NW structure. In addition, it can be observed that the quasi-TE mode has a slightly higher effective index compared to the quasi-TM mode as the width of the waveguide is bigger than its height, which means that the light is more confined in the core region for the quasi-TE mode than the quasi-TM mode. The normalized power confinements in both the guiding and cladding regions for the above two modes, with the variation of the wavelength are presented in Fig. 6.4.

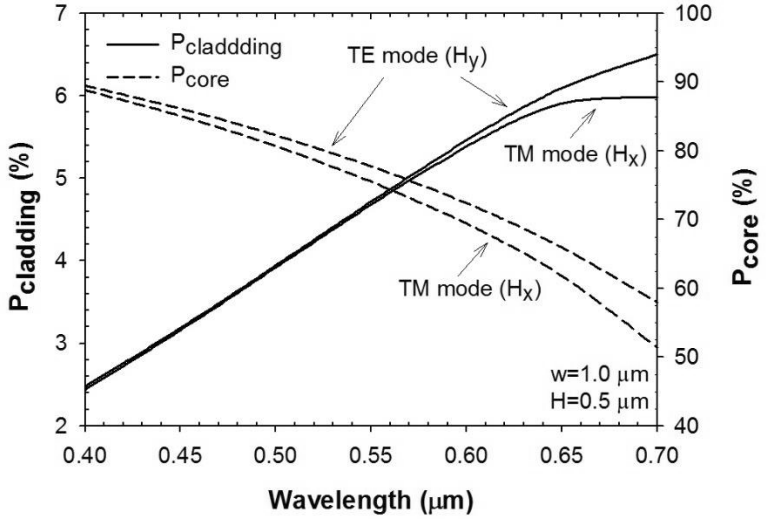

Figure 6.4: Variation of power confinement in the cladding region (sensing region) and the core region (ormocomp) with the operating wavelength for the quasi-TM (H_x^{11}) and quasi-TE modes (H_y^{11}).

It can be seen from Fig. 6.4 that the power confinements in the core region are decreased by a larger wavelength as shown by dashed lines while the power confinement in the cladding region shown by solid lines are increased with larger wavelength. At the short wavelength, the light is more confined in the NW. Therefore, the evanescent field extending into the cladding region is less compared to that at the long wavelength. The cladding region, where the evanescent field extends, is considered to be the sensing area for our work. Thus, the relatively larger power confinement in the cladding is a key design parameter to achieve better sensitivity. However, the power loss in the substrate is also greater with the higher operating wavelength because it is close to the cutoff wavelength leading the light to spread more into the substrate. To obtain high power confinement in the cladding region, together with a good confinement in the guiding area as shown in Fig. 6.4, the 650 nm wavelength (red region) is selected as the operating wavelength in the following studies and in the experimental work.

6.2.1.2. The effect of the structure width (w)

With the operating wavelength fixed at 650 nm (red light source), the effect of the waveguide width on the fundamental mode field has been studied as shown in Fig. 6.5. The study assumes a structure with a fixed height of 0.5 μm and its width is varied between 0.5 μm and 1.0 μm. Water (n_c =1.333) is considered as the cladding material because it is generally a good solvent in aqueous solutions for many sensing applications [214].

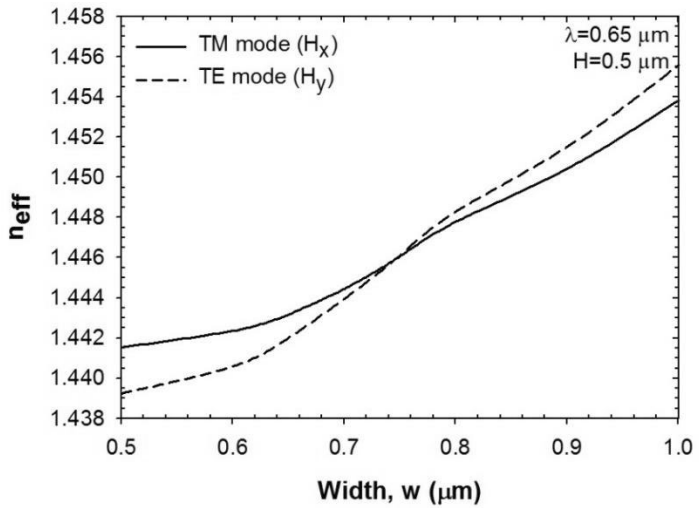

Figure 6.5: The change in the effective index as a function of the structure width in the range between 0.5 μm and 1.0 μm for both quasi-TM and quasi-TE modes.

The effective indices of the fundamental quasi-TM and quasi-TE modes, increase with the increase of the width of the NW, allowing the light to be more confined due to the greater volume of the guiding region. At a width of 0.75 μm, the effective index obtained in both the quasi-TM and quasi-TE modes is about 1.446, which is close to the refractive index of the fused silica substrate, thus reaching cut-off. Therefore, the light starts extending into the substrate leading to a large power loss when the width of the structure is less than 0.75 μm. The H_x field profiles of the light confinement for two different widths of the NW are shown in Fig. 6.6.

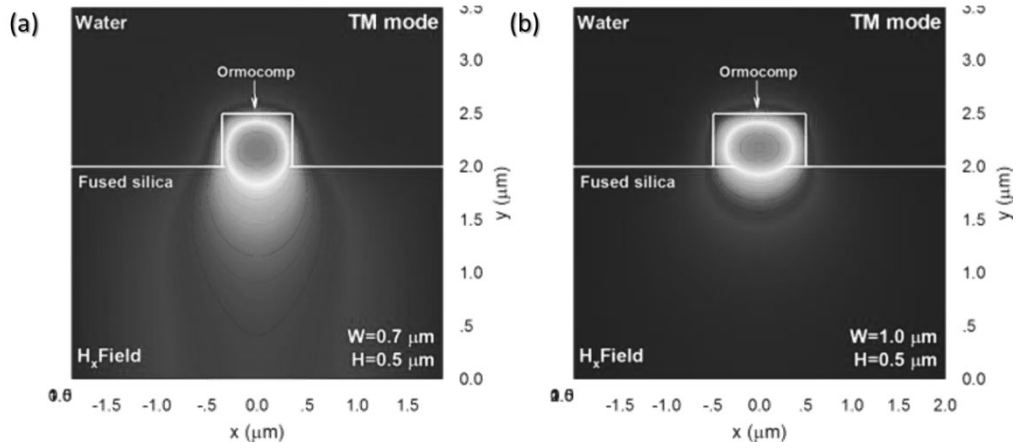

Figure 6.6: H_x modal field profiles excited at (a) w=0.7 μm and (b) w=1.0 μm for the quasi-TM mode.

Fig. 6.6(a) shows the extension of H_x-field well into the substrate region when the structure has a width of w=0.70 μm and mode reaches its cutoff. Fig. 6.6(b) shows the well-confined H_x-field in the 1.0 μm wide core region. The normalized power confinement in the sensing region and in the core with respect to the structural width can be seen in Fig. 6.7.

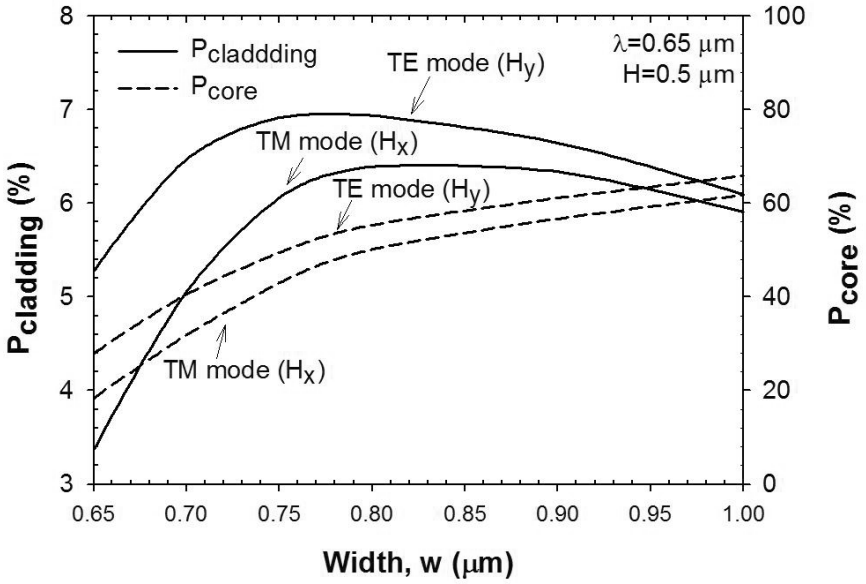

Figure 6.7: The variation of power confinement in the cladding region (sensing region) and core region (ormocomp) with the structure width for quasi-TM (H_x^{11}) and quasi-TE (H_y^{11}) modes.

The maximum power confinement in the cladding region is achieved when the structure has a width of w=0.80 μm. For a width larger than 0.80 μm, the power confinement in the cladding region is slightly decreased due to a larger confinement in the core region. For a structure width below 0.80 μm, the power confinement in both the cladding and guiding regions is significantly decreased because the power is lost in the substrate region. The optical field extends in the substrate when the mode reached the cutoff limit.

The cutoff limit for this NW structure can also be identified by studying the spot size, which is considered as the area where the field intensity is above the value of 1/*e* of its maximum intensity. The change in the spot size with respect to the width of the NW is shown in Fig. 6.8. From the numerical modelling, it can be noted that this waveguide remains single-mode when the width, w, is reduced

below 1.55 µm and 1.65 µm, for the quasi-TE and the quasi-TM modes, respectively.

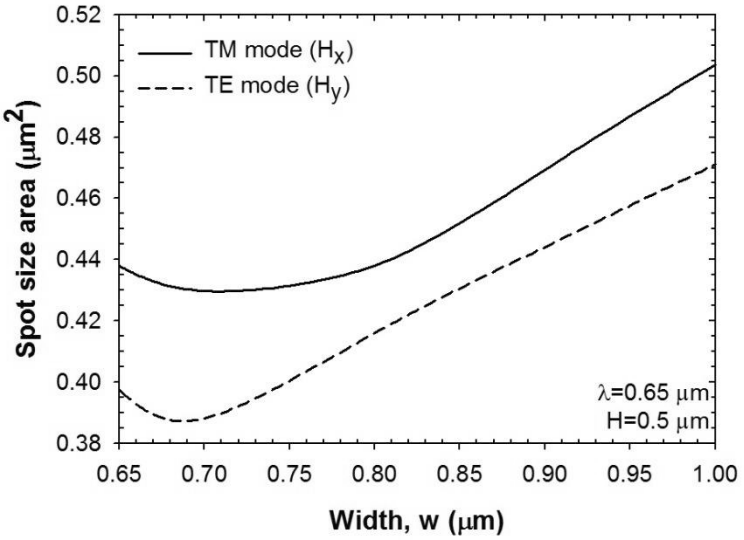

Figure 6.8: Variations of spot size area with the width of the NW varied from 0.65 µm to 1.00 µm.

The spot size of the NW with w>0.75 µm increases with its width. This is due to the large core area in the guiding region. The smallest spot size represents the region closer to the cutoff limit. The quasi-TM mode has a bigger spot size compared to the quasi-TE mode and approaches its cutoff limit before the quasi-TE mode. For the quasi-TM mode, the structure is close to the cutoff when the structure width is close to 0.80 µm whereas the NW structure can be scaled down to 0.70 µm for the quasi-TE mode. For the smaller NWs, with dimensions below the cutoff limit, the spot size becomes larger due to the expansion of the light in the substrate.

6.2.1.3. The effect of the structure height (H)

To avoid the cut-off limit, the width of the ormocomp NWs has to be larger than 0.8 µm. From Fig. 6.7, the maximum power confinement in the sensing region is achieved at a width of about 0.80 µm. However, in the fabrication process, 1.0 µm wide NWs are fabricated because the structures might shrink during the nanoimprint process. Therefore, the ormocomp NWs with a width of w=1.0 µm and at operating wavelength of λ=650 nm are considered. Next, variations of the

effective indices with the structure height for both quasi-TM and quasi-TE modes are shown in Fig. 6.9

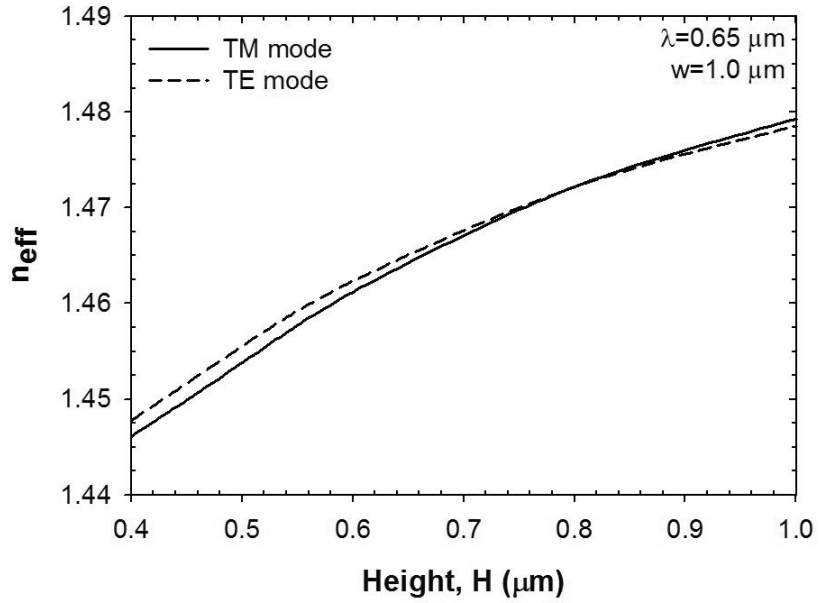

Figure 6.9: Change of effective index as a function of the waveguide height for both quasi-TM and quasi-TE modes.

As the structure height increases, the effective index of the NW is also increased because the ormocomp guiding region allows a larger volume of light to be confined. At smaller heights, the effective index decreases, approaching the refractive index of the glass substrate. Hence, the power confinement in the substrate is increased, leading to low optical power confined in the sensing area. The variations of the normalized power confinement in the sensing region and the guiding region are presented in Fig. 6.10.

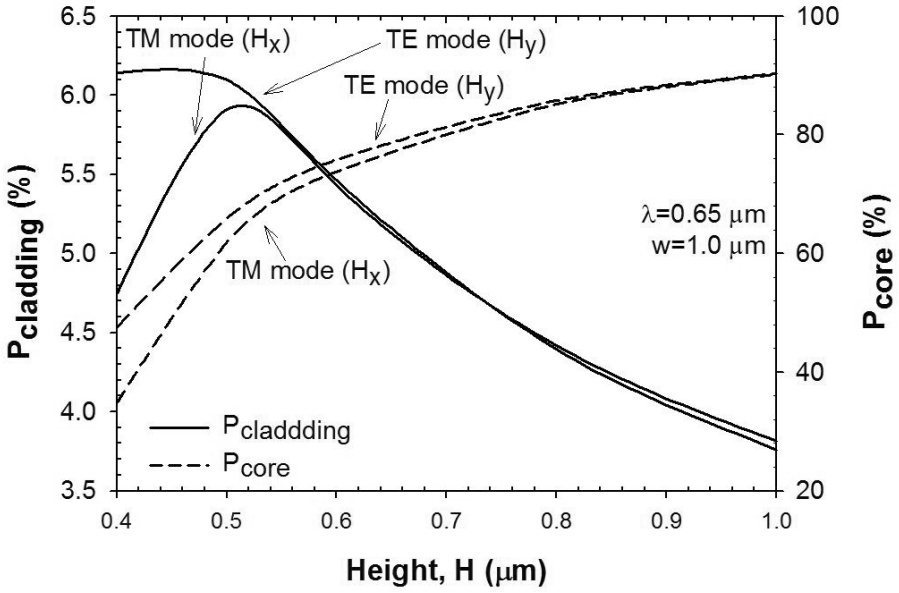

Figure 6.10: Variation of power confinement in the cladding region (sensing region) and core region (ormocomp) with the structure height for quasi-TM and quasi-TE modes.

The normalized power confinement in the cladding, which is the sensing region, is reduced when the structure height increases because the light is more confined inside the core. It can also be observed that the normalized power confinement in the guiding region is increased with the increase of the height. At the structure height of 0.5 μm, the optical power in the sensing region is close to its maximum for the quasi-TM mode. For heights less than 0.5 μm, the normalized power confinement in the cladding for quasi-TM mode drops dramatically, where for the quasi-TE mode a slight reduction is observed. Therefore, the quasi-TM mode attains cutoff before the quasi-TE mode does.

6.2.1.4. The sensitivity (S)

To prevent the NW operating near the cutoff region, the NW with dimensions w=1.0 μm and H=0.5 μm at an operating wavelength of λ=650 nm is considered in the next study. The NW is intended to be used in biosensing applications in which the cladding material is an aqueous solution. Therefore, sensitivity over the cladding material with the refractive index in the range of 1.333 to 1.400 is studied. The sensitivity of the NW (S_{nw}) can be calculated using equations $S_{wg}=\Delta n_{eff}/\Delta n$ which is already described in Chapter 5.

The sensitivity of this NW structure with respect to the refractive index of the cladding material is shown in Fig. 6.11.

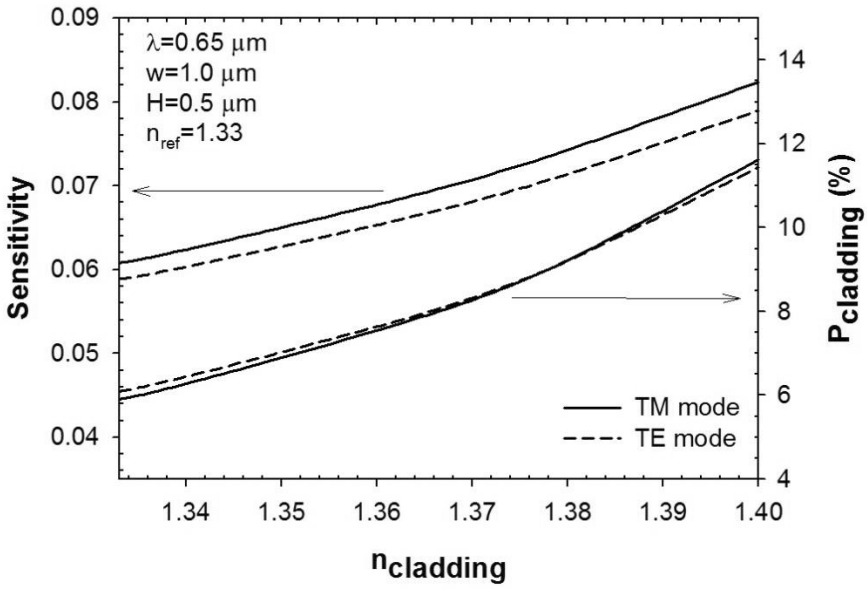

Figure 6.11: Sensitivity and the cladding percentage power confinement of the NW when the refractive index of the cladding material is varied from 1.333 to 1.40.

It can be observed from Fig. 6.11 that the sensitivity of the quasi-TM mode of the NW (presented along the left y-axis) is slightly greater than that of the quasi-TE mode. The sensitivity for both the above modes increases when the refractive index of the cladding material is increased. Even though the quasi-TE mode has a greater effective index, the ratio of the effective index change with respect to the cladding index change, defined as the sensitivity ($S_{wg} = \frac{\Delta n_{eff}}{\Delta n}$), is less. The greater effective index difference in the quasi-TM mode can be enhanced by increasing the field intensity at the interface between the cladding material and the guiding region where the evanescent field exists. It can be observed from the change in the cladding normalized power confinement with the variation of the cladding refractive index, shown along the right hand side y-axis of Fig. 6.11, that as the cladding refractive index increases, the power confinement in the cladding also increases, thus improving the sensitivity of the device.

After optimizing the dimensions of the polymer NW under investigation, the structure with a width of w=1.0 μm and a height of h=0.5 μm is considered in order

to obtain the single-mode propagation and still be able to achieve a higher power confinement in the sensing region.

6.2.2 Ormocomp nanowire rib waveguide with trapezoidal-shaped

In this section, we present the simulation results of the fabricated NW structure which is shown in Fig. 6.12(a). The NW from the fabrication process has a rib waveguide structure with slab thickness (t). This layer is the result of the residual ormocomp layer from the nanoimprint process. A schematic of the fabricated NW structure is presented in Fig. 6.12(b).

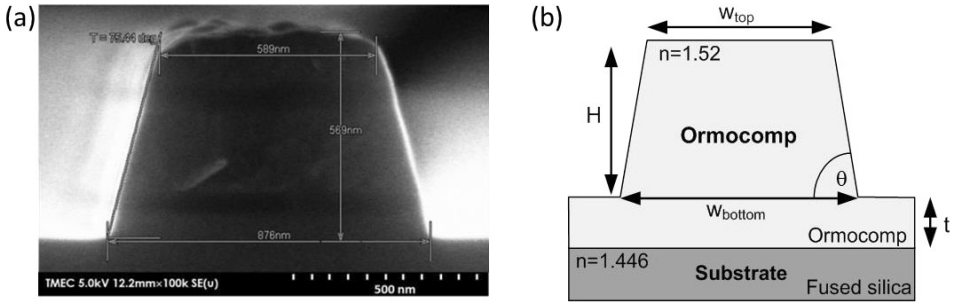

Figure 6.12: (a) SEM image of a fabricated ormocomp NW showing the non-vertical sidewalls. (b) Schematic cross-section of a fabricated ormocomp NW with rib waveguide structure.

The NW core has a non-vertical sidewall structure (trapezoidal-shaped) due to the limitation of the fabrication process we had. The sidewall angle is measured to be 65°. Theoretical study of the modal fields, the power confinement and the sensitivity of the modes identified are carried out for different slab thicknesses (t), operating wavelengths (λ) and cladding materials (n_c). This trapezoidal-shaped waveguide has the fixed dimensions of height h=0.5 µm, top-width w_{top}=1.0 µm and bottom-width w_{bottom}=1.5 µm. The operating wavelength is in visible region, λ=400-700 nm. The cladding material considered in the simulations has a refractive index in the range between 1.333 and 1.400.

6.2.2.1. The effect of the operating wavelength (λ)

The fundamental mode field inside the NW is studied using a full-vectorial **H**-field FEM. The slab thickness (t) obtained from the fabrication is measured to be

t=2 μm. Therefore, the NW with slab thickness fixed at 2 μm is considered to numerically study the guided optical modes and their power confinement. First, variation of the effective index of the NWs is studied over the operating wavelength as presented in Fig. 6.13.

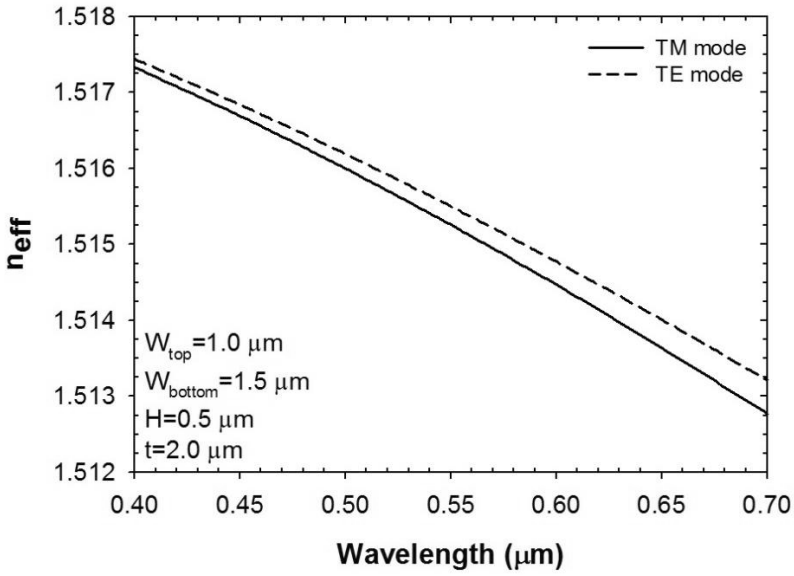

Figure 6.13: Variation of the effective index as a function of the operating wavelength for the quasi-TM mode and quasi-TE mode.

Similar to the behaviour of the conventional structure NWs as presented in Section 6.2.1, the effective index of the NWs is decreased when the operating wavelength increases because the light with longer wavelengths becomes less confined in the relatively small NWs. This leads to larger field extensions in the cladding region, as can be seen from the graph of normalized power confinement. The changes of power confinements in the core and cladding regions over the wavelength are presented in Fig. 6.14.

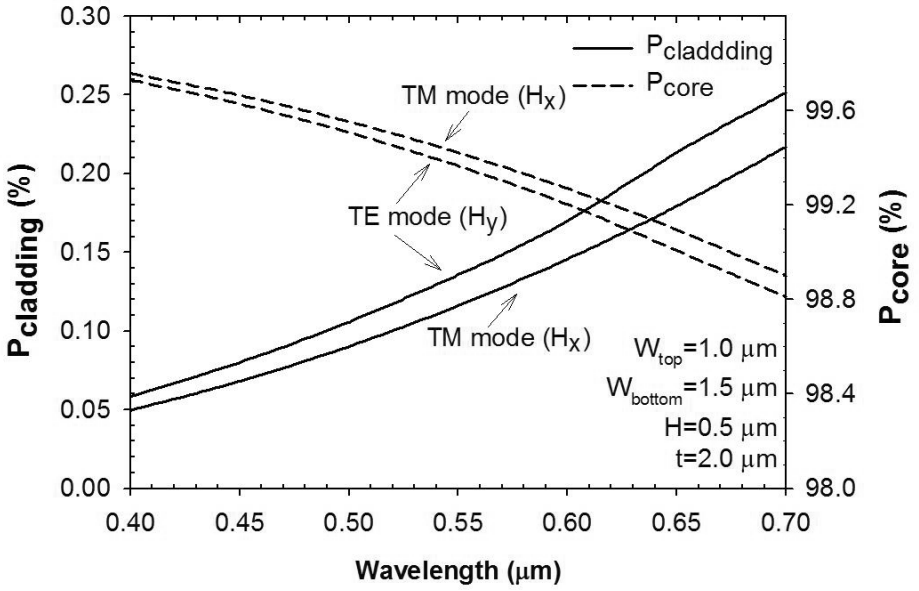

Figure 6.14: Graph of power confinements in the cladding and core regions of the quasi-TM mode NW with non-vertical sidewall with the operating wavelength in the visible region (400-700 nm).

It can be observed from the characteristics in Fig. 6.14, there is less confinement of the optical field in the guiding region at a large wavelength. Therefore, the normalized power confinement in the cladding region is greater due to the large evanescent fields. Even though the power confinement in the cladding region is increased with the operating wavelength, this is found to be much smaller compared to that obtained from the conventional structure NWs. This is due to the presence of lower slab region of ormocomp. At the operating wavelength of 0.65 μm, the normalized power confinement about only 0.21% is captured. Therefore, the ormocomp slab layer thickness is another important parameter that affects the performance of the ormocomp NWs.

6.2.2.2. The effect of the slab thickness (t)

The power confinement in the cladding region is quite small because the light is mostly confined in the slab layer of the NWs. This 2 μm thick slab layer occurs from the nanoimprint process. The **H**-field profiles for the quasi-TM and quasi-TE modes for the structure with the slab thickness of 2.0 μm are shown in Figs. 6.15 (a) and (b), respectively.

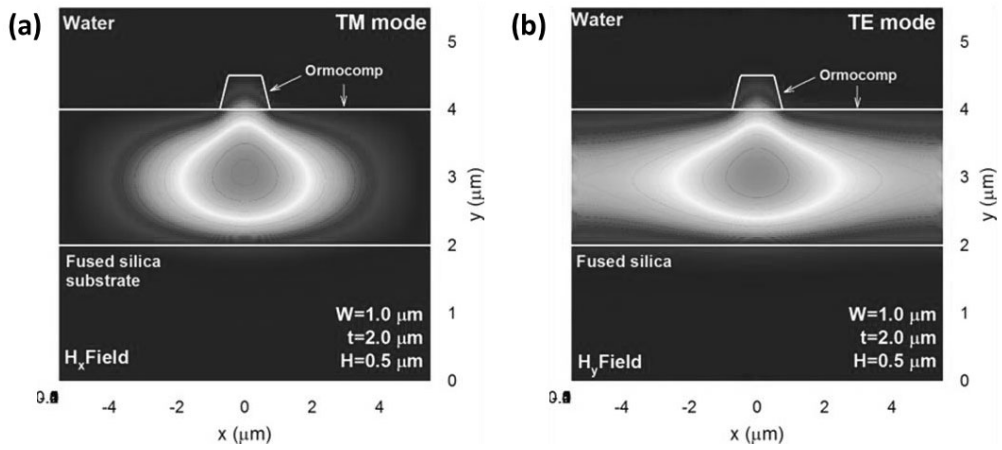

Figure 6.15: Dominant **H**-field of the quasi-TM mode (left) and quasi-TE mode (right) guided in the rib waveguide with a slab thickness of 2.0 μm.

From the optical field profiles shown in Fig. 6.15, it can be observed that the light is mostly confined in the slab layer resulting in smaller power confinement at the core/cladding interface. By changing the slab thickness, the characteristic of the polymer rib NW with non-vertical sidewall including the effective index and power confinement can be modified. The change of the effective index when varying the slab thickness for quasi-TM and quasi-TE modes is shown in Fig. 6.16.

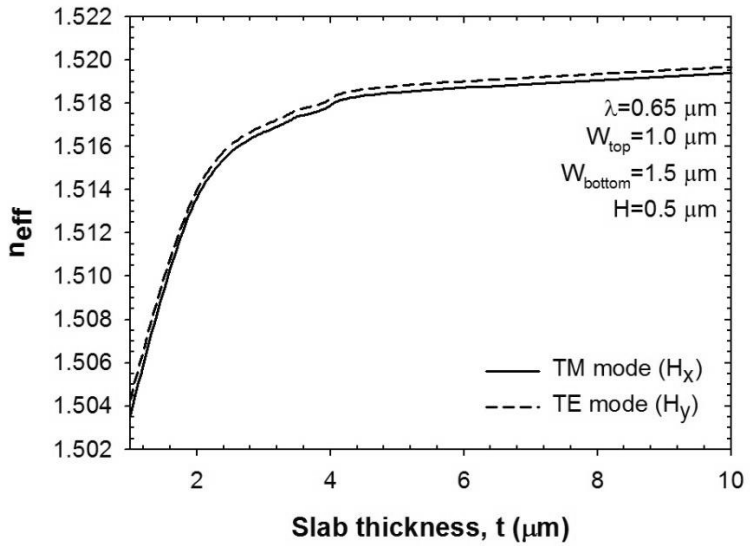

Figure 6.16: Graph of the effective index change with the slab thickness (t) for the NW rib waveguide with H= 0.5 μm, w_{top}=1.0 μm and w_{bottom}=1.5 μm.

Similar to a vertical sidewalls NW, the quasi-TE mode has a slightly higher effective index than the quasi-TM mode because the width of the NW is also larger here than its height. With the slab thickness between 1 to 5 μm, the effective

index is increased rapidly when the slab layer is larger. For slab thickness greater than 5 μm, the core height of the NW is too small compared to the slab layer and it cannot influence the change in the effective index of the whole structure. Therefore, the effective index value becomes almost constant at around 1.52, which is the refractive index of the NW.

The graph of the normalized power confinement in the guiding region and the cladding region with respect to the slab thickness is shown in Fig. 6.17.

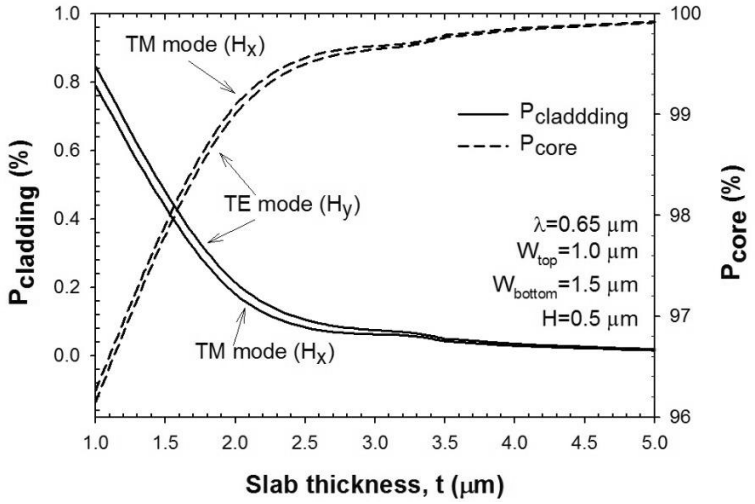

Figure 6.17: Variation in the normalized power confinement in the cladding and the core region with the slab thickness (t).

As the slab thickness increases from 1 μm to 2.5 μm, the normalized power confinement in the cladding region significantly decreases. On the other hand, the normalized power confinement in the guiding region is increased rapidly. At the thick slab layer (t > 2.5 μm), the normalized power confinement in both the cladding region and the guiding region changes only slightly because most of the light is confined in the slab layer.

With the fixed slab thickness of 2.0 μm, the normalized confinement is found to be only 0.2% in the cladding region. The power confinement in the cladding region can be improved by reducing the thickness of the excess ormocomp layer.

6.2.2.3. The sensitivity (S)

The sensitivity of the fabricated ormocomp NWs is studied with the change in the cladding index. The cladding materials considered here are water and the

glycerol solution that have refractive indices of 1.333 and 1.365, respectively. With the different cladding materials, the sensitivity is calculated from Equation 5.4 and shown in Fig. 6.18.

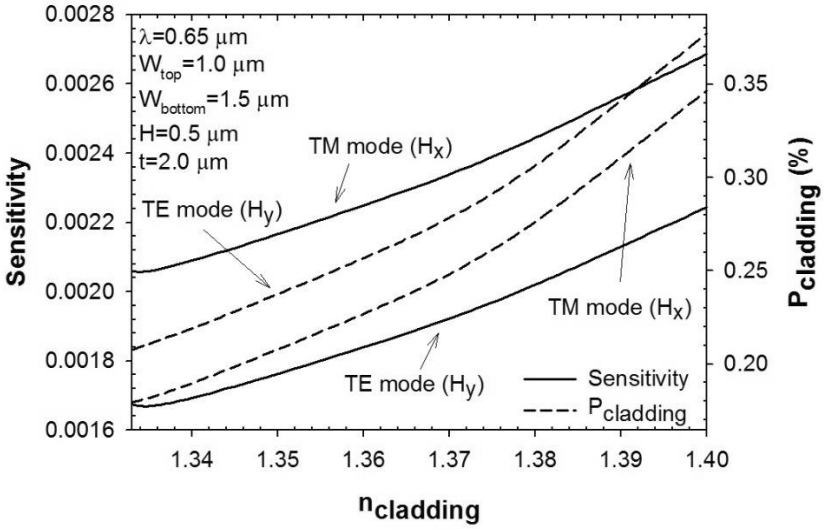

Figure 6.18: Sensitivity and the normalized power confinement in the cladding of the rib waveguide ormocomp NW with non-vertical sidewall when the refractive index of the cladding material is varied in the range of 1.333 to 1.400.

The sensitivity of the NW is improved when the refractive index of the cladding material increases for both the quasi-TM and quasi-TE modes. Similar to the conventional ridge waveguides, the quasi-TM mode also has a higher sensitivity than the quasi-TE mode. However, the sensitivity calculated for the fabricated NWs structure is lower by two orders of magnitude than the sensitivity calculated for the designed NWs structure. This is because the modal field of fabricated nanowire rib waveguide shifts away from the cladding region to the slab region leading to small power confinement in the sensing region as confirmed by simulations.

In addition, highly slanted waveguides can induce polarisation rotation, thus leading to mode coupling [25]. The above effect has been considered in the simulations of the device. However, it is found that it does not have a significant contribution to the NWs due to the lower index contrast and the structure examined being almost symmetric in the present work.

In order to enhance the power confinement at the core/cladding interface, the slab layer has to be removed and this can be done during the nanoimprint

process. However, another way to increase the amount of light at the interface for the slab structure NWs is the use of surface plasmon resonance (SPR). Therefore, a thin gold layer is coated on the NWs to study the effect of the surface plasmon resonance.

6.3 Gold-coated ormocomp nanowire waveguides

The gold-coated ormocomp NWs are theoretically studied in this section. Similar to the non-gold-coated waveguide as described in Section 6.2, there are two different structures considered in this work, which are ridge structure with vertical sidewalls and rib structure with non-vertical sidewalls. Initially, the vertical sidewalls waveguides are considered in order to introduce polarisation-independence of the gold-coated waveguides. However, due to the fabrication limitation, the ridge structure with vertical sidewalls could not be fabricated in a size comparable to the wavelength. Therefore, the non-vertical sidewalls waveguides are included in the study to support the experimental work.

6.3.1 Ridge structure with vertical sidewalls (Polarisation-independent SPR)

In this part, a conventional waveguide structure which is a ridge structure with vertical sidewalls is considered to study for the effect of the surface plasmon resonance (SPR). A thin gold layer is assumed to be coated on the top and at the sides of the waveguide. However, a 0.5 µm wide and 1.0 µm high NW could not be fabricated to achieve vertical sidewalls due to a limitation in the fabrication process we had. Hence, 10 µm x 10 µm waveguide, which is a part of the feed waveguide in an integrated NW structure introduced in Chapters 2 and 4, is studied both theoretically and experimentally. The fabricated gold-coated ridge waveguide with a vertical sidewall is shown in Fig. 6.19(a) and its schematic for the theoretical study is shown in Fig. 6.19(b).

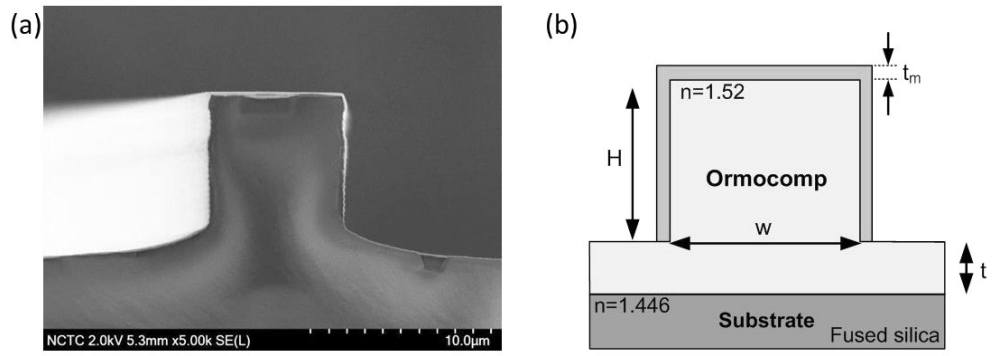

Figure 6.19: (a) SEM image of a fabricated ormocomp waveguide showing the vertical sidewalls with a thin gold layer at the top and sides. (b) Schematic cross-section of a gold-coated ormocomp waveguide. Gold is coated on the top and the sides of the waveguide.

It can be clearly seen from the bright part in Fig. 6.19(a) that the waveguide is coated with thin gold layers on the top and the sides. A gold thickness of 100 nm is coated on the waveguide using the sputtering technique in order to introduce plasmonic modes at the vertical sidewalls and the top metal surface of the waveguide, according to the polarisation of the optical field.

Surface plasmon resonance is the oscillation of the electrons at the interface between dielectric and electric materials. The resonance occurs when the momentum of the photons from the incident light matches the momentum of the oscillated electrons at some specific wavelength called the resonance wavelength. The absorption due to SPR at the resonance wavelength provides a large power confinement in the sensing area. Hence, the sensitivity of the NWs can be improved [157-161].

With the presence of SPR, light is guided as a plasmonic mode. The first order resonance condition at the semi-infinite dielectric/metal interface is given by [215]:

$$\beta_{sp} = \frac{2\pi}{\lambda}\sqrt{\frac{\varepsilon'_m(\lambda)\varepsilon_c}{\varepsilon'_m(\lambda)+\varepsilon_c}} \tag{6.1}$$

where β_{sp} is the propagation constant for the SPR mode. The resonance is occurred when the propagation constant of the guided mode equals to β_{sp} where λ is the operating wavelength in free space. ε'_m is the real part of the dielectric

constant of the metal, which is a wavelength dependent parameter and ε_c is the dielectric constant of the cladding material ($\varepsilon_c = n_c^2$). The surface plasmon resonance exists when ε_m' is negative and its magnitude is larger than ε_c ($\varepsilon_m' < 0$ and $|\varepsilon_m'| > \varepsilon_c$). The equation 6.1 is varied only for the semi-infinite metal layer in which the thickness of the metal layer is not considered. The ormocomp waveguides are coated with a gold layer of thickness about 100 nm. Therefore, a resonance condition for the finite metal layer is required instead of semi-infinite. The analytical form of the resonance condition for the finite dielectric/metal interface can be calculated from the incident light reflectivity where the metal thickness is the key parameter [215].

In our work, the numerical method is used to study the SPR in ormocomp waveguides instead of using analytical formulation. The full-vectorial **H**-field FEM is the numerical method used here to study the characteristics of the gold-coated ormocomp waveguides with the effect of the SPR. By using the FEM, the metal thickness is also taken into consideration when β_{sp} is calculated. At the top surface, the oscillation of the electrons introduces SPR quasi-TM mode with dominant H_x/E_y field as shown in Fig. 6.20(a). On the other hand, at the vertical sidewalls, SPR quasi-TE mode is formed with dominant H_y/E_x field as shown in Fig. 6.20(b).

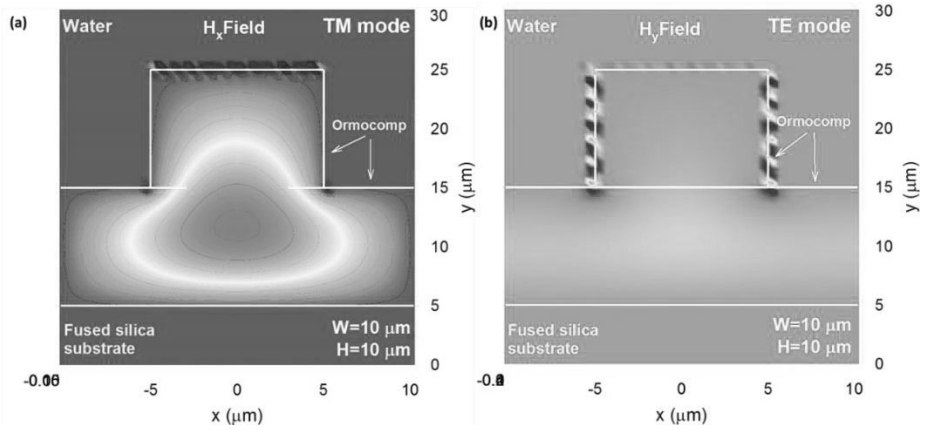

Figure 6.20: 2D **H**-field of the light guided in golthe d-coated ormocomp waveguide for (a) quasi-TM mode, H_x field and (b) quasi-TE mode, H_y field.

The waveguide in Fig. 6.19 can be characterised as polarisation-independent SPR waveguide in terms of the ability to detect SPR wavelengths in sensing

applications without the use a polarizer in an integrated sensor system, thus providing a simpler configuration with increased reliability. In addition, the polarisation-independent mechanism allows the integrated SPR sensor to be scaled down in the manufacturing and packaging process.

In this section, the full-vectorial **H**-field finite element method (FEM) is used to simulate the optical modes in the waveguide structure calculating the effective index, resonance wavelength and its shift in different cladding materials such as water (n=1.333) and iso-propanol solutions (n=1.344, 1.351 and 1.365) in the visible region (λ=400-700 nm).

6.3.1.1. The resonance wavelength (λ_{res})

To achieve polarisation independence, the waveguide designed has an equal width and height of 10 µm with a 100 nm thick gold layer coated at the sides and on the top. In this work, 64800 first-order triangular elements are used to represent one half of the gold-coated waveguide structure. With the FEM, the size of the triangles can be varied for each individual part of the waveguide to achieve a higher computational efficiency. In this case, the vertical resolution of 1.67 nm is obtained for the 100 nm thick gold layer.

Gold has a complex refractive index ($\tilde{n}$) which is defined by $\tilde{n} = n + j\kappa$ where κ is the extinction coefficient [216]. Both n and κ are wavelength dependent [202]. This complex refractive index is used to calculate for the dielectric constant, sometimes called the complex relative permittivity of gold ($\widetilde{\varepsilon_r}$), which is the required parameter in the FEM simulations. The dielectric constant of gold can be calculated as follow [216]:

$$\widetilde{\varepsilon_r} = \tilde{n}^2 = (n + j\kappa)^2 \tag{6.2}$$

The $\widetilde{\varepsilon_r}$ varies with the wavelength. The value of $\widetilde{\varepsilon_r}$ in the whole visible spectrum for this work is given in Appendix B.

First, a variation of effective index (n_{eff}) and loss of the fundamental quasi-TM and quasi-TE modes over the visible region in water cladding are studied as shown in Fig. 6.21

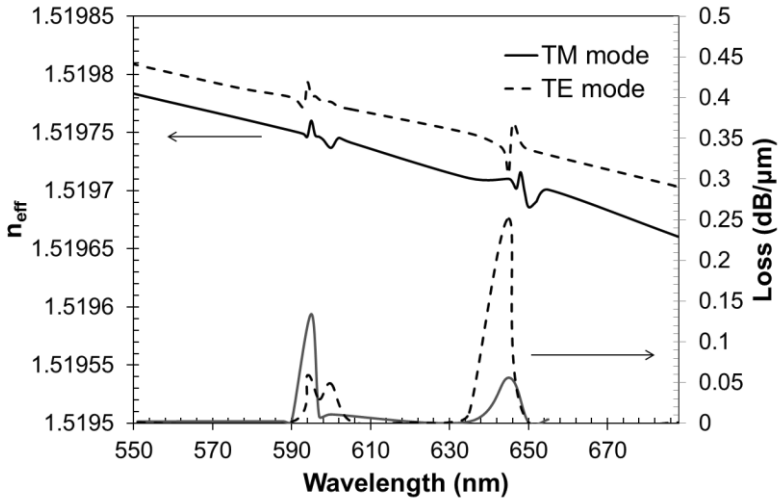

Figure 6.21: Change of effective indices (n_{eff}) and loss over the operating wavelength in the visible region for quasi-TM and quasi-TE modes.

The effective index of the gold-coated ormocomp waveguide is reduced with the operating wavelength. As for the larger wavelength, power confinement in the core is reduced. However, as the ormocomp waveguide structure was relatively larger, there is no modal cut-off in the wavelength range considered here. The loss for this waveguide structure involves the light guided outside the waveguide core which includes the light extended into the substrate and also the sensing region (metal/cladding interface). For this 10 μm size waveguide operating in the visible wavelength, most of the light is confined in the core. Hence, the loss in the substrate is negligible and only the loss in the sensing region, which is in the metal layer in this case, is calculated by using equation 6.3. The loss shows its peak at the SPR wavelength because the plasmonic mode located at metal/cladding interface is dominant compared to the dielectric mode.

$$Loss\ (dB) = 10log_{10}\frac{I_{out}}{I_{in}} \tag{6.3}$$

where I_{in} is an input intensity and I_{in} is an output intensity.

The effective index variation graph shows several peaks at some specific locations indicating the resonance phenomena. In this case, the two dominant resonance wavelengths (λ_{SPR}) are located at λ_{SPR1}=595 nm and λ_{SPR2}=648 nm. The effective index of the fundamental plasmonic mode is usually higher than the

dominant dielectric mode. The thickness of the gold layer is fixed at 100 nm to ensure guidance of fundamental and higher-order plasmonic modes. The higher order plasmonic modes have lower effective indices and this allows different order plasmonic modes to be coupled with the dielectric mode at different resonance wavelengths leading to several resonance peaks to occur. In addition, the effective index of the quasi-TE mode is slightly higher than the quasi-TM mode because there are two metal/cladding interfaces at the vertical sides of the ormocomp waveguide for the quasi-TE mode but only one metal/cladding interface for the quasi-TM mode at the top of the waveguide. However, the resulting resonance wavelengths for both the quasi-TM and quasi-TE modes are almost identical.

The 2D optical field for a dielectric mode obtained from the **H**-field FEM is compared with the optical field images from the experimental field profile at a non-resonance wavelength and at resonance wavelength as shown in Figs. 6.23 and 6.24, respectively.

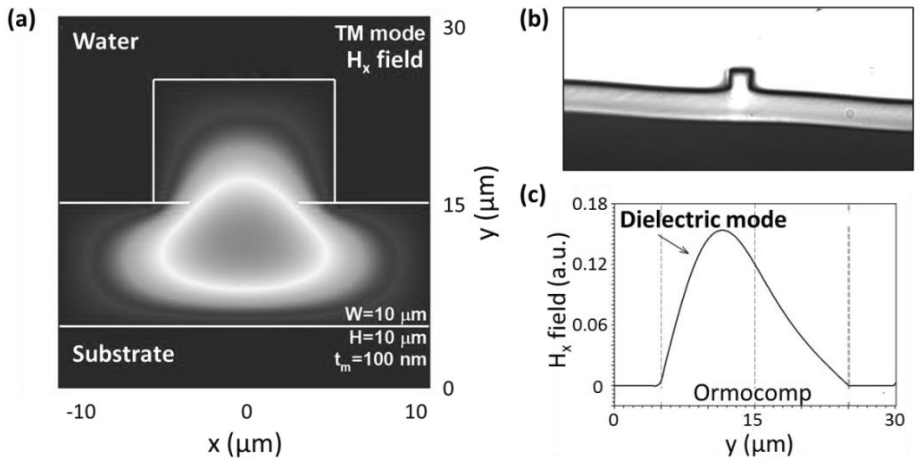

Figure 6.22: Modal field profile excited in the ormocomp waveguide at a non-resonance wavelength from (a) FEM simulation, (b) experiment, and (c) H_x field of the guided mode along the y-axis

It can be observed that the dielectric mode is well confined in the core of the gold-coated ormocomp waveguide at the non-resonance wavelength. The ormocomp waveguide has a quasi-rib-structure, so some of the light in the core of the waveguide is extended into the rib layer as can be seen from the simulation in Fig. 6.22(a) which compares well with the image from CCD camera in the

experimental setup as shown in Fig. 6.22 (b). The dominant field variation along the y-axis is also shown in Fig. 6.22 (c) which clearly identifies this as a pure dielectric mode.

In addition, the gold-coated ormocomp waveguide has two dielectric/electric interfaces which are the ormocomp/gold and the cladding/gold interfaces. Therefore, the plasmonic modes occurring at the metal layer are also plasmonic supermodes which are coupled modes between fundamental dielectric mode and odd-like fundamental plasmonic supermodes. At the resonance wavelength, the plasmonic modes are induced and coupled with the dielectric mode to form a supermode. The optical image from the CCD camera in the experiment, Fig. 6.23(b), shows a good agreement to the simulation result, shown in Fig. 6.23(a), in which the plasmonic mode are mostly confined at the metal/cladding interface and the dielectric mode confined in the core and rib layer. The numerically simulated shown $H_{x\text{-}y}$ profile at the centre of the waveguide is in Fig. 6.23(c) which clearly shows the plasmonic peaks at the metal-dielectric interfaces. The dielectric mode is dominant at the non-resonance wavelength but the plasmonic mode is dominant at the resonance wavelength.

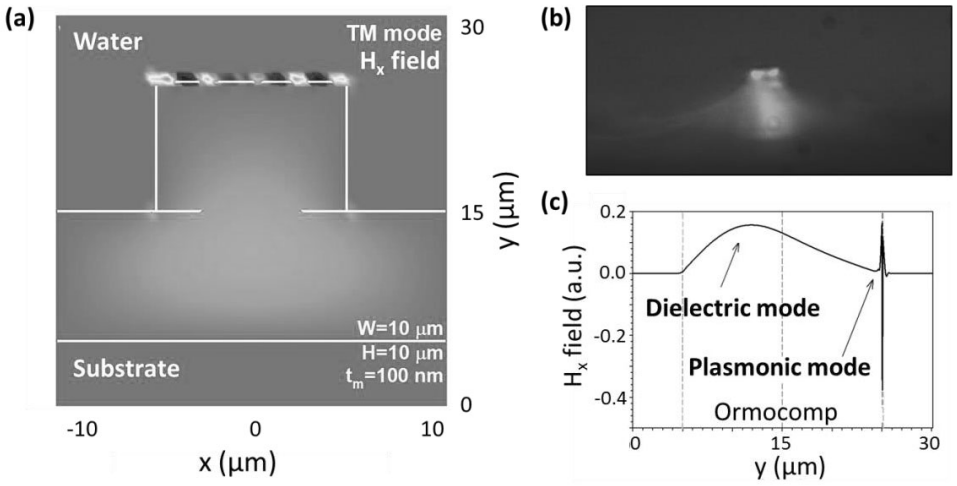

Figure 6.23: Modal field profile excited in the ormocomp waveguide at the resonance wavelength from (a) FEM simulation, (b) experiment, and (c) H_x field of the coupled dielectric-plasmonic mode along the y-axis.

There are other coupled dielectric-plasmonic modes occurred over the wavelength such as the fundamental dielectric mode coupled with the even-like

plasmonic mode. They can also have higher order variation in other transverse direction. The effective index of the even-like plasmonic mode is lower than that of the odd-like plasmonic mode, but by adjusting waveguide parameters it may be possible to couple this plasmonic mode to the core dielectric mode. However, only the coupled mode between the fundamental dielectric and the odd-like plasmonic mode is studied in this work as shown in Fig. 6.24 for water cladding.

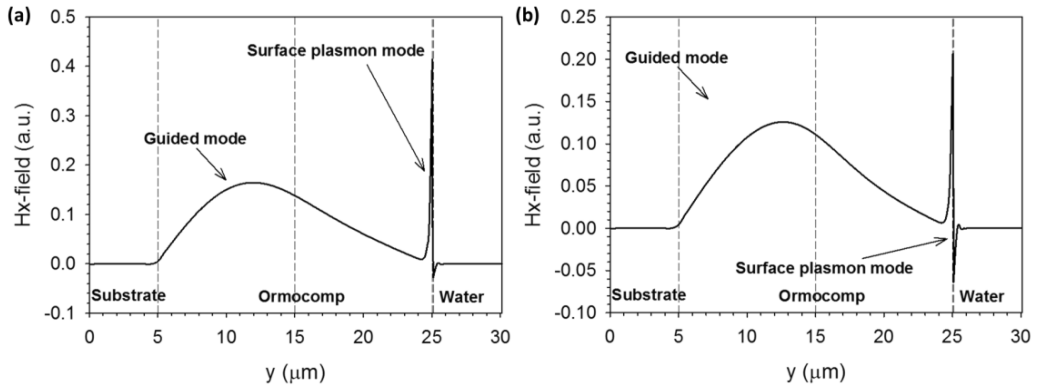

Figure 6.24: H_x-field of the coupled dielectric-plasmonic mode in water cladding along the y-axis at the SPR wavelengths where (a) λ_{SPR1}= 595 nm (b) λ_{SPR2}= 648 nm.

With the large field at the interface for the surface plasmon mode at the resonance wavelength, the power confinement in the sensing region is also expected to be enhanced. The normalized power confinement in the sensing region, which is the metal/cladding interface is obtained by using the FEM simulation, is shown in Fig. 6.25.

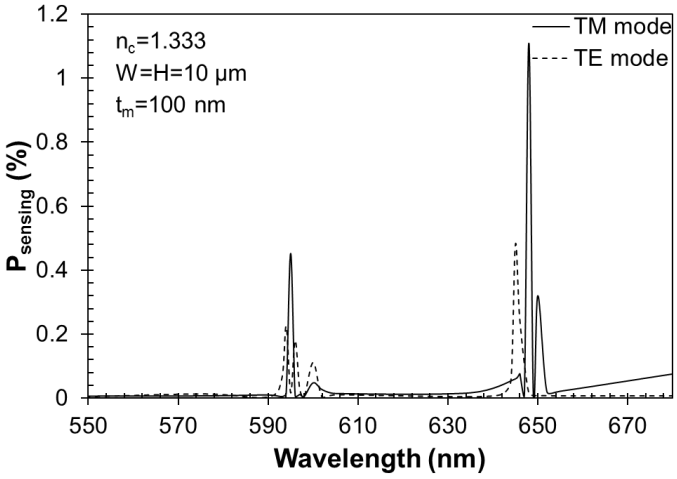

Figure 6.25: Graph of normalized power confinement in the sensing region of the ormocomp waveguide in water cladding calculated by using an in-house FEM program for quasi-TM and quasi-TE modes.

The resonance wavelengths can be identified from power confinement in the sensing region graph where the peaks representing high power confinement occur. There are several peaks occurring due to multiple plasmonic modes possible in the thicker gold layer. From the numerical simulations, the minimum thickness of the gold layer allowing the dominant plasmonic mode to occur is identified as 80 nm. However, in our fabricated guides, the actual gold thickness is around 100±20 nm. For a thicker gold layer, several plasmonic modes are occurred resulting in several SPR peaks in the simulation results. Considering only the coupled modes between the fundamental dielectric and odd-like fundamental plasmonic supermode, there are two distinct peaks for both the quasi-TM and the quasi-TE modes when the gold layer thickness is 100 nm.

6.3.1.2. The resonance shift and sensitivity

In this work, the gold-coated ormocomp waveguides are tested with four different cladding materials with different refractive indices to study the resonance shift. The four different cladding materials are water and three different concentrations of isopropanol solutions with the refractive index of 1.333, 1.344, 1.351 and 1.365, respectively. In order to investigate the resonance wavelength for each cladding material, only the lowest order symmetric plasmonic mode, which is the fundamental dielectric-plasmonic coupled mode, is tracked as presented in Fig. 6.26.

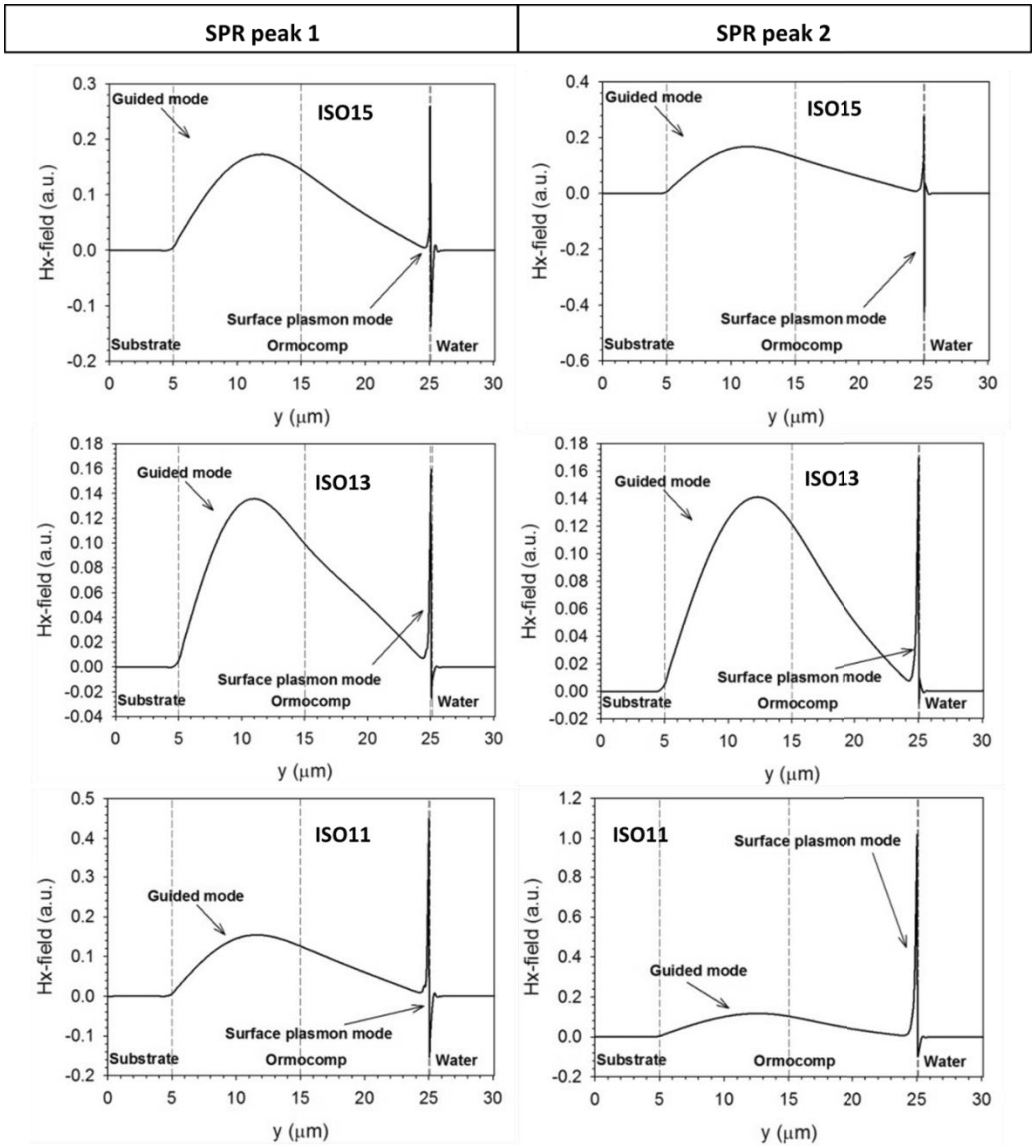

Figure 6.26: H_x-field of the coupled dielectric-plasmonic mode in three different isopropanol solutions along the y-axis at the resonance wavelengths where ISO15, ISO13 and ISO11 have refractive index of 1.344, 1.351 and 1.365, respectively.

From Fig. 6.26, it can be clearly observed that all the modes are the coupled modes between fundamental dielectric mode and odd-like fundamental plasmonic supermode.

In order to obtain the resonance wavelengths for each cladding material, the effective index and power confinement in the sensing region are examined as shown in Fig. 6.27.

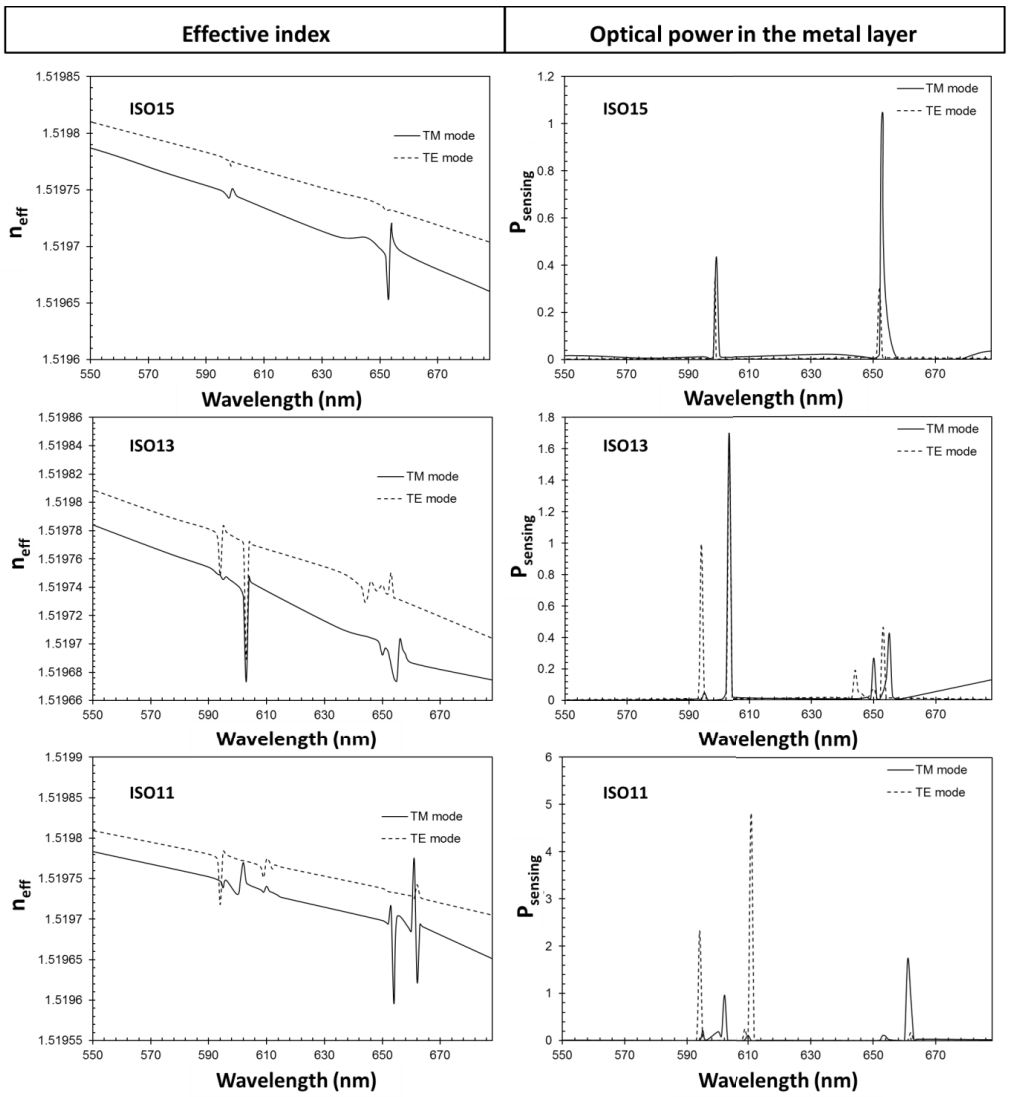

Figure 6.27: Graphs of the effective index of the gold-coated ormocomp waveguide and optical power in the sensing region with the wavelength for both quasi-TM and quasi-TE modes in three different claddings including ISO15, ISO13 and ISO11.

The resonance peak wavelengths of the quasi-TM and quasi-TE modes of the gold-coated ormocomp waveguide, in different cladding materials, obtained from Fig. 6.27 are presented in Table 6.1.

Table 6.1: Simulation results of the resonance peaks of the gold-coated ormocomp waveguide in different cladding materials for quasi-TM and quasi-TE modes

n	TM mode		TE mode	
	Resonance peak 1	Resonance peak 2	Resonance peak 1	Resonance peak 2
1.333	595 nm	646 nm	593 nm	645 nm
1.344	599 nm	652 nm	598.6 nm	652 nm
1.351	603 nm	655 nm	603 nm	655 nm
1.365	610 nm	661 nm	611 nm	662 nm

The resonance peaks for both the quasi-TM and quasi-TE modes occur at nearly the same wavelength because the waveguide is designed with equal height and width (but with single-side or double-side metal cladding) leading to a small difference in their effective indices. Two resonance peaks are located about 50 nm away from each other. They are the coupled supermodes between fundamental dielectric mode and odd-like fundamental plasmonic supermode. The resonance peaks for each cladding material are given in Table 6.1 and plotted as shown in Fig. 6.28.

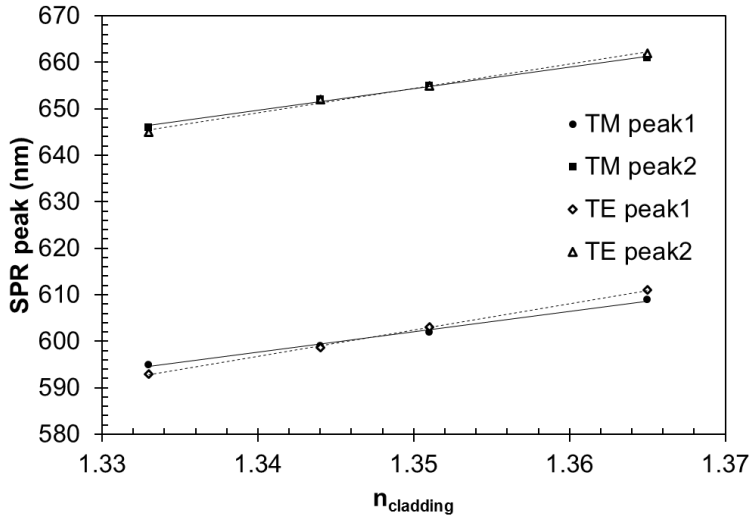

Figure 6.28: Variations of the two resonance peaks with the cladding index, obtained from the numerical simulations for each cladding material in both the quasi-TM and quasi-TE modes.

It can be observed from Fig. 6.28 that the resonance peak wavelength has a linear relationship with the refractive index of the cladding material for both the

quasi-TM and quasi-TE modes. The regression lines of the quasi-TM modes, which are represented by solid lines, almost perfectly fit the data with R-squared of 0.9929 and 0.9960 for resonance peaks 1 and 2, respectively. For the quasi-TE modes, the regression lines are represented by dashed lines with R-squared of 0.9755 and 0.9935 for resonance peaks 1 and 2, respectively. The slopes of the quasi-TE modes are slightly higher than the slopes of the quasi-TM mode for both resonance peaks which means that the quasi-TE mode has a higher sensitivity compared to the quasi-TM mode. This is due to the larger surface area (double) at the two vertical sides of the waveguide for the quasi-TE mode compared to the single surface on the top of the waveguide for the quasi-TM mode. The sensitivity of the gold-coated ormocomp waveguides with vertical sidewalls can be interpreted from the slope of the plot in Fig. 6.28 as presented in Table 6.2.

Table 6.2: Sensitivity of the gold-coated ormocomp waveguide with vertical sidewalls for quasi-TM and quasi-TE modes.

Mode	Resonance Peak	Sensitivity (nm/RIU)
TM mode	Peak 1	475.64
	Peak 2	400.46
TE mode	Peak 1	538.19
	Peak 2	514.15

The sensitivity of the waveguide in the quasi-TE mode is slightly higher than that in the quasi-TM mode because, for the quasi-TE mode, the SPR exhibits at both the vertical sides.

6.3.2 Rib structure with non-vertical sidewalls (quasi-TM mode SPR)

In this section, the gold-coated ormocomp NW with a designed structure allowing only the propagation of fundamental optical mode is studied theoretically. The vertical sidewalls NW cannot be achieved in the fabrication process available to the candidate. Hence, the structure of the fabricated NWs has non-vertical sidewalls with the sidewall angle θ=65°. In this case, only the quasi-TM mode is considered because the oscillation of the electron is normal to x-axis allowing the dominant H_x/E_y field to be observed. At the sidewall, the electrons

oscillate with an angle of 65° to the y-axis. Therefore, the quasi-TE mode with the dominant H_y/E_x field cannot be observed straightforwardly. In addition, the metal thickness at the sidewalls is thinner compared to the thickness at the top surface. Hence, the metal layer at the sidewalls is assumed to be negligible in the theoretical study. A cross-section of the ormocomp NW coated with 50 nm thick gold layer on top is shown in Fig. 6.29.

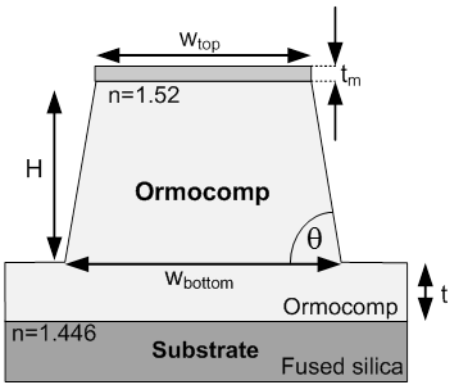

Figure 6.29: A cross-section of the fabricated ormocomp NW coated with a gold layer on the top surface.

The gold-coated ormocomp NWs are studied theoretically with the FEM for their resonance wavelengths and their shifts with different cladding materials. For this structure, 4500 first-order triangular elements are used to represent its half in the FEM with a vertical resolution of 0.8 nm is achieved inside the 50 nm thick metal layer. The operating wavelength is in the 400-700 nm range, which is in the visible region. The refractive index of the cladding materials in this study are taken as 1.333 (water), 1.351 (ISO13: Iso-propanol solution with 1:3 volume ratio) and 1.356 (ISO11: Iso-propanol solution with 1:1 volume ratio).

6.3.2.1. The resonance wavelength (λ_{res})

The light propagates in the ormocomp NWs coated with a thin gold layer on the top surface as the quasi-TM mode where the dominant electric field component (E_y) is normal to the dielectric/metal interface. First, the gold-coated ormocomp NWs with water cladding are studied theoretically over the operating wavelength. A comparison of the effective index values of the un-coated NW and gold-coated NW is shown in Fig. 6.30.

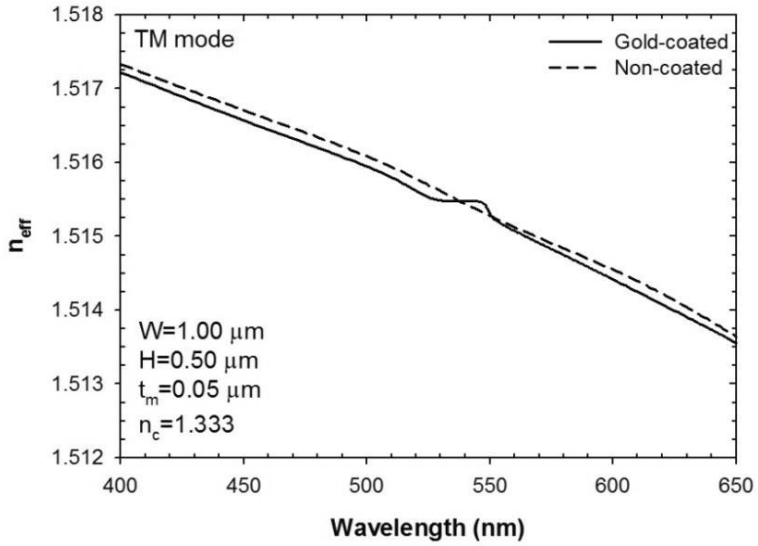

Figure 6.30: A comparison of the effective index between un-coated NW and gold-coated NW in water cladding over the operating wavelength.

Effective indices of both the NWs decrease with the larger operating wavelength. The ormocomp NW coated with gold layer has a lower effective index because gold has a complex refractive index ($\tilde{n}$) which is defined by $\tilde{n} = n + j\kappa$ where κ is the extinction coefficient [216]. The extinction coefficient indicates the amount of light absorbed by the material. Here, both the n and κ are wavelength dependent [202].

The resonance peak can also be seen in Fig. 6.30. Even though the effective index of the gold-coated ormocomp NWs is lower than the corresponding un-coated NWs, at some specific wavelength, where the resonance occurs, the effective index of the gold-coated NW becomes higher. In the case of water cladding, the resonance occurs at λ=546 nm. The 2D H_x field contour and its variation long the y-axis at the non-resonance and resonance wavelength are presented in Fig. 6.31.

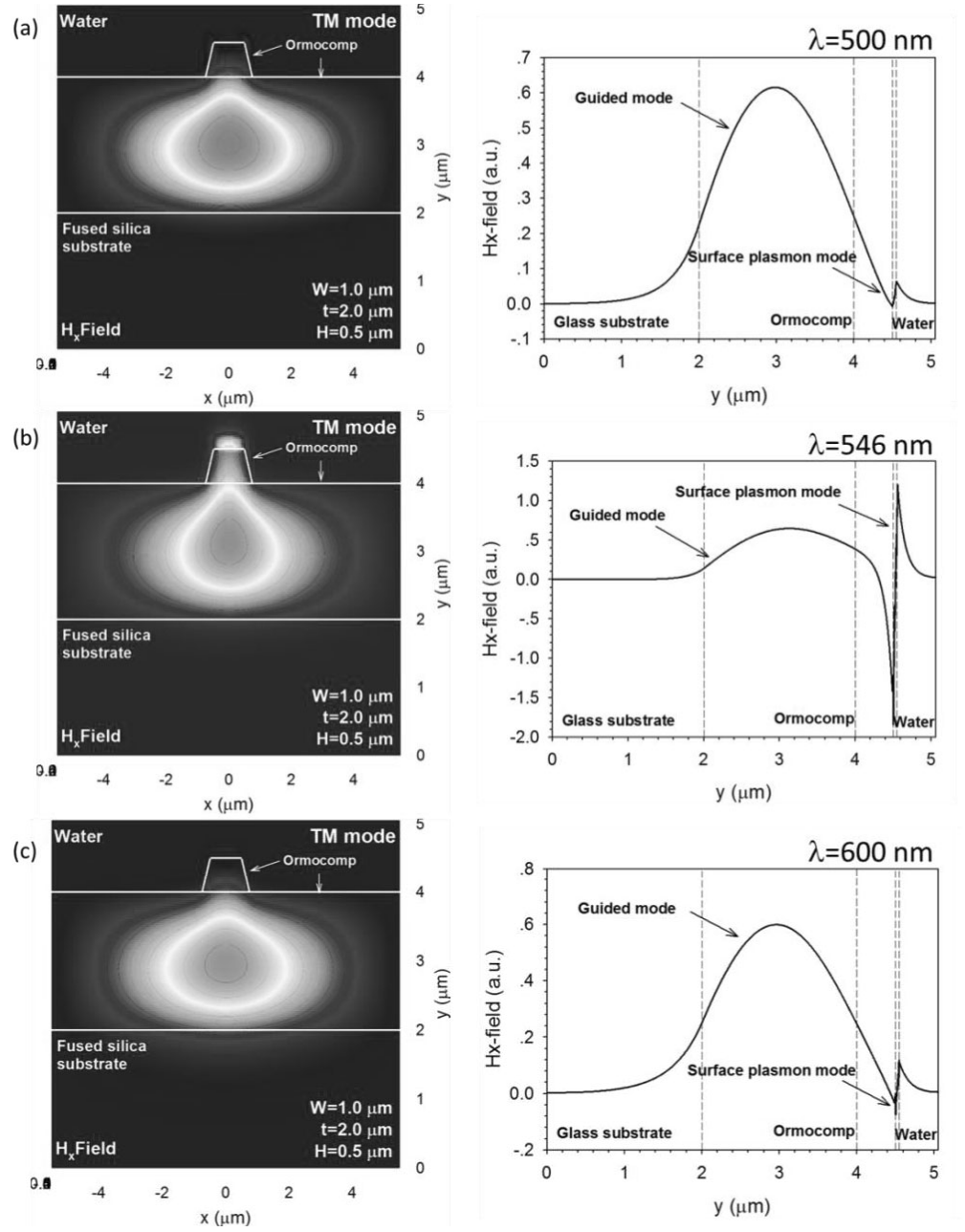

Figure 6.31: 2D optical fields and H_x field in y-axis at (a) λ=500 nm (b) λ=545 nm (the resonance wavelength) (c) λ=600 nm.

There are two modes present in the gold-coated ormocomp NWs which are the dielectric mode (guided mode) and the plasmonic mode. These two modes couple with each other to form a supermode when their effective indices are very close. At the resonance wavelength in Fig. 6.31(b), the plasmonic mode is stronger than the dielectric mode. On the other hand, the dielectric mode is dominant at other wavelengths (Figs. 6.31(a) and (c)). According to the large surface plasmon mode at the resonance wavelength, the power confinement in the sensing region

is also expected to be improved. The graph showing the linear-fit of normalized power confinement in the sensing region, which is the metal/cladding interface, is presented in Fig. 6.32.

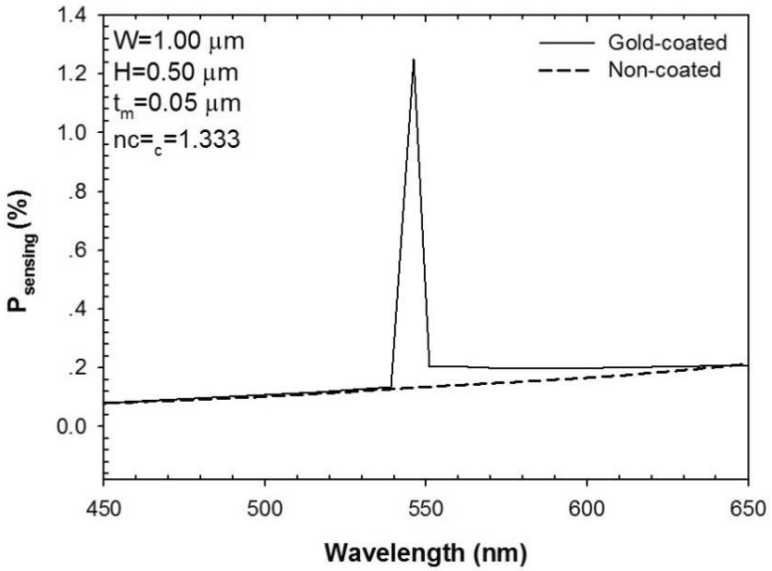

Figure 6.32: Comparison of the normalized power confinement in the sensing region between gold-coated ormocomp NWs (linear-fit) and un-coated ormocomp NWs over the operating wavelength.

A comparison of the normalized power confinement in the sensing region between gold-coated and un-coated ormocomp NWs is also shown in Fig. 6.32. The power confinement in the sensing region generally increases with the operating wavelength. The resonance peak from the linear-fit can be observed at the resonance wavelength which is at λ=550 nm. The graph shows that the power confinement in the gold-coated ormocomp NW is 10 times higher than the un-coated NWs at the resonance wavelength.

6.3.2.2. The resonance shift and sensitivity

For the 50 nm-gold-coated ormocomp NWs with water cladding, the resonance wavelength is found to occur at 546 nm. However, the resonance wavelength shifts with a different refractive index of the cladding material. The cladding materials considered in this theoretical study are water (n=1.333) and two different volume ratios of iso-propanol solutions (n=1.351 and n=1.365).

The exiting guide modes, their modal field distribution and their power confinement in ormocomp NWs with the effect of SPR are theoretically studied over the wavelength and the different cladding materials. As mentioned earlier, there are two possible optical modes in this NW structure, the dielectric mode inside the ormocomp region and the plasmonic mode at the dielectric/metal interface. These two modes can be clearly separated or coupled with each other to become a supermode depending on the parameters of the NW structure, especially the height of the NW. In our work, the coupled dielectric-plasmonic mode is obtained for all three different cladding materials, which are water and two iso-propanol solutions with different concentrations, as shown in Fig. 6.33.

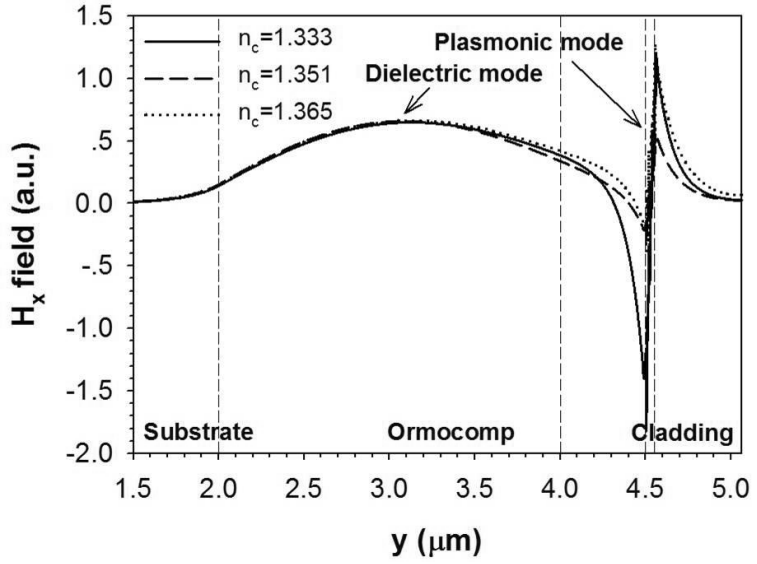

Figure 6.33: H_x field of coupled dielectric-plasmonic mode along the y-axis for three different cladding indices at a specific wavelength.

From Fig. 6.33, the supermode coupling between the dielectric mode and odd-like (antisymmetric) plasmonic supermode is clearly seen from the H_x profile along the y-direction at a specific operating wavelength. The odd-like supermode is the mode where the superposition of those two modes have opposite field polarity [217]. The variation of the effective index of the allowed modes in three different cladding mediums with respect to the operating wavelength is shown in Fig. 6.34.

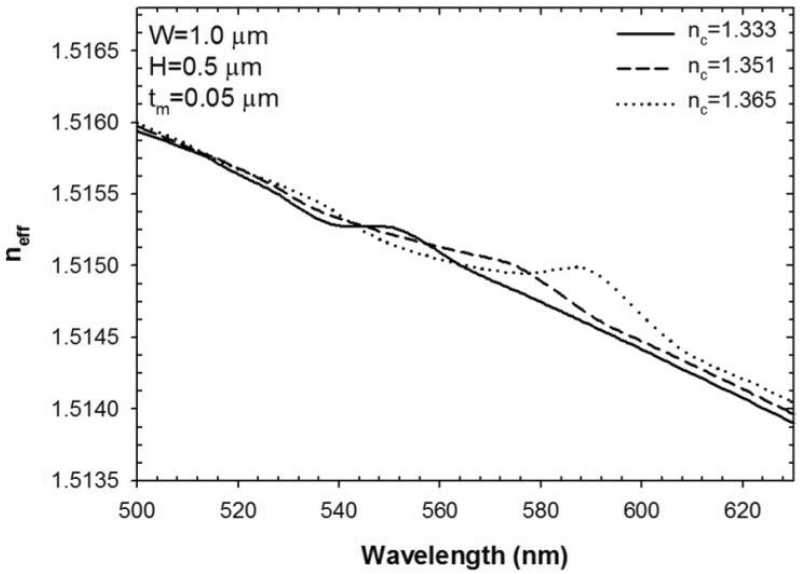

Figure 6.34: Change in the effective index of the gold-coated ormocomp NW in different cladding materials with operating wavelength. The peak indicates the wavelength where the SPR is excited.

Effective indices of the optical mode decrease when the wavelength is increased regardless of the value of the cladding index because the wavelength becomes larger compared to the dimension of the NW. However, the graph of effective indices in Fig. 6.34 shows the peak at a specific wavelength for each cladding material, which can be considered to be the SPR wavelength. The effective index of the plasmonic mode is normally higher than that of the fundamental dielectric mode. Hence, the effective index of the coupled dielectric-plasmonic mode occurring at the resonance wavelength is slightly higher than the dielectric mode alone.

At the wavelength where the SPR occurs, the power confinement in the sensing region which is at the gold/cladding interface also increases because the evanescent field at the interface is enhanced. The graph of the power confinement in the sensing area and the wavelength is shown in Fig. 6.35.

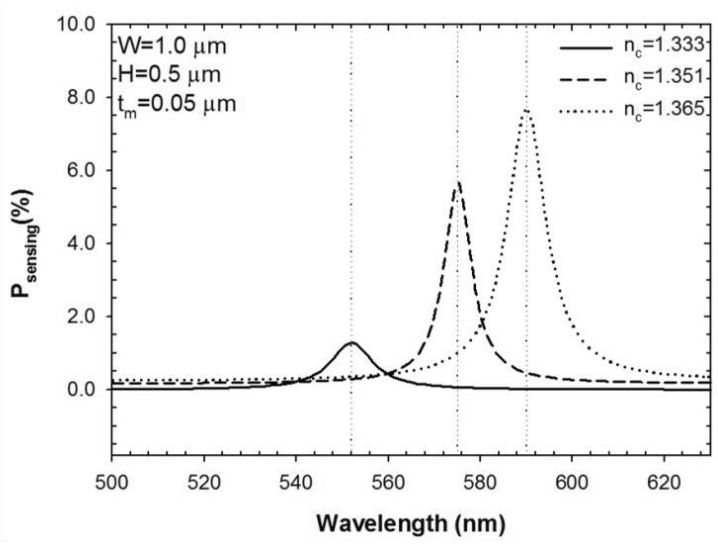

Figure 6.35: Variation of power confinement in the sensing region of the NW at different cladding-indices with the operating wavelength. The highest power confinement is obtained at the SPR wavelength.

The power confinement of the quasi-TM mode in the sensing region of the gold-coated ormocomp NW with water cladding, is 10 times higher than that the ormocomp NW with the same parameters but without the gold layer. The resonance peak wavelength where the SPR signal occurs for each cladding material can be recognized from the peak in both the effective index (Fig. 6.34) and power confinement graphs (6.35). For the water cladding structure, the SPR signal is obtained at 551 nm wavelength. The plasmonic modes in iso-propanol solution are observed at the wavelengths of 576 nm and 590 nm for the cladding index of 1.351 and 1.365, respectively. As the cladding index increases, a redshift of SPR peak wavelength is observed.

Beside the cladding material, the thickness of the metal layer is another important parameter which affects the resonance peak position. For the gold-coated NW, the SPR occurs at both the core/metal and the cladding/metal interfaces. These two plasmonic modes couple with each other and form the supermode of symmetric (even-) or antisymmetric (odd-) resonance [159, 166, 167]. With thicker metal layer, the antisymmetric surface plasmon mode has a redshift while the symmetric surface plasmon mode obtains a blueshift [218]. For our work, the antisymmetric supermode (odd-like supermode) is considered. The

relation between the SPR peak wavelengths for each cladding material with different metal thickness for an odd-plasmonic supermode is shown in Fig. 6.36.

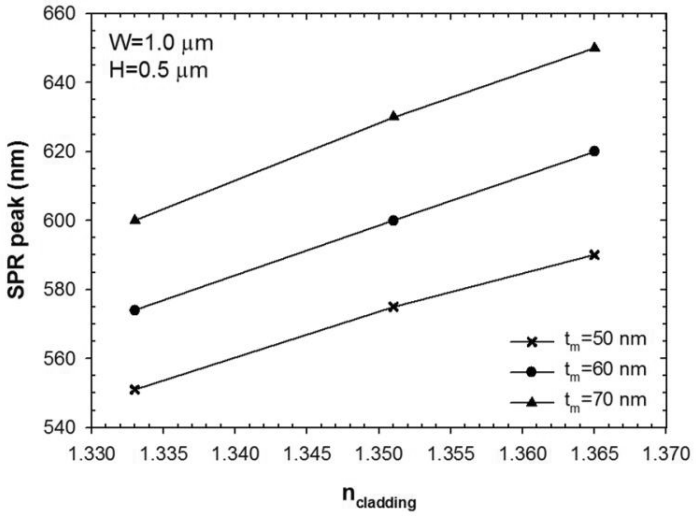

Figure 6.36: Graph of SPR peak wavelength of an ormocomp NW with three different cladding materials and gold coating thickness of 50, 60 and 70 nm. The redshift occurs for the antisymmetric modes when the thickness of gold layer is increased.

The metal thicknesses of 50, 60 and 70 nm are considered. For a very thin metal layer, the enhancement of the evanescent fields by SPR is less compared to the enhancement in the case of thicker metal layer. However, if the thickness of the metal layer is too large, the coupling between the core mode and surface plasmon mode does not occur. Hence, the power confinement and sensitivity at the cladding/metal interface is inhibited. From Fig. 6.36, a redshift of about 25-30 nm is observed in each cladding index when the metal thickness is increased by 10 nm. The sensitivity of the NWs can be obtained from the slope in 6.36 which is presented in 6.3.

Table 6.3: Sensitivity of the gold-coated ormocomp NW with non-vertical sidewalls for quasi-TM and quasi-TE modes.

Metal thickness (nm)	Sensitivity (nm/RIU)
50	1250.00
60	1406.25
70	1562.50

As the thickness of the gold layer increase from 50 nm to 70 nm, the sensitivity also increases due to a larger volume of the SPR at the sensing region.

6.4 Summary

Numerical analyses of the un-coated and gold-coated ormocomp NWs have been presented in this chapter. The modal fields and the power confinement in the cladding region (sensitive area) for both quasi-TM and quasi-TE modes are studied in order to optimize the dimensions of the NW structure for the un-coated ormocomp NWs. Smaller NWs have higher sensitivity compared to a large waveguide due to the extension of the optical field in their cladding area. However, due to instrument limitations in the fabrication process, a non-vertical sidewall NW, with a top-width of w_{top}= 1.0 µm and a height of H= 0.5 µm, is the smallest possible NW that was possible for this work. The sensitivity of the non-vertical sidewall NWs is less than that of the vertical sidewall structure. However, the fabrication of vertical sidewall for wavelength-scale structures has proven to be a very challenging task. The closest structures to the perfectly vertical structures were trapezoidal-shaped structures with base angle of 65°.

In order to improve the sensitivity of the NWs by enhancing the light interaction in the sensing area, a thin gold layer is deposited on the surface of the waveguide to introduce the SPR. The SPR occurs when the momentum of the photons in the incident light matches with the momentum of the electron oscillation. The effect of SPR on ormocomp waveguides have been studied both theoretically and experimentally. These experimental results are discussed in Chapter 7.

The full-vectorial **H**-field FEM is used to study theoretically the existing guided modes, their distribution and their normalized power confinement in the NWs with vertical resolution of 0.8 nm in the sensing region. The modes presented here are the supermodes formed due to the coupling between the dielectric mode in the core and the plasmonic supermode at the dielectric/metal interface. For the gold-coated NWs, the two plasmonic modes at the ormocomp/gold and cladding/gold interfaces are coupled and form a symmetric or an antisymmetric mode (even or odd mode). In this work, the odd-like plasmonic supermode is considered.

With the gold layer on the top surface of the NW, the SPR is introduced at the interface where the evanescent field exists and the power confinement is increased by a factor of ten, at a specific wavelength called the resonance wavelength, allowing a larger amount of light interaction with the analyte materials. From the different cladding materials examined, it has been observed that those with higher cladding refractive index exhibit higher resonance. Also, the normalized power confinement in the sensing region, at the cladding/gold interface, is enhanced when the cladding index is increased.

The resonance peak also depends on the thickness of the metal layer. For the vertical sidewall structure, the minimum thickness of the gold layer was calculated to be 80 nm in order to have a dominant plasmonic mode at the SPR wavelength. For metal thickness less than 80 nm, the plasmonic mode is not dominant. Hence, a 100 nm thick gold layer is coated both at the top and at the sides of the 10x10 µm waveguide and the SPR is introduced for both the quasi-TE and TM polarisations. There are two resonance peaks observed because there are two different plasmonic modes coupled with the dielectric modes. Both the TM and TE modes have almost identical resonance wavelength for each cladding material. Hence, a polarizer is not required and polarisation-independent waveguides are obtained. Consequently, a simple and compact integrated SPR sensor can be achieved.

On the other hand, the gold layer with the thickness of 50 nm is considered to be coated only at the top of the wavelength-scale waveguide. With a thicker metal layer, the odd-mode has a redshift. A redshift of about 25-30 nm is observed when the metal thickness is increased by 10 nm for the wavelength-scale waveguide. The sensitivity of the NWs can reach up to 1406.25 nm/RIU.

7. Experimental characterisation of ormocomp nanowire waveguides

7.1 Introduction

The experimental effort of this research work was devoted to the characterisation of the ormocomp nanowire waveguides (NWs). This chapter consists of three main parts which are (i) the optical imaging process, (ii) the extraction of the attenuation coefficient of both un-coated and gold-coated waveguides, and (ii) the analysis of surface plasmon resonance wavelength and its shift for gold-coated waveguides including the polarisation-independent and TM mode waveguide structures. The NWs used in the characterisations are the ormocomp waveguides fabricated using the nanoimprint method as described in Chapter 4.

First, the focus of the experiments is to obtain an image of the optical field at the output of the waveguides representing the guided signal. The optical images are then processed to obtain the intensity, which is later used to extract the attenuation coefficient for the un-coated NWs (α_{nw}). The operating wavelength used in the experiments for the un-coated NWs is 633 nm, which is, in fact, a red light source. Three cladding mediums used in the experiments are air (n = 1.000), water (n = 1.333) and glycerol solution (n = 1.365). The scattering caused by the surface roughness affects the attenuation coefficient of the un-coated ormocomp NWs.

In the experimental characterisation of the gold-coated NWs, the optical setup used is similar to the one used for the un-coated NWs. However, for surface plasmon resonance (SPR) analysis a beam splitter and a spectrometer are required. The attenuation coefficient of the gold-coated NWs and the feed waveguides are extracted. The SPR peak and its wavelength shift, with the change of the refractive index of the cladding materials, are analyzed. The cladding materials of interest in the SPR experiments are (i) water (n=1.333), (ii) iso-

propanol solutions with volume ratios in a way that the refractive indices are 1.351 and (iii) 1.365. The attenuation coefficient of the gold-coated NW is mainly affected by the SPR.

7.2 Optical imaging

As it was described in Chapter 4, the integrated ormocomp NWs were fabricated on a glass substrate and designed to be connected to a feed waveguide via a tapered waveguide as shown in Fig. 7.1. The light is coupled into the NW from the feed waveguide and the output light is detected through the tapered waveguides.

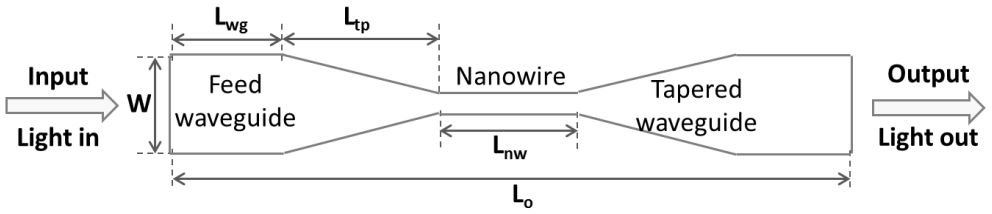

Figure 7.1: Schematic of ormocomp NW attached to tapered waveguides and feed waveguides, used in the experimental characterisation.

A set of NWs including two reference waveguides and four with different length of NWs are fabricated to extract the attenuation coefficient of the feed waveguide (α_{wg}), the attenuation coefficient of the tapered waveguide (α_{tp}) and the attenuation coefficient of NW (α_{nw}), individually. Fig. 7.1 (not drawn to scale) shows the total length of the integrated NW device (L_o) is 5 mm. The taper length (L_{tp}) is 260 µm and the four NWs have a length (L_{nw}) of 250, 500, 1000 and 2000 µm, respectively. The width of the feed waveguide (W) is 10 µm whereas the width of the NW (W_{nm}) is 1 µm. There are eight sets of the NWs on one glass substrate as shown in Fig. 7.2.

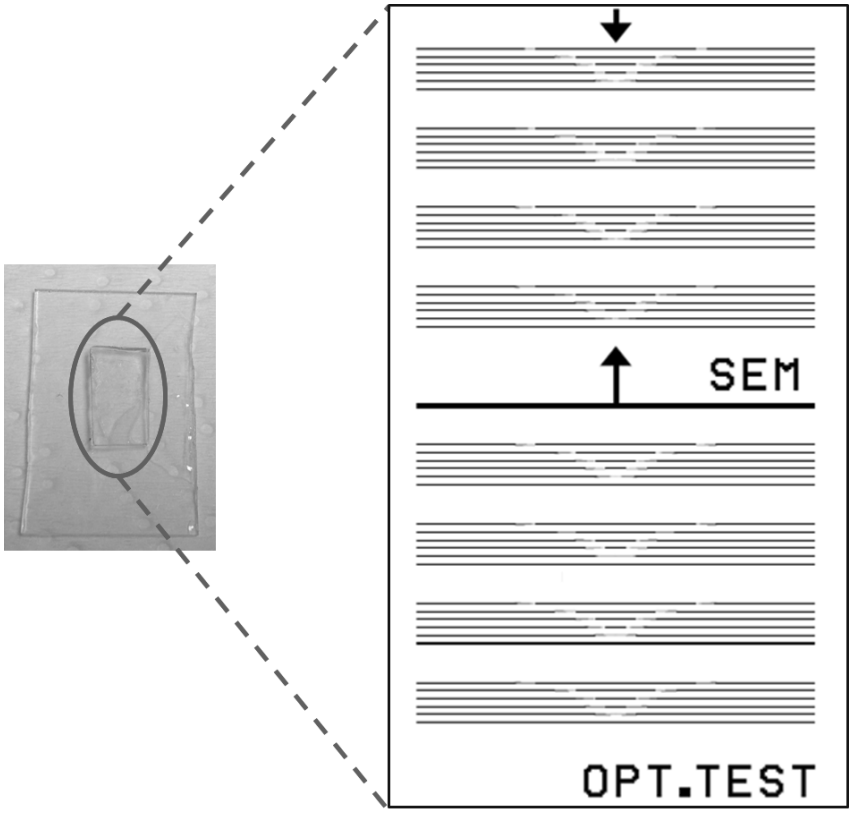

Figure 7.2: Pattern of the NWs on a glass substrate. There are eight sets of the NWs on one glass substrate. Each set contains two reference waveguides and four of different lengths NWs.

Fig. 7.2 reveals that there is a 100 µm wide waveguide included in the middle of the substrate. This wide waveguide plays an important role in the alignment process as is described later.

The first experiment was carried out to image the optical fields of the output signals. An optical setup is needed for the optical imaging process. It mainly consists of a light source, a multimode optical fibre, a sample stand, an xyz-stage, objective lens with various magnifications and CCD cameras. The optical setup schematic utilized to image the optical signal and characterize the optical properties of the ormocomp NWs is shown in Fig. 7.3.

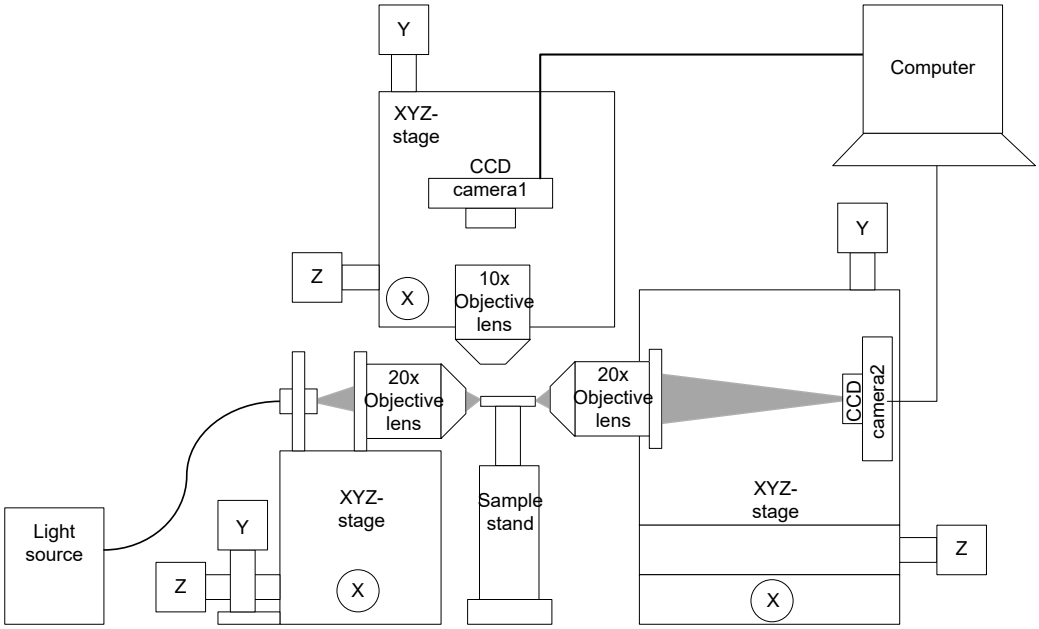

Figure 7.3: Schematic of the optical setup to image the output signal. It mainly consists of a red light source, objective lens and CCD cameras.

From Fig. 7.3, the red LED (λ=633 nm) is connected to a multimode optical fibre and is used as a light source. An objective lens with a magnification of 20x is used to focus the light and also to enhance the input signal. For the alignment process, an objective lens with a magnification of 10x connected to a CCD camera is used to align the optical fibre and the specific ormocomp NW on a glass substrate. Following the alignment, the focused light is coupled into the specific NW and then propagates along the wire. The output signal is detected by another CCD camera connected to a 20x objective lens which is used to magnify the output image. The actual setup is shown in Fig. 7.4.

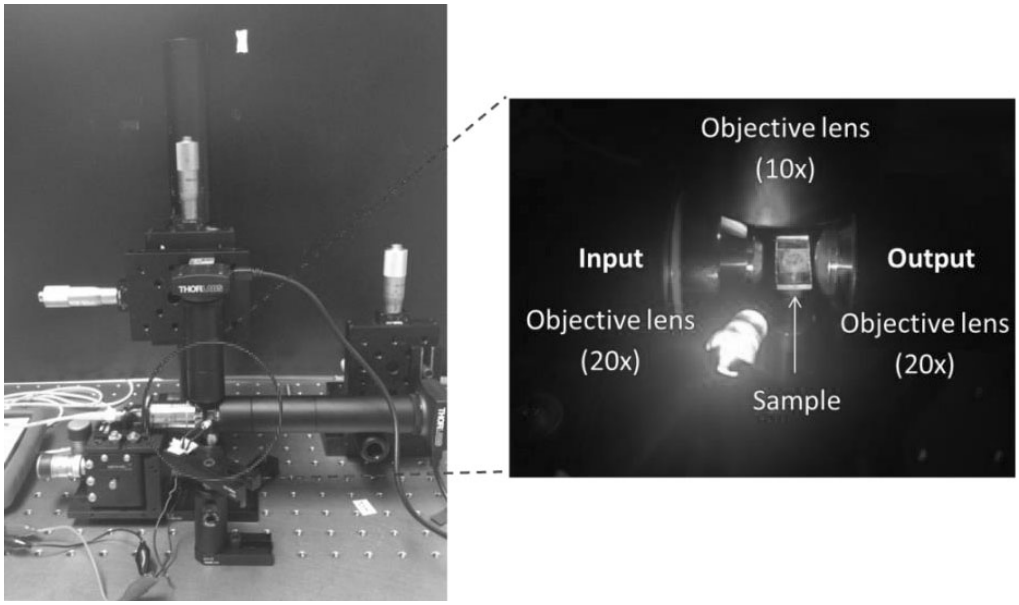

Figure 7.4: Actual optical setup used to characterize the attenuation coefficient of the un-coated ormocomp NWs.

During the experiments, all the processes involved took place in a dark room in order to reduce noise caused by the ambient light. In the dark room, the alignment process is critical. Therefore, an additional LED is added separately as a light source only for the alignment. The alignment setup consists of xyz-stage and CCD camera connected with a 10x objective lens which is placed above the NWs sample. The image obtained for the alignment setup is shown in Fig. 7.5. It is focused by adjusting the x-stage.

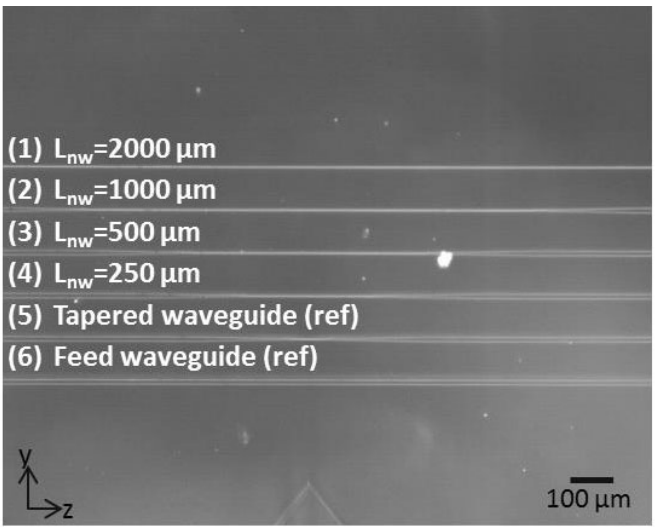

Figure 7.5: Pattern of NWs imaged by the CCD camera connected with a 10x objective lens in the alignment process.

Fig. 7.5 shows the top view of a set of the NWs which includes two reference waveguides (no.(5) and (6)) and four NWs with different lengths (L_{nw}=250, 500, 1000 and 2000 µm). In order to couple the light into a single NW, the CCD camera connected with the 10x objective lens is moved by the z-stage to the edge of the glass substrate as shown in Fig. 7.6.

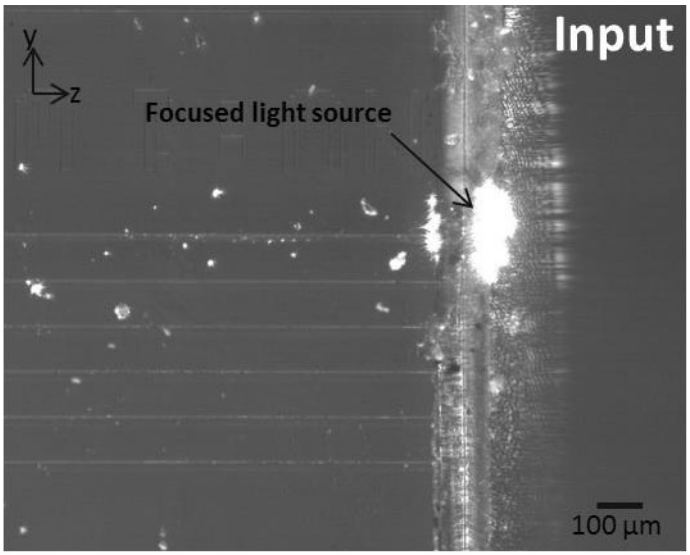

Figure 7.6: Image of alignment process in order to couple the light into a specific NW. The CCD camera is moved to the edge of the NW where the light source is focused and aligned into NW.

In the alignment process, the red light source is placed on an xyz-stage. It is focused into a specific NW by a 20x objective lens which can be observed from the bright spot in Fig. 7.6 which indicates the position of the light source aligned to the first NW that has a length of L_{nw}=2000 µm. The size of the focused light or the bright spot can be adjusted by moving the z-stage. In addition, the NW has a small height of H= 0.5 µm which makes alignment in the y-direction very challenging. Besides that, the optical output signal can be very weak due to the optical losses in the cladding and substrate.

At the other end of the NWs, another CCD camera connected with the 20x objective lens is placed to detect the output signal. The image of the NWs at the other end captured by the CCD camera is shown in Fig. 7.7

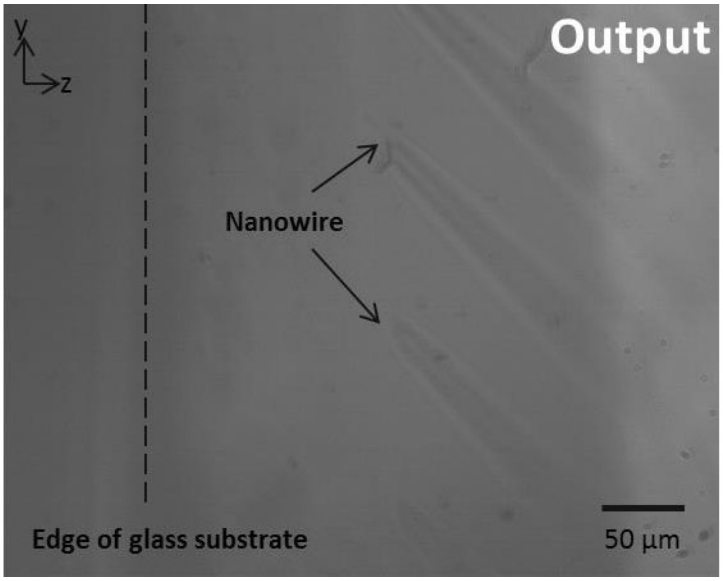

Figure 7.7: Image of the NWs at the other end by the CCD camera connected with a 20x objective lens. The optical output cannot be observed from this image.

From Fig. 7.7, another end of the NWs can be clearly seen by the CCD camera. However, it is reasonably difficult to observe the optical output signal. This is because the glass substrate is bigger than the length of the integrated NWs and the relative height of the NW (H=0.5 µm) are very small compared to the space between the NW end and the glass edge which is about 150 µm. These lead to the optical loss at the output. Hence, it is hard to observe a weak signal output from the NWs by CCD camera.

In order to observe the optical output signal, the test is performed again on the wider waveguide. Therefore, instead of coupling the light into the small NW, the light source is coupled into a 100 µm wide waveguide as shown in Fig. 7.8. The 100 µm wide waveguide is a thick line located in the middle of the substrate in Fig. 7.2. The light source is moved to the 100 µm wide waveguide by adjusting the x-stage and focused and aligned into the waveguide by tuning the z-stage and y-stage, respectively. In order to obtain the maximum output signal, the xyz-stage has to be carefully adjusted.

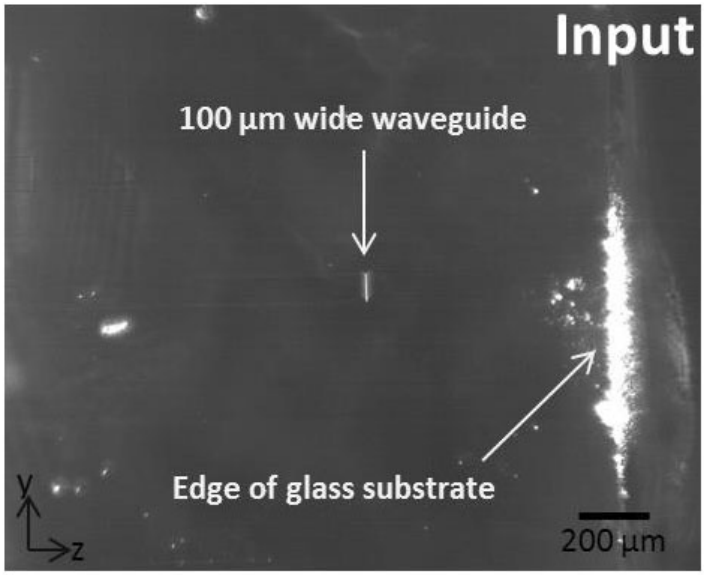

Figure 7.8: Image of the light coupled into 100 µm wide waveguide by CCD camera connected with the 10x objective lens in the alignment process.

Due to the wider structure of the waveguide compared to the NWs, the optical output signal can be observed at the other side of the waveguide by a CCD camera connected with a 20x objective lens as shown in Fig. 7.9(b). The image of the waveguide at the output before coupling the light is also shown in Fig. 7.9(a) in order to be able to distinguish the output signal.

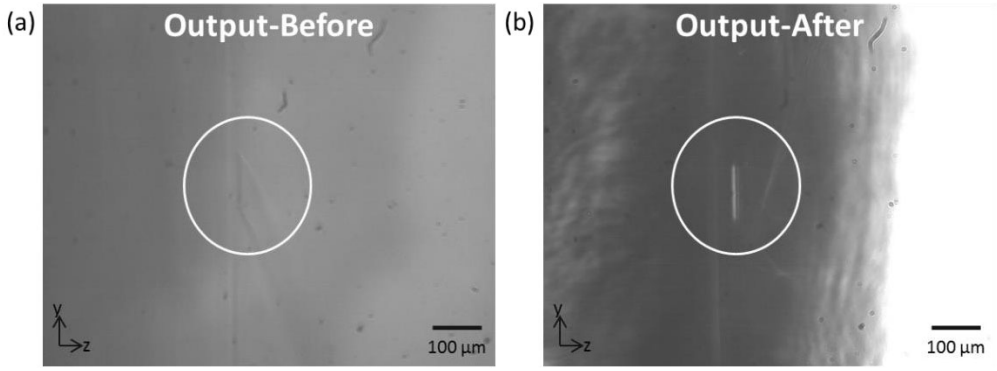

Figure 7.9: Image at the output of a 100 µm wide waveguide (a) before coupling the light and (b) after coupling the light at the input of the NW.

After getting the signal from the 100 µm wide waveguide, we are assured that the light can be coupled in and out the NWs, but the output signals are too weak to be detected by the current setup. Therefore, the 20x objective lens is replaced with the 40x objective lens in order to magnify the output signal before detecting with the CCD cameral. With the use of the 40x objective lens, the optical output

signal from the NW is successfully observed by the CCD camera as shown in Fig. 7.10.

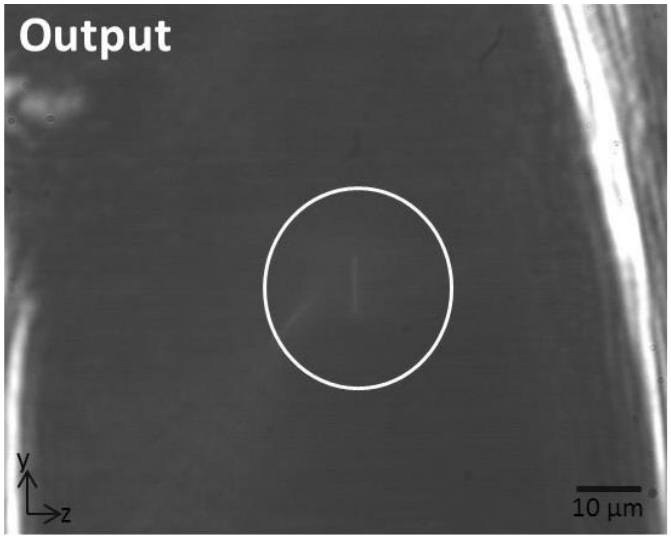

Figure 7.10: Image of the output signal from the NW detected by the CCD camera connected with the 40x objective lens.

However, the output signal is still weak due to the optical loss at the output. As mentioned earlier, the glass substrate is bigger than the whole length of the integrated NWs (L_o= 5 mm) leading to the optical loss at the output. To reduce the optical loss at the output, the NWs have to be fabricated again on a smaller glass substrate in order to have the length of the NWs to match the length of the underneath substrate. Consequently, both ends of the integrated NWs are located at the edge of the glass substrate. A 4 mm wide glass substrate is used for the new fabrication instead of 5 mm, which is used earlier.

The detection of optical field at the output of the newly fabricated ormocomp NWs became relatively easier because an optical loss at the output due to the size mismatch between the NW and the substrate is minimized. An image of the optical output signal from the NW fabricated on a 4 mm wide glass substrate is shown in Fig. 7.11.

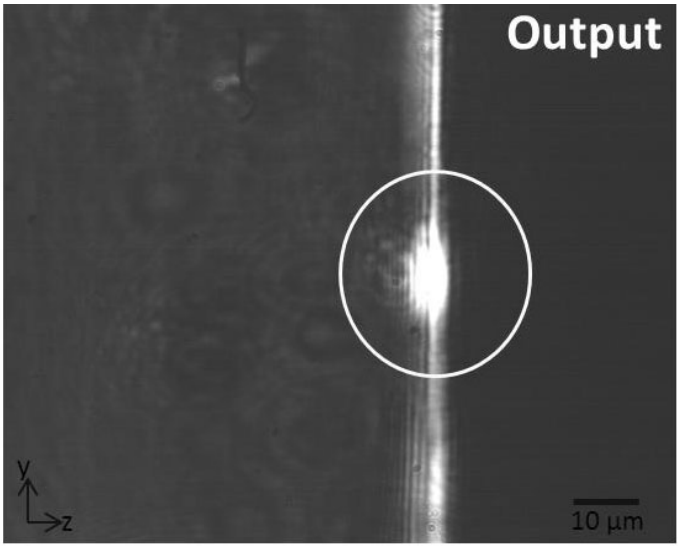

Figure 7.11: Image of the output signal obtained from the newly fabricated NWs on a smaller glass substrate. The signal is detected exactly at the edge of the substrate.

Using the newly fabricated NWs, the output signal can be detected exactly at the edge of the glass substrate. It is clearly seen that the output signal from the newly fabricated waveguide is much stronger than the previous one. The output signal obtained from the CCD camera is computed numerically to quantify the optical intensity.

An iris diaphragm is placed in front of the CCD camera to allow only the output signal from the NW to be detected by CCD camera. The optical output detected by the CCD camera after passing through the iris is shown in Fig. 7.12(a). The image of the optical field output is then computed by an in-house code to obtain the output intensity. In order to obtain the average output intensity from the CCD camera image, the highest intensity point in the image needs to be located first. After that, the points where the intensity is more than 70% of the maximum intensity have to be located. The high-intensity points are now located randomly. Therefore, the centre of high-intensity points is marked and enclosed by a square boundary. The average intensity is finally calculated from the intensity profile located inside the boundary. The average intensity of one NW is presented in Fig. 7.12(b).

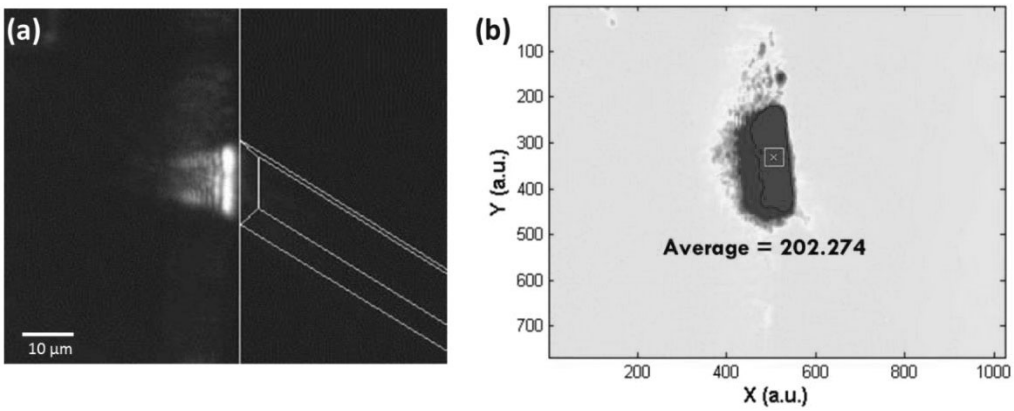

Figure 7.12: Image of the optical field detected by the CCD camera at the output of (a) one specific NW. (b) Average intensity image of the output signal computed by the in-house code.

It can be observed that the guided optical field image obtained from the CCD camera, as shown in Fig. 7.12(b), matches the optical field image from the simulation shown in Chapter 6, where the field is more confined in the slab layer. In the simulation, it is shown that part of the field extends into the cladding region. However, the percentage of the normalized power confinement in the cladding region is very small and cannot be observed in the experiment using the camera images.

To study the polarisation-independent SPR, ridge waveguides with vertical sidewalls are fabricated with 10x10 µm dimensions. With this structure, the light source can be easily aligned and selectively guided inside the waveguide as shown in Fig. 7.13.

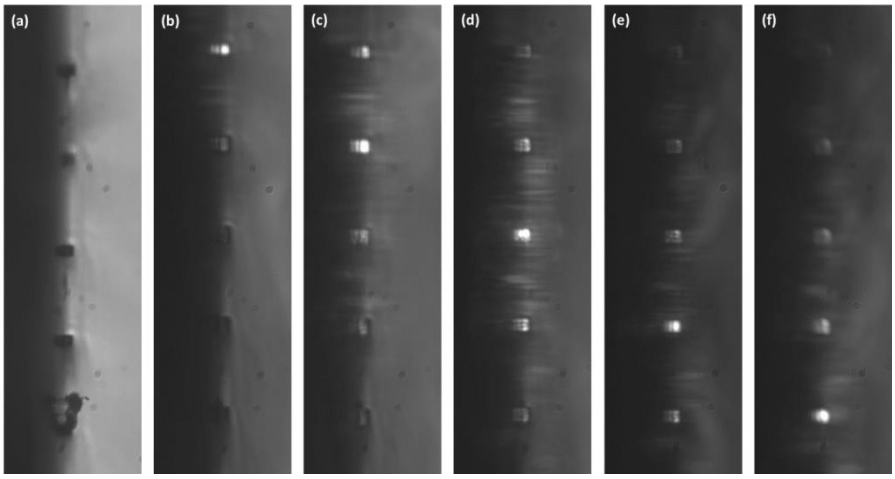

Figure 7.13: (a) Image of the end of the waveguide. (b) to (f) Images of the light coupling in each waveguide showing that the light can be selectively guided into a specific waveguide.

Fig. 7.13(a) shows the image of the end of the waveguide array. It is seen from Figs. 19(b) to 7.13(f) that the light can be selectively guided into a specific waveguide. It can also be noted that the confinement of light in each deep structure waveguide is well inside the core area, unlike the shallow structure in a previous work where the light is confined in the rib layer. At the output, the light is observed to be confined more in the wide waveguide compared to the NW structure as shown in Fig. 7.14 for a rib waveguide.

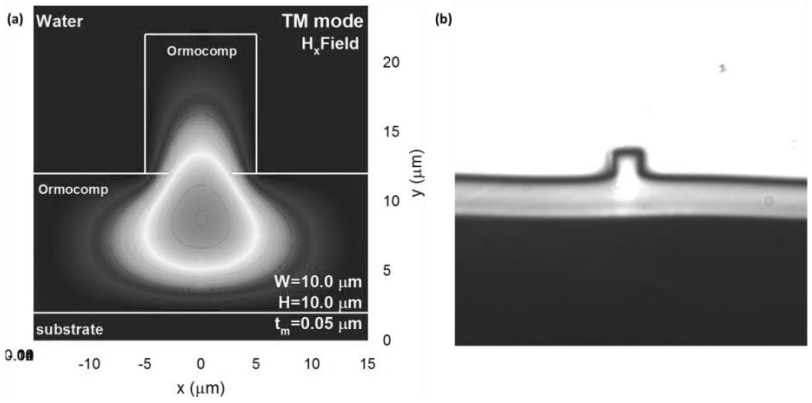

Figure 7.14: Modal field profiles excited in the feed waveguide with W_{wg} = 10 µm and H = 10 µm from (a) simulation and (b) experiment.

Due to a large structure of the waveguide compared to the NW, Fig. 7.14, shows that the optical field can be guided inside the core of the feed waveguide. The numerical simulations and experimental measurements are consistent with the light confined in both core and rib layer

7.3 Extraction of attenuation coefficient

After obtaining the output intensity from the NW, the attenuation coefficient can be calculated using Beer-Lambert law [219]:

$$I = I_o e^{-2\alpha L} \tag{7.1}$$

where I is the intensity of the transmitted light, I_o is the intensity of the incident light, α is the attenuation coefficient and L is the path length. However, since the proposed NW structure is also enhanced by the feed and tapered waveguides, their attenuation coefficients (α_{wg} and α_{tp}) are also presented together with the attenuation coefficient of the NW (α_{nw}). With the presence of the feed and tapered waveguides, Equation (7.1) can be extended to the following equations:

$$I_j = I_o e^{-2\alpha_{wg} L_{wg}^j} . e^{-2\alpha_{tp} 2L_{tp}} . e^{-2\alpha_{nw} L_{nw}^j} \tag{7.2}$$

$$\frac{I_j}{I_o} = e^{-2\alpha_{wg}(L_o - 2L_{tp} - L_{nw}^j)} . e^{-4\alpha_{tp} L_{tp}} . e^{-2\alpha_{nw} L_{nw}^j} \tag{7.3}$$

$$ln\left(\frac{I_j}{I_o}\right) = -2\alpha_{wg}(L_o - 2L_{tp} - L_{nw}^j) - 4\alpha_{tp} L_{tp} - 2\alpha_{nw} L_{nw}^j \tag{7.4}$$

where L_{wg}^j is the length of the waveguide. It equals to $L_o - 2L_{tp} - L_{nw}^j$, where L_{tp} is the taper length which is 260 µm and L_{nw}^j is the length of the NWs which are 250, 500, 1000 and 2000 µm. L_o is the total length of the integrated NWs which is 5000 µm.

By rearranging Equation (7.4), a linear equation can be obtained as shown below:

$$ln\left(\frac{I_j}{I_o}\right) = 2(\alpha_{wg} - \alpha_{nw}) L_{nw}^j - \left[2\alpha_{wg}(L_o - 2L_{tp}) + 4\alpha_{tp} L_{tp}\right] \tag{7.5}$$

The intensity of incident light (I_o), in this work is the intensity of the light transmitted from the reference feed waveguide. The intensity of transmitted light (I_j) represents the intensity of the light transmitted from each NW. The term

$\left[2\alpha_{wg}\left(L_o - 2L_{tp}\right) + 4\alpha_{tp}L_{tp}\right]$ is a constant term and the term $2\left(\alpha_{wg} - \alpha_{nw}\right)$ = $\Delta\alpha$ is the slope of the linear equation. The ratio of light transmitted inside the non-vertical sidewalls NW over the feed waveguide with air-cladding can be fitted into a linear plot as demonstrated in Fig. 7.15.

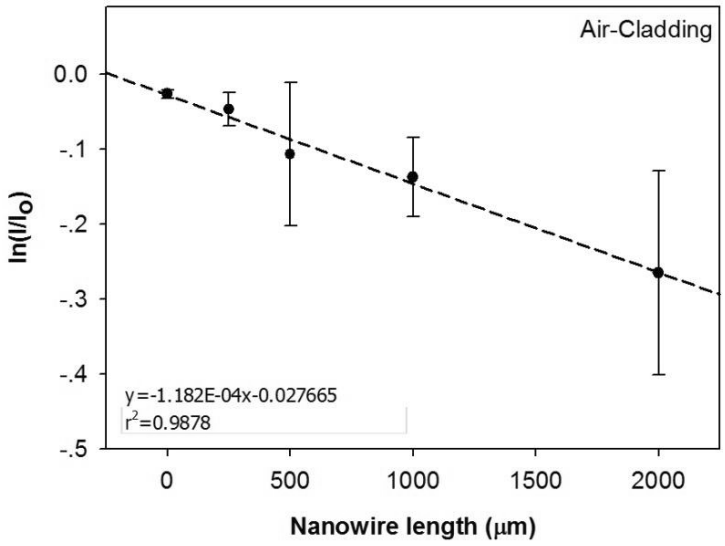

Figure 7.15: The linear relation between $ln(I_j/I_o)$ and the length of the NW ($L_{nw,j}$) obtained experimentally, where the slope is $\Delta\alpha$ for air cladding.

The relation of the attenuation coefficient between the air-cladding feed waveguide and NW, obtained from the slope of the line, can be calculated to be $2\left(\alpha_{wg} - \alpha_{nw}\right) = \Delta\alpha = -1.1824\ cm^{-1}$, where the negative sign represents a greater attenuation coefficient in the NW than the feed waveguide. This is due to the higher losses occurring in the NW for a larger field of a structure with smaller size. In the experiment, water (n=1.333) and glycerol solution (the mixture of water and glycerol with the volume ratio of 4:1, n=1.365) are also considered as cladding mediums. For water cladding, the calculated $\Delta\alpha$ is about $-1.063\ cm^{-1}$ whereas $\Delta\alpha = -1.023\ cm^{-1}$ is obtained for glycerol solution cladding as shown in Figs. 7.16 (a) and (b), respectively.

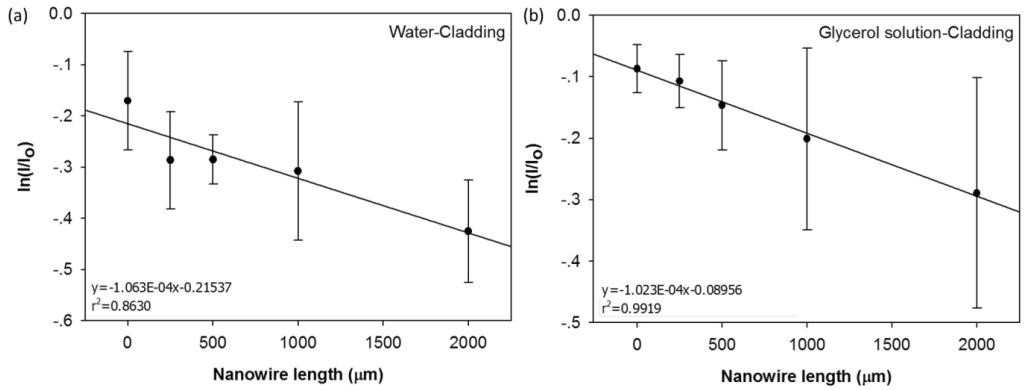

Figure 7.16: The linear relation between $ln(I_j/I_o)$ and length of the NW ($L_{nw,j}$) where the slope is $\Delta\alpha$ for (a) water cladding and (b) glycerol solution cladding.

It can be noted that $\Delta\alpha$ is reduced when the refractive index of the cladding material is increased as the index contrast is reduced. The large error bars in Figs. 7.15 and 7.16 are because the tests were carried out with different samples which might have a variation of surface roughness. The change in $\Delta\alpha$ over the different cladding materials obtained from the experiment is shown in the Fig. 7.17.

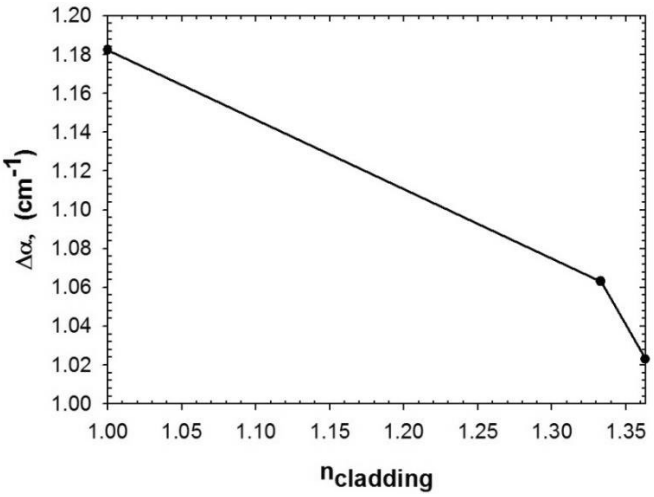

Figure 7.17: Change of attenuation coefficient difference ($\Delta\alpha$) with the cladding material including air, water and glycerol solution.

Fig. 7.17 shows the slope from Figs. 7.15 and 7.16. The power confinement in the guiding region decreases with the increase of the refractive index of the cladding material (smaller $\Delta\alpha$). Hence, the attenuation coefficient is increased if the NW with a relatively smooth surface is considered. However, the fabricated NW does not have a smooth surface. The surface roughness arises from the fabrication process used here and this causes scattering loss [220]. The increase

of the cladding index reduces the difference of the refractive index between the core and the cladding ($\Delta\alpha$). Hence, the scattering due to the surface roughness is reduced, leading to a smaller attenuation coefficient. In this work, only the scattering from the interface between the core and the cladding is considered. The scattering effect from the core/substrate interface is assumed to be negligible due to the smooth surface of thr glass substrate. The relation between scattering from surface roughness and the attenuation coefficient (α) derived from the simple theory of surface scattering [220] is defined as follows:

$$\alpha = \frac{2\sigma_{12}^2\kappa^3}{\beta n_1^2(h + (1/\gamma_0) + (1/\gamma_2))} \tag{7.6}$$

where σ is the root-mean-squares of the surface roughness, κ is the transverse propagation constant in the core region ($\kappa = \sqrt{k_o^2 n^2 - \beta^2}$), γ is the transverse propagation in the cladding region ($\gamma = \sqrt{\beta^2 - k_o^2 n^2}$), β is the modal propagation constant and *h* is the thickness of the NW. The derivation of the attenuation coefficient from the surface scattering in the Equation (7.6) is given in Appendix C. The average surface roughness of ormocomp NWs measured from AFM is found to be around 0.10 µm. The attenuation coefficient (α) due to the scattering effect with different cladding materials is calculated as shown in Fig. 7.18.

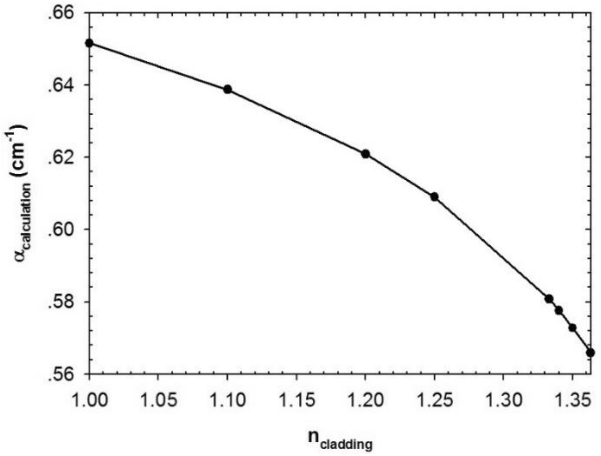

Figure 7.18: Results from the calculation of the attenuation coefficient of the NW over the cladding material with the effect of scattering from the surface roughness.

It can be observed from Fig. 7.18 that the variation of the attenuation coefficient obtained from the calculation with the refractive index of the cladding material has a similar trend with the experimental measurements in Fig. 7.17. The attenuation coefficient decreases as the refractive index of the cladding material increases. This is due to the scattering effect from the surface roughness.

To study the sensitivity of the NWs affected by the scattering from surface roughness, the change of the attenuation coefficient over the change of the refractive index of the cladding material is calculated. The attenuation coefficient difference when changing the cladding material from water (n=1.333) to glycerol solution (n=1.365) is investigated over the root-mean-square roughness (R_q) as shown in Fig. 7.19.

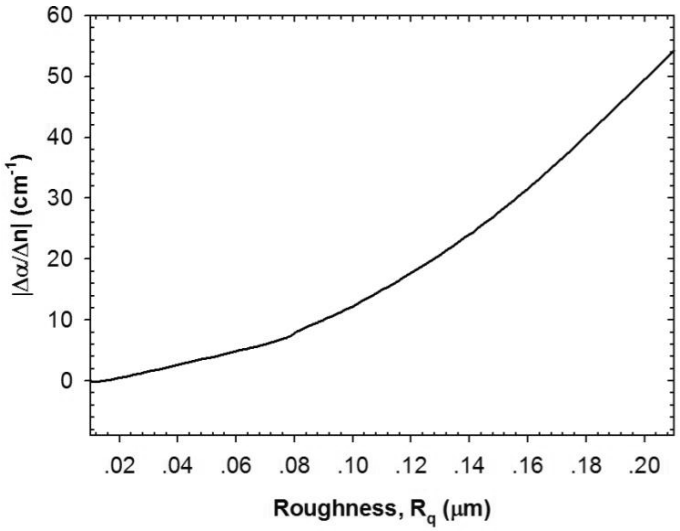

Figure 7.19: Change of attenuation coefficient over the change of cladding material with surface roughness from the numerical calculations.

With the same cladding material, the NW structure with the rough surface has higher scattering loss than a NW with a smooth surface. The scattering loss at the surface of the NW enhances the sensitivity because there is more light interaction at the interface between the core and cladding regions. Fig. 7.19 shows the normalized value of the change in the attenuation coefficient over the change in the cladding index with the surface roughness. In the experimental work, the change of the attenuation coefficient over the change of cladding refractive index is around 1.88 cm^{-1} with the root-mean-square roughness of 0.10 μm. It has a

lower sensitivity compared to the calculation which may be due to external factors such as instrument resolution and environmental control.

7.4 Analysis of the surface plasmon resonance peak and its shift

The next step is to characterize the ormocomp NWs coated with the thin gold layer. A thin gold layer introduces surface plasmon resonance (SPR) at the dielectric/electric interfaces enhancing the optical power in the sensing region. The gold-coated ormocomp NW on the glass substrate is shown in Fig. 7.20.

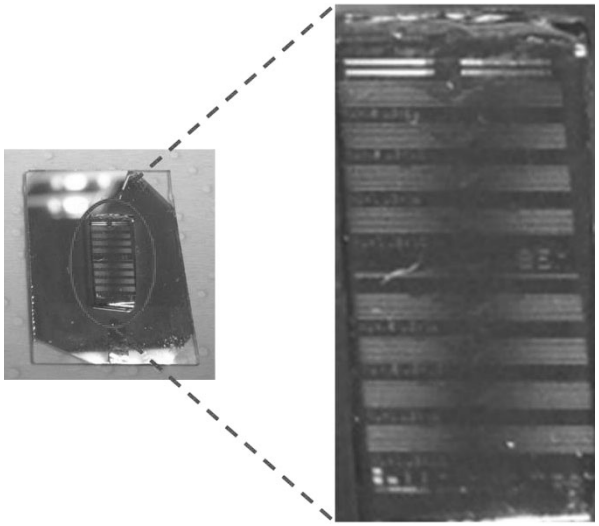

Figure 7.20: Gold-coated ormocomp NWs on a glass substrate.

In order to analyze the SPR signal, a similar optical setup to the one used in the previous study has been utilized. However, some additional optical devices are required including a polarizer, beam splitter, a positive lens and a spectrometer. The light source was also changed from the red LED to white LED in order to have the operating wavelengths over the whole visible region because the resonance occurs at different wavelengths for different cladding materials. The optical setup for the SPR analysis is shown in Fig. 7.21.

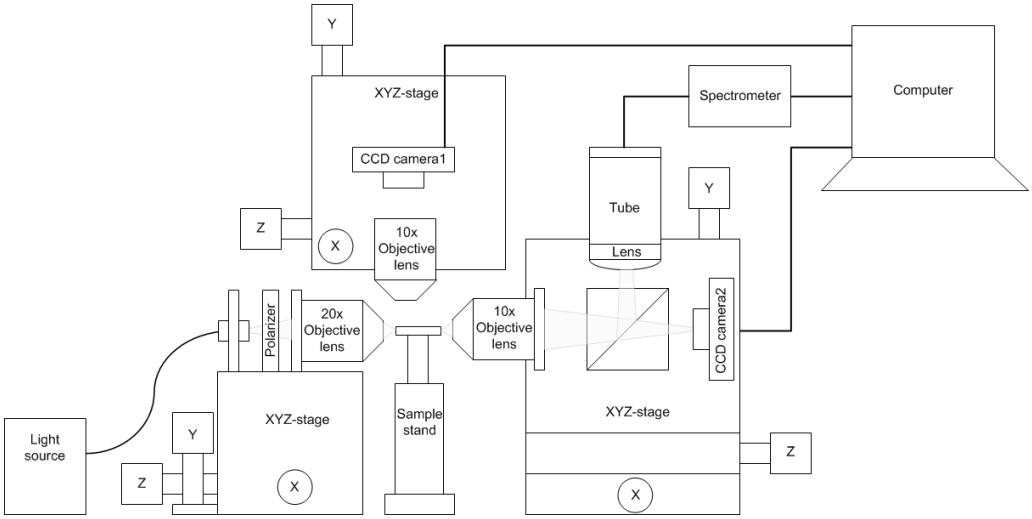

Figure 7.21: Optical setup for the study and analysis of SPR in the gold-coated NWs.

There are 2 types of waveguide structures in this SPR study including (i) the 10x10 µm ridge waveguide with vertical sidewalls and (ii) the 0.5x1.0 µm rib waveguide with non-vertical sidewalls. The waveguide with vertical sidewalls represents the polarisation-independent SPR because the plasmonic modes can occur as both TE and TM modes are almost identical which can be identified by using a polarizer. For the non-vertical sidewalls structure, only TM mode SPR at the top surface of the waveguide is detected using polarizer because the plasmonic modes are mixed between TE and TM modes at the slanted sides.

7.4.1 Ridge structure with vertical sidewalls (Polarisation-independent SPR)

The ormocomp waveguide with vertical sidewalls structure exhibits SPR at both the top and sides of the waveguide through TM and TE modes, respectively. From the simulations, the minimum thickness of the gold layer needed in order to have significant plasmonic modes is 80 nm. Hence, a 100 nm thick of gold layer is coated on the waveguide using the sputtering technique to ensure the SPR effect.

The warm white LED (λ=350-1000 nm) coupled to a multimode optical fibre is used as a broadband light source (Thorlabs: MWWHF1). The spectrum of the light source is shown in Fig. 7.22.

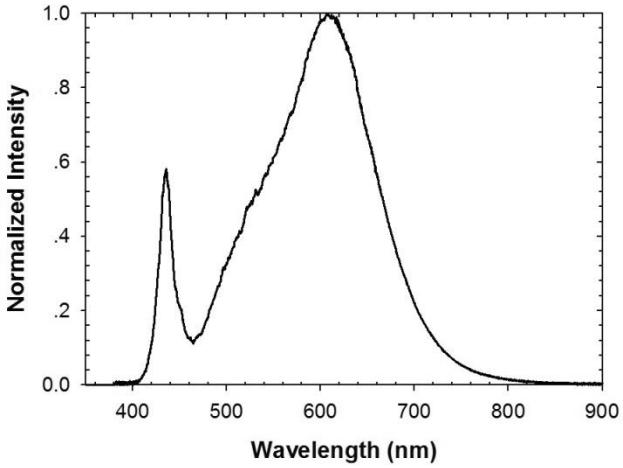

Figure 7.22: Spectrum of the warm white light source (Thorlabs: MWWHF1).

An objective lens with a magnification of 20x is used to focus the light and also to enhance the input signal. For the alignment process, an objective lens with a magnification of 10x connected to a CCD camera is used to align the optical fibre and the specific ormocomp waveguide. Following the alignment, the focused light is coupled into the specific waveguide and then allowed to propagate along it. The output signal is detected by a separate CCD camera connected to a 20x objective lens which is used to magnify the output image. The actual complete experimental setup is shown in Fig. 7.23.

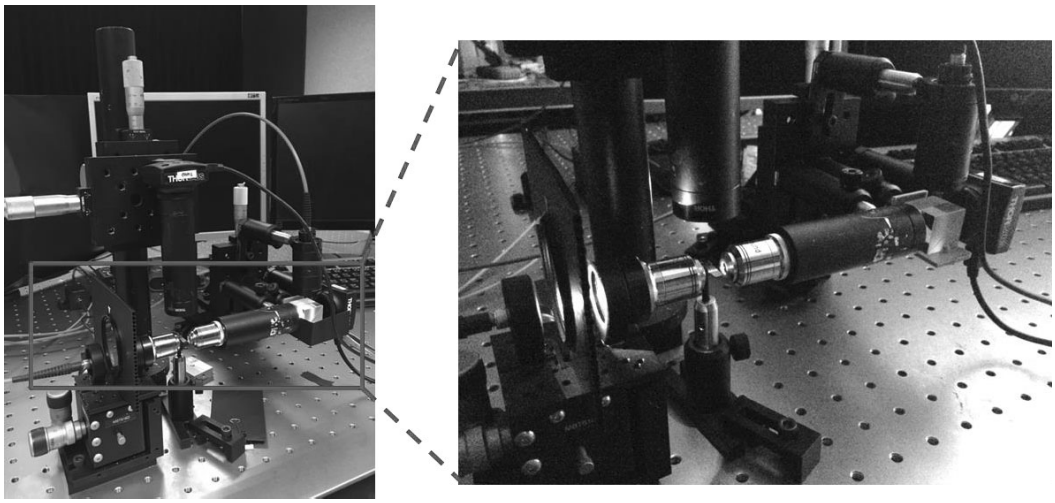

Figure 7.23: Actual optical setup for optical characterisation of the gold-coated ormocomp NWs.

At the end of the NW, the output signal is divided into two equivalent beams by a beam splitter. One signal is imaged on the CCD camera and the other part is

sent to a compact spectrometer to measure the intensity of the transmitted light affected by SPR.

The transmitted output signal is used to study the resonance peak which can occurs when the momentum of electron oscillation matches the momentum of the photons in the incident light. From Beer-Lambert law, the transmittance (T) is the fraction of light passing through the waveguide (I) over the incident light (I_o) in a specific wavelength as presented in Equation (7.7) [219].

$$T = \frac{I}{I_o} \tag{7.7}$$

The incident light (I_o) in this case is the intensity of the light propagating in the waveguide with air cladding where I is the output intensity when the light propagates along the gold-coated ormocomp waveguide with water cladding. Hence, air is considered to be the cladding material for the incident light because the SPR absorption wavelength in the air/metal interface is in the infrared (IR) region but the waveguides are operated in the invisible region. When the cladding medium changes from air to water, the intensity of light at the output is reduced at some specific wavelengths for TM mode. This is due to the absorption of SPR between metal layer and water medium. At some specific wavelength, supermodes occur due to the fact that the dielectric mode is coupled with the plasmonic mode. In addition, the plasmonic mode itself is also a supermode from the coupling between the plasmonic mode at the ormocomp/gold interface and the cladding/gold interface. There are two distinct dielectric-plasmonic supermodes that can be observed in the experiment from the dip in the transmissivity as shown in Fig. 7.24.

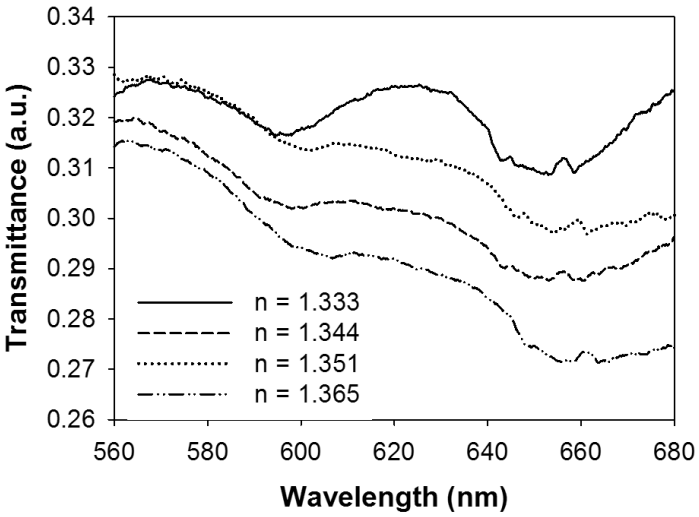

Figure 7.24: Graph of transmittance of the gold-coated waveguide with four different cladding solutions over the wavelength in the visible region. The redshift is observed as the cladding-index increases.

The transmissivity dip occurs due to the absorption of the SPR between the metal layer and the cladding medium. The gold-coated ormocomp waveguides are tested with 4 different cladding materials, which are water and three different volume ratios of iso-propanol solutions with refractive index of 1.333, 1.344, 1.351 and 1.365, to study the resonance peaks and their shifts.

The SPR is sensitive to the change of the cladding index, which can be studied by investigating the wavelength shift with different refractive indices of cladding materials. The cladding materials used in this study are water (n=1.333) and iso-propanol solutions. The solutions are prepared with different volume ratios of iso-propanol to water. With 1:1 volume ratio (ISO11), the solution has a refractive index of 1.365. The index of 1.351 and 1.344 are measured for the ratio of 1:3 (ISO13) and 1:5 (ISO15), respectively. The solutions used as cladding media with their refractive indices and mixing ratios are presented in Table 7.1.

Table 7.1: Cladding materials with their refractive indices and mixing ratios.

Solution (Cladding materials)	Mixture by volume ratio		Refractive index (n)
	Iso-propanol	Water	
Water	0	1	1.333
ISO15	1	5	1.344
ISO13	1	3	1.351
ISO11	1	1	1.365

The resonance wavelengths can be investigated for each cladding material by matching the transmittance graph with a polynomial curve as demonstrated in Fig. 7.25.

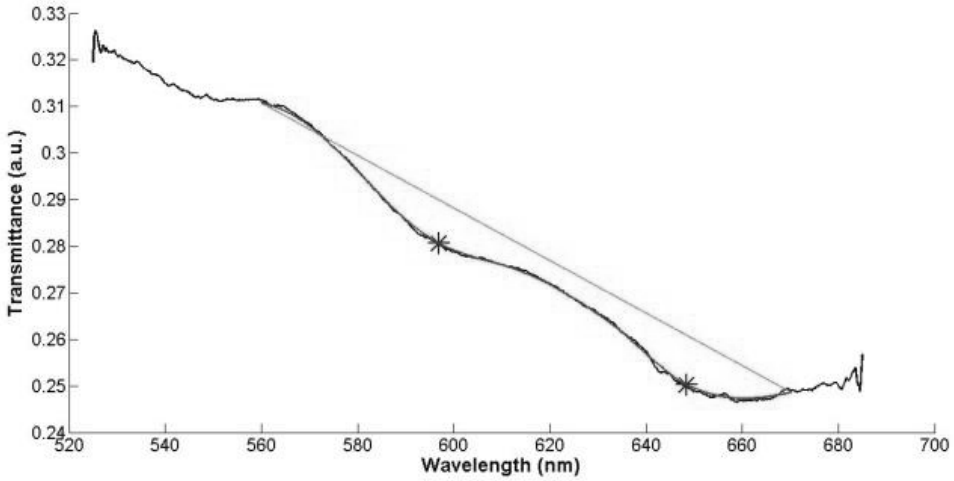

Figure 7.25: Investigation of the two resonance peaks of polarisation-independent SPR waveguide using polynomial curve fitting.

The two resonance wavelengths for both quasi-TM and quasi-TE modes of the gold-coated ormocomp waveguides in different cladding materials obtained from the experiment are presented in Table 7.2.

Table 7.2: Experimental results of the resonance peaks of the gold-coated ormocomp waveguide in different cladding materials for quasi-TM and quasi-TE modes

n	TM mode		TE mode	
	Resonance peak 1	Resonance peak 2	Resonance peak 1	Resonance peak 2
1.333	592.34 nm	649.26 nm	598.01 nm	646.81 nm
1.344	601.84 nm	654.35 nm	600.63 nm	649.93 nm
1.351	606.31 nm	656.37 nm	601.63 nm	654.13 nm
1.365	609.97 nm	660.57 nm	612.56 nm	659.66 nm

It can be observed that the resonance peaks occur for both the quasi-TM and quasi-TE modes at similar wavelengths. Hence, a polarisation-independent gold-coated ormocomp waveguide has been successfully fabricated. The resonance peaks from Table 7.2 can be plotted so that we have a comparison with the resonance peaks obtained from the numerical simulations are shown in Fig. 7.26.

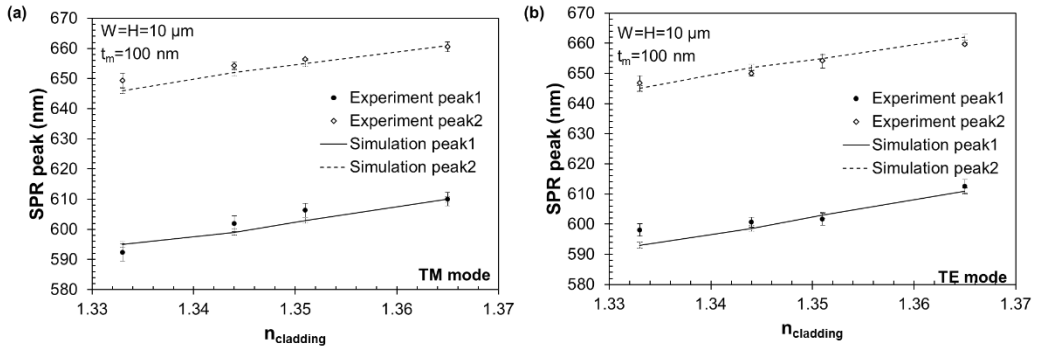

Figure 7.26: Comparison of the resonance peaks obtained from the experiment and simulations for both TM and TE modes.

It can be observed from Fig. 7.26 that the resonance peaks obtained from the experiment have a similar trend compared to the simulation results. The error bars for experimental work come from 50 individual measurements. For the simulation results, the error bars show the results of SPR wavelengths for various

metal thicknesses in the range between 80-120 nm. Gold thickness is a key parameter in order to match the simulation results with experimental results. Initially, the gold thickness was optimized using the FEM. The minimum thickness of the gold layer was calculated to be 80 nm in order to have a dominant plasmonic mode at the SPR wavelength. For metal thickness less than 80 nm, the plasmonic mode is not dominant. For metal layer thicker than 120 nm, the dynamic range of SPR peak becomes smaller which means the spectrum of SPR peak is more broadened due to the coupling between several plasmonic modes. It can be observed that the error bars from simulation and experiment are overlapped. Hence, it can be confirmed that the actual thickness of the metal layer is around 100±20 nm. There are two different resonance peaks in both the experimental and simulation results, which means there are two distinguish plasmonic supermodes which are coupled with the dielectric mode. These two resonance peaks are located about 50 nm away from each other. The quasi-TM and quasi-TE modes have similar resonance wavelengths so the polarizer in the experiment can be removed because the waveguides are polarisation independent allowing a compact integrated optical sensor with surface plasmon resonance system to be obtained. Both experimental and simulation results show a redshift when the refractive index of the cladding material is increased.

To use this gold-coated ormocomp waveguide for refractive index sensing applications, the sensitivity is calculated from the linear regression of the experimental results and it is found to be 544.55 nm/RIU with resolution 5.3x10-3 RIU. The sensitivity and resolution of the waveguide can be further improved by optimizing the dimensions of the waveguide itself and the thickness of the gold layer.

7.4.2 Rib structure with non-vertical sidewalls (TM mode SPR)

The ormocomp NWs with non-vertical sidewalls have a sidewall angle of 65°. These are coated with gold layer with a thickness of 50 nm. The plasmonic modes at the slanted sidewalls consist of SPR in both TE and TM modes. This assumption is confirmed by the experimental work as there is an insignificant effect of SPR in

TE mode at the sidewalls. The thin metal layer at the top surface introduces the coupling of SPR between the ormocomp/gold and the cladding/gold interfaces in TM mode only.

The cold white LED (λ=400-700 nm) connected with a multimode optical fibre is used as a broadband light source (Thorlabs: MCWHF1). The spectrum of the light source is shown in Fig. 7.27.

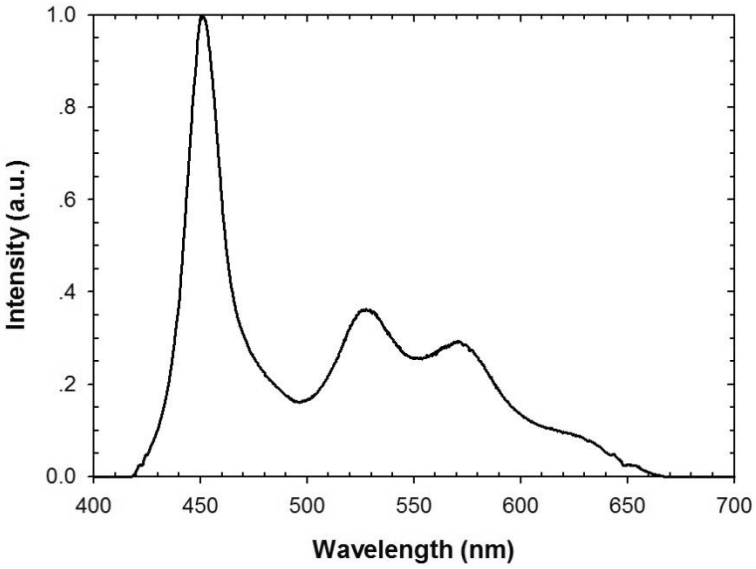

Figure 7.27: Spectrum of the cold white light source (Thorlabs: MCWHF1).

It can be seen from Fig. 7.27 that the intensity of the light source when λ>600 nm is quite low. The input light from the light source is considered to be an unpolarised light, so a polarizer is needed in the optical setup in order to be able to select the TM mode signal for the SPR from the top surface of the NW. The objective lens with the magnification of 20x is used to focus the light for the input signal. In the alignment process, an objective lens with a magnification of 10x connected to a CCD camera working as an optical microscope to align the optical fibre and the NW on the glass substrate. With the alignment, the focused light is coupled into a specific NW and then propagates along that wire. At the end of the NW, the output signal is divided into two equivalent beams by a beam splitter. One signal is imaged by the CCD camera. The other part of the output signal is detected by a spectrometer to measure the intensity of the light affected by the SPR. The actual optical setup for the SPR analysis is shown in Fig. 7.28.

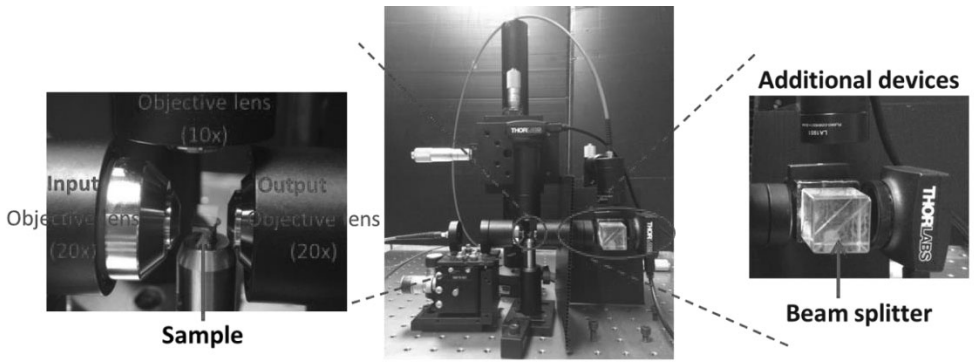

Figure 7.28: The actual optical setup used for the SPR analysis.

A spectrometer is used to measure the transmittance (T) of the light propagating along the NW. First, the transmittance of light propagating along different NWs has to be obtained. It can be achieved by measuring the light intensity of the output signal when the cladding medium is air and water, respectively.

The transmittance (T) of the output signal obtained in TM and TE modes are shown in Fig. 7.29.

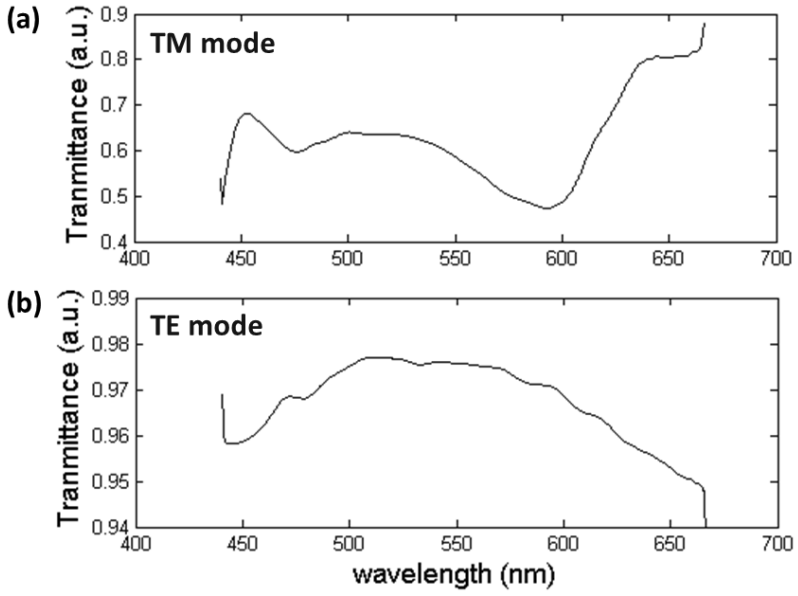

Figure 7.29: (a) Light transmittance in the TM mode. (b) Light transmittance in the TE mode.

From Fig. 7.29(a), a dip of the transmission spectrum is the region where the momentum of light source matches with the momentum of SPR in the TM mode.

The intensity of the transmittance in the TE mode is shown in Fig. 7.29(b). It can be seen that there is no significant dip in the transmitted signal. Hence, the SPR at the NW sidewalls is negligible in this case.

The transmittance in the TM mode shown in Fig. 7.29(a) demonstrates only the transmittance of one specific NW. In order to extract the attenuation coefficient of the NW (α_{nw}) individually, the transmittance of all NWs in one set has to be obtained in which the attenuation coefficient of the feed waveguide (α_{nw}) and tapered waveguide (α_{tp}) can be eliminated. The intensities of the output signals measured by the spectrometer are computed with a graphical user interface (GUI). The codes for all GUI analyses are built in-house.

The optical output intensities of four different length NWs in air cladding and water cladding are measured and then computed using the GUI to obtain their transmittances. The lengths of the NWs considered are 250, 500, 1000 and 2000 µm. The transmittance spectrum of each NW then smoothed as demonstrated in Fig. 7.30.

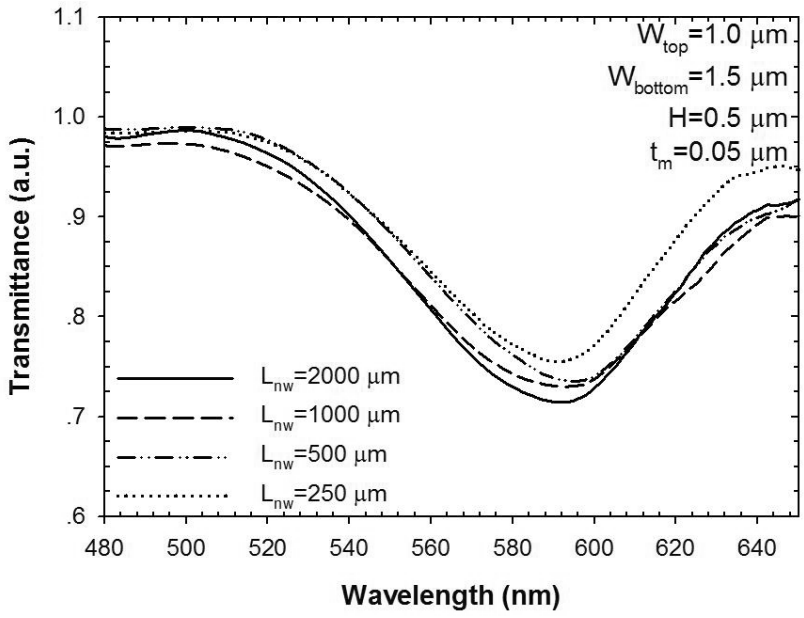

Figure 7.30: Transmittance of gold-coated NWs with lengths 250, 500, 1000, 2000 µm over the wavelength in the visible region. The transmittance decreases for longer NWs due to the SPR absorption.

It can be seen that the longest NW (L_{nw}=2000 µm) represented by the solid line, has the lowest transmittance. The dotted line represents the shortest NW

(L_{nw}=250 µm) which has the highest transmittance. It can be concluded that the longest NW has the highest SPR absorption.

From Equation (7.7), the transmittance (T) can also be written in term of the attenuation coefficient (α) as presented in Equation (7.8):

$$T = e^{-\alpha(\lambda)L} \tag{7.8}$$

where α is the attenuation coefficient which is a function of wavelength (λ). L represents the path length. As mentioned earlier, a NW has been designed to be easily used in conjunction with other optical devices so it is integrated with the feed and tapered waveguides at its ends. Therefore, the attenuation property of one integrated NW (α) is a combination of the attenuation coefficients of the feed waveguide (α_{wg}), the tapered waveguide (α_{tp}) and the NW itself (α_{nw}).

In order to extract α_{nw} individually, α_{wg} and α_{tp} have to be investigated and isolated. This can be achieved by using the transmittance result of the reference feed waveguide and tapered waveguide in the NW set. The transmittance of light propagated in the feed waveguide (T_{wg}) can be expressed by in Equation (7.9):

$$T_{wg} = e^{-\alpha_{wg}(\lambda)L_{wg}} \tag{7.9}$$

where L_{wg} is the length of the feed waveguide which is equal to the total length of the sample in this case ($L_{wg} = L_o$ =5000 µm). The attenuation coefficient α_{wg} is obtained by rearranging Equation (7.9) as presented in Equation (7.10):

$$\alpha_{wg}(\lambda) = \frac{-ln(T_1)}{L_o} \tag{7.10}$$

Similar to the feed waveguide, the transmission of light in the tapered waveguide (T_{tp}) and its attenuation coefficient (α_{tp}) can be written as shown in Equations (7.11) and (7.12), respectively:

$$T_{tp} = e^{-\alpha_{wg}(\lambda)(L_o - 2L_{tp})} . e^{-2\alpha_{tp}(\lambda)L_{tp}} \tag{7.11}$$

$$\alpha_{tp}(\lambda) = \frac{-\alpha_{wg}(\lambda)(L_o - 2L_{tp}) - ln(T_1)}{2L_{tp}} \tag{7.12}$$

Therefore, the attenuation coefficient of the NW (α_{nw}) can be calculated using Equation (7.13):

$$\alpha_{nw}(\lambda) = \frac{-\alpha_{wg}(\lambda)(L_o - 2L_{tp} - L_{nw}) - 2\alpha_{tp}(\lambda)L_{tp} - ln(T_{nw})}{L_{nw}} \tag{7.13}$$

where L_o is 5000 µm and L_{tp} is 260 µm. From the above equations, the attenuation coefficient of each part can be calculated. However, the α_{tp} seems to have some distortion. Thus, the calculation of α_{nw} is carried out by neglecting the term of α_{tp}. The attenuation coefficients of the feed waveguide and the NW from several experiments are computed as demonstrated in Fig. 7.31.

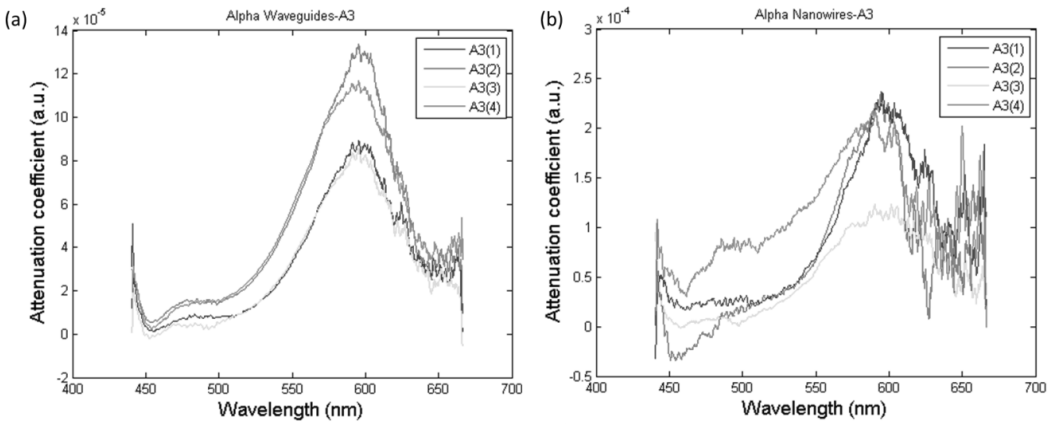

Figure 7.31: Attenuation coefficients of feed waveguides and NWs from several experiments computed.

Then the average of the attenuation coefficient is calculated and smoothened. The average attenuation coefficient of feed waveguides and gold-coated ormocomp NW is presented in Fig. 7.32.

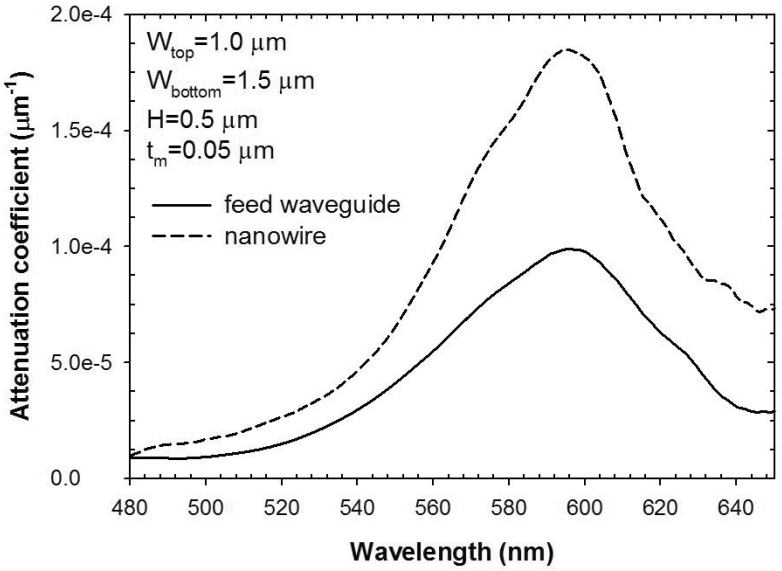

Figure 7.32: Graph of the average attenuation coefficient of the feed waveguide and gold-coated ormocomp NWs wavelength. The NWs have higher SPR absorption compared to the feed waveguide.

From Fig. 7.32, the average attenuation coefficient of the NWs is represented with the dashed line and the average attenuation coefficient of the feed waveguide is represented by the solid line. The absorption peak for both the feed waveguide and the NWs is at λ =590 nm. The feed waveguide has an absorption coefficient of $\alpha_{wg} = 1.03 \times 10^{-4}\ \mu m^{-1}$ (or 0.45 dB/mm), which is lower than the absorption coefficient of the NWs with value $\alpha_{nw} = 1.93 \times 10^{-4}\ \mu m^{-1}$ (or 0.84 dB/mm). This is because the feed waveguide is a multimode waveguide but the NW is a single mode waveguide. In the multimode waveguide, the power is distributed to many modes, causing a reduction of optical power in each mode. In addition, each mode has different SPR momentum. Therefore, the absorption peak of the SPR in each mode is located at a different wavelength, causing the broadening of the absorption peak in the feed waveguide.

The transmitted intensity of the light propagating in the NWs with different cladding materials at the output is then measured by the spectrometer. After that, the transmittance is calculated using equation (7.7) and computed with another GUI as presented in Fig. 7.33.

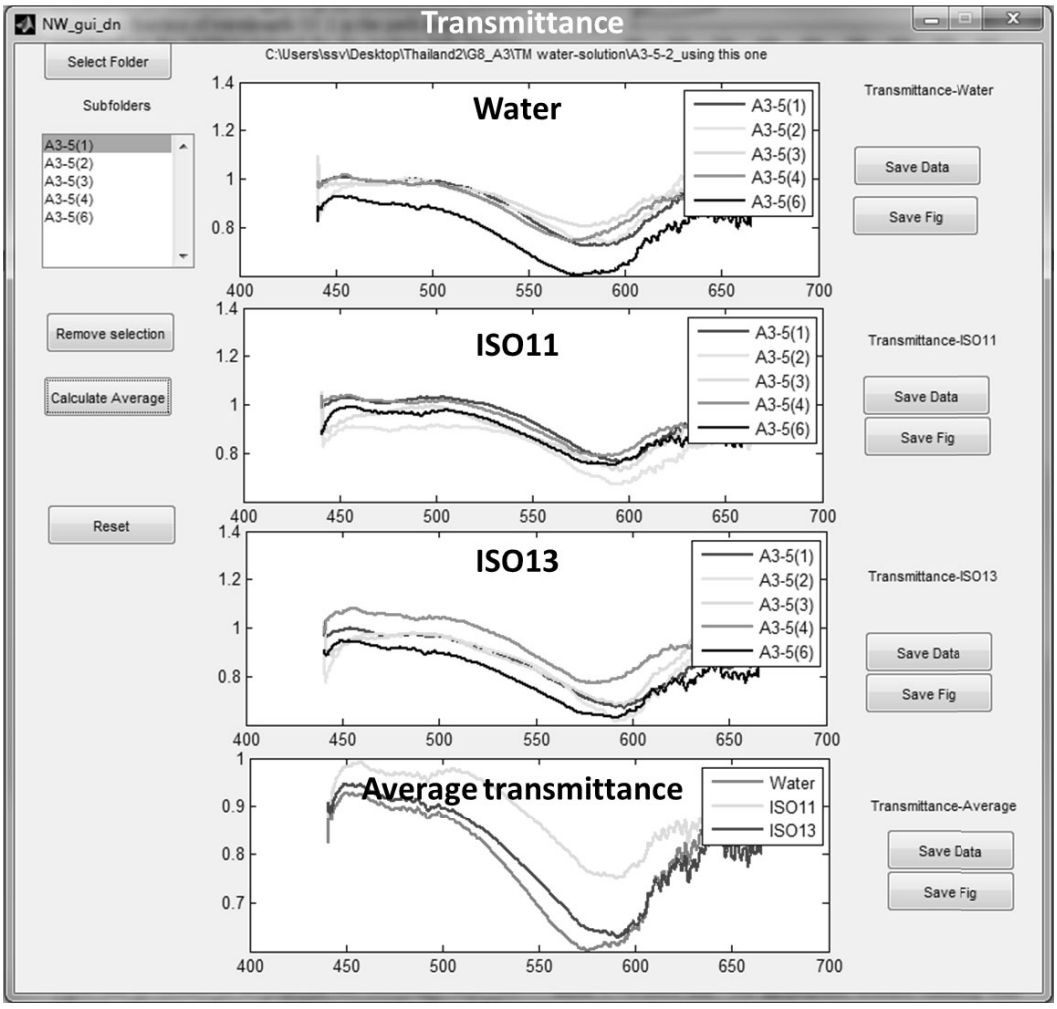

Figure 7.33: GUI for computing the transmittance of all NWs in three different cladding mediums including (i) water, (ii) ISO11 and (iii) ISO13 and their averages.

From the average transmittance obtained in the bottom image of the GUI, the resonance peaks, where the momentum of the photons matches with the momentum of the electron oscillation, are investigated for each cladding material. For accurate results, the resonance peak is examined by fitting the transmittance curve with a polynomial curve fitting algorithm as presented in Fig. 7.34.

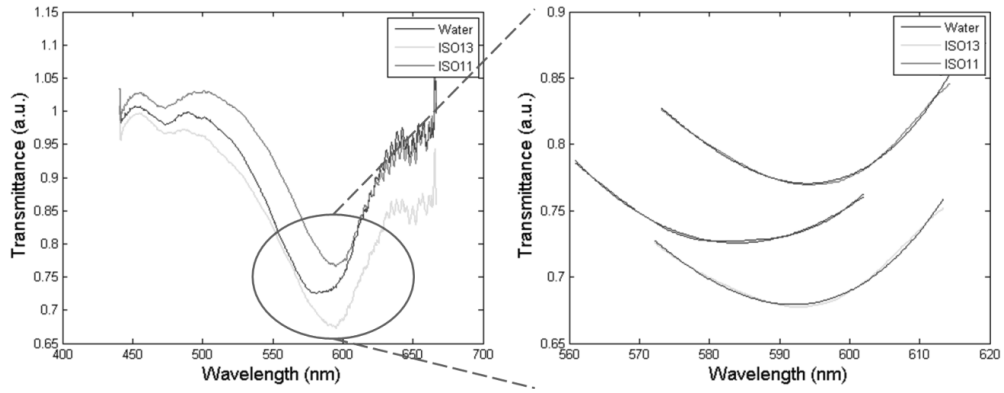

Figure 7.34: Investigation of the resonance peak using polynomial curve fitting.

After fitting the transmittance graph with the polynomial curve, the minimum value of the transmittance is then located. It is seen that it is at a different wavelength for each cladding material, as shown in Fig. 7.35

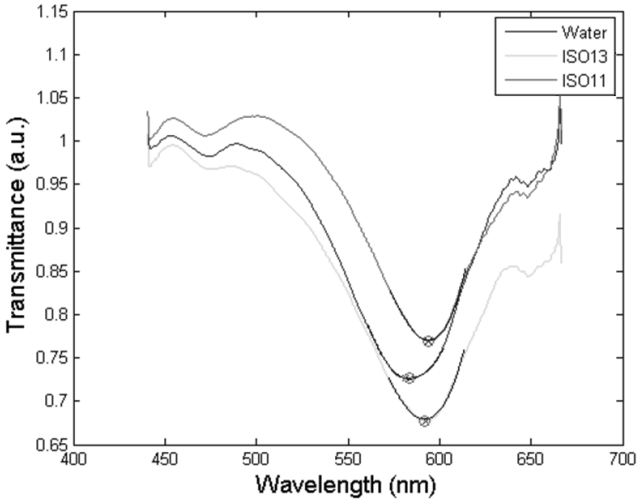

Figure 7.35: Resonance peaks located at specific wavelengths for each cladding material.

Then, the attenuation coefficients of the NWs showing the SPR peak wavelength for the three cladding materials are calculated and computed using Equation (7.13). The graph of the attenuation coefficient is then smoothened as demonstrated in Fig. 7.36.

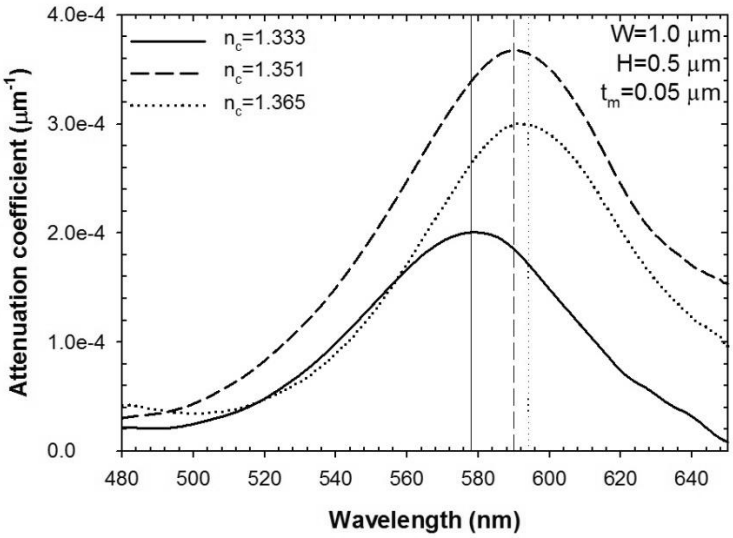

Figure 7.36: Graph between the attenuation coefficients of the NW for different cladding materials and wavelengths. It shows the SPR absorption peaks and their positions. The redshift is observed as the cladding index increases.

As the cladding index increases, the SPR peak is shifted to a higher wavelength. According to simulation results, the redshift occurs with a higher refractive index of the cladding material. The attenuation coefficient of the gold-coated NWs is the combination of the attenuation from scattering due to the surface roughness, the SPR and the light coupling as presented in the following equation [221]:

$$\alpha_{nw} = \alpha_{scattering} + \alpha_{SPR\ absorption} + \alpha_{material\ absorption} \qquad (7.14)$$

It can be observed that the attenuation coefficient of the gold-coated NWs increases when the refractive index of the cladding material increases. Unlike the attenuation coefficient of the un-coated ormocomp NWs, it is reduced when the cladding index increases. Therefore, the SPR is the dominant factor that affects the attenuation coefficient in the gold-coated ormocomp NWs while the scattering from the surface roughness is the main factor for the un-coated NWs. The attenuation from the material absorption can be negligible because ormocomp has very low absorption in the visible region [145].

The average SPR peak wavelength for those three cladding materials is shown in Fig. 7.37. The comparison of the peak positions between the simulation results and experimental results is also presented in Fig. 7.37.

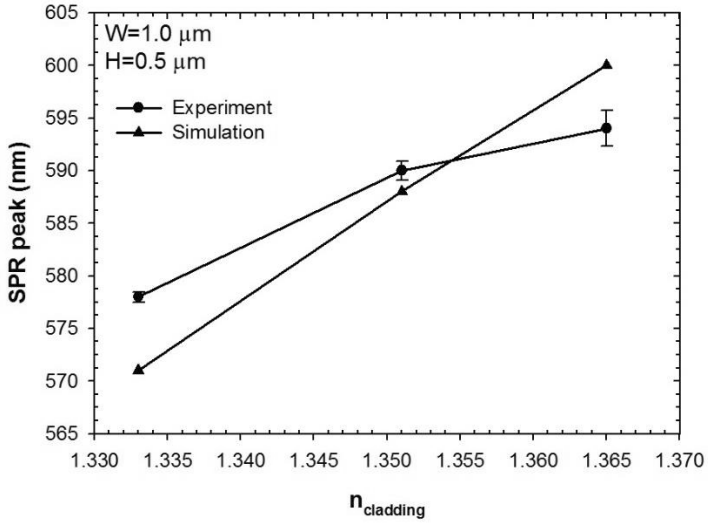

Figure 7.37: Comparison of the SPR peak wavelength between the experimental result and the simulation result for three cladding materials. The peak position of the NW coated with a metal thickness of 55 nm is the best match with the experimental work.

From the experimental work, the SPR peak wavelength for the water cladding (n=1.333) is about 578±0.5 nm. For the ISO13 solution with a refractive index of 1.351, the peak position is at 590±0.9 nm. For the largest cladding index in this work (n=1.365), the SPR is observed at the wavelength of 594±1.7 nm. The SPR peak from the experiment has the best fit with 55 nm gold-coated NW in the simulation. The comparison shows the same trend of the peak shift with the cladding index. However, at n=1.361, the peak position result obtained in the experiment is significantly lower than the simulation result. This could be due to the intensity of the light source spectrum as shown in Fig. 7.27, which provides a low signal at λ>600 nm. Therefore, a distortion occurs at the highest cladding index, where the peak position should be around 610 nm. Furthermore, the large surface roughness as a result of the fabrication process also has an impact on the results of the experimental work. The surface roughness of the NW is measured to be around 0.1-0.2 μm.

7.5 Summary

This chapter presented the experimental results of both un-coated and gold-coated ormocomp NWs. For the un-coated ormocomp NWs, the attenuation

coefficient of the NW is extracted. The optical setup to image the optical signal for the attenuation coefficient extraction mainly consists of the red light source with λ=633 nm, the objective lens, the sample stand and the CCD cameras. Initially, the optical field at the output could not be detected due to its weak signal. The output signal is quite weak because both ends of the NWs are not at the edge of the glass substrate leading to a large coupling loss. After fabrication of new NWs on a smaller glass substrate, the output signal is improved substantially and thus it was clearly detected. The intensity of the output signal is computed using MATLAB. The attenuation coefficient of the un-coated NWs is studied for different cladding materials including air, water and glycerol solutions.

With a higher refractive index of cladding material, the optical field is extended deeper into the cladding area, thus causing a higher attenuation coefficient when the surface roughness is neglected for an ideally smooth surface. Nevertheless, the attenuation coefficient tends to reduce when increasing the cladding index. This is because the light scattered from the surface roughness of the core/cladding region is reduced when changing the cladding medium from water (n=1.333) to glycerol solution with a higher index (n=1.365). The scattering effect from the rougher surface provides a greater change in the attenuation coefficient over the change of refractive index. Therefore, the scattering from the surface roughness is the dominant factor causing the change in the attenuation coefficient of the un-coated ormocomp NWs.

Further enhancement of the light interaction at the core/cladding interface can be achieved by coating the top surface of the fabricated NW with a metallic layer, thus improving the sensitivity of the fabricated NW. A thin gold layer, coated by the sputtering technique exhibits surface plasmon resonance and enhances the evanescent fields in the sensing region, leading to an improvement of the sensitivity of the NWs. The optical setup for the SPR analysis is similar to the setup for the un-coated NWs. Only a beam splitter, a positive lens and a spectrometer are added in the setup. The light source is changed from a red light source to broadband light source in order to cover the visible spectrum. The cladding materials considered for the gold-coated ormocomp NWs are water and three

different volume ratios of iso-propanol solutions (ISO15, ISO13 and ISO11). The operating wavelength is in the visible region (400-700 nm).

The SPR peak wavelength is clearly observed for both polarisation-independent and TM mode SPR structures. The redshift occurs when the refractive index of the cladding material is increased. For polarisation-independent structure, a waveguide with a dimension of 10 µm width and height is considered. There are two resonance peaks observed because there are two different plasmonic modes coupled with the dielectric modes. Both the TM and TE modes have almost identical resonance wavelength for each cladding material. Hence, a polarizer is not required and polarisation-independent waveguides are obtained. Consequently, a simple and compact integrated SPR sensor can be achieved. The simulation and experimental results show an excellent agreement in their images, resonance peaks and their shifts. With a larger refractive index of the cladding material, redshift occurs. The sensitivity of the gold-coated ormocomp waveguide is around 544.55 nm/RIU, and the resolution is 5.3×10^{-3} RIU and these can be further improved by optimizing the waveguide dimensions and metal thickness.

For TM mode SPR structure, the extracted attenuation coefficient of the NW is 1.93×10^{-4} μm^{-1}, or 0.84 dB/mm and it is the result of measuring the transmittance with a spectrometer. The NW has a higher attenuation coefficient than the feed waveguide which means that the NW is more sensitive compared to the feed waveguide. Also, longer NWs have larger SPR absorption. In addition, the attenuation coefficient of the gold-coated ormocomp NWs increases with the refractive index of the cladding material. Therefore, the SPR is the main factor causing the change of the attenuation coefficient. It is clearly seen that the SPR is sensitive to the change of the cladding index which is an important factor in sensing applications.

8. General summary and suggestions for further work

8.1 Conclusion

In this PhD research, the design, fabrication, as well as the theoretical and experimental characterisations of nanowire waveguides (NWs) for optical sensing applications, were carried out. Two types of waveguides were considered in the present study, the silicon and the ormocomp based polymer waveguides. Both types of waveguides were designed and fabricated by using the top-down techniques. Silicon NWs investigated were of a horizontal slot type structure while ormocomp NWs were of rib-waveguide like structure. Due to constraints of the laboratory facilities available, characteristics of the silicon NWs were studied only theoretically, while those of the ormocomp NWs were studied both theoretically and experimentally.

NWs were designed to be connected with feed and tapered waveguides at both the ends, thus enabling their effective use as integrated optical devices for sensing applications. Feed and tapered waveguides also reduce the insertion loss when the NW is coupled to a light source or other optical device. In order to attain maximum sensitivity of the NW devices, key dimensions of the structure, such as the width and the height were optimized according to the power confinement of the fundamental guided optical modes obtained in the sensing area of each structure examined. This was considered to be the core/cladding interface and the slot region for the ormocomp and the silicon NWs, respectively.

The full-vectorial **H**-field variational formulation of the Finite Element Method (FEM), where the magnetic field is continuous across the boundaries of the finite elements has been used for the theoretical characterisation of the NW structures examined. The guided optical modes that contribute to the enhancement of the sensitivity were identified using the above approach and their characteristics, such as effective index, attenuation constant and power confinement, with the variation of key structure parameters, were investigated.

The main fabrication process used for the ormocomp optical waveguides and NWs was the nanoimprint method, which was considered suitable for these type of structures, due to its capability for mass production, with relatively low cost and time. However, the nanoimprint method requires a mold to stamp on the ormocomp layer, therefore, in our case, silicon NWs were used as a master mold, and PDMS as a soft mold to transfer the pattern from the silicon mold onto the ormocomp layer.

Oxidation, LPCVD, photolithography and dry etching were the main processes used to fabricate the master mold silicon NWs. The fabricated silicon NWs have a horizontal slot structure. An unavoidable fact is that the silicon NWs have non-vertical sidewall structures and this is due to the limiting resolution of the stepper machine in the photolithography process. Hence, trapezoidal-shaped NWs were produced. The dimensions of the fabricated NWs considered in the theoretical study were a height of H=0.5 µm, a top-width of W_{top}=1.0 µm, a bottom-width of W_{bottom}=1.5 µm, and a sidewall angle of θ=65°. In addition, the fabricated ormocomp NWs have the rib-waveguide like structure due to an excess ormocomp planar layer created during the imprint process. The thickness of the rib layer was found to be 2 µm. To achieve vertical sidewall structures, silicon waveguides with a dimension of 10 µm x 10 µm were fabricated.

The silicon NWs with horizontal slot structure were studied theoretically to detect the effective index change with the change of the refractive index of the analyte material. The analyte material considered in the study was DNA and the detection of DNA hybridisation was investigated. The DNA hybridisation is a process where two single-stranded DNAs (ssDNA) are combined with each other to form double-stranded DNA (dsDNA) and vice versa. The horizontal slot NWs were also connected with feed and tapered waveguides which can be used to mechanically support the horizontal slot NWs when the solid-slot region is replaced with gas or liquid materials. The optimized dimensions of the silicon NWs for the width, the slot height and the silicon core height were found to be W=1.0 µm, H_s=0.1 µm and H=0.16 µm, respectively. The horizontal slot waveguide

proposed to detect DNA hybridisation in which a sensitivity of 893.5 nm/RIU is obtained theoretically.

The characterisation of the ormocomp waveguides and NWs was divided into two main parts. First, the attenuation coefficient of the polymer NW was studied over the NW lengths for three different cladding materials, specifically air (n=1), water (n=1.333) and glycerol solution (n=1.365). The presence of surface roughness on the NWs was also included in this study. Secondly, the polymer NWs were coated with thin gold layer which facilitates the exhibition of the surface plasmon resonance (SPR) property. For non-vertical sidewalls NW, only the TM mode SPR is considered. For vertical sidewalls waveguide, both TM and TE plasmonic modes are supported and their SPR response can be adjusted to consider it as polarisation-independent waveguide structure. The absorption peaks of the SPR and their shifts were studied for different cladding materials involving water and three different volume ratios of iso-propanol solutions with the refractive indices of 1.33, 1.344, 1.351 and 1.365, respectively.

The characteristics of the non-metal coated ormocomp NWs were investigated first by studying their attenuation coefficient which can be affected by the volume absorption and the surface scattering. For these types of structure, the surface scattering is the dominant factor of the attenuation loss in the NWs. The relation of the attenuation coefficient between the feed waveguide and the NW ($\Delta\alpha$) in air cladding was found to be $-1.1824\ cm^{-1}$ (-5.132 dB/cm), where the negative sign represents a greater attenuation coefficient in the NW than the feed waveguide. For water cladding, the value of $\Delta\alpha$ was $-1.063\ cm^{-1}$ (-4.613 dB/cm) whereas $\Delta\alpha = -1.023\ cm^{-1}$ (4.440 dB/cm) was measured for glycerol solution cladding.

In order to increase the interaction at the core/cladding interface, SPR was introduced by coating the thin metal layer on the surface of the NWs. In this study, a 50 nm and 100 nm thick gold layer were deposited on the non-vertical sidewalls NWs and vertical sidewalls waveguide, respectively, using the sputtering technique. As in the case of the un-coated ormocomp NWs, the characteristic of the gold-coated ormocomp NWs was investigated by studying their attenuation

coefficient. However, the attenuation coefficient of the gold-coated ormocomp NWs is mainly affected by the absorption of the SPR. For vertical sidewalls structure, the SPR is dominant in both TM (top surface) and TE (sidewalls) modes. However, only TM mode SPR is significant in the non-vertical sidewall structures. At the slanted sidewalls, the SPR mode is mixed between TM and TE modes.

The extracted attenuation coefficient of the feed waveguide (α_{wg}) was found to be $1.03\ cm^{-1}$. It was lower than the attenuation coefficient of the NWs (α_{nw}) which was $1.93\ cm^{-1}$. The normalized power confinement in the sensing area (gold/cladding interface) was found to be 10 times higher than in the core region of the un-coated ormocomp NWs. The optical guided modes considered here, were the coupled supermodes between the dielectric mode in the ormocomp NW and the plasmonic supermode. In addition, the plasmonic supermode is the coupled mode between the two plasmonic modes at the ormocomp/gold and the cladding/gold interfaces.

The demonstration of the gold-coated ormocomp NWs was performed to detect the change of effective index of the NW when the refractive index of the analyte solution is changed. With the four different cladding refractive indices (n=1.333, 1.344, 1.351 and 1.365), the SPR peak wavelengths were clearly observed, with the redshift occurring in both the theoretical and the experimental results when the refractive index of the cladding material was increased for both non-vertical sidewall (TM mode SPR) and vertical sidewall (polarisation-independent) structures. The peak position also depends on the thickness of the metal layer. A redshift of about 25-30 nm was observed when the metal thickness was increased by 10 nm.

For the polarisation-independent structures, the oscillation of the electrons introduces SPR quasi-TE mode with dominant H_y/E_x field at the vertical sidewalls. On the other hand, at the top surface SPR quasi-TM mode is formed with dominant H_x/E_y field. These structures can be characterised as polarisation-independent SPR waveguide in terms of the ability to detect SPR wavelengths in sensing applications without the use a polarizer in an integrated sensor system, thus providing a simpler configuration with increased reliability. In addition, the

polarisation-independent mechanism allows the integrated SPR sensor to be scaled down in the manufacturing and packaging process.

In summary, the scattering from the surface roughness is the dominant factor providing a large attenuation coefficient for the un-coated ormocomp NWs, where the SPR is the main effect for the gold-coated ormocomp NWs. In addition, the demonstration of the gold-coated ormocomp NWs to detect the wavelength shifts, when there is a change of the refractive index of the analyte solution, is possible.

8.2 Suggestions for future work

The power confinement in the sensing area of the gold-coated ormocomp NWs can be further improved by having a ridge-waveguide structure instead of a rib waveguide. It can be achieved by the possible improvement of the nanoimprint process to minimize the excess ormocomp layer. The ormocomp can be mixed with an ormothin to reduce the viscosity resulting in thickness reduction. In addition, the spin speed can also be increased from 3000 rpm to 6000 rpm during the spin coating of the ormocomp layer in order to make the coating thinner [145]. Furthermore, the integrated gold-coated ormocomp NWs can be designed to have an enclosed structure to improve their performance.

In the future, the gold-coated ormocomp NWs can have a surface functionalisation in order to be able to selectively detect specific materials such as DNA, proteins, enzymes and metal ions. To be used as a sensor, the robustness and temperature-sensitive issues will also need to be considered. The sensitivity can be further improved by optimizing the structure dimension and metal thickness.

Appendix A **Assembly of element matrices**

In FEM, the continuum structure is discretized into a simple element which is a first-order triangular element in this case and then each element is assembled together with respect to the shape functions and nodal field values of each triangular element. For the optical waveguide, the solution obtained by the FEM can be represented as a standard eigenvalue problem as in equation (3.32). In order to assemble the elements, equation (3.30) is considered. The nodal magnetic field vector $\{H\}_e$ over the cross-section of the triangular element and the shape function matrix $[N]^T$ are shown in equation (A.1) and (A.2), respectively**.**

$$\{H\}_e = \begin{bmatrix}\{H_x\}_e & \{H_y\}_e & \{H_z\}_e\end{bmatrix}^T \tag{A.1}$$

where $\{H_x\}$, $\{H_y\}$, $\{H_z\}$ are the nodal field vectors along each axis

$$[N]^T = \begin{bmatrix}\{N\} & \{0\} & \{0\} \\ \{0\} & \{N\} & \{0\} \\ \{0\} & \{0\} & j\{N\}\end{bmatrix} \tag{A.2}$$

where {N} is the shape function vector and {0}, is the null vector. The term j arises, as for lossless cases H_z component is 90° out of phase with the transverse components. Therefore, equation (3.30) can be written as follow.

$$\{H\}_e = \begin{bmatrix} N_1 & N_2 & N_3 & 0 & 0 & 0 & 0 & 0 & 0 \\ 0 & 0 & 0 & N_1 & N_2 & N_3 & 0 & 0 & 0 \\ 0 & 0 & 0 & 0 & 0 & 0 & jN_1 & jN_2 & jN_3 \end{bmatrix} \begin{Bmatrix} H_{x1} \\ H_{x2} \\ H_{x3} \\ H_{y1} \\ H_{y2} \\ H_{y3} \\ H_{z1} \\ H_{z2} \\ H_{z3} \end{Bmatrix} \tag{A.3}$$

With the Maxwell's equation, $(\nabla \times \mathbf{H})_e$ can be defined as:

$$(\nabla \times \boldsymbol{H})_e = [\nabla \times][N]^T\{H\}_e$$

$$= \begin{bmatrix} 0 & -\frac{\partial}{\partial z} & \frac{\partial}{\partial y} \\ \frac{\partial}{\partial z} & 0 & -\frac{\partial}{\partial x} \\ -\frac{\partial}{\partial y} & \frac{\partial}{\partial x} & 0 \end{bmatrix} [N]^T\{H\}_e \tag{A.4}$$

From equation (A.4), it can be written as follow.

$$(\nabla \times \boldsymbol{H})_e = [Q]^T\{H\}_e \tag{A.5}$$

where the matrix $[Q]$ is defined in equation (A.6).

$$[Q] = \begin{bmatrix} \{0\} & -j\beta\{N\} & -\frac{\partial\{N\}}{\partial y} \\ j\beta\{N\} & \{0\} & \frac{\partial\{N\}}{\partial x} \\ j\frac{\partial\{N\}}{\partial y} & -j\frac{\partial\{N\}}{\partial x} & \{0\} \end{bmatrix} \tag{A.6}$$

The solution to the optical waveguide problem can be obtained from Euler's equation, which can be transformed to a discretized form as in equation (3.31). By assuming isotropic media $[\varepsilon_r] = \varepsilon_r$ and substituting equation (A.5) into (3.31), the resulting element equation is shown below.

$$\frac{1}{\varepsilon_r}\iint_\Omega \left(\{H\}_e{}^T[Q]^*[Q]^T\{H\}_e\right)d\Omega - k_o^2 \iint_\Omega \{H\}_e{}^T[N]^*[N]^T\{H\}_e = 0 \tag{A.7}$$

By summing all the elements over the cross-section of the guide, the above equation can be expressed in matrix form based on the standard eigenvalue problem as shown in equation (A.8).

$$[A]\{H\} - k_o^2[B]\{H\} = 0 \tag{A.8}$$

where, $[A]$ and $[B]$ are global matrices of the eigenvalue equation. They are the summation of the element matrices for each triangular element of the discretized cross-section of the optical waveguide which can be expressed by the following equations.

$$[A] = \sum_e [A]_e = \sum_e \iint_e \frac{1}{\varepsilon_e} [Q]^* [Q]^T dxdy \tag{A.9}$$

$$[B] = \sum_e [B]_e = \sum_e \iint_e \frac{1}{\varepsilon_e} [N]^* [N]^T dxdy \tag{A.10}$$

where $1/\varepsilon_e$ is the relative dielectric permittivity of the element and $[A]_e$ and $[B]_e$ are the element matrices which may be evaluated as follows:

For matrix $[A]_e$:

$$[A] = \frac{1}{\varepsilon_e} \iint_e \begin{bmatrix} \{0\} & j\beta\{N\} & -\frac{\partial\{N\}}{\partial y} \\ -j\beta\{N\} & \{0\} & \frac{\partial\{N\}}{\partial x} \\ -j\frac{\partial\{N\}}{\partial y} & j\frac{\partial\{N\}}{\partial x} & \{0\} \end{bmatrix} \begin{bmatrix} \{0\} & j\beta\{N\}^T & j\frac{\partial\{N\}^T}{\partial y} \\ -j\beta\{N\}^T & \{0\} & -j\frac{\partial\{N\}^T}{\partial x} \\ -\frac{\partial\{N\}^T}{\partial y} & \frac{\partial\{N\}^T}{\partial x} & \{0\} \end{bmatrix} dxdy =$$

$$\frac{1}{\varepsilon_e} \iint_e \begin{bmatrix} \beta^2\{N\}\{N\}^T + \frac{\partial\{N\}}{\partial y}\frac{\partial\{N\}^T}{\partial y} & -\frac{\partial\{N\}}{\partial y}\frac{\partial\{N\}^T}{\partial x} & \beta\{N\}\frac{\partial\{N\}^T}{\partial x} \\ -\frac{\partial\{N\}}{\partial y}\frac{\partial\{N\}^T}{\partial x} & \beta^2\{N\}\{N\}^T + \frac{\partial\{N\}}{\partial x}\frac{\partial\{N\}^T}{\partial x} & \beta\{N\}\frac{\partial\{N\}^T}{\partial y} \\ \beta\{N\}\frac{\partial\{N\}^T}{\partial x} & \beta\{N\}\frac{\partial\{N\}^T}{\partial y} & \frac{\partial\{N\}}{\partial y}\frac{\partial\{N\}^T}{\partial y} + \frac{\partial\{N\}}{\partial x}\frac{\partial\{N\}^T}{\partial x} \end{bmatrix} dx \tag{A.11}$$

The resulting matrix is a 9x9 real symmetric matrix. By using the shape function coefficients and the relation for a triangular element, the various terms can be determined as follow.

$$\iint_e N_1^i N_2^j N_3^k dxdy = \frac{i!j!k!}{(i+j+k+2)!} (2xArea) \tag{A.12}$$

For the element matrix $[B]_e$:

$$[B] = \iint_e [N]^* [N]^T dxdy$$
$$= \iint_e \begin{bmatrix} \{N\} & \{0\} & \{0\} \\ \{0\} & \{N\} & \{0\} \\ \{0\} & \{0\} & j\{N\} \end{bmatrix} \begin{bmatrix} \{N\}^T & \{0\}^T & \{0\}^T \\ \{0\}^T & \{N\}^T & \{0\}^T \\ \{0\}^T & \{0\}^T & j\{N\}^T \end{bmatrix} dxdy \tag{A.13}$$

$$= \begin{bmatrix} \{N\}\{N\}^T & \{0\}\{0\}^T & \{0\}\{0\}^T \\ \{0\}\{0\}^T & \{N\}\{N\}^T & \{0\}\{0\}^T \\ \{0\}\{0\}^T & \{0\}\{0\}^T & \{N\}\{N\}^T \end{bmatrix} dxdy$$

where the various terms can be evaluated by using equation (A.12).

Appendix B **Dielectric constant of materials used in this work**

B.1 Gold (Au)

The complex dielectric constant of gold ($\widetilde{\varepsilon_r}$) is calculated from the complex refractive index of gold ($\tilde{n}$) [202] as show in in the following equations [216]:

$$\widetilde{\varepsilon_r} = \varepsilon_r + i\varepsilon_i = \tilde{n}^2 = (n + j\kappa)^2 \quad \text{(B.14)}$$

$$\varepsilon_r = n^2 - \kappa^2 \quad \text{(B.15)}$$

$$\varepsilon_i = 2n\kappa \quad \text{(B.16)}$$

where ε_r is the real part of the complex dielectric constant and ε_i represents the imaginary part. Here, n is the refractive index and κ is the extinction coefficient. The values of the refractive index (n) and extinction coefficient (κ) of gold in the visible region is plotted as shown in Fig. B.1. $\widetilde{\varepsilon_r}$ is wavelength dependence due to the material dispersion. The value of $\widetilde{\varepsilon_r}$ of gold in the visible region using in this work is presented in Table B.1.

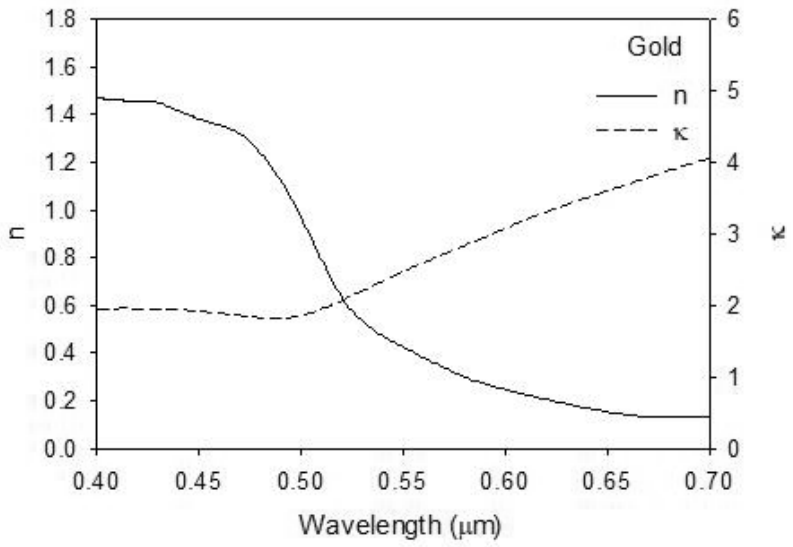

Figure B.1: Graph of refractive index (n) and extinction coefficient (κ) of gold in the visible region

Table B.1: The complex dielectric constant of gold ($\widetilde{\varepsilon_r}$) in the visible region (400-700 nm)

λ (μm)	$n + j\kappa$	$\widetilde{\varepsilon_r}$
0.39995	1.658+1.956i	-1.076972+6.486096i
0.40651	1.647+1.95938i	-1.1265609844+6.45419772i
0.41328	1.636+1.958i	-1.157268+6.406576i
0.42029	1.628+1.95138i	-1.1574999044+6.35369328i
0.42754	1.616+1.94i	-1.152144+6.27008i
0.43504	1.596+1.9245i	-1.15648425+6.143004i
0.4428	1.562+1.904i	-1.185372+5.948096i
0.45086	1.502+1.87588i	-1.2629217744+5.63514352i
0.4592	1.426+1.846i	-1.37424+5.264792i
0.46787	1.346+1.81463i	-1.4811660369+4.88498396i
0.47687	1.242+1.796i	-1.683052+4.461264i
0.48622	1.087+1.79738i	-2.0490058644+3.90750412i
0.49594	0.916+1.84i	-2.546544+3.37088i
0.50606	0.755+1.9565i	-3.25786725+2.954315i
0.5166	0.608+2.12i	-4.124736+2.57792i
0.5276	0.492+2.32625i	-5.1693750625+2.28903i
0.53907	0.402+2.54i	-6.289996+2.04216i
0.545	0.3743+2.6314i	-6.78416547+1.96986604i
0.5463	0.3682+2.654i	-6.90814476+1.9544056i
0.547	0.3648+2.6662i	-6.9755434+1.94525952i
0.548	0.3601+2.6822i	-7.06452483+1.93172044i
0.549	0.3554+2.6985i	-7.15559309+1.9180938i
0.55	0.3507+2.7138i	-7.24171995+1.90345932i

0.55105	0.346+2.73063i	-7.3366241969+1.88959596i
0.552	0.343+2.7422i	-7.40201184+1.8811492i
0.557	0.3271+2.8019i	-7.7436492+1.83300298i
0.56	0.3173+2.8377i	-7.951862+1.80080442i
0.561	0.3141+2.8494i	-8.02042155+1.78999308i
0.562	0.311+2.8616i	-8.09203356+1.7799152i
0.56357	0.306+2.88i	-8.200764+1.76256i
0.57	0.2872+2.9096i	-8.38328832+1.67127424i
0.572	0.2814+2.9189i	-8.44079125+1.64275692i
0.574	0.2757+2.9281i	-8.49775912+1.61455434i
0.57668	0.268+2.94063i	-8.5754807969+1.57617768i
0.578	0.2649+2.9436i	-8.59460895+1.55951928i
0.58	0.2602+2.9478i	-8.6218208+1.53403512i
0.582	0.2555+2.9521i	-8.64961416+1.5085231i
0.584	0.2509+2.9564i	-8.67735015+1.48352152i
0.588	0.2416+2.9639i	-8.72633265+1.43215648i
0.59041	0.236+2.97i	-8.765204+1.40184i
0.592	0.2333+2.9751i	-8.79679112+1.38818166i
0.596	0.2266+2.9875i	-8.87380869+1.353935i
0.6	0.22+3i	-8.9516+1.32i
0.60481	0.212+3.015i	-9.045281+1.27836i
0.61	0.2058+3.0304i	-9.14097052+1.24731264i
0.617	0.1974+3.0513i	-9.27146493+1.20465324i
0.61993	0.194+3.06i	-9.325964+1.18728i

0.622	0.1919+3.0612i	-9.33411983+1.17488856i
0.625	0.1889+3.0632i	-9.34751103+1.15727696i
0.63	0.1838+3.0064i	-9.00465852+1.10515264i
0.63582	0.178+3.07i	-9.393216+1.09292i
0.65255	0.166+3.15i	-9.894944+1.0458i
0.67019	0.161+3.44581i	-11.8476855561+1.10955082i
0.68	0.1605+3.633i	-13.17292875+1.166193i
0.68881	0.16+3.8i	-14.4144+1.216i
0.70849	0.161+4.08769i	-16.6832885361+1.31623618i
0.72932	0.164+4.357i	-18.956553+1.429096i
0.75143	0.17+4.61019i	-21.2249518361+1.5674646i
0.77491	0.176+4.86i	-23.588624+1.71072i

B.2 Silicon (Si)

Similar to the gold, the complex dielectric constant of silicon ($\widetilde{\varepsilon_r}$) can be calculated from the complex refractive index of silicon ($\tilde{n}$) [222] as shown in the equation (B.14). The refractive index (n) values and the extinction coefficient (κ) of silicon in the visible region are plotted as shown in Fig. B.2. The value of $\widetilde{\varepsilon_r}$ of silicon in the visible region as used in this work is presented in Table B.2.

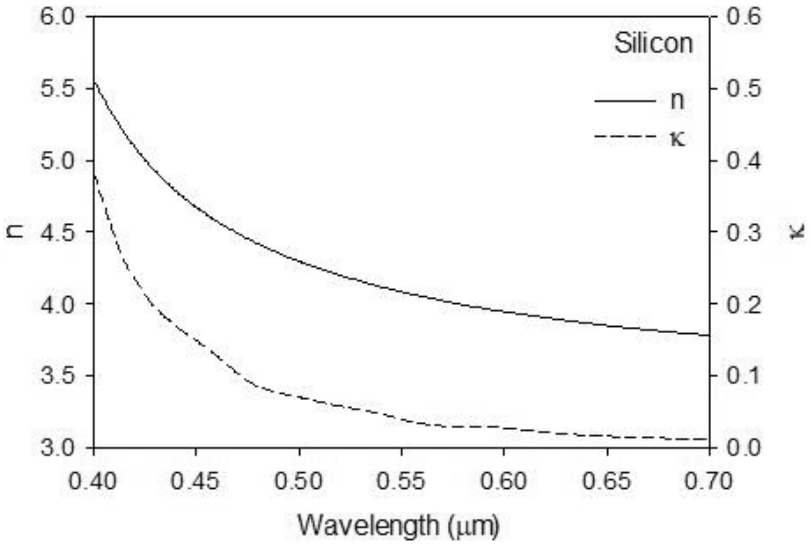

Figure B.2: Graph of refractive index (n) and extinction coefficient (κ) of silicon in the visible region

Table B.2: The complex dielectric constant of silicon ($\widetilde{\varepsilon_r}$) in the visible region (400-700 nm)

λ (μm)	$\boldsymbol{n + j\kappa}$	$\boldsymbol{\widetilde{\varepsilon_r}}$
0.3999	5.57+0.387i	30.875131+4.31118i
0.4133	5.222+0.269i	27.196923+2.809436i
0.4275	4.961+0.203i	24.570312+2.014166i
0.4428	4.753+0.163i	22.56444+1.549478i
0.4592	4.583+0.13i	20.986989+1.19158i
0.4769	4.442+0.09i	19.723264+0.79956i
0.4959	4.32+0.073i	18.657071+0.63072i
0.5166	4.215+0.06i	17.762625+0.5058i
0.5391	4.123+0.048i	16.996825+0.395808i
0.5636	4.042+0.032i	16.33674+0.258688i
0.5904	3.969+0.03i	15.752061+0.23814i
0.6199	3.906+0.022i	15.256352+0.171864i

0.6525	3.847+0.016i	14.799153+0.123104i
0.6888	3.796+0.013i	14.409447+0.098696i
0.7293	3.752+0.01i	14.077404+0.07504i
0.7749	3.714+0.008i	13.793732+0.059424i

B.3 Silica (SiO_2)

The dielectric constant of silica (ε_r) is taken as equal to n^2 as the extinction coefficient considered here to be equal to zero [223]. The values of the refractive index (n) of the SiO_2 in the visible region is plotted as shown in Fig. B.2. The value of ε_r of SiO_2 in the visible region using in this work is presented in Table B.3.

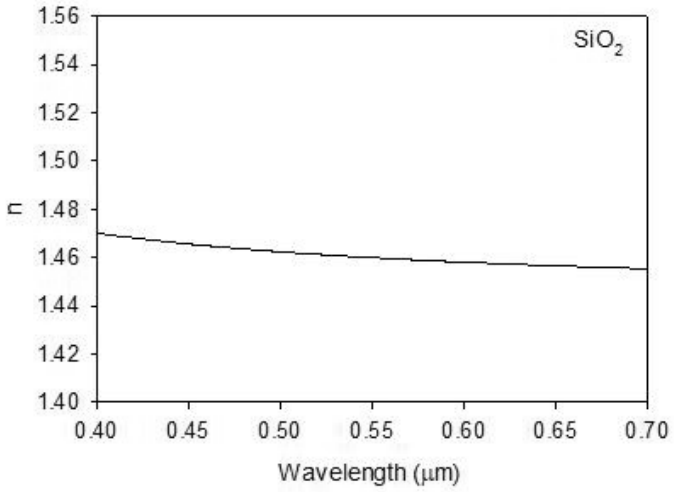

Figure B.3: Graph of refractive index (n) of SiO_2 in the visible region

Table B.3: The dielectric constant of silica (ε_r) in the visible region (400-700 nm)

λ (μm)	n	$\varepsilon_r = n^2$
0.3917	1.47105251	2.16399549
0.4055	1.46952865	2.15951445
0.4197	1.46812182	2.15538168
0.4345	1.46680482	2.15151638
0.4498	1.46558083	2.14792717

0.4657	1.46443603	2.14457289
0.4821	1.46337193	2.14145742
0.4991	1.46237644	2.13854485
0.5167	1.46144499	2.13582146
0.5349	1.46057308	2.13327372
0.5537	1.45975629	2.13088841
0.5732	1.45898656	2.12864179
0.5934	1.45826079	2.12652453
0.6143	1.45757581	2.12452723
0.636	1.4569256	2.12263221
0.6584	1.45631041	2.12084
0.6816	1.4557247	2.1191344
0.7056	1.45516603	2.11750817
0.7305	1.45462988	2.11594807
0.7562	1.45411617	2.11445382

B.4 Ormocomp

Similar to the SiO_2, the dielectric constant of ormocomp is equal to n^2 as the extinction coefficient is considered to be equal to zero. The average refractive index of the ormocomp used in this work is equal to 1.52 [145] in the visible region. Hence, the value of 2.31 is used as the dielectric constant (ε_r) over the wavelength range considered in this work.

Appendix C **Derivation of the attenuation coefficient from surface scattering**

The scattering losses from a symmetric slab waveguide was first studied by Marcuse in 1969 [224]. In 1971 Tien [220] studied the loss from surface scattering for an asymmetric waveguide in which the two surfaces of the waveguide scatter differently as the refractive indices of the substrate and cladding materials are different. The power attenuation for the asymmetric waveguide can be derived as follows [220].

$$\alpha = K^2\left(\frac{cos^3\theta_1}{2sin\theta_1}\right)\left[\frac{1}{h + \left({}^1/_{\gamma_0}\right) + \left({}^1/_{\gamma_2}\right)}\right] \tag{C.1}$$

where h is the thickness of the waveguide, and γ_0 and γ_2 are the transverse propagation constant of substrate and cladding, respectively. K is constant which can be defined as follow [220];

$$K = \frac{4\pi}{\lambda}\left(\sigma_{12}^2 + \sigma_{10}^2\right)^{1/2} \tag{C.2}$$

where σ_{10} and σ_{12} are the surface roughness at the core/substrate and core/cladding interfaces, respectively. λ is the operating wavelength.

For this work, we assume that the scattering effect arises only from the surface roughness (σ) at core/cladding interface. At the core/substrate interface, the surface is assumed to be smooth and $\sigma_{10} = 0$. The fabricated waveguide structure for this work is shown in Fig. C.1. Therefore, the Equation (C.1) can be derived as;

$$\alpha = \left(\frac{4\pi}{\lambda}\right)^2(\sigma^2)\left(\frac{cos^3\theta_1}{2sin\theta_1}\right)\left[\frac{1}{h + \left({}^1/_{\gamma_0}\right) + \left({}^1/_{\gamma_2}\right)}\right] \tag{C.3}$$

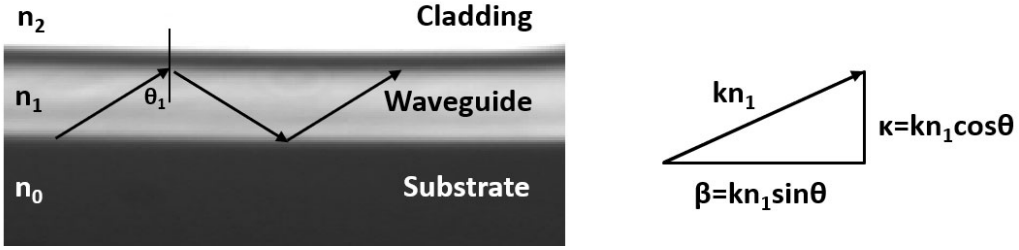

Figure C.1: The fabricated ormocomp waveguide showing the wave motion.

For the reflection angle θ_1, the wave in a waveguide mode propagates as the zigzag wave motion in which the propagation constant (β) can be defined as follow [220];

$$\beta = kn_1 sin\theta_1 \tag{C.4}$$

where n_1 is the refractive index of the core waveguide and k is the wavenumber which equals to $2\pi/\lambda$. For the zigzag wave motion, β is in the horizontal direction. The transverse propagation constant in the core region (κ), which is a component in the vertical direction of the zigzag wave motion, is defined by the following equation [220].

$$\kappa = kn_1 cos\theta_1 \tag{C.5}$$

From Equations (c.4) and (c.5), the attenuation loss (α) in the Equation (C.3) can be derived as follows;

$$\alpha = 4k^2(\sigma_{12}^2)\left(\frac{\kappa^3/(kn_1)^3}{\beta/kn_1}\right)\left[\frac{1}{h + (1/\gamma_0) + (1/\gamma_2)}\right] \tag{C.6}$$

$$\alpha = \frac{2\sigma_{12}^2\kappa^3}{\beta n_1^2(h + (1/\gamma_0) + (1/\gamma_2))} \tag{C.7}$$

The transverse propagation constant of substrate (γ_0) and cladding (γ_2) can be calculated as $\gamma_0 = \sqrt{\beta^2 - k_o^2 n_0^2}$ and $\gamma_2 = \sqrt{\beta^2 - k_o^2 n_2^2}$, respectively, where n_0 is the refractive index of the substrate and n_2 is the refractive index of the cladding material.

Appendix D **List of publications**

1. C. Viphavakit, W. Patchoo, S. Boonruang, C. Themistos, M. Komodromos, W. S. Mohammed and B. M. A. Rahman, "Demonstration of Polarization-Independent Surface Plasmon Resonance Polymer Waveguide for Refractive Index Sensing." *Journal of Lightwave Technology* 35, no. 14 (2017): 3012-3019.

2. C. Viphavakit, S. Boonruang, C. Themistos, M. Komodromos, W. S. Mohammed and B. M. A. Rahman, “Surface plasmon resonance-enhanced light interaction in an integrated ormocomp nanowire," Optical and Quantum Electronics 48 no.5 (2016): 291.

3. C. Viphavakit, M. Komodromos, C. Themistos, W. S. Mohammed, K. Kalli, and B. Azizur Rahman, "Optimization of a horizontal slot waveguide biosensor to detect DNA hybridization," Applied Optics 54, 4881-4888 (2015).

4. C. Viphavakit, S. Boonruang, C. Themistos, M. Komodromos, W. S. Mohammed and B. M. A. Rahman, "Effect of surface plasmon resonance on the attenuation coefficient of an Ormocomp nanowire," in OWTNM London 2015, (XXIII International Workshop on Optical Wave and Waveguide Theory and Numerical Modelling, 2015), 76.

5. C. Viphavakit, N. Atthi, S. Boonruang, C. Themistos, W. S. Mohammed, K. Kalli, B. M. A. Rahman and M. Komodromos, "Characterization of polymer nanowires fabricated using the nanoimprint method," in SPIE Photonics Europe, (International Society for Optics and Photonics, 2014), 912632-912632-912610.

6. B. M. A. Rahman, K. Kejalakshmy, C. Viphavakit, C. Themistos, M. Rajarajan and K. Grattan, "Rigorous Design and Optimization of a New Generation of Optical Sensors," Journal of the Indian Institute of Science 94, 245-260 (2014).

7. C. Viphavakit, N. Atthi, S. Boonruang, C. Themistos, M. Komodromos, W. S. Mohammed and B. M. A. Rahman, "Realization of a polymer nanowire optical transducer by using the nanoimprint technique," Applied Optics 53, 7487-7497 (2014).

References

[1] J. Fluitman and T. Popma, "Optical waveguide sensors," *Sensors and Actuators,* vol. 10, pp. 25-46, 1986.

[2] R. P. Main, "Fibre optic sensors—future light," *Sensor Review,* vol. 5, pp. 133-139, 1985.

[3] K. Kyuma, S. Tai, and M. Nunoshita, "Development of fibre optic sensing systems—A review," *Optics and Lasers in Engineering,* vol. 3, pp. 155-182, 1982.

[4] K. Schmitt, B. Schirmer, C. Hoffmann, A. Brandenburg, and P. Meyrueis, "Interferometric biosensor based on planar optical waveguide sensor chips for label-free detection of surface bound bioreactions," *Biosensors and Bioelectronics,* vol. 22, pp. 2591-2597, 2007.

[5] J. Hu, N. Carlie, N.-N. Feng, L. Petit, A. Agarwal, K. Richardson*, et al.*, "Planar waveguide-coupled, high-index-contrast, high-Q resonators in chalcogenide glass for sensing," *Optics letters,* vol. 33, pp. 2500-2502, 2008.

[6] X. Wang, S.-S. Kim, R. Roßbach, M. Jetter, P. Michler, and B. Mizaikoff, "Ultra-sensitive mid-infrared evanescent field sensors combining thin-film strip waveguides with quantum cascade lasers," *Analyst,* vol. 137, pp. 2322-2327, 2012.

[7] Q. Liu, J. S. Kee, and M. K. Park, "A refractive index sensor design based on grating-assisted coupling between a strip waveguide and a slot waveguide," *Optics express,* vol. 21, pp. 5897-5909, 2013.

[8] W.-G. Jung, S.-W. Kim, K.-T. Kim, E.-S. Kim, and S.-W. Kang, "High-sensitivity temperature sensor using a side-polished single-mode fiber covered with the polymer planar waveguide," *IEEE Photonics Technology Letters,* vol. 13, pp. 1209-1211, 2001.

[9] A. Datesman, S. Baker, M. Wagner, D. Angeley, and E. Black, "Multiple-mode planar-waveguide sensor, fabrication materials and techniques," ed: Google Patents, 2004.

[10] M. R. Ghadiri, K. Motesharei, S.-Y. Lin, M. J. Sailor, and K.-P. S. Dancil, "Porous semiconductor-based optical interferometric sensor," ed: Google Patents, 2001.

[11] A. Ganjoo, H. Jain, C. Yu, R. Song, J. V. Ryan, J. Irudayaraj*, et al.*, "Planar chalcogenide glass waveguides for IR evanescent wave sensors," *Journal of Non-crystalline solids,* vol. 352, pp. 584-588, 2006.

[12] H. Ma, A. K.-Y. Jen, and L. R. Dalton, "Polymer-based optical waveguides: materials, processing, and devices," *Advanced Materials,* vol. 14, pp. 1339-1365, 2002.

[13] R. A. Bergh, H. C. Lefevre, and S. H. J, "An overview of fibre optic gyroscope," *Journal of Lightwave Technology,* pp. 91-107, 1984.

[14] R. Kist, S. Drope, and H. Wölfelschneider, "Fiber Fabry-Perot thermometer for medical applications," in *Locoregional high frequency hyperthermia and temperature measurement*, 1986, pp. 103-108.

[15] J. H. Lyle and C. W. Pitt, "Vortex shedding fluid flowmeter using optical fibre sensor," *Electronics Letters,* vol. 17, pp. 244-245, 1981.

[16] A. J. A. Bruinsma, P. Van Zuylen, C. W. Lamberts, and A. J. T. de Krijger, "Fibre-optic strain measurement for structural integrity monitoring," in *2nd International Conference on Optical Fiber Sensors*, 1984, pp. 399-402.

[17] K. T. V. Grattan, A. W. Palmer, and D. P. S. Saini, "Frustrated-total-internal-reflection fiber-optic pressure sensor," *Journal of Lightwave Technology,* vol. 3, pp. 1130-1134, 1985.

[18] T. E. Hansen, "A fiberoptic micro-tip pressure transducer for medical applications," *Sensors and Actuators,* vol. 4, pp. 545-554, 1983.

[19] M. Nagai, M. Shimizu, and N. Ohgi, "Sensitive liquid sensor for long distance leak detection," in *2nd International Conference on Optical Fiber Sensors*, 1984, pp. 207-210.

[20] D. H. McMahon, R. A. Soref, and L. E. Sheppard, "Sensitive fieldable photoelastic fiber-optic hydrophone," *Journal of Lightwave Technology,* vol. 2, pp. 469-478, 1984.

[21] M. D. DeGrandpre, L. W. Burgess, P. L. White, and D. S. Goldman, "Thin film planar waveguide sensor for liquid phase absorbance measurements," *Analytical Chemistry,* vol. 62, pp. 2012-2017, 1990.

[22] C. R. Rao and A. Govindaraj, *Nanotubes and nanowires*. London: Royal Society of Chemistry, 2011.

[23] G. Shen, P.-C. Chen, K. Ryu, and C. Zhou, "Devices and chemical sensing applications of metal oxide nanowires," *Journal of Materials Chemistry,* vol. 19, pp. 828-839, 2009.

[24] E. Stern, A. Vacic, and M. A. Reed, "Semiconducting nanowire field-effect transistor biomolecular sensors," *IEEE Transactions on Electron Devices,* vol. 55, pp. 3119-3130, 2008.

[25] J. Goldberger, A. I. Hochbaum, R. Fan, and P. Yang, "Silicon Vertically Integrated Nanowire Field Effect Transistors," *Nano Letters,* vol. 6, pp. 973-977, 2006/05/01 2006.

[26] C. Yang, C. J. Barrelet, F. Capasso, and C. M. Lieber, "Single p-type/intrinsic/n-type silicon nanowires as nanoscale avalanche photodetectors," *Nano Letters,* vol. 6, pp. 2929-2934, 2006.

[27] P. J. Pauzauskie and P. Yang, "Nanowire photonics," *Materials Today,* vol. 9, pp. 36-45, 2006.

[28] A. B. Greytak, C. J. Barrelet, Y. Li, and C. M. Lieber, "Semiconductor nanowire laser and NW electro-optic modulators," *Applied Physics Letters,* vol. 87, pp. 151103-151103-3, 2005.

[29] R. Yan, D. Gargas, and P. Yang, "Nanowire photonics," *Nature Photonics,* vol. 3, pp. 569-576, 2009.

[30] G. A. O'Brien, A. J. Quinn, D. A. Tanner, and G. Redmond, "A single polymer nanowire photodetector," *Advanced Materials,* vol. 18, pp. 2379-2383, 2006.

[31] J. B. K. Law and J. T. L. Thong, "Simple fabrication of a ZnO nanowire photodetector with a fast photoresponse time," *Applied Physics Letters,* vol. 88, pp. 133114-133114-3, 2006.

[32] Q. Yang, X. Guo, W. Wang, Y. Zhang, S. Xu, D. H. Lien*, et al.*, "Enhancing sensitivity of a single ZnO micro-/nanowire photodetector by piezo-phototronic effect," *ACS Nano,* vol. 4, p. 6285, 2010.

[33] K. M. Rosfjord, J. K. W. Yang, E. A. Dauler, A. J. Kerman, V. Anant, B. M. Voronov*, et al.*, "Nanowire single-photon detector with an integrated optical cavity and anti-reflection coating," *Optics Express,* vol. 14, pp. 527-534, 2006.

[34] Q. Shu, J. Wei, K. Wang, S. Song, N. Guo, Y. Jia*, et al.*, "Efficient energy conversion of nanotube/nanowire-based solar cells," *Chemical Communications,* vol. 46, pp. 5533-5535, 2010.

[35] M. Yun, N. V. Myung, R. P. Vasquez, J. Wang, and H. Monbouquette, "Nanowire growth for sensor arrays," *Nanofabrication Technologies,* vol. 5220, pp. 37-45, 2003.

[36] D. J. Sirbuly, A. Tao, M. Law, R. Fan, and P. Yang, "Multifunctional nanowire evanescent wave optical sensors," *Advanced Materials,* vol. 19, pp. 61-66, 2006.

[37] L. Pichon, R. Rogel, A.-C. Salaun, E. Jacques, F. Demami, and G. Godem-Wenga, "Fully compatible cmos technology polysilicon nanowires for integrated gas sensing application," *Journées GDR" Nanofils, Nanotubes Semiconducteurs,* 2011.

[38] X. J. Huang and Y. K. Choi, "Chemical sensors based on nanostructured materials," *Sensors and Actuators B: Chemical,* vol. 122, pp. 659-671, 2007.

[39] H. Liu, J. Kameoka, D. A. Czaplewski, and H. G. Craighead, "Polymeric nanowire chemical sensor," *Nano Letters,* vol. 4, pp. 671-675, 2004/04/01 2004.

[40] L. Hood, J. R. Heath, M. E. Phelps, and B. Lin, "Systems biology and new technologies enable predictive and preventative medicine," *Science,* vol. 306, pp. 640-3, Oct 22 2004.

[41] J. F. Hsu, B. R. Huang, C. S. Huang, and H. L. Chen, "Silicon nanowires as pH sensor," *Japanese Journal of Applied Physics,* vol. 44, p. 2626, 2005.

[42] F. Patolsky, G. Zheng, and C. M. Lieber, "Nanowire sensors for medicine and the life sciences," *Nanomedicine,* vol. 1, pp. 51-65, Jun 2006.

[43] E. Stern, J. F. Klemic, D. A. Routenberg, P. N. Wyrembak, D. B. Turner-Evans, A. D. Hamilton*, et al.*, "Label-free immunodetection with CMOS-compatible semiconducting nanowires," *Nature,* vol. 445, pp. 519-22, Feb 1 2007.

[44] F. Dell'Olio and V. M. N. Passaro, "Optical sensing by optimized silicon slot waveguides," *Optics Express,* vol. 15, pp. 4977-4993, 2007.

[45] D. M. Leung, X. Kan, B. M. A. Rahman, N. Kejalakshmy, and K. T. V. Grattan, "Optimizing the power confinement in silicon slot waveguides by use of finite element method," in *SPIE/OSA/IEEE Asia Communications and Photonics*, 2011, pp. 83071A-83071A-6.

[46] B. Adhikari and S. Majumdar, "Polymers in sensor applications," *Progress in Polymer Science,* vol. 29, pp. 699-766, 2004.

[47] J. Huang, S. Virji, B. H. Weiller, and R. B. Kaner, "Polyaniline nanofibers: facile synthesis and chemical sensors," *Journal of the American Chemical Society,* vol. 125, pp. 314-315, 2003.

[48] X. Wang, C. Drew, S.-H. Lee, K. J. Senecal, J. Kumar, and L. A. Samuelson, "Electrospun nanofibrous membranes for highly sensitive optical sensors," *Nano Letters,* vol. 2, pp. 1273-1275, 2002.

[49] K. Ramanathan, M. A. Bangar, M. Yun, W. Chen, N. V. Myung, and A. Mulchandani, "Bioaffinity sensing using biologically functionalized conducting-polymer nanowire," *Journal of the American Chemical Society,* vol. 127, pp. 496-497, 2005.

[50] Y. Zhang, J. Wu, M. Aagesen, and H. Liu, "III–V nanowires and nanowire optoelectronic devices," *Journal of Physics D: Applied Physics,* vol. 48, p. 463001, 2015.

[51] L. E. Jensen, M. T. Björk, S. Jeppesen, A. I. Persson, B. J. Ohlsson, and L. Samuelson, "Role of surface diffusion in chemical beam epitaxy of InAs nanowires," *Nano Letters,* vol. 4, pp. 1961-1964, 2004.

[52] Y. Zhang, M. Aagesen, J. V. Holm, H. I. Jørgensen, J. Wu, and H. Liu, "Self-catalyzed GaAsP nanowires grown on silicon substrates by solid-source molecular beam epitaxy," *Nano letters,* vol. 13, pp. 3897-3902, 2013.

[53] J. Noborisaka, J. Motohisa, and T. Fukui, "Catalyst-free growth of GaAs nanowires by selective-area metalorganic vapor-phase epitaxy," *Applied Physics Letters,* vol. 86, p. 213102, 2005.

[54] A. M. Morales and C. M. Lieber, "A laser ablation method for the synthesis of crystalline semiconductor nanowires," *Science,* vol. 279, pp. 208-211, 1998.

[55] A. Singh, G. Scotti, V. Jokinen, and S. Franssila, "Laser direct writing of thick hybrid polymer microstructures," in *Solid-State Sensors, Actuators and Microsystems (TRANSDUCERS & EUROSENSORS XXVII), 2013 Transducers & Eurosensors XXVII: The 17th International Conference on*, 2013, pp. 1083-1086.

[56] J. Meier, W. S. Mohammed, A. Jugessur, L. Qian, M. Mojahedi, and J. S. Aitchison, "Group velocity inversion in AlGaAs nanowires," *Optics Express,* vol. 15, pp. 12755-12762, 2007.

[57] C. Themistos, M. Rajarajan, B. M. A. Rahman, and K. T. V. Grattan, "Characterization of silica nanowires for optical sensing," *Journal of Lightwave Technology.,* vol. 27, pp. 5537-5542, 2009.

[58] J. Wang and D. Dai, "Highly sensitive Si nanowire-based optical sensor using a Mach–Zehnder interferometer coupled microring," *Optics Letters,* vol. 35, pp. 4229-4231, 2010.

[59] A. W. Snyder and J. Love, *Optical Waveguide Theory* vol. 190. London: Springer, 1983.

[60] M. Koshiba, *Optical Waveguide Analysis*. New York: McGraw-Hill, 1992.

[61] L. Tong, J. Lou, and E. Mazur, "Single-mode guiding properties of subwavelength-diameter silica and silicon wire waveguides," *Optics Express,* vol. 12, pp. 1025-1035, 2004.

[62] J. Lou, L. Tong, and Z. Ye, "Modeling of silica nanowires for optical sensing," *Optics Express,* vol. 13, pp. 2135-2140, 2005.

[63] B. MacCraith, V. Ruddy, C. Potter, B. O'Kelly, and J. McGilp, "Optical waveguide sensor using evanescent wave excitation of fluorescent dye in sol-gel glass," *Electronics Letters,* vol. 27, pp. 1247-1248, 1991.

[64] D. Strickland and G. Mourou, "Compression of amplified chirped optical pulses," *Optics Communications,* vol. 55, pp. 447-449, 1985.

[65] T. A. Birks and Y. W. Li, "The shape of fiber tapers," *Journal of Lightwave Technology,* vol. 10, pp. 432-438, 1992.

[66] J. Knight, G. Cheung, F. Jacques, and T. Birks, "Phase-matched excitation of whispering-gallery-mode resonances by a fiber taper," *Optics Letters,* vol. 22, pp. 1129-1131, 1997.

[67] T. Koch, U. Koren, G. Eisenstein, M. Young, M. Oron, C. Giles*, et al.*, "Tapered waveguide InGaAs/InGaAsP multiple-quantum-well lasers," *IEEE Photonics Technology Letters,* vol. 2, pp. 88-90, 1990.

[68] O. Mitomi, K. Kasaya, and H. Miyazawa, "Design of a single-mode tapered waveguide for low-loss chip-to-fiber coupling," *IEEE Journal of Quantum Electronics,* vol. 30, pp. 1787-1793, 1994.

[69] Y. Shani, C. Henry, R. Kistler, K. Orlowsky, and D. Ackerman, "Efficient coupling of a semiconductor laser to an optical fiber by means of a tapered waveguide on silicon," *Applied Physics Letters,* vol. 55, pp. 2389-2391, 1989.

[70] C.-H. Dong, X.-F. Ren, R. Yang, J.-Y. Duan, J.-G. Guan, G.-C. Guo*, et al.*, "Coupling of light from an optical fiber taper into silver nanowires," *Applied Physics Letters,* vol. 95, pp. 221109-221109-3, 2009.

[71] P. B. I. Duport, D. Khalil, and R. Rimet, "Study of linear tapered waveguides made by ion exchange in glass," *Applied Physics,* vol. 25, pp. 913-918, 1992.

[72] R. K. Winn and J. H. Harris, "Coupling from multimode to single-mode linear waveguides using horn shaped Structures," *IEEE Transaction on Microwave Theory and Techniques,* vol. 23, pp. 92-97, 1975.

[73] H. Zhenguang, R. Srivastava, and R. V. Ramaswamy, "Low-loss small-mode passive waveguides and near-adiabatic tapers in BK7 glass " *Journal of Lightwave Technology,* vol. 7, pp. 1590-1596, 1989.

[74] K. Mizuuchi, K. Yamamoto, and T. Taniuchi, "High-efficiency coupling of laser diodes in tapered proton-exchanged waveguides," *Electronics Letters,* vol. 26, pp. 1992-1994, 1990.

[75] P. Suchoski and R. V. Ramaswamy, "Design of single-mode step-tapered waveguide sections," *IEEE Journal of Quantum Electronics,* vol. 23, pp. 205-211, 1987.

[76] S. Kumar and S. K. Raghuwanshi, "Performance study of parabolically versus exponentially tapered multimode interference coupler," *Trends Opto Electro Optical Commun (STM Journals, India),* vol. 2, pp. 8-17p, 2012.

[77] J.-J. Wu, "A multimode interference coupler with exponentially tapered waveguide," *Progress in Electromagnetics Research C,* vol. 1, pp. 113-122, 2008.

[78] S. Hettrick, J. Wang, C. Li, J. Wilkinson, and D. Shepherd, "An experimental comparison of linear and parabolic tapered waveguide lasers and a demonstration of broad-stripe diode pumping," *Journal of Lightwave Technology,* vol. 22, pp. 845-849, 2004.

[79] A. M. Rashed and D. R. Selviah, "Source misalignment in multimode polymer tapered waveguides for optical backplanes," *Optical Engineering,* vol. 46, pp. 015401(1)-015401(7), 2007.

[80] F. Demami, L. Ni, R. Rogel, A. Salaun, and L. Pichon, "Silicon nanowires synthesis for chemical sensor applications," *Procedia Engineering,* vol. 5, pp. 351-354, 2010.

[81] S. Natarajan, M. Agostinelli, and S. Akbar, "A 14nm logic technology featuring 2nd-generation FinFET transistors, air-gapped interconnects, self-aligned double patterning and a 0.0588 um^2 SRAM cell size," *Int'l Electron Devices Meeting (IEDM),* pp. 3-7, 2014.

[82] S. Novak, C. Parker, D. Becher, M. Liu, M. Agostinelli, M. Chahal*, et al.*, "Transistor aging and reliability in 14nm tri-gate technology," *2015 IEEE International Reliability Physics Symposium (IRPS),* pp. 2F. 2.1-2F. 2.5, 2015.

[83] X. Duan, Y. Huang, Y. Cui, J. Wang, and C. M. Lieber, "Indium phosphide nanowires as building blocks for nanoscale electronic and optoelectronic devices," *Nature,* vol. 409, pp. 66-69, 2001.

[84] W. Lu and C. M. Lieber, "Nanoelectronics from the bottom up," *Nature Materials,* vol. 6, pp. 841-850, 2007.

[85] Y. Huang, X. Duan, Y. Cui, L. J. Lauhon, K.-H. Kim, and C. M. Lieber, "Logic gates and computation from assembled nanowire building blocks," *Science,* vol. 294, pp. 1313-1317, 2001.

[86] A.-C. Salaün, "Silicon Nanowires-based: synthesis, surface functionalization, for chemical and biosensing applications," *NAMIS International Auumn School 2010 Institue of Industrial Science*.

[87] H. Liu, J. Kameoka, S. Verbridge, and H. G. Craighead, "Polymeric Nanowire Architecture and Nanodevices," Cornell University, 2005.

[88] F. Gu, L. Zhang, X. Yin, and L. Tong, "Polymer single-nanowire optical sensors," *Nano Letters,* vol. 8, pp. 2757-2761, 2008.

[89] J. Kameoka, D. Czaplewski, H. Liu, and H. Craighead, "Polymeric nanowire architecture," *Journal of Materials Chemistry,* vol. 14, pp. 1503-1505, 2004.

[90] S. A. Harfenist, S. D. Cambron, E. W. Nelson, S. M. Berry, A. W. Isham, M. M. Crain*, et al.*, "Direct drawing of suspended filamentary micro-and nanostructures from liquid polymers," *Nano Letters,* vol. 4, pp. 1931-1937, 2004.

[91] N. T. Kemp, D. McGrouther, J. W. Cochrane, and R. Newbury, "Bridging the gap: polymer nanowire devices," *Advanced Materials,* vol. 19, pp. 2634-2638, 2007.

[92] H. Fang, D. Yuan, R. Guo, S. Zhang, R. P. Han, S. Das*, et al.*, "Fabrication of patterned polymer nanowire arrays," *ACS Nano,* vol. 5, pp. 1476-1482, 2010.

[93] L. J. Guo, "Nanoimprint lithography: methods and material requirements," *Advanced Materials,* vol. 19, pp. 495-513, 2007.

[94] T. Mårtensson, P. Carlberg, M. Borgström, L. Montelius, W. Seifert, and L. Samuelson, "Nanowire arrays defined by nanoimprint lithography," *Nano Letters,* vol. 4, pp. 699-702, 2004.

[95] V. R. Almeida, Q. Xu, C. A. Barrios, and M. Lipson, "Guiding and confining light in void nanostructure," *Optics Letters,* vol. 29, pp. 1209-1211, 2004.

[96] V. R. Almeida, Q. Xu, R. R. Panepucci, C. A. Barrios, and M. Lipson, "Light guiding in low index materials using high-index-contrast waveguides," in *MRS Proceedings*, 2003.

[97] Q. Xu, V. R. Almeida, R. R. Panepucci, and M. Lipson, "Experimental demonstration of guiding and confining light in nanometer-size low-refractive-index material," *Optics Letters,* vol. 29, pp. 1626-1628, 2004.

[98] T. Fujisawa and M. Koshiba, "Polarization-independent optical directional coupler based on slot waveguides," *Optics Letters,* vol. 31, pp. 56-58, 2006.

[99] T. Fujisawa and M. Koshiba, "Theoretical investigation of ultrasmall polarization-insensitive 1 x 2 multimode interference waveguides based on sandwiched structures," *IEEE Photonics Technology Letters,* vol. 18, pp. 1246-1248, 2006.

[100] T. Fujisawa and M. Koshiba, "All-optical logic gates based on nonlinear slot-waveguide couplers," *JOSA B,* vol. 23, pp. 684-691, 2006.

[101] C. A. Barrios, M. J. Bañuls, V. González-Pedro, K. B. Gylfason, B. Sánchez, A. Griol*, et al.*, "Label-free optical biosensing with slot-waveguides," *Optics Letters,* vol. 33, pp. 708-710, 2008.

[102] S. Lee, S. C. Eom, J. S. Chang, C. Huh, G. Y. Sung, and J. H. Shin, "Label-free optical biosensing using a horizontal air-slot SiNx microdisk resonator," *Optics Express,* vol. 18, pp. 20638-20644, 2010.

[103] R. Bernini, N. Cennamo, A. Minardo, and L. Zeni, "Planar waveguides for fluorescence-based biosensing: optimization and analysis," *IEEE Sensors Journal,* vol. 6, pp. 1218-1226, 2006.

[104] T. Claes, J. G. Molera, K. De Vos, E. Schacht, R. Baets, and P. Bienstman, "Label-free biosensing with a slot-waveguide-based ring resonator in silicon on insulator," *IEEE Photonics Journal,* vol. 1, pp. 197-204, 2009.

[105] P. Muellner, N. Finger, and R. Hainberger, "Lateral leakage in symmetric SOI rib-type slot waveguides," *Optics Express,* vol. 16, pp. 287-294, 2008.

[106] P. Müllner, N. Finger, and R. Hainberger, "Leakage studies on SOI slot waveguide structures," *Integrated Optoelectronic Devices,* pp. 68980U-68980U-10, 2008.

[107] A. Densmore, D.-X. Xu, P. Waldron, S. Janz, P. Cheben, J. Lapointe*, et al.*, "A silicon-on-insulator photonic wire based evanescent field sensor," *IEEE Photonics Technology Letters,* vol. 18, pp. 2520-2522, 2006.

[108] F. Prieto, B. Sepulveda, A. Calle, A. Llobera, C. Domínguez, A. Abad*, et al.*, "An integrated optical interferometric nanodevice based on silicon technology for biosensor applications," *Nanotechnology,* vol. 14, pp. 907-912, 2003.

[109] V. Passaro, F. Dell'Olio, C. Ciminelli, and M. N. Armenise, "Efficient chemical sensing by coupled slot SOI waveguides," *Sensors,* vol. 9, pp. 1012-1032, 2009.

[110] T. Dar, J. Homola, B. M. A. Rahman, and M. Rajarajan, "Label-free slot-waveguide biosensor for the detection of DNA hybridization," *Applied Optics,* vol. 51, pp. 8195-8202, 2012.

[111] C. A. Barrios, K. B. Gylfason, B. Sánchez, A. Griol, H. Sohlström, M. Holgado*, et al.*, "Slot-waveguide biochemical sensor," *Optics Letters,* vol. 32, pp. 3080-3082, 2007.

[112] M. D. Malinsky, K. L. Kelly, G. C. Schatz, and R. P. Van Duyne, "Chain length dependence and sensing capabilities of the localized surface plasmon resonance of silver nanoparticles chemically modified with alkanethiol self-assembled monolayers," *Journal of the American Chemical Society,* vol. 123, pp. 1471-1482, 2001.

[113] S. Elhadj, G. Singh, and R. F. Saraf, "Optical properties of an immobilized DNA monolayer from 255 to 700 nm," *Langmuir,* vol. 20, pp. 5539-5543, 2004.

[114] S.-H. Yang, M. L. Cooper, P. R. Bandaru, and S. Mookherjea, "Giant birefringence in multi-slotted silicon nanophotonic waveguides," *Optics Express,* vol. 16, pp. 8306-8316, 2008.

[115] X. Tu, X. Xu, S. Chen, J. Yu, and Q. Wang, "Simulation demonstration and experimental fabrication of a multiple-slot waveguide," *IEEE Photonics Technology Letters,* vol. 20, pp. 333-335, 2008.

[116] H. Sun, A. Chen, and L. Dalton, "Enhanced evanescent confinement in multiple-slot waveguides and its application in biochemical sensing," *IEEE Photonics Journal,* vol. 1, pp. 48-57, 2009.

[117] L. Vivien, D. Marris-Morini, A. Griol, K. B. Gylfason, D. Hill, J. Alvarez*, et al.*, "Vertical multiple-slot waveguide ring resonators in silicon nitride," *Optics Express,* vol. 16, pp. 17237-17242, 2008.

[118] C. A. Barrios, B. Sánchez, K. B. Gylfason, A. Griol, H. Sohlström, M. Holgado*, et al.*, "Demonstration of slot-waveguide structures on silicon nitride/silicon oxide platform," *Optics Express,* vol. 15, pp. 6846-6856, 2007.

[119] C. A. Barrios, Q. Xu, J. Shakya, C. Manolatou, and M. Lipson, "Compact silicon slot-waveguide disk resonator," in *Lasers and Electro-Optics, 2006 and 2006 Quantum Electronics and Laser Science Conference. CLEO/QELS 2006. Conference on*, 2006, pp. 1-2.

[120] C. A. Barrios and M. Lipson, "Electrically driven silicon resonant light emitting device based on slot-waveguide," *Optics Express,* vol. 13, pp. 10092-10101, 2005.

[121] D. W. Brenner, "Empirical potential for hydrocarbons for use in simulating the chemical vapor deposition of diamond films," *Physical Review B,* vol. 42, pp. 9458-9471, 1990.

[122] B. E. Deal and A. Grove, "General relationship for the thermal oxidation of silicon," *Journal of Applied Physics,* vol. 36, pp. 3770-3778, 1965.

[123] P. Mullner and R. Hainberger, "Structural optimization of silicon-on-insulator slot waveguides," *IEEE Photonics Technology Letters,* vol. 18, pp. 2557-2559, 2006.

[124] R. Sun, P. Dong, N. N. Feng, C. Y. Hong, J. Michel, M. Lipson*, et al.*, "Horizontal single and multiple slot waveguides: optical transmission at λ= 1550 nm," *Optics Express,* vol. 15, pp. 17967-17972, 2007.

[125] J. Galan, P. Sanchis, J. Blasco, and J. Marti, "Study of high efficiency grating couplers for silicon-based horizontal slot waveguides," *IEEE Photonics Technology Letters,* vol. 20, pp. 985-987, 2008.

[126] D. M. H. Leung, N. Kejalakshmy, B. M. A. Rahman, and K. T. V. Grattan, "Rigorous modal analysis of silicon strip nanoscale waveguides," *Optics Express,* vol. 18, pp. 8528-8539, 2010.

[127] F. Patolsky, G. Zheng, and C. M. Lieber, "Nanowire-based biosensors," *Analytical Chemistry,* vol. 78, pp. 4260-4269, 2006.

[128] R. B. Thompson, *Fluorescence Sensors and Biosensors*: CRC Press, 2005.

[129] W. G. Cox and V. L. Singer, "Fluorescent DNA hybridization probe preparation using amine modification and reactive dye coupling," *Biotechniques,* vol. 36, pp. 114-123, 2004.

[130] P. Alivisatos, "The use of nanocrystals in biological detection," *Nature Biotechnology,* vol. 22, pp. 47-52, 2004.

[131] X. Gao, W. C. W. Chan, and S. Nie, "Quantum-dot nanocrystals for ultrasensitive biological labeling and multicolor optical encoding," *Journal of Biomedical Optics,* vol. 7, pp. 532-537, 2002.

[132] N. Elfstrom, R. Juhasz, I. Sychugov, T. Engfeldt, A. E. Karlstrom, and J. Linnros, "Surface charge sensitivity of silicon nanowires: size dependence," *Nano Letters,* vol. 7, pp. 2608-12, Sep 2007.

[133] G. Rong, A. Najmaie, J. E. Sipe, and S. M. Weiss, "Nanoscale porous silicon waveguide for label-free DNA sensing," *Biosensors and Bioelectronics,* vol. 23, pp. 1572-1576, 2008.

[134] G. Veldhuis, O. Parriaux, H. Hoekstra, and P. Lambeck, "Sensitivity enhancement in evanescent optical waveguide sensors," *Journal of lightwave technology,* vol. 18, p. 677, 2000.

[135] J. Wang, S. He, and D. Dai, "Silicon-nanowire-based optical sensor with high sensitivity and large measurement range by using Mach-Zehnder interferometer-coupled microring," in *Asia Communications and Photonics Conference and Exhibition*, 2010, pp. 79900V-79900V-6.

[136] L. Tong, R. R. Gattass, J. B. Ashcom, S. He, J. Lou, M. Shen*, et al.*, "Subwavelength-diameter silica wires for low-loss optical wave guiding," *Nature,* vol. 426, pp. 816-819, 2003.

[137] K. M. Byun, S. J. Kim, and D. Kim, "Design study of highly sensitive nanowire-enhanced surface plasmon resonance biosensors using rigorous coupled wave analysis," *Optics Express,* vol. 13, pp. 3737-3742, 2005.

[138] K. Kim, S. J. Yoon, and D. Kim, "Nanowire-based enhancement of localized surface plasmon resonance for highly sensitive detection: a theoretical study," *Optics Express,* vol. 14, pp. 12419-12431, 2006.

[139] H. Becker and L. E. Locascio, "Polymer microfluidic devices," *Talanta,* vol. 56, pp. 267-287, 2002.

[140] X. Ren, M. Bachman, C. Sims, G. Li, and N. Allbritton, "Electroosmotic properties of microfluidic channels composed of poly (dimethylsiloxane)," *Journal of Chromatography B: Biomedical Sciences and Applications,* vol. 762, pp. 117-125, 2001.

[141] C.-W. Tsao and D. L. DeVoe, "Bonding of thermoplastic polymer microfluidics," *Microfluidics and Nanofluidics,* vol. 6, pp. 1-16, 2009.

[142] R. Feng and R. J. Farris, "Influence of processing conditions on the thermal and mechanical properties of SU8 negative photoresist coatings," *Journal of Micromechanics and Microengineering,* vol. 13, pp. 80-88, 2003.

[143] T. Sikanen, S. Tuomikoski, R. A. Ketola, R. Kostiainen, S. Franssila, and T. Kotiaho, "Characterization of SU-8 for electrokinetic microfluidic applications," *Lab on a Chip,* vol. 5, pp. 888-896, 2005.

[144] G. Grützner, J. Klein, M. Vogler, and A. Schleunitz, "UV-curable hybrid polymers for optical applications: technical challenges, industrial solutions, and future developments," in *SPIE MOEMS-MEMS*, 2014, pp. 897406-897406-12.

[145] *UV-Curable Hybrid Polymers for Micro Optical Components*.

[146] K.-H. Haas and K. Rose, "Hybrid inorganic/organic polymers with nanoscale building blocks: precursors, processing, properties and applications," *Reviews on Advanced Materials Science,* vol. 5, pp. 47-52, 2003.

[147] D. D. L. Chung, *Composite Materials for Electromagnetic Applications*. London: Springer, 2003.

[148] !!! INVALID CITATION !!! {}.

[149] C. Sanchez, P. Belleville, M. Popall, and L. Nicole, "Applications of advanced hybrid organic–inorganic nanomaterials: from laboratory to market," *Chemical Society Reviews,* vol. 40, pp. 696-753, 2011.

[150] K. Mohamed, M. Alkaisi, and R. Blaikie, "The replication of three dimensional structures using UV curable nanoimprint lithography," *Journal of Vacuum Science & Technology B,* vol. 26, pp. 2500-2503, 2008.

[151] S. Aura, T. Sikanen, T. Kotiaho, and S. Franssila, "Novel hybrid material for microfluidic devices," *Sensors and Actuators B: Chemical,* vol. 132, pp. 397-403, 2008.

[152] T. Sikanen, S. Aura, L. Heikkila, T. Kotiaho, S. Franssila, and R. Kostiainen, "Hybrid ceramic polymers: New, nonbiofouling, and optically transparent materials for microfluidics," *Analytical Chemistry,* vol. 82, pp. 3874-3882, 2010.

[153] R. Houbertz, G. Domann, C. Cronauer, A. Schmitt, H. Martin, J.-U. Park*, et al.*, "Inorganic–organic hybrid materials for application in optical devices," *Thin Solid Films,* vol. 442, pp. 194-200, 2003.

[154] R. Buestrich, F. Kahlenberg, M. Popall, P. Dannberg, R. Müller-Fiedler, and O. Rösch, "ORMOCER® s for optical interconnection technology," *Journal of Sol-Gel Science and Technology,* vol. 20, pp. 181-186, 2001.

[155] M. Popall, A. Dabek, M. Robertsson, S. Valizadeh, O. Hagel, R. Buestrich*, et al.*, "ORMOCER® S–inorganic-organic hybrid materials for e/o-interconnection-technology," *Molecular Crystals and Liquid Crystals,* vol. 354, pp. 123-142, 2000.

[156] M. Wang, J. Hiltunen, S. Uusitalo, J. Puustinen, J. Lappalainen, P. Karioja*, et al.*, "Fabrication of optical inverted-rib waveguides using UV-imprinting," *Microelectronic Engineering,* vol. 88, pp. 175-178, 2011.

[157] M. Fukuda, T. Aihara, K. Yamaguchi, Y. Y. Ling, K. Miyaji, and M. Tohyama, "Light detection enhanced by surface plasmon resonance in metal film," *Applied Physics Letters,* vol. 96, pp. 153107(1)-153107(3), 2010.

[158] J. Homola, "Present and future of surface plasmon resonance biosensors," *Analytical and Bioanalytical Chemistry,* vol. 377, pp. 528-539, 2003.

[159] J. Homola, "Surface plasmon resonance sensors for detection of chemical and biological species," *Chemical Reviews,* vol. 108, pp. 462-493, 2008.

[160] R. J. Green, R. A. Frazier, K. M. Shakesheff, M. C. Davies, C. J. Roberts, and S. J. Tendler, "Surface plasmon resonance analysis of dynamic biological interactions with biomaterials," *Biomaterials,* vol. 21, pp. 1823-1835, 2000.

[161] P. Englebienne, A. V. Hoonacker, and M. Verhas, "Surface plasmon resonance: principles, methods and applications in biomedical sciences," *Journal of Spectroscopy,* vol. 17, pp. 255-273, 2003.

[162] C. R. Lavers and J. S. Wilkinson, "A waveguide-coupled surface-plasmon sensor for an aqueous environment," *Sensors and Actuators B: Chemical,* vol. 22, pp. 75-81, 1994.

[163] J. Homola, J. Čtyroký, M. Skalský, J. Hradilova, and P. Kolářová, "A surface plasmon resonance based integrated optical sensor," *Sensors and Actuators B: Chemical,* vol. 39, pp. 286-290, 1997.

[164] F. Liu, Y. Rao, Y. Huang, W. Zhang, and J. Peng, "Coupling between long range surface plasmon polariton mode and dielectric waveguide mode," *Applied Physics Letters,* vol. 90, p. 141101, 2007.

[165] S. Patskovsky, A. V. Kabashin, M. Meunier, and J. H. Luong, "Silicon-based surface plasmon resonance sensing with two surface plasmon polariton modes," *Applied Optics,* vol. 42, pp. 6905-6909, 2003.

[166] J. J. Burke, G. I. Stegeman, and T. Tamir, "Surface-polariton-like waves guided by thin, lossy metal films," *Physical Review B,* vol. 33, p. 5186, 1986.

[167] G. I. Stegeman, D. G. Hall, and J. J. Burke, "Surface-polaritonlike waves guided by thin, lossy metal films," *Optics Letters,* vol. 8, pp. 383-385, 1983.

[168] J. Čtyroký, J. Homola, P. Lambeck, S. Musa, H. Hoekstra, R. Harris*, et al.*, "Theory and modelling of optical waveguide sensors utilising surface plasmon resonance," *Sensors and Actuators B: Chemical,* vol. 54, pp. 66-73, 1999.

[169] M. Weisser, B. Menges, and S. Mittler-Neher, "Refractive index and thickness determination of monolayers by multi mode waveguide coupled surface plasmons," *Sensors and Actuators B: Chemical,* vol. 56, pp. 189-197, 1999.

[170] M. Hochberg, T. Baehr-Jones, C. Walker, and A. Scherer, "Integrated plasmon and dielectric waveguides," *Optics Express,* vol. 12, pp. 5481-5486, 2004.

[171] S. Patskovsky, A. V. Kabashin, M. Meunier, and J. H. Luong, "Near-infrared surface plasmon resonance sensing on a silicon platform," *Sensors and Actuators B: Chemical,* vol. 97, pp. 409-414, 2004.

[172] P. I. Nikitin, A. Beloglazov, M. Valeiko, J. Creighton, A. Smith, N. Sommerdijk*, et al.*, "Silicon-based surface plasmon resonance chemical sensors," *Sensors and Actuators B: Chemical,* vol. 38, pp. 53-57, 1997.

[173] P. I. Nikitin, A. Beloglazov, M. Valeiko, J. Creighton, and J. D. Wright, "Silicon-based surface plasmon resonance combined with surface-enhanced Raman scattering for chemical sensing," *Review of Scientific Instruments,* vol. 68, pp. 2554-2557, 1997.

[174] I. Abdulhalim, M. Zourob, and A. Lakhtakia, "Surface plasmon resonance for biosensing: a mini-review," *Electromagnetics,* vol. 28, pp. 214-242, 2008.

[175] R. D. Harris and J. S. Wilkinson, "Waveguide surface plasmon resonance sensors," *Sensors and Actuators B: Chemical,* vol. 29, pp. 261-267, 1995.

[176] A. Krishnan, T. Thio, T. Kim, H. Lezec, T. Ebbesen, P. Wolff*, et al.*, "Evanescently coupled resonance in surface plasmon enhanced transmission," *Optics Communications,* vol. 200, pp. 1-7, 2001.

[177] K. Byun, S. Kim, and D. Kim, "Design study of highly sensitive nanowire-enhanced surface plasmon resonance biosensors using rigorous coupled wave analysis," *Optics Express,* vol. 13, pp. 3737-3742, 2005.

[178] L. He, M. D. Musick, S. R. Nicewarner, F. G. Salinas, S. J. Benkovic, M. J. Natan*, et al.*, "Colloidal Au-enhanced surface plasmon resonance for ultrasensitive detection of DNA hybridization," *Journal of the American Chemical Society,* vol. 122, pp. 9071-9077, 2000.

[179] S. Wu, H. Ho, W. Law, C. Lin, and S. Kong, "Highly sensitive differential phase-sensitive surface plasmon resonance biosensor based on the Mach–Zehnder configuration," *Optics Letters,* vol. 29, pp. 2378-2380, 2004.

[180] Y. S. Chu, W. H. Hsu, C. W. Lin, and W. S. Wang, "Surface plasmon resonance sensors using silica-on-silicon optical waveguides," *Microwave and Optical Technology Letters,* vol. 48, pp. 955-957, 2006.

[181] P. Debackere, S. Scheerlinck, P. Bienstman, and R. Baets, "Surface plasmon interferometer in silicon-on-insulator: novel concept for an integrated biosensor," *Optics Express,* vol. 14, pp. 7063-7072, 2006.

[182] P. Debackere, R. Baets, and P. Bienstman, "Bulk sensing experiments using a surface-plasmon interferometer," *Optics Letters,* vol. 34, pp. 2858-2860, 2009.

[183] P. Debackere, D. Taillaert, K. De Vos, S. Scheerlinck, P. Bienstman, and R. Baets, "Si based waveguide and surface plasmon sensors," *Integrated Optoelectronic Devices 2007,* pp. 647719-647719-10, 2007.

[184] J. Dostalek, J. Čtyroký, J. Homola, E. Brynda, M. Skalský, P. Nekvindova*, et al.*, "Surface plasmon resonance biosensor based on integrated optical waveguide," *Sensors and Actuators B: Chemical,* vol. 76, pp. 8-12, 2001.

[185] X. Yin and L. Hesselink, "Goos-Hänchen shift surface plasmon resonance sensor," *Applied Physics Letters,* vol. 89, pp. 261108(1)-261108(3), 2006.

[186] W. R. Headley, G. T. Reed, S. Howe, A. Liu, and M. Paniccia, "Polarization-independent optical racetrack resonators using rib waveguides on silicon-on-insulator," *Applied Physics Letters,* vol. 85, pp. 5523-5525, 2004.

[187] A. Wexler, "Computation of electromagnetic fields," *IEEE Transactions on Microwave Theory and Techniques,* vol. 17, pp. 416-439, 1969.

[188] N. Morita, J. R. Mautz, and N. Kumagai, *Integral Equation Methods for Electromagnetics*. Boston: Artech house, 1990.

[189] O. C. Zienkiewicz and R. L. Taylor, *The Finite Element Method* vol. 3. London: McGraw-hill 1977.

[190] M. Feit and J. Fleck Jr, "Computation of mode properties in optical fiber waveguides by a propagating beam method," *Applied Optics,* vol. 19, pp. 1154-1164, 1980.

[191] T. Okoshi and S. Kitazawa, *The beam propagation method*. Boston: Artech House, 1990.

[192] M. Feit and J. Fleck, "Computation of mode properties in optical fiber waveguides by a propagating beam method," *Applied Optics,* vol. 19, pp. 1154-1164, 1980.

[193] S. S. A. Obayya, B. M. A. Rahman, and H. A. El-Mikati, "New full-vectorial numerically efficient propagation algorithm based on the finite element method," *Journal of Lightwave Technology,* vol. 18, pp. 409-414, 2000.

[194] D. H. Choi and W. J. Hoefer, "The finite-difference-time-domain method and its application to eigenvalue problems," *IEEE Transactions on Microwave Theory and Techniques,* vol. 34, pp. 1464-1470, 1986.

[195] D. Gallagher and P. Design, "Photonic CAD matures," *IEEE LEOS NewsLetter,* pp. 8-14, 2008.

[196] J.-M. Jin and J. Jin, *The Finite Element Method in Electromagnetics*. New York: Wiley 2002.

[197] T. B. Koch, J. B. Davies, and D. Wickramasinghe, "Finite element/finite difference propagation algorithm for integrated optical device," *Electronics Letters,* vol. 25, pp. 514-516, 1989.

[198] K. Kawano and T. Kitoh, *Introduction to Optical Waveguide Analysis: Solving Maxwell's Equation and The Schrödinger Equation*. New york: John Wiley & Sons, 2001.

[199] B. M. A. Rahman and J. B. Davies, "Finite-element solution of integrated optical waveguides," *Journal of Lightwave Technology,* vol. 2, pp. 682-688, 1984.

[200] B. M. A. Rahman and J. B. Davies, "Penalty function improvement of waveguide solution by finite elements," *IEEE Transactions on Microwave Theory and Techniques,* vol. 32, pp. 922-928, 1984.

[201] C. Themistos, B. M. A. Rahman, and K. T. V. Grattan, "Finite-element analysis of lossy TE-TM modes in metal-clad optical waveguides," *Applied Optics,* vol. 37, pp. 5747-54, Aug 20 1998.

[202] P. B. Johnson and R.-W. Christy, "Optical constants of the noble metals," *Physical Review B,* vol. 6, pp. 4370-4379, 1972.

[203] M. J. Madou, *Fundamentals of Microfabrication: The Science of Miniaturization*. Florida: CRC press, 2002.

[204] G. Celler and S. Cristoloveanu, "Frontiers of silicon-on-insulator," *Journal of Applied Physics,* vol. 93, pp. 4955-4978, 2003.

[205] G. T. Reed and A. P. Knights, *Silicon Photonics: An Introduction*. London: John Wiley & Sons, 2004.

[206] J. Geisler, G. Beaven, and J. P. Boutruche, *Optical Fibres: EPO Applied Technology Series* vol. 5. Oxford: Elsevier, 2014.

[207] K. Oh and U. C. Paek, *Silica Optical Fiber Technology for Devices and Components: Design, Fabrication, and International Standards*. New Jersey: John Wiley & Sons, 2012.

[208] W. Shi, S. Han, W. Huang, and J. Yu, "High mobility organic field-effect transistor based on water-soluble deoxyribonucleic acid via spray coating," *Applied Physics Letters,* vol. 106, pp. 043303.1-043303.5, 2015.

[209] K. P. R. Nilsson and O. Inganäs, "Chip and solution detection of DNA hybridization using a luminescent zwitterionic polythiophene derivative," *Nature Materials,* vol. 2, pp. 419-424, 2003.

[210] N. Liu, M. Mesch, T. Weiss, M. Hentschel, and H. Giessen, "Infrared perfect absorber and its application as plasmonic sensor," *Nano Letters,* vol. 10, pp. 2342-2348, 2010.

[211] J. Xie, X. Jiang, Y. Zhong, Y. Lu, S. Wang, X. Wei*, et al.*, "Stem-loop DNA-assisted silicon nanowires-based biochemical sensors with ultra-high sensitivity, specificity, and multiplexing capability," *Nanoscale,* vol. 6, pp. 9215-9222, 2014.

[212] S. Golmohammadi and A. Ahmadivand, "Fano resonances in compositional clusters of aluminum nanodisks at the UV spectrum: a route to design efficient and precise biochemical sensors," *Plasmonics,* vol. 9, pp. 1447-1456, 2014.

[213] S. Boonruang and W. S. Mohammed, "Effect of the cladding layer on resonance response in guided mode resonance structures and its sensing applications," *JOSA B,* vol. 28, pp. 671-678, 2011.

[214] S. Zumdahl, *Chemistry*. New York: Houghton Mifflin, 1997.

[215] H. Raether, *Surface Plasmons on Smooth Surfaces*. New York: Springer, 1988.

[216] F. Wooten, *Optical Properties of Solids*. New York: Academic press, 2013.

[217] D. M. Pozar, *Microwave Engineering*. New Jersey: John Wiley & Sons, 2009.

[218] J. Tang and S. He, "Optical Magnetic Response in a Single Metal Nanobrick," *arXiv preprint arXiv:1102.2692,* 2011.

[219] A. D. McNaught, *Compendium of Chemical Terminology* vol. 1669. Oxford: Blackwell Science 1997.

[220] P. K. Tien, "Light waves in thin films and integrated optics," *Applied Optics,* vol. 10, pp. 2395-2413, 1971.

[221] J. R. Howell, R. Siegel, and M. P. Menguc, *Thermal Radiation Heat Transfer*. London: CRC press, 2011.

[222] D. E. Aspnes and A. Studna, "Dielectric functions and optical parameters of si, ge, gap, gaas, gasb, inp, inas, and insb from 1.5 to 6.0 ev," *Physical review B,* vol. 27, p. 985, 1983.

[223] I. Malitson, "Interspecimen comparison of the refractive index of fused silica," *Josa,* vol. 55, pp. 1205-1209, 1965.

[224] D. Marcuse, "Mode conversion caused by surface imperfections of a dielectric slab waveguide," *Bell System Technical Journal,* vol. 48, pp. 3187-3215, 1969.